

## AN ABSTRACT OF THE DISSERTATION OF

Steven A. Czyz for the degree of Doctor of Philosophy in Nuclear Engineering  
presented on November 22, 2019.

Title: A Beta-Gamma Radioxenon Detection System using Ultra-Bright Inorganic  
Scintillators and Solid State Detectors

Abstract approved:

---

Abi T. Farsoni

The atmospheric detection of four radioxenon isotopes ( $^{131\text{m}}\text{Xe}$ ,  $^{133\text{m}}\text{Xe}$ ,  $^{133}\text{Xe}$ , and  $^{135}\text{Xe}$ ) released during a nuclear detonation is a key tool utilized by the Comprehensive Nuclear-Test-Ban Treaty Organization (CTBTO) to identify clandestine nuclear weapon testing activity. These radioxenon isotopes all decay via the near-simultaneous release of an electron and a photon, which allows them to be easily discriminated from background at extremely low concentrations ( $\leq 1 \text{ mBq/m}^3$ ). Detection systems employed in the International Monitoring System (IMS) that utilize this technique, though effective, make use of costly and archaic technologies which yield suboptimal energy resolutions and are subject to memory effect.

The PIPS-SrI<sub>2</sub>(Eu) is a prototype radioxenon detection system that makes use of modern technologies to address these problems and work towards improving performance. This system utilizes custom D-shaped SrI<sub>2</sub>(Eu) scintillators coupled to silicon photomultipliers as photon detectors and a pair of passivated implanted planar

silicon wafers for electron detection. Coincidences are identified in hardware in real-time using a field programmable gate array-based multi-channel digital pulse processor. The system demonstrates a memory effect of  $0.318 \pm 0.026\%$ , a  $\sim 15\times$  improvement relative to plastic scintillators. Minimum Detectable Concentration (MDC) estimates in terms of  $\text{mBq/m}^3$  air calculated for  $^{131\text{m}}\text{Xe}$ ,  $^{133\text{m}}\text{Xe}$ ,  $^{133}\text{Xe}$ , and  $^{135}\text{Xe}$ , respectively, using the parameters from the Xenon International gas processing unit and assuming a black sample and zero memory effect yield sensitivities of  $0.12 \pm 0.03$ ,  $0.27 \pm 0.05$ ,  $0.15 \pm 0.02$ , and  $1.00 \pm 0.08$ , respectively. These optimistic MDC estimates compare well with other radioxenon detection systems utilized in the International Monitoring System (IMS). A new spectral deconvolution approach using a maximum likelihood and region sectioning, designated Regional Spectral Deconvolution (RSD), was also designed and tested. This method increased convergence speed by nearly two orders of magnitude and performed similarly to traditional spectral deconvolution methods in terms of accuracy. However, RSD did not demonstrate significant improvement in low count rate situations that was expected when compared to these traditional spectral deconvolution methods.

©Copyright by Steven A. Czyz

November 22, 2019

All Rights Reserved

A Beta-Gamma Radioxenon Detection System using Ultra-Bright Inorganic  
Scintillators and Solid State Detectors

by  
Steven A. Czyz

A DISSERTATION  
submitted to  
Oregon State University

in partial fulfillment of  
the requirements for the  
degree of

Doctor of Philosophy

Presented November 22, 2019

Commencement June 2020

Doctor of Philosophy dissertation of Steven A. Czyz presented on November 22,  
2019

APPROVED:

---

Major Professor, representing Nuclear Engineering

---

Head of the School of Nuclear Science of Engineering

---

Dean of the Graduate School

I understand that my dissertation will become part of the permanent collection of Oregon State University libraries. My signature below authorizes release of my dissertation to any reader upon request.

---

Steven A. Czyz, Author

## ACKNOWLEDGEMENTS

It is interesting to me how many points a life can pivot on. As I sit in a conference hotel in Germany, writing this and reflecting on my graduate career, I see that so many people have contributed to who and what I have become and have put me on the path that has led me to here. It is worth saying that I don't regret a thing.

-----

I would like to acknowledge my advisor, Dr. Abi Farsoni, with my deepest gratitude. His patient guidance, but even more so his intuition of when to step aside to let me struggle and learn independently, have pushed me to be self-sufficient and to develop a skillset that will follow me for the rest of my career. Learning, designing, building, testing, analyzing, then traveling, presenting, networking: being his student has impacted my life in so many ways, and I won't ever stop being thankful for that.

Of course, my family. Knowing that your family is proud of you, truly proud of you, that you've achieved what they've always believed that you could, is a sublime thing. But who am I, if not the person they raised me to be? I am so lucky to have the family that I do; one that entertained my childhood interests to read and to learn, one that has supported me through my whole life, and one that I always look forward to being with for the late night talks, the classic dinner spreads, and the endless laughs.

The friends that were there in the beginning, the friends that are there in the end. They are the ones that make the good times the best times, that make the bad times bearable, and for everything in between. It always astounds me how many people I have in my corner, and I only hope that I can be there for them in the very same way.

My lab mates, for helping me in a myriad of ways through my studies. Specifically, I'd like to acknowledge Harish Gadey, for being right there with me during the most exciting and most deflating experiments as well as for keeping my head in the right place when life and research took sour turns. I'd also like to acknowledge the folks at PNNL, specifically Matt Cooper, for helping me wrestle with and understand some of the more frustrating and involved data analysis.

My doctoral committee: Dr. Kenneth Krane, Dr. Haori Yang, Dr. Camille Palmer, and Dr. Solomon Yim, for providing me feedback and making sure that my work was the best that it could be.

Finally, the Consortium of Verification Technology, for providing the financial support that allowed me to pursue my graduate education.

## TABLE OF CONTENTS

1.	INTRODUCTION.....	1
1.1.	The Problem and the Solution.....	1
1.2.	Continuing Efforts .....	2
1.3.	Goals .....	3
2.	LITERATURE REVIEW.....	5
2.1.	Physics of Radioxenon.....	5
2.1.1.	Production .....	5
2.1.1.1.	Other Gases.....	7
2.1.2.	Emission from Underground.....	7
2.1.3.	Radioactive Decay.....	8
2.1.3.1.	Beta Decay and Isomeric Transitions.....	8
2.1.3.2.	True Coincidence and Beta-Gamma Coincidence.....	10
2.1.4.	Interference.....	12
2.2.	Detectors and Hardware.....	12
2.2.1.	Scintillation Detectors .....	12
2.2.1.1.	Gamma Spectroscopy .....	16
2.2.1.2.	SrI <sub>2</sub> (Eu).....	17
2.2.2.	Solid State Detectors .....	21
2.2.2.1.	Semiconductor Physics.....	21
2.2.2.2.	Silicon Photomultipliers (SiPMs).....	25
2.2.2.3.	PIPSBox.....	27
2.2.3.	Field Programmable Gate Arrays (FPGAs) .....	30



2.3.	Algorithms and Calculations.....	32
2.3.1.	Radioxenon Identification- ROI Method .....	32
2.3.2.	Statistical Methods .....	33
2.3.2.1.	Statistical Methods- Least Squares.....	35
2.3.2.2.	Statistical Methods- Maximum Likelihood.....	35
2.3.2.3.	Hybrid and Other Methods .....	37
2.3.3.	MDC Calculation .....	38
2.3.4.	Signal Processing .....	41
2.3.4.1.	Digital Filtering and Filter Design.....	41
2.3.4.2.	Triggering .....	44
2.3.4.3.	Coincidence Identification.....	45
2.4.	Previous Noble Gas Detector Design Principles .....	46
2.4.1.	Gas Processing Unit .....	46
2.4.2.	Beta-Gamma Coincidence.....	47
2.4.2.1.	ARSA and the Xenon International.....	48
2.4.2.2.	SAUNA .....	50
2.4.2.3.	ARIX .....	52
2.4.2.4.	Phoswich, and others .....	53
2.4.2.5.	Alternative Materials .....	54
2.4.3.	Gamma Spectroscopy.....	56
2.4.3.1.	SPALAX <sup>TM</sup> .....	56
2.4.4.	Non-Radioxenon Detectors .....	57
2.4.5.	Previous Oregon State University Detection Systems .....	58
2.4.5.1.	TECZT.....	58
2.4.5.2.	CASP .....	60

2.4.5.3.	Stilbene-CZT .....	61
2.4.5.4.	PIPS-CZT .....	62
3.	MATERIALS AND METHODS .....	65
3.1.	Detector Infrastructure .....	67
3.1.1.	Photon Detector: $\text{SrI}_2(\text{Eu})+\text{SiPMs}$ .....	67
3.1.2.	Electron Detector: PIPSBox <sup>TM</sup> .....	71
3.1.3.	Eight-Channel Digital Pulse Processor (DPP8) .....	72
3.1.3.1.	Design and Function.....	72
3.1.3.2.	Coincidence Module.....	75
3.1.4.	Power Supply .....	76
3.1.5.	Holder and Detector Setup .....	78
3.1.6.	Vacuum Pump .....	80
3.2.	Simulation .....	82
3.2.1.	PTRAC .....	83
3.3.	Statistical Modeling .....	83
3.3.1.	Regional Spectral Deconvolution (RSD) .....	83
3.3.2.	Python Package .....	85
3.4.	Experimentation .....	86
3.4.1.	Characterization of $\text{SrI}_2(\text{Eu})$ .....	87
3.4.2.	Characterization of PIPSBox .....	87
3.4.3.	Characterization of Full Detector.....	88
3.4.3.1.	TRIGA and Sample Preparation.....	88
3.4.3.2.	Efficiency.....	89
4.	RESULTS.....	91

4.1.	Simulation .....	91
4.1.1.	Model .....	91
4.1.2.	Solid Angle.....	91
4.1.3.	Spectra.....	92
4.1.3.1.	Backscatter Reduction .....	94
4.1.3.2.	Efficiency.....	96
4.2.	SrI <sub>2</sub> (Eu)+SiPM Characterization .....	97
4.2.1.	Digital Integrating Board .....	97
4.2.1.1.	Design.....	97
4.2.1.2.	Temperature Study .....	98
4.2.1.3.	Initial Characterization of the SrI <sub>2</sub> (Eu) Crystals.....	100
4.2.1.4.	Pulse Shape Investigation.....	101
4.2.1.5.	Digital Integration Methodology .....	103
4.2.1.6.	Positional Dependence and <sup>137</sup> Cs Spectrum .....	103
4.2.2.	Analog Integrating Board.....	106
4.2.2.1.	Preamplifier Board Design .....	111
4.2.2.2.	Pulse Shape and Oscillations.....	112
4.2.3.	CSP Time Constant Comparison.....	114
4.2.3.1.	Comparison Using Digital Equipment .....	114
4.2.3.2.	Comparison Using Analog Equipment.....	117
4.2.4.	Coincidence Timing Analysis .....	118
4.3.	PIPSBox Characterization .....	119
4.3.1.	Preamplifier and Noise Threshold.....	119
4.4.	Evaluation of Full Detector.....	124
4.4.1.	Background .....	124

4.4.2.	Radioxenon Measurements: $^{131\text{m}}\text{Xe}$ .....	125
4.4.2.1.	Coincidence Measurement .....	125
4.4.2.2.	PIPSBox Backscatter .....	128
4.4.2.3.	PIPSBox Timing Response .....	129
4.4.3.	Radioxenon Measurements: $^{133/133\text{m}}\text{Xe}$ .....	130
4.4.3.1.	Coincidence Measurement .....	131
4.4.3.2.	Memory Effect Evaluation .....	137
4.4.4.	Radioxenon Measurements: $^{135}\text{Xe}$ .....	138
4.4.4.1.	Coincidence Measurement .....	138
4.4.5.	Constant Fraction Discriminator .....	140
4.5.	MDC Calculations .....	145
4.6.	Statistical Methods.....	148
4.6.1.	Code Structure.....	148
4.6.2.	Initial Investigations.....	150
4.6.3.	Involved Investigations .....	152
5.	CONCLUSIONS AND FUTURE WORK .....	157
	Bibliography .....	159
	Appendix.....	181

## LIST OF FIGURES

<u>Figure</u>	<u>Page</u>
Fig. 1. The PIPS-SrI <sub>2</sub> (Eu) radioxenon detection system prototype .....	3
Fig. 2. Multiple ratio isotope plot with a separation line indicating the different ratios of radioxenon isotope activity associated with different radioxenon sources [25]. A unique plot may be defined comparing the ratios for any of the radioxenon isotopes .....	5
Fig. 3. The beta spectrum of <sup>36</sup> Cl [39] .....	9
Fig. 4. Decay scheme of <sup>60</sup> Co, exemplifying coincident decay through the emission of a beta immediately followed by cascading photons [42].....	10
Fig. 5. The energy structure of an inorganic scintillator [47] .....	14
Fig. 6. The contributions of the fast and the slow de-excitation components to a total scintillation pulse [51]. Scintillators can have more than one slow component .....	16
Fig. 7. The same peak with three different energy resolutions. All peaks integrate to 1 .....	16
Fig. 8. The mode of photon interaction in a medium as it relates to incident energy of the photon and atomic number, or Z number, of the medium [42] .....	17
Fig. 9. (a) Light non-proportionality of SrI <sub>2</sub> (Eu); (b) relative spectrum shift vs. temperature for a variety of energies [61]; (c) energy resolution with respect to temperature [62]; (d) energy non-proportionality measured (markers) and simulated (dashed lines) for electrons (red dashed line, blue markers) and photons (black dashed line, red and green markers) [59].....	19
Fig. 10. Absorbance and radioluminescence of the Eu <sup>2+</sup> impurity in SrI <sub>2</sub> (Eu) crystals. The overlap of the absorbance and radioluminescence contributes to absorption and reemission of scintillation light and results in a long decay time in large crystals [56] .....	21
Fig. 11. (a) A p-type semiconductor lattice (left) and energy diagram (right); (b) an n-type semiconductor lattice (left) and energy diagram (right) [68] .....	23
Fig. 12. (a) Depletion region in a p-n semiconductor, with no external bias applied; (b) reverse biasing configuration applied to improve the proportionality and performance of a semiconductor detector, with radiation	

creating an electron/hole pair in the depletion region. Note the increased width of the depletion region due to the reverse bias [67] .....	25
Fig. 13. Cross section of a Hamamatsu n-on-p photodiode experiencing an avalanche [73] .....	25
Fig. 14. (a) Physical layout of a 1x1 SiPM. Typical SiPMs are comprised of several thousand unique APDs connected in parallel [75]; (b) cross section of an SiPM [76].....	26
Fig. 15. PIPSBox detector: (left) silicon wafer detector in aluminum assembly, without carbon window; (right) fully assembled PIPSBox gas cell, with carbon window [17].....	28
Fig. 16. Sketches indicating the PIPSBox dimensions and internal structure [71] ....	28
Fig. 17. The internal structure of an FPGA, with configurable logic blocks (CLBs) defining the internal logic and I/O Blocks (IOBs) providing means for the FPGA to communicate with the surrounding circuitry [98].....	31
Fig. 18. (a) Regions of interest defined exclusively indicating the radioxenon isotope signatures on a 2D coincidence histogram plot [40]; (b) 10 regions of interest defined for the radioxenon isotopes of interest, plus $^{214}\text{Pb}$ (the radon daughter), on a 2D coincidence histogram plot without background [102] .....	33
Fig. 19. The critical level $L_c$ and the detection level $L_d$ , with the acceptable amount of false positives denoted by $\alpha$ and false negatives denoted by $\beta$ . $k$ are abscissa for the normal distribution, $\mu$ is the mean for the source (S) and background (B), $\sigma$ is the standard deviation of the normal distribution, and $H$ is the hypothesis being presented. Note that $\alpha$ and $\beta$ do not have to be the same, as is the case here [117].....	39
Fig. 20. Convolution process using a four-element filter on an incoming stream of data [119] .....	42
Fig. 21. Hardware implementation of a four-element filter. <i>Reg</i> indicates a shift register that delays the input signal by one clock cycle [119].....	43
Fig. 22. Trigger walking, where using a leading edge trigger will result in different trigger times for pulses with a fixed rise time but different amplitudes [122].....	44
Fig. 23. A depiction of a constant fraction discriminator being used on a pulse from a charge sensitive preamplifier. The blue pulse is the original, but temporally shifted, pulse, the red is the copied and scaled pulse, and the black is the subtracted pulse.....	45

Fig. 24. Schematic exemplifying a full radioxenon detection system, from sampling to detection [10]; (a) piston compressor pump, (b) heat exchanger, (c) dual air drying/CO <sub>2</sub> removal columns, (d) mass-flow controller, (e) cryogenic air-chiller, (f) initial radon "pre-trap," (g) main charcoal trap for xenon trapping, (h) nitrogen bottle/generator, (i-j) mass flow controllers for nitrogen flow, (k) CO <sub>2</sub> -removal traps, (l) radon removal trap, (m) final charcoal trap for xenon transfer into counting system, (n) beta-gamma coincidence spectrometer, (o) residual gas analyzer, (p) path to archive bottles .....	47
Fig. 25. A 2D sketch of the original ARSA detection system [14] .....	49
Fig. 26. The Xenon International system and required additional apparatuses; (a) external view; (b) internal view.....	50
Fig. 27. A sketch of the original SAUNA detectors [12] .....	51
Fig. 28. The SAUNA III system [150] .....	52
Fig. 29. A sketch of the detector unit for the ARIX radioxenon detection system [151] .....	53
Fig. 30. Geometry of the PhosWatch detector [165] .....	54
Fig. 31. The 24-element silicon PIN detector during assembly. When completely assembled the silicon surrounds the gas volume on all 6 sides [127] .....	55
Fig. 32. The detector in SPALAX NG, or SPALAX New Generation, with a PIPSBox placed on an HPGe for both high resolution electron and photon detection [180].....	57
Fig. 33. The TECZT detector, with quarter for scale [44].....	59
Fig. 34. 2D energy histogram of the TECZT detector in response to <sup>131m</sup> Xe when running in coincidence mode. The lines between 31 keV and 129 keV are due to incomplete energy deposition from backscattered conversion electrons [20].....	60
Fig. 35. (a) the CASP detector, with CZT and plastic scintillator visible. The plastic scintillator is mounted on the SiPM array, and as such the SiPM array is not visible; (b) the system assembled inside an aluminum box, to shield from light and other sources of electromagnetic interference [89] .....	60
Fig. 36. The Stilbene-CZT, using the same board as was used for the CASP system. As in Fig. 35, the array of SiPMs is underneath the scintillator and is not visible [23].....	61

Fig. 37. The PIPS-CZT system shown (a) outside of [45] and (b) inside of [87] the aluminum box and with associated readout electronics .....	63
Fig. 38. The PIPS-SrI <sub>2</sub> (Eu) detection system, sketched in Solidworks .....	66
Fig. 39. Cross sectional view of the PIPS-SrI <sub>2</sub> (Eu) detector, showing the 6 possible coincidence patterns that might occur in the detector .....	67
Fig. 40. (left) a sketch of the SrI <sub>2</sub> (Eu) detector; (right) the manufactured and packaged SrI <sub>2</sub> (Eu) detectors, completely assembled save for the front-end readout and socket .....	69
Fig. 41. The PIPSTBox-2x1200-500A used in this research .....	71
Fig. 42. The Canberra custom 2-channel preamplifier for use with the PIPSTBox.....	72
Fig. 43. A flow diagram demonstrating the application and utility of the FrontPanel software development kit [202] .....	73
Fig. 44. The DPP8, an 8 channel, 14-bit, 125 MHz, FPGA-based digital pulse processor that can process coincidence pulses from up to 8 independent detecting bodies in hardware in real-time .....	73
Fig. 45. The structure and workflow of the FPGA onboard the DPP8. The FPGA was designed using VHDL.....	75
Fig. 46. (a) Unpopulated board; (b) populated board; (c) output voltage from the EMCO DC-DC converters.....	77
Fig. 47. (a)Sketch of power supply, indicating how the power is routed to all components of the experimental setup. Blue arrows indicate voltage being supplied, while red arrows indicate pulse signal; (b) assembled power supply box. The banana plugs are not used in this experiment, but are included on the box to provide easy accessibility in future experiments.....	78
Fig. 48. The holder for the PIPS-SrI <sub>2</sub> (Eu) system, shown from two different angles. The two SrI <sub>2</sub> (Eu) crystals are held in place alongside the PIPSTBox, which is itself held secure in the center. A long groove is in place to hold the injection tube steady. The grey PLC in the middle is a model of the PIPSTBox for demonstration purposes .....	79
Fig. 49. The PIPS-SrI <sub>2</sub> (Eu) system inside the aluminum box, as seen from above. The PIPSTBox is powered and has signal read out via the two BNC connections to the bottom right, while the two SrI <sub>2</sub> (Eu) are powered by the single +5 V jack in the center and have their signal read out by the two BNC connections on the bottom left .....	80



Fig. 50. (from left to right, top row then bottom row): Welch Duo-Seal 1400(B-01) pump, with clear exhaust tube; DuraChoice analog gauge for observing evacuation rates and vacuum strength far from 0 torr; TPI 605 digital vacuum gauge, for observing evacuation rate and vacuum strength below 12 torr; Luer system for evacuating the PIPSBox of radioxenon gas.....	82
Fig. 51. (a) simulated $^{131m}\text{Xe}$ signature in the PIPS-SrI <sub>2</sub> (Eu); (b) the same signature, with unequal region sectioning applied. All regions have roughly equal counts .....	85
Fig. 52. 2D spectra generated in MCNP6 using ptrac for the PIPS-SrI <sub>2</sub> (Eu) system, with Gaussian broadening applied to the peaks in MATLAB to create a statistical spread. From top left to bottom right: 45 keV C.E. in coincidence with 31 keV X-rays, 0-346 keV $\beta$ in coincidence with 31 keV X-rays, 0-346 keV $\beta$ spectrum in coincidence with 81 keV $\gamma$ -rays, 129 keV C.E. in coincidence with 31 keV X-rays, 0-199 keV C.E. in coincidence with 31 keV X-rays, 0-910 keV $\beta$ spectrum in coincidence with 250 keV $\gamma$ -rays .....	86
Fig. 53. Generation of individual samples of xenon gas, where 99.99% pure xenon gas of a certain isotope is drawn into a syringe for irradiation in the TRIGA reactor.....	88
Fig. 54. The model of the PIPS-SrI <sub>2</sub> (Eu) as visualized using MCNPX VisEd, showing the SrI <sub>2</sub> (Eu) crystal in aluminum shell (left), PIPSBox with aluminum chassis and gas cell (right), and the entire system collectively (center). Red is aluminum, gold is SrI <sub>2</sub> (Eu), carbon windows are green, silicon detectors are dark blue, and the gas cell is light blue .....	91
Fig. 55. Simulated spectra, in order, for 31 keV, 81 keV, and 250 keV photons in SrI <sub>2</sub> (Eu) and spectra for the 0-346 keV beta, 0-910 keV beta, and the 45 keV, 129 keV, 199 keV, and 214 keV C.E.s in the PIPSBox. Doppler broadening was applied in MATLAB. Axes were chosen to agree with the axes chosen in the experimental presentations shown later in this work .....	93
Fig. 56. Percentage of total electron histories modeled in MCNP6 that deposit enough energy to trigger both silicon detectors, as a function of energy threshold. Due to attenuation in the sample gas, 45 keV electrons from $^{133}\text{Xe}$ experienced negligible (<0.01%) multi-volume energy depositions and are not included in this plot [45].....	95
Fig. 57. Histogram of simulated results from 129 keV C.E.s interacting in the PIPSBox .....	95

Fig. 58. Top view of the front-end readout PCB designed and fabricated for SrI <sub>2</sub> (Eu)+SiPM detector .....	98
Fig. 59. Response of a 2x2 J-Series SiPM array coupled to a CsI(Tl) crystal to <sup>137</sup> Cs at various temperatures with a fixed biasing voltage (~27 V). Higher temperatures result in lower gains due to lower over-voltages .....	99
Fig. 60. <sup>137</sup> Cs energy spectra collected from the two SrI <sub>2</sub> (Eu)+SiPM detectors using the RX1200 .....	100
Fig. 61. Measurement of <sup>137</sup> Cs using the SrI <sub>2</sub> (Eu) crystal, showing the fast rise time “lip” from the same event at three different time scales. The yellow signal is sourced from the output of the readout circuit board (post-voltage sensitive preamplifier), while the blue signal is sourced from the output of the SiPMs .....	102
Fig. 62. (a) Angular dependence of energy resolution for 662 keV in the SrI <sub>2</sub> (Eu) detector. A general trend of improving resolution as the source moves further from the SiPMs can be seen. The cause of the large increase in FWHM at position 6 is unclear, but might be a statistical aberration; (b) Spectrum of <sup>137</sup> Cs taken at position 8 (furthest from the SiPMs) .....	105
Fig. 63. The <sup>241</sup> Am variable X-ray source, with X-rays emitted from 6 foils at energies given in the adjacent table .....	106
Fig. 64. The Cremat charge sensitive preamplifier mounted on the test board (detector not pictured) .....	107
Fig. 65. A single pulse from <sup>137</sup> Cs taken from the SrI <sub>2</sub> (Eu) detector using the Cremat preamplifier and test board. All three images show the same pulse at different time scales.....	108
Fig. 66. <sup>135</sup> Xe as measured by the SrI <sub>2</sub> (Eu) with the Cremat preamplifier and test board. (a) shows the full spectrum, while (b) and (c) show the 31 keV and 662 keV photopeaks, respectively. Note the very slight tailing effect in the 662 keV photopeak .....	110
Fig. 67. Results from the (a) Mo and (b) Ag foil from the <sup>241</sup> Am source. The resolutions were 49% and 35% FWHM, respectively. Note the symmetry of the photopeaks .....	110
Fig. 68. The analog integrating preamplifier board. Right angle sockets hold the CR-113 charge sensitive preamplifier slightly above, and parallel to, the main circuitry of the board, allowing for an unobtrusive design. The board interfaces directly with the SiPM readout of the SrI <sub>2</sub> (Eu) detectors. ....	112

Fig. 69. (a) Oscillatory behavior due to the switching regulator, as seen riding on a 31 keV pulse; (b, c) plots of the performance of the LT8410 switching regulator [205], causing ripple very similar to those observed in this signal.....	113
Fig. 70. A comparison of the two Cremat boards in terms of impact of resolution of the 31 keV and 662 keV photons across various peaking times and flat top times (1 sample = 8 ns). The resolutions of the two photopeaks, in terms of % FWHM, are multiplied together to give a “squared” FWHM resolution. Note the small range of the y-axes in all plots .....	115
Fig. 71. Resolution for the 31 keV and 662 keV photopeak from $^{137}\text{Cs}$ determined using an analog amplification circuit with shaping times of 0.5, 1, 2, 4, 8, and 12 $\mu\text{s}$ .....	118
Fig. 72. (left) the output of each individual $\text{SrI}_2(\text{Eu})$ crystal when run in coincidence mode measuring $^{137}\text{Cs}$ ; (right) 2D coincidence histogram of the data. $\text{SrI}_2(\text{Eu})_1$ is the brighter crystal, and $\text{SrI}_2(\text{Eu})_2$ is the dimmer. Note the predominance of high-energy triggers in the dimmer crystal .....	118
Fig. 73. A pulse from one of the PIPSBox channels as triggered by an electron .....	120
Fig. 74. X-rays from $^{137}\text{Cs}$ in $\text{Si}_1$ . All measurements use a 3.2 $\mu\text{s}$ peaking time for amplitude identification filter. The flat top times for each plot range from 0 to 4.8 $\mu\text{s}$ , in increments of 80 ns.....	122
Fig. 75. The combined 22 keV X-ray from $^{109}\text{Cd}$ and 31 keV X-ray from $^{137}\text{Cs}$ , using a peaking time of 3.2 $\mu\text{s}$ and flat top times of (from top left to bottom right) 0, 200 ns, 400 ns, and 600 ns. The best resolution for the combined peak was 44.5%, achieved using 200 ns flat top time. Note that the x-axis of these plots are miscalibrated by roughly 25%, and that the photopeak should occur at 22 keV.....	123
Fig. 76. 48-hour background measurement taken with the PIPS- $\text{SrI}_2(\text{Eu})$ detector .....	125
Fig. 77. (a) 2D coincidence histogram spectrum for $^{131\text{m}}\text{Xe}$ ; (b) 1D histogram for each detecting body individually, as well as the combination of the two $\text{SrI}_2(\text{Eu})$ spectra and the summation of the signal from the two PIPS channels.....	126
Fig. 78. Reduction of the backscatter in the PIPSBox (each spectrum normalized).....	129
Fig. 79. Coincidence count rate between $\text{Si}_1$ and $\text{Si}_2$ with a varying coincidence timing windows [45].....	130

Fig. 80. A decay model showing branching ratios and energies of several important decay paths for $^{133}\text{Xe}$ .....	131
Fig. 81. (a) 2D coincidence histogram spectrum for $^{133}\text{Xe}$ and $^{133\text{m}}\text{Xe}$ ; (b) 1D histogram for each detecting body individually, as well as the combination of the two $\text{SrI}_2(\text{Eu})$ spectra and the summation of the signal from the two PIPS channels .....	132
Fig. 82. (a) 2D coincidence histogram spectrum for $^{133}\text{Xe}$ , after $^{133\text{m}}\text{Xe}$ has decayed; (b) 1D histogram for each detecting body individually, as well as the combination of the two $\text{SrI}_2(\text{Eu})$ spectra and the summation of the signal from the two PIPS channels .....	133
Fig. 83. $\text{SrI}_2(\text{Eu})_1$ histogram of photons observed in triple coincidence, from (a) the first measurement, with $^{133\text{m}}\text{Xe}$ , and (b) the second measurement, with no $^{133\text{m}}\text{Xe}$ . Note the higher incidence of X-ray triple coincidences compared to gamma triple coincidences in the first experiment.....	134
Fig. 84. X-ray gated spectrum of $^{133/133\text{m}}\text{Xe}$ taken with (a) PIPS- $\text{SrI}_2(\text{Eu})$ and (b) stilbene-CZT [23]. A resolution of 19.1% FWHM was reported for the stilbene-CZT (itself an improvement upon plastic scintillators [89]), compared to 6.6% FWHM for the PIPS- $\text{SrI}_2(\text{Eu})$ .....	135
Fig. 85. Memory effect in the PIPS- $\text{SrI}_2(\text{Eu})$ system after being exposed to $^{133}\text{Xe}$ for several weeks; (a) before extraction; (b) after extraction.....	138
Fig. 86. (a) 2D coincidence histogram spectrum for $^{135}\text{Xe}$ ; (b) 1D histogram for each detecting body individually, as well as the combination of the two $\text{SrI}_2(\text{Eu})$ spectra and the summation of the signal from the two PIPS channels.....	139
Fig. 87. The CFD for the $\text{SrI}_2(\text{Eu})$ and PIPS channels in coincidence for $^{131\text{m}}\text{Xe}$ data (top row) and the leading edge triggers (bottom row). The scaled signal is in red, the original delayed signal to be subtracted is in blue, and the zero-crossing subtracted signal is in black. The leftmost four plots are using a moving average filter of 0 samples, while the four plots on the right use a moving average filter is 51 samples .....	142
Fig. 88. Simulation of the moving average filter with a square wave .....	143
Fig. 89. Synthetic experimental spectra generated using the Python package, with different sectioning superimposed. In (a), the four radioxenon isotopes and background each have 1000 events contributing to the spectrum. The spectrum is divided into 50 subregions. In (b), $^{131\text{m}}\text{Xe}$ contributes 300 events, $^{133}\text{Xe}$ contributes 500 events, and background contributes 1000 events. The spectrum is here divided into 10 subregions .....	149

Fig. 90. Experimental spectrum for a low count rate scenario. The results of the solves for this data set are shown in Table 11 .....	151
Fig. 91. Highly localized segmentation based on the high statistics regions of the traditional ROIs. The segmentation in these regions is very fine, and are indistinguishable from each other in this plot .....	153

## LIST OF TABLES

<u>Table</u>	<u>Page</u>
Table 1. Cumulative fission yields of the radioxenon isotopes of interest for two key isotopes used in nuclear weapon testing [28] .....	6
Table 2. Decay properties of radioxenon isotopes and the radon daughters of interest with a summed decay path intensity of $> 1\%$ [43], as well as target minimum detectable concentrations, set by Xenon International, for implementation in the IMS [15]. The target MDC as set by the CTBTO remains $\leq 1 \text{ mBq/m}^3$ air for $^{133}\text{Xe}$ [11]. Beta energies given are the maximum, or end-point energy, of the emission spectrum .....	11
Table 3. A comparison of key properties of several noteworthy photon detectors ....	19
Table 4. Parameters for the PIPSBox-2 $\times$ 1200-500A [88] .....	29
Table 5. Efficiencies determined via MCNP6 simulation for different ROIs, as determined using ptrac and thresholds of 15 keV and 28 keV for photons and electrons, respectively .....	96
Table 6. Best resolutions achieved with each of the $\text{SrI}_2(\text{Eu})$ crystals using digital pulse processing. Preamplifiers with $\tau = 50 \text{ }\mu\text{s}$ and $\tau = 100 \text{ }\mu\text{s}$ were evaluated.....	117
Table 7. Experimental absolute efficiency from $^{131\text{m}}\text{Xe}$ measurements .....	128
Table 8. Experimental absolute efficiency from $^{133/133\text{m}}\text{Xe}$ measurements .....	137
Table 9. Experimental absolute efficiency from $^{135}\text{Xe}$ measurements .....	140
Table 10. MDCs for the PIPS- $\text{SrI}_2(\text{Eu})$ system and the PIPS-CZT system, using ARSA gas processing parameters and Xenon International gas processing parameters.....	147
Table 11. Results of a few different trials of the dataset shown in Fig. 90. Note that exact run times vary based on the computer conducting the solve .....	151
Table 12. A list of different combinations of the library isotopes used to create various synthetic spectra.....	154

## DEDICATION

*To every single one that hasn't, but could, if only they were given the chance.*

## A BETA-GAMMA RADIOXENON DETECTION SYSTEM USING ULTRA-BRIGHT INORGANIC SCINTILLATORS AND SOLID STATE DETECTORS

### 1. INTRODUCTION

#### 1.1. The Problem and the Solution

The disastrous consequences of a potential nuclear weapon attack need no introduction. In an effort to halt further development and proliferation of such dangerous weapons the Comprehensive Nuclear-Test-Ban Treaty (CTBT), which bans all nuclear weapon testing activity, was adopted by the United Nations General Assembly in 1996 [1]. Though the treaty has not been ratified by all necessary countries to take full effect, the Vienna-based Preparatory Commission for the Comprehensive Nuclear-Test-Ban Treaty Organization (CTBTO) has nevertheless been tasked with building up a verification regime capable of identifying nuclear weapon testing activity anywhere on the Earth at any time, including clandestine underground tests. This International Monitoring System (IMS) consists of 321 monitoring stations and 16 laboratories, located all around the world, that constantly monitor for seismic, hydroacoustic, infrasound, and atmospheric radionuclide signatures consistent with a nuclear weapon test [2].

Of key interest to this work is the radionuclide detection systems used in the IMS. The rapid fission of uranium and plutonium releases several isotopes of radioxenon gas ( $^{131\text{m}}\text{Xe}$ ,  $^{133}\text{Xe}$ ,  $^{133\text{m}}\text{Xe}$ , and  $^{135}\text{Xe}$  being of primary interest) in large quantities and in specific isotopic ratios, providing a way to differentiate a nuclear weapon detonation from other radioxenon-producing processes [3]–[6]. The chemically inert nature of xenon allows the atoms to escape underground testing facilities and travel large distances [7], [8], and ideal half-lives (several hours to several days) prevent significant buildup of the isotopes in the atmosphere which would hamper sensitivity.



## 1.2. Continuing Efforts

40 radionuclide monitoring stations are currently established in the IMS, with a potential expansion to 80 stations [9]. These monitoring stations contain systems that automatically sample the atmosphere, extract as much xenon as possible, and inject the sample into a radiation detector [10]. The CTBTO specifies that the detectors used in the IMS must be able to detect  $^{133}\text{Xe}$  in the atmosphere with a minimum detectable concentration (MDC) of  $\leq 1 \text{ mBq/m}^3$  air [11]. These systems use various approaches to detect the radioxenon: those working with coincidence identification techniques use largely archaic technologies such as photomultiplier tubes in conjunction with materials with suboptimal energy resolution such as NaI(Tl) and memory effect such as plastic scintillators [12]–[15], while systems using high resolution gamma spectroscopy require bulky cooling systems to function [16], [17]. These detectors are also extremely costly, running on the order of  $\sim \$500,000$  plus yearly maintenance fees. The systems that utilize coincidence identification use the Region of Interest (ROI) method to identify radioxenon in a sample, which involves defining ranges of energies within which counts are summed and associated with a specific radioxenon isotope [18]. These efforts, though effective, have been outperformed in some cases by statistical spectral deconvolution methods [19], particularly in low count rate situations.

Several prototype radioxenon detection systems have been designed previously at Oregon State University to address some of the issues highlighted above by using modern technologies in novel configurations and with digital pulse processing techniques [20]–[23]. The systems have all exclusively utilized the ROI method. These previous designs have seen varying degrees of success. The system presented here, the PIPS-SrI<sub>2</sub>(Eu), aims to build upon several of the shortcomings of these previous systems, such as slow charge carrier drift time, poor solid angle, memory effect, and lackluster photon resolution at low energies. The system utilizes a pair of SrI<sub>2</sub>(Eu) scintillators, each coupled to an array of silicon photomultipliers (SiPMs), for high resolution photon detection, while a silicon-based detector known as the

PIPSBox acts as a gas cell and a two-volume electron detector. The system combines several positive aspects from the previously designed systems, while avoiding the shortcomings: it shows minimal memory effect, achieves good energy resolution for both electrons and photons, has a high solid angle when compared to the previously designed PIPS-CZT system, and addresses conversion electron backscatter effectively using specialized electronics. When using the ROI method to determine the MDC of the four radioxenon isotopes of interest, the prototype detection system performs promisingly when compared to state-of-the-art radioxenon detection systems, provided certain assumptions such as a blank atmospheric sample and negligible memory effect hold. Complementing this, a new statistical radioxenon identification method based on region sectioning and spectral deconvolution using maximum likelihood is presented. This method performs competitively when compared to other statistical radioxenon identification methods. The PIPS-SrI<sub>2</sub>(Eu) can be seen in Fig. 1.



**Fig. 1.** The PIPS-SrI<sub>2</sub>(Eu) radioxenon detection system prototype

### 1.3. Goals

This dissertation covers the design, construction, and characterization of a prototype multi-material radioxenon detector utilizing a PIPSBox for electron

detection and a pair of  $\text{SrI}_2(\text{Eu})$  scintillators coupled to an array of silicon photomultipliers (SiPMs) for photon detection. The algorithms and digital pulse processing techniques used in the operation of the detector are also discussed. The dissertation also details the theoretical and mathematical underpinnings of a new spectral deconvolution technique for radioxenon identification, as well as its implementation and performance evaluation. Specific efforts undertaken and described include:

- General system design and material selection
- Hardware and Field Programmable Gate Array (FPGA) digital logic design
- Monte Carlo N-Particle code (MCNP<sup>®</sup>6) [24] simulation
- Characterization of the  $\text{SrI}_2(\text{Eu})$ +SiPM detectors and the PIPSBox, separately and together, via lab check sources and radioxenon sources
- Optimization of system performance via hardware and software modifications
- Region of Interest (ROI) determination, background measurement, and Minimum Detectable Concentration (MDC) calculation
- Development of a statistical spectral deconvolution approach for radioxenon identification
- Implementation and testing of the spectral deconvolution approach in Python
- Relevant challenges, solutions, and potential improvements to the system and the statistical radioxenon identification method

## 2. LITERATURE REVIEW

### 2.1. Physics of Radioxenon

The physics being analyzed guides all aspects of the design of the detectors and the algorithms used in this research. As such, the production mechanisms of radioxenon, how it reaches the atmosphere, why it is looked for, how it is looked for, and potential problems that arise due to the physics of it and other isotopes in relation to it are all important factors that must be thoroughly understood.

#### 2.1.1. *Production*

Radioxenon isotopes are produced in natural processes, reactor operations, and nuclear detonations. Because they are produced by these various processes, it is not the absolute concentration of the isotopes in the atmosphere but the ratios that are key to identifying a nuclear explosion:  $^{135}\text{Xe}/^{133}\text{Xe}$ ,  $^{135}\text{Xe}/^{133\text{m}}\text{Xe}$ ,  $^{135}\text{Xe}/^{131\text{m}}\text{Xe}$ ,  $^{133\text{m}}\text{Xe}/^{133}\text{Xe}$ ,  $^{133\text{m}}\text{Xe}/^{131\text{m}}\text{Xe}$ , and  $^{133}\text{Xe}/^{131\text{m}}\text{Xe}$  [10]. A separation line, the exact location of which is the subject of ongoing study and depends on the specific identification criteria of the user, is defined in a multiple ratio isotope plot to distinguish these regions [6]. An example of one of these multiple ratio isotope plots can be seen in Fig. 2.

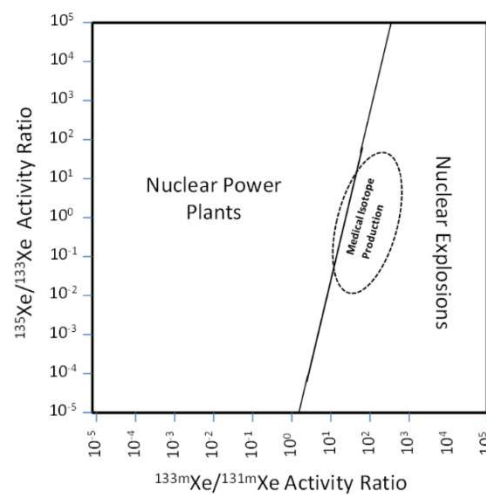


**Fig. 2.** Multiple ratio isotope plot with a separation line indicating the different ratios of radioxenon isotope activity associated with different radioxenon sources [25]. A unique plot may be defined comparing the ratios for any of the radioxenon isotopes

Ratios observed due to a nuclear weapon detonation are different from ratios due to emissions from reactors at equilibrium operation [26]. However, a prompt ventilation from medical isotope production facilities following the fresh irradiation of low enriched or high enriched uranium used for medical isotopes can look similar to a nuclear weapon detonation [27]. This suggests that medical isotope production activity might be monitored to avoid potential misattribution of radioxenon observations to a nuclear weapon test.

$^{133\text{m}}\text{Xe}$ ,  $^{133}\text{Xe}$ , and  $^{135}\text{Xe}$  all have high fission yields from a  $^{235}\text{U}$  or  $^{239}\text{Pu}$  fission device, with the 6.5-7.5% yield of  $^{133}\text{Xe}$  and  $^{135}\text{Xe}$  being especially noteworthy [28]. The yields of the four radioxenon isotopes of interest from  $^{235}\text{U}$  and  $^{239}\text{Pu}$  are given in Table 1. The high fission yield and relatively lengthy half-life ( $\sim 5.2$  days) of  $^{133}\text{Xe}$  makes the isotope particularly critical to atmospheric monitoring, as it allows for significant amounts of activity to escape an underground testing chamber and diffuse through the atmosphere before decaying to the point of undetectability. However, this longer half-life also contributes to natural background more strongly than other isotopes that have high fission yields but shorter half-lives, such as  $^{135}\text{Xe}$  ( $\sim 9.1$  hours) [29].  $^{131\text{m}}\text{Xe}$  has a fission yield orders of magnitude lower than  $^{133\text{m}}\text{Xe}$ ,  $^{133}\text{Xe}$ , and  $^{135}\text{Xe}$ , resulting in a significantly lower yield from a nuclear weapon detonation than the other three isotopes. However, it is still produced in significant quantities in nuclear fuel reprocessing and in medical isotope production and use, and for this reason  $^{131\text{m}}\text{Xe}$  is important for differentiating between a weapon detonation and other radioxenon emitting events [3].

**Table 1.** Cumulative fission yields of the radioxenon isotopes of interest for two key isotopes used in nuclear weapon testing [28]

Isotope	$^{235}\text{U}$	$^{235}\text{U}$	$^{239}\text{Pu}$	$^{239}\text{Pu}$
	(thermal yield)	(fast yield)	(thermal yield)	(fast yield)
$^{131\text{m}}\text{Xe}$	$0.0313 \pm 0.003$	$0.0365 \pm 0.0031$	$0.041 \pm 0.004$	$0.0444 \pm 0.0044$
$^{133\text{m}}\text{Xe}$	$0.189 \pm 0.015$	$0.190 \pm 0.015$	$0.216 \pm 0.016$	$0.223 \pm 0.021$
$^{133}\text{Xe}$	$6.60 \pm 0.11$	$6.61 \pm 0.13$	$6.99 \pm 0.13$	$7.03 \pm 0.33$
$^{135}\text{Xe}$	$6.61 \pm 0.22$	$6.32 \pm 0.18$	$7.36 \pm 0.24$	$7.50 \pm 0.23$

### *2.1.1.1. Other Gases*

Non-traditional radioxenon isotopes have been investigated for potential use as atmospheric monitoring tools.  $^{125}\text{Xe}$  has a short half-life ( $16.9 \pm 0.2$  h) and a low fission yield, but the very high neutron capture cross section of  $^{124}\text{Xe}$  (146.7 b for thermal neutrons, 2.714 mb for 14 MeV neutrons) could result in significant quantities of  $^{125}\text{Xe}$  being produced in a nuclear test via neutron activation of the surrounding air [30].  $^{127}\text{Xe}$ , though not useful for nuclear test monitoring directly, is useful for calibrating radioxenon detection systems [31].

Other noble gas radioisotopes such as  $^{37}\text{Ar}$  and  $^{85}\text{Kr}$  are also produced in underground nuclear detonations in significant quantities, but these isotopes are difficult or impossible to use for atmospheric nuclear test monitoring applications.  $^{37}\text{Ar}$  is produced via the  $^{40}\text{Ca}(n,\alpha)^{37}\text{Ar}$  reaction with the calcium ubiquitous to the Earth's crust [32]. It has an ideal half-life of several weeks and has a very low natural background compared to the quantity released in a nuclear detonation. However,  $^{37}\text{Ar}$  decays via release of a 2.82 eV Auger electron: a low energy difficult to measure reliably.  $^{85}\text{Kr}$  has a large atmospheric background presence of  $\sim 1.5$  Bq/m<sup>3</sup> in the northern hemisphere due to a long half-life (on the order of a dozen years), making measurement insensitive to changes due to prompt emissions from a weapon test [11].

### *2.1.2. Emission from Underground*

A study on trace gas emissions along fault lines indicates that fracture networks (natural or human-induced from mining, or the nuclear explosion itself) tend to promote diffusion of gas from a nuclear test to the surface, particularly in stormy conditions with low barometric pressures [33]. A study of the prompt and delayed releases of atmospheric radioxenon from underground nuclear tests indicates that there is no clear correlation between depth of burial and activity release, nor between explosive yield and activity release [34]. The study also found that releases from uncontrolled tests typically occur within several hours of the initiating event, while more frequent operational releases typically have delays of one day up to a week. Further study indicates that leaks and operational releases at the time of detonation

are not necessarily required for the long distance detection of the radioxenon signals, though the decay of the isotopes during a lengthy vent would obviously alter the ratios of the radioxenon isotopes expected from the detonation [35]. Atmospheric transport models such as the FLEXPART Lagrangian dispersion model [36] and subsurface transport models such as one based on the n-Isothermal, Unsaturated Flow and Transport (NUFT) code [37], are the current methods of choice to model and understand the transport characteristics of noble gas releases from a nuclear explosion.

### ***2.1.3. Radioactive Decay***

The four radioxenon isotopes of interest all decay via beta-gamma, or electron-photon, coincidence. It is important then to understand coincidence decay as well as various decay processes in general.

#### ***2.1.3.1. Beta Decay and Isomeric Transitions***

Beta-minus decay, often simply referred to as beta decay, is moderated by the weak force and occurs primarily in neutron-rich nuclei. During the decay, an unstable nucleus decays through the conversion of a neutron to a proton, antineutrino, and electron, the latter of which is referred to as the beta particle. These electrons originate directly from the nucleus, not the electron shells. Because of the antineutrino introducing a third particle into the system to carry momentum, beta particles are not emitted at fixed energy. Rather the total Q-value of the decay, a fixed value representative of the total energy of the decay process, is shared between the daughter nucleus, the emitted beta particle, and the antineutrino. As such, the energy of emitted beta particles are defined by a spectrum of energy ranging from zero (where the full decay energy is shared between the daughter nucleus and the antineutrino, and the beta particle carries away no energy) to nearly the full Q-value of the decay (where the antineutrino is virtually at rest and nearly all the decay energy is split between the daughter nucleus and the beta, in accordance with conservation laws) [38]. An example of a beta spectrum can be seen in the beta energy distribution of  $^{36}\text{Cl}$ , as shown in Fig. 3.

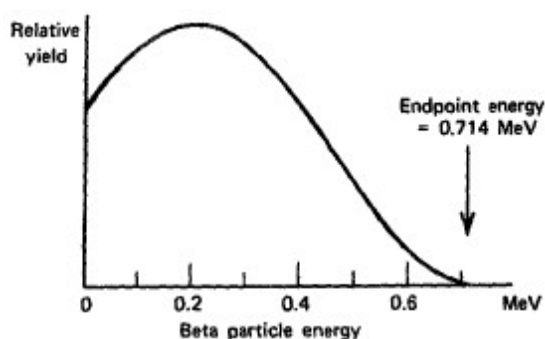


**Fig. 3.** The beta spectrum of  $^{36}\text{Cl}$  [39]

Beta decay sometimes produces an unstable daughter nucleus known as a nuclear isomer, or metastable, state. The excited nucleus undergoes further decay known as an isomeric transition to a lower energy or ground state with a half-life dictated by the difference in spin between the initial and final state. This isomeric transition can occur via the release of one, or several, gamma rays of discrete energy, or via a competing process known as internal conversion. During internal conversion, the nuclear excitation energy is directly transferred from the nucleus to an electron in the orbital shells of the atom, without an intermediary state (thus differentiating it from a self-induced photoelectric effect). As there is no change in the constituent parts of the nucleus during this process, the atomic numbers remain unchanged before and after the decay. The emitted monoenergetic electron, known as a conversion electron, carries the energy of de-excitation minus the binding energy of the electron shell it was liberated from. The conversion electron leaves a hole in the electron shell it was emitted from, which is then subsequently filled by an electron from a higher energy orbital dropping into the more tightly bound orbital. This energy liberated via this process is equal to the difference in binding energies of the two electron shells, and results in the emission of either a characteristic X-ray or a loosely bound electron in the outer electron shell known as an Auger electron. The X-ray is emitted in very close proximity in time with the initial conversion electron; in other words, they are in coincidence. As there are many possible sources for this replacement electron within the atom, the coincident X-ray can have one of several discrete energies. The proximity of some of these energy levels means that the X-rays are often too close together in energy for the resolution of the detector to successfully discriminate



between. As such, characteristic X-rays with tight energetic proximity are often considered collectively when considering coincident events [40].

### 2.1.3.2. True Coincidence and Beta-Gamma Coincidence

A true coincidence is a decay, or series of decays, where two or more detectable quanta that stem from the same radioactive event are emitted within a time frame comparable to the time resolution of the detection system [41]. By this definition, a fission chain reaction is, for example, not a true coincidence event, because subsequent decays occur in different particles, not the particle initiating the event. The decay of  $^{137}\text{Cs}$ , which decays to  $^{137\text{m}}\text{Ba}$  via the emission of a beta particle and then subsequently decays to  $^{137}\text{Ba}$  after  $\sim 2.5$  minutes via the emission of a 662 keV gamma ray, is also not a true coincidence decay due to the lengthy intermediate state of  $^{137\text{m}}\text{Ba}$ . One familiar example of true coincidence decay is  $^{60}\text{Co}$ , which decays with a 99.88% branching ratio to  $^{60}\text{Ni}$  via the emission of a beta followed by a cascade of two unique gamma rays with an intermediary state of negligible half-life. This can be defined as a true coincidence event because all these quanta are produced in a cascade from the same particle and originate from the same decay event, and all within a very short period of time. The coincidence decay scheme of  $^{60}\text{Co}$  can be seen in Fig. 4.

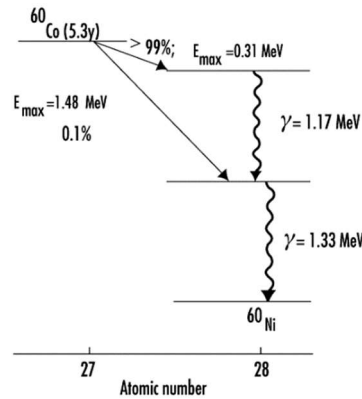


**Fig. 4.** Decay scheme of  $^{60}\text{Co}$ , exemplifying coincident decay through the emission of a beta immediately followed by cascading photons [42]

All four radioxenon isotopes of interest decay via beta-gamma, or electron-photon, coincidence. By exploiting this fact and utilizing coincidence measurement techniques, it is possible to mitigate the influence of background on a spectrum and

significantly increase the sensitivity of the radioxenon detection system: by requiring the occurrence of two uniquely identifiable events, each resulting in a deposition of a certain amount of energy, within a very small timing window, random background effects can be reduced by up to four orders of magnitude [3]. The decay properties of the radioxenon isotopes of interest are shown in Table 2.

Of the three systems utilized by the IMS, two of the three (SAUNA and ARIX) utilize beta-gamma coincidence techniques. The third, SPALAX, utilizes high resolution gamma spectroscopy with high purity germanium (HPGe) detectors to identify differences in the energies of photon emissions (including the K-shell X-rays) with high precision [16]. However, new designs of this system are also moving towards implementing beta-gamma coincidence-gating methods in addition to the high resolution gamma spectroscopy as a way to further improve minimum detectable concentration [17].

**Table 2.** Decay properties of radioxenon isotopes and the radon daughters of interest with a summed decay path intensity of  $> 1\%$  [43], as well as target minimum detectable concentrations, set by Xenon International, for implementation in the IMS [15]. The target MDC as set by the CTBTO remains  $\leq 1$  mBq/m<sup>3</sup> air for <sup>133</sup>Xe [11]. Beta energies given are the maximum, or end-point energy, of the emission spectrum

Isotope (half-life, days)	Decay energy (keV)	Summed intensity of decay path (%)	Target MDCs (mBq/m <sup>3</sup> ) set by Xenon International
<sup>131m</sup> Xe ( $t_{1/2} = 11.86$ days)	31 keV* X-ray + 129 keV CE	53.8	0.3 (threshold) 0.15 (objective)
<sup>133</sup> Xe ( $t_{1/2} = 5.24$ days)	31 keV* X-ray + 45 keV CE + 346 keV beta	46.9	0.3 (threshold) 0.15 (objective)
	81 keV gamma + 346 keV beta	37.3	
<sup>133m</sup> Xe ( $t_{1/2} = 2.20$ days)	31 keV* X-ray + 199 keV CE	54.9	0.3 (threshold) 0.15 (objective)
<sup>135</sup> Xe ( $t_{1/2} = 0.38$ days)	250 keV gamma + 910 keV beta	90	1.0 (threshold) 0.5 (objective)
	31 keV* X-ray + 214 keV CE + 915 keV beta	5.7	
<sup>214</sup> Pb ( $t_{1/2} = 26.8$ min)	242 keV gamma + 730 keV beta	7.43	---
	295 keV gamma + 730 keV beta	19.3	
	352 keV gamma + 670 keV beta	37.6	

\*These X-rays are from the K-shell and are spaced too closely to uniquely discern.

### ***2.1.4. Interference***

Some of the radioxenon isotopes experience interference in their regions of interest (ROIs), which are ranges of energies defined by the resolution of a detector where a count from a decay are likely to be observed. These interferences can come from other radioxenon isotopes or from  $^{214}\text{Pb}$  and  $^{214}\text{Bi}$ , daughters of radon not possible to completely remove from the atmospheric sample. Some interferences are dependent on the detector in question: for example, detectors that experience electron backscatter have increased interference in the  $^{131\text{m}}\text{Xe}$  ROI from the higher energy electrons from  $^{133}\text{Xe}$  and  $^{133\text{m}}\text{Xe}$  not fully depositing their energy before backscattering out of the detector [44], [45]. Other interferences are universal and an inherent consequence of the physics of the radioxenon. All detectors experience the interference from the  $^{133}\text{Xe}$  beta in the metastable ( $^{131\text{m}}\text{Xe}$  and  $^{133\text{m}}\text{Xe}$ ) ROIs, and Compton scatter from higher energy photons influence all ROIs at a lower energy.  $^{214}\text{Pb}$  specifically interferes with the 250 keV photon ROI of  $^{135}\text{Xe}$  via beta-gamma coincidence at a photon energy of 242 keV, in addition to Compton scattering of the higher energy photons into the lower energy ROIs.  $^{214}\text{Bi}$  interferes specifically with the 81 keV photon ROI of  $^{133}\text{Xe}$  via beta-gamma coincidence at a photon energy of 79.3 keV. Some techniques exist for addressing these interferences, including spectral deconvolution [46], defining additional ROIs and using known branching ratios to subtract an appropriate number of interfering counts out of each of the ROIs [18], and simply improving detector resolution to reduce the size of the ROIs.

## **2.2. Detectors and Hardware**

Just as the physics of radioxenon are key to determining the design of a detection system, understanding of the structure and physics of certain materials and certain features of data processing units are also key to optimizing it.

### ***2.2.1. Scintillation Detectors***

The basic operating principle of a scintillation detector is simple: radiation enters the detection volume and deposits energy. The energy causes excitation in the

structure of the scintillation material, the de-excitation of which results in the emission of visible light photons. These visible light photons are then detected via some light collection device, such as photomultiplier tube (PMT) or silicon photomultiplier (SiPM) [47], [48].

Scintillation detectors are widely divided into two categories: organic and inorganic. Organic scintillators, which include plastics, tend to be inexpensive, fast, and have poor energy resolution when compared to inorganics (though some organic scintillators, such as stilbene, are organic crystals and defy several expectations typically associated with organic scintillators [49]). Organic scintillators are molecular in structure and are comprised of light elements, which make them excellent electron detectors by minimizing backscatter, but poor photon detectors. The structure of non-crystalline organic scintillators makes them particularly vulnerable to memory effect, a phenomenon where the heavy gas (such as radon or radioxenon) being measured diffuses into the walls of the scintillator and continues to decay even after the sample is extracted [50].

As the scintillation detector used in the PIPS-SrI<sub>2</sub>(Eu) is an inorganic scintillator, further discussion will be limited to inorganic scintillators. Inorganic scintillators tend to be comprised of heavier elements than organic scintillators, which results in a higher density, higher stopping power, and more electrons in the medium for photons to interact with. Inorganic scintillators also provide a higher light yield on average than organic scintillators (by a factor of  $\sim 4\times$  on average [51]), which results in a better energy resolution. These qualities make inorganic scintillators ideal for photon detection. The scintillators have a crystal lattice structure, and electrons are only available in discrete bands: the valence band, where electrons are effectively bound at the lattice site, and the conduction band, where electrons have enough energy to freely migrate through the crystal. The energy difference between these two bands is known as the band gap, and in this region no electrons may exist. Inorganic scintillators tend to be largely proportional excepting extremes of energy, with low energy electrons being particularly noteworthy.

Using a pure crystal as a scintillator has several drawbacks. The excitation of valence electrons into the conduction band and their subsequent de-excitation back into the valence band is an inefficient (i.e.: slow) process in a pure crystal. Furthermore, photons that are emitted in such a de-excitation have energies that precisely match the bandgap, increasing the likelihood that they are reabsorbed into the medium by exciting further valence electrons. Even if they were not to be reabsorbed, the band gap is generally of such an energy that the scintillation photons lie outside of the visible range. To make the de-excitations more efficient, self-absorption less likely, and to bring the wavelengths of the scintillation photons into the visible light range, inorganic scintillators are typically doped with small concentrations of impurities. These impurities, known as activators, are sites in the lattice that energetically exist within the bandgap. These sites are quickly ionized by the electrons in the valence band of the bulk crystal, giving electrons in the conduction band places to readily de-excite back to the valence band. The bulk scintillator is transparent to the photons emitted in this manner due to the difference in energy between the photons that de-excite at the impurity sites and the energy of the band gap of the bulk crystal, promoting more efficient light transport. If the impurity is chosen properly, the emission spectrum of the scintillation photons largely falls within the range of visible light. A depiction of the energy structure of an inorganic scintillator is shown in Fig. 5.

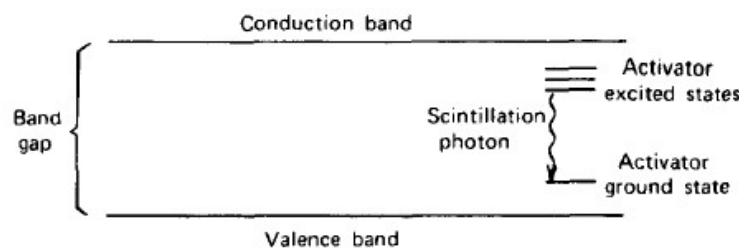


**Fig. 5.** The energy structure of an inorganic scintillator [47]

Scintillators have characteristic decay times associated with them. Decay times are quoted as half-lives, and the rate of emission of scintillation photons with time can be well-modeled with a decaying exponential. Migration time for electrons in the conduction band is typically very fast, on the order of nanoseconds, and so it is the

half-lives of the excited states that determine the decay time of the scintillator. The de-excitation process described in the previous paragraph, known as fluorescence, is the dominant mode of de-excitation and is considered the fast component. The other major process of de-excitation is known as phosphorescence, which occurs when an electron cannot directly decay from the activator excited state to the ground state and must be raised to a higher state before it can de-excite. Phosphorescence occurs across significantly longer time scales than fluorescence and contributes a slow component to the decay of the scintillator. Another contributing factor to slow components in a scintillator is self-absorption and reemission, which is particularly detrimental in large scintillators with long de-excitation times and significant overlap in absorption and radioluminescence spectra. Slow components introduced in this manner also have a degree of unpredictability in terms of their impact as well as some depth-of-interaction dependence: interactions close to the light collection device produce photons that, if emitted traveling farther away from the collection surface, must traverse the entire length of the crystal and back before being collected. This can result in enough self-absorption to impact the perceived height of the scintillation pulse.

Depending on the ratio of the light yield via fluorescence vs. phosphorescence and the respective half-lives of the processes, as well as the impact of self-absorption and reemission, the slow component of the scintillator can have a strong impact on the performance of the scintillator. In cases such as NaI(Tl), the main slow component contributes to about 9% of the total light yield, with a half-life of  $\sim 0.15$  seconds. This is so long when compared to the  $\sim 230$  ns half-life of the fast component that in almost all but high count rate measurements it can be safely ignored. In other cases where the slow component is only a few times slower than the fast component or when there is significant amounts of reabsorption and reemission of scintillation light, the influence of the slow component on the shape of the pulse must be accounted for. An example of the contribution of fast and slow components to a total scintillation pulse can be seen in Fig. 6.

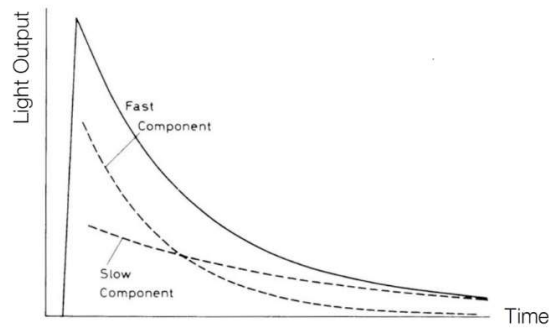


**Fig. 6.** The contributions of the fast and the slow de-excitation components to a total scintillation pulse [51]. Scintillators can have more than one slow component

#### 2.2.1.1. *Gamma Spectroscopy*

Photons that are emitted during radioactive decay are released at discrete and unique energies. By plotting the number of photons emitted as a function of energy, a histogram indicating the energy of the emitted photon can be generated and from this the emitting isotope can be identified. Theoretically, the peak indicating the energy of the photon should be a delta function; however, variations caused by noise in the detection system and statistical fluctuations in the number of signal carriers in the detecting medium (scintillation photons in the case of scintillators) cause the peak to adopt a Gaussian shape. The difference of resolution is demonstrated in Fig. 7. The value of good energy resolution is clear: if multiple photons are closely spaced in energy, it is difficult to distinguish the peaks without a high resolution detector.

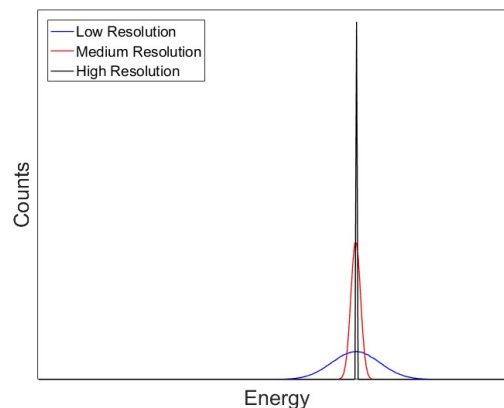


**Fig. 7.** The same peak with three different energy resolutions. All peaks integrate to 1

It is not just statistical concerns but also concerns of basic physics that modify the shape of a photon spectrum. A photon deposits energy in a medium via interaction with electrons, which is facilitated through one of three ways: photoelectric effect, Compton scattering, or pair production. The frequency of occurrence of a certain type of interaction is determined by energy and by the atomic number, or Z number, of the interaction medium. The relationship is depicted in Fig. 8.

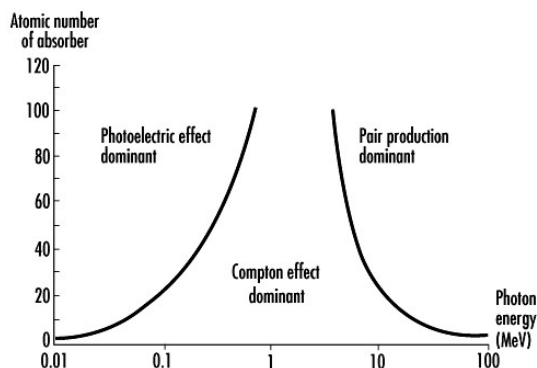


**Fig. 8.** The mode of photon interaction in a medium as it relates to incident energy of the photon and atomic number, or Z number, of the medium [42]

A single photopeak is observed only when the entire energy of the photon is deposited in the detection medium, which occurs in the cases of photoelectric effect or pair production (provided that neither annihilation photon escapes the volume). The Compton effect results in a plateau of counts at energies below the photopeak, which can cause unwanted interference and potentially obscure the photopeaks of photons that may have energies in this region. Having the most counts possible in the photopeak in relation to the surrounding energies is ideal for achieving optimum energy resolution, and as such the Compton effect should in most cases be mitigated as much as possible. This can be achieved by choosing high-Z scintillation materials, which is characteristic of inorganic scintillators.

#### 2.2.1.2. $SrI_2(Eu)$

Strontium iodide is a relatively new scintillation material. Though europium-doped strontium iodide for scintillation purposes was initially discovered in the late 1960s [52], it did not see frequent use until more recently. Thanks in large part to the



efforts of Cherepy and Beck and Lawrence Livermore National Lab,  $\text{SrI}_2(\text{Eu})$  has resurfaced and has been the subject of much scrutiny for gamma spectroscopy applications [53]–[59]. Compared to  $\text{NaI}(\text{Tl})$  (the scintillator most commonly used for photon detection in beta-gamma radioxenon detection systems),  $\text{SrI}_2(\text{Eu})$  demonstrates significantly better energy resolution, having demonstrated resolutions on the order of 2-3% FWHM at 662 keV compared to 6-8% of  $\text{NaI}(\text{Tl})$ . This is largely due to the exceptional brightness of  $\text{SrI}_2(\text{Eu})$ —almost twice as luminous as  $\text{NaI}(\text{Tl})$ . Varying light output is observed depending on the level of  $\text{Eu}^{2+}$  doping, with a peak light output observed at 5% doping [60].  $\text{SrI}_2(\text{Eu})$  maintains proportionality within about 2% across a range of temperatures typically encountered in the field ( $\sim 15\text{--}50^\circ\text{C}$ ) (Fig. 9a), with a nearly energy independent percent relative photopeak shift of about 20% across the temperature range of  $15^\circ\text{C}$  to  $60^\circ\text{C}$  (Fig. 9b) [61]. Energy resolution was found to depreciate from 2.5% FWHM to 3.4% FWHM across the temperature range of  $-30^\circ\text{C}$  to  $50^\circ\text{C}$ .  $\text{SrI}_2(\text{Eu})$  also has excellent light proportionality across a wide range of energies when at a fixed temperature, with a photon light yield of  $\pm 2\%$  the light yield from a 300 keV photon interaction across a range of  $\sim 15\text{--}3000$  keV (Fig. 9c) [59].  $\text{SrI}_2(\text{Eu})$  has the advantage of no intrinsic radioactivity that other high resolution scintillators such as  $\text{LaBr}_3(\text{Ce})$  have. The density of  $\text{SrI}_2(\text{Eu})$  is also higher than  $\text{NaI}(\text{Tl})$  with a comparable  $Z_{\text{eff}}$ , giving the crystal a high stopping power for photons. This results in needing less material to fully absorb impinging radiation, reducing detector size and cost. Though materials such as coplanar and pixelated CZT might offer still higher resolutions, the response time of CZT is inherently limited by the slow electron drift time through the bulk of the crystal [44]. A comparison between  $\text{SrI}_2(\text{Eu})$  and various other photon detectors can be seen in Table 3.

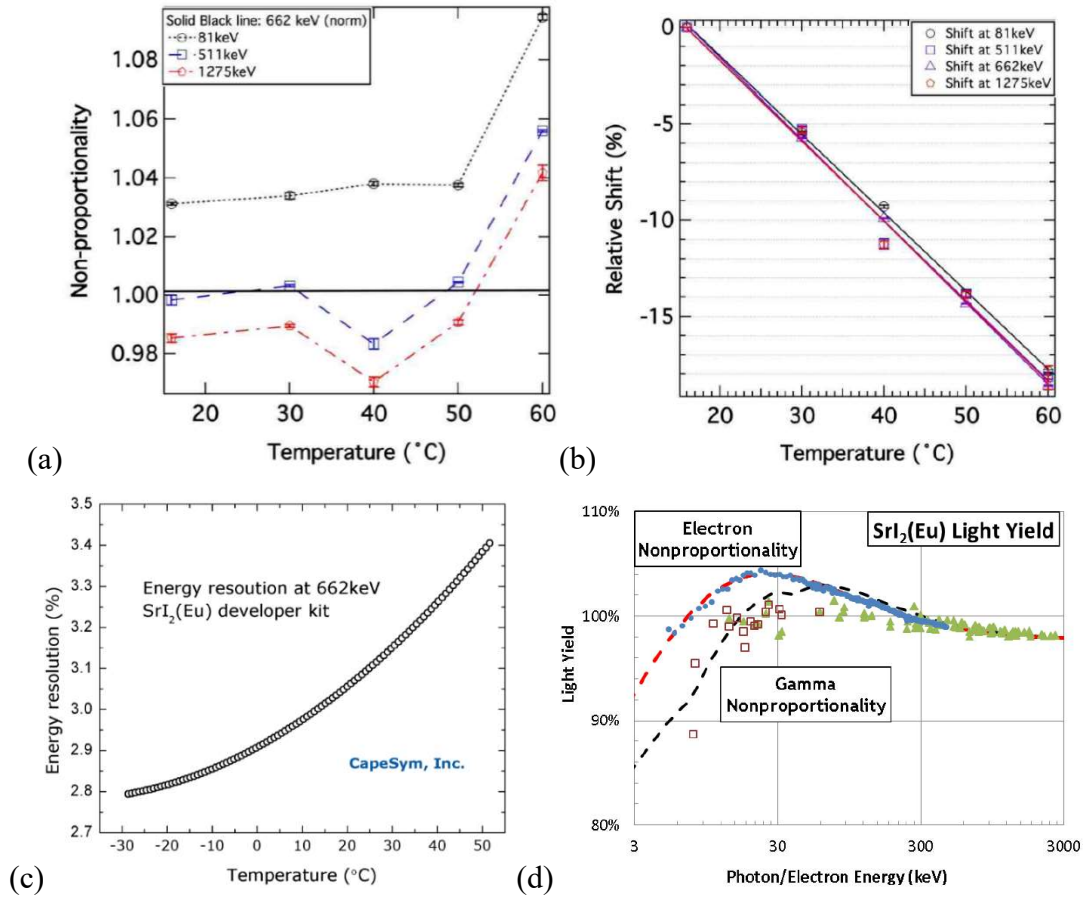


**Fig. 9.** (a) Light non-proportionality of  $\text{SrI}_2(\text{Eu})$ ; (b) relative spectrum shift vs. temperature for a variety of energies [61]; (c) energy resolution with respect to temperature [62]; (d) energy non-proportionality measured (markers) and simulated (dashed lines) for electrons (red dashed line, blue markers) and photons (black dashed line, red and green markers) [59]

**Table 3.** A comparison of key properties of several noteworthy photon detectors

	$\text{SrI}_2(\text{Eu})$ [59]	$\text{LaBr}_3(\text{Ce})$ [59]	$\text{NaI}(\text{Tl})$ [65]	Coplanar CZT [66]
<b>Density (<math>\text{g}/\text{cm}^3</math>)</b>	4.6	5.1	3.67	5.8
<b><math>Z_{\text{eff}}</math></b>	49	47	50	50
<b># Photons/MeV</b>	85,000	60,000	38,000	---
<b>Best Res. (FWHM) @ 662 keV</b>	2.3%	2.5%	6%	$\sim 1.5\%$
<b>Response Time</b>	$< 100$ ns	$< 100$ ns	$< 100$ ns	$\sim 1000$ ns per cm thickness

Working with  $\text{SrI}_2(\text{Eu})$  does pose some noteworthy difficulties. It is hygroscopic, meaning that the crystal must be completely sealed and isolated from the environment to prevent exposure to moisture. Alternative non-hygroscopic crystals, such as LYSO and BGO, have significantly poorer energy resolution when compared to  $\text{SrI}_2(\text{Eu})$  [63], and consequently are a somewhat unattractive option for radioxenon detection applications. Many inorganic scintillators, including those used in beta-gamma coincidence radioxenon detection systems such as  $\text{NaI}(\text{Tl})$  [12]–[15], are also hygroscopic, so this is not a challenge unique to  $\text{SrI}_2(\text{Eu})$ . Nevertheless, the hygroscopic nature of the crystal can result in difficulties in terms of collecting the scintillation light without the permanent coupling of the crystal to a light collection device. The long de-excitation time of  $\text{Eu}^{2+}$  causes rather long decay times, which can be a point of concern if the scintillator is used in a high count rate situation. Self-attenuation is also a concern, as the substantial overlap of the  $\text{Eu}^{2+}$  optical absorption and emission curves results in the tendency to reabsorb and re-emit scintillation light from additional activators as the photons propagate through the crystal. The absorption and radioluminescence spectra for an  $\text{SrI}_2(\text{Eu})$  crystal are shown in Fig. 10. Though this does not typically cause any significant issues in terms of gross light collection, it does cause issues with respect to pulse decay properties and results in a lengthening of pulse lifetime, red-shift of scintillation photons, and a reduction in total pulse height [57]. This is particularly important for large scintillators, where the light must travel longer distances and thus has a higher probability of self-absorption; when using analog readout, energy resolution was observed to degrade by a factor of two for 662 keV between a 3 mm thick crystal and a 15 mm thick crystal [64]. Additional difficulties when using analog electronics may present themselves when trying to acquire small and/or inexpensive parts to produce long enough integration times to account for the various possible pulse lengths. This degradation can be remedied via a physical tapering of the crystal, to create a shorter and more uniform effective light path, or via using digital corrections and pulse fitting prior to histogramming the spectrum.

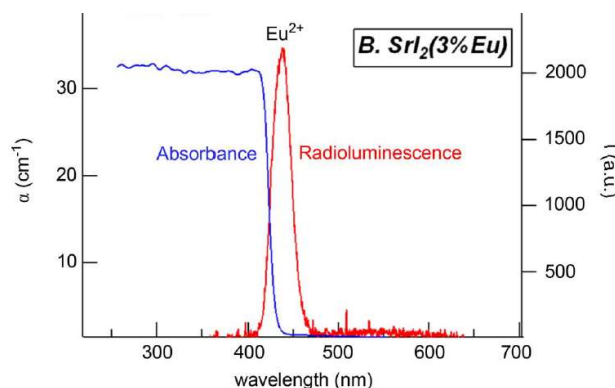


**Fig. 10.** Absorbance and radioluminescence of the  $\text{Eu}^{2+}$  impurity in  $\text{SrI}_2(\text{Eu})$  crystals. The overlap of the absorbance and radioluminescence contributes to absorption and reemission of scintillation light and results in a long decay time in large crystals [56]

### 2.2.2. Solid State Detectors

Solid state radiation detectors first became available in the 1960s [67], but high dark current and poor signal-to-noise ratios hindered their widespread use. Modern advances in semiconductor detector design have come to address these problems, and since the mid-2000s a plethora of new devices applying solid state detector technologies have come to market.

#### 2.2.2.1. Semiconductor Physics

Like inorganic scintillators, semiconductors are lattice structures, with valence and conduction bands governing the electron structure of the bulk solid [68]. The operation of semiconductor detectors involves applying a voltage bias across the bulk material to collect electrons that have been excited into the conduction band following radiation exposure. The bandgap in semiconductors is on the order of about 1 eV, which means that it takes less energy to excite an electron from the valence band to the conduction band than in scintillators. This means more signal carriers per unit energy, which in turn implies superior resolution. If the band gap is too small, such as the 0.665 eV band gap of HPGGe detectors at room temperature, thermal perturbations are sufficient to excite electrons from the valence to the conduction band. This generates a large amount of unwanted dark current: signal without any radiation stimulus. Perhaps fortunately, the bandgap is sensitive to temperature

changes: higher temperatures reduce the width of the bandgap, while lower temperatures increase it. By cooling HPGe with liquid nitrogen, the band gap can be increased to 0.746 eV: just enough such that the electrons cannot be thermally excited across the band gap [69]. Silicon has a bandgap on the order of 1.12 eV at room temperature, sufficient to avoid thermal excitation without additional cooling.

When an electron is excited into the conduction band, it leaves a hole behind in the valence band. This hole can be effectively modeled as a positive charge in the valence band—an electron moving in the +x direction from a valence band location to occupy a hole is equivalent to the movement of a positive charge in the -x direction. In an intrinsic semiconductor, the number of electrons in the conduction band is at all times equal to the number of vacancies, or holes, left in the valence band—i.e.: there is no dominant charge carrier. However, by adding small quantities of impurities this equilibrium can be altered such that either electrons or holes become the dominant charge carrier. The impurities are taken from either group III or group V from the periodic table and introduce sites in the band gap that are very close to, but just above, the valence band (in the case of group III impurities) or very close to, but just below, the conduction band (in the case of group V impurities). Impurities are never added in significant enough quantities to alter the bulk properties of the lattice.

When a group III impurity is introduced the semiconductor is known as p-type: the impurity has one less electron than the surrounding silicon atoms, and the proximity of the acceptor level to the valence band allows for valence electrons to easily jump from the valence band to the impurity acceptor level. This in effect inserts an additional hole into the lattice structure without a corresponding electron in the conduction band, making holes the dominant signal carrier. N-type semiconductors are created when group V impurities are introduced to the lattice, and work in the exact opposite way to p-type semiconductors: the impurity has one more electron than the surrounding silicon atoms, and the proximity of the donor level to the conduction band allows for the electrons to easily jump from the impurity donor level into the conduction band. This in effect inserts an additional electron into the conduction band without a corresponding hole in the valence band, making electrons

the dominant signal carriers. The structure and band diagrams for p-type and n-type semiconductors can be seen in Fig. 11.

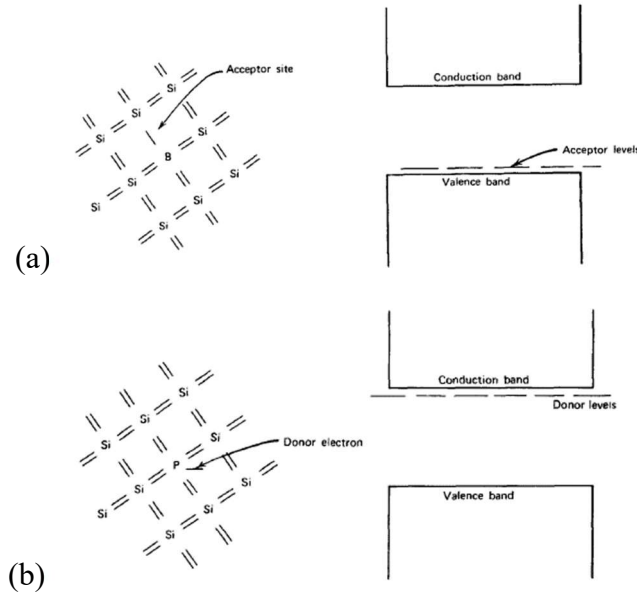


**Fig. 11.** (a) A p-type semiconductor lattice (left) and energy diagram (right); (b) an n-type semiconductor lattice (left) and energy diagram (right) [68]

By coupling an n-type and p-type semiconductor together, a junction is formed. Due to the gradient between free electrons and free holes across the contact point, free electrons on the n-side drift into the p-type material and free holes on the p-side drift into the n-type material. Stationary positive and negative charges, respectively, are left behind in the region surrounding the contact point. This in turn results in a static net electric field across the region known as the depletion region, which is the active part of the radiation detector. If radiation interacting in this region generates electron/hole pairs, the holes are naturally inclined to be swept to the n-side and electrons are naturally inclined to be swept to the p-side due to the electric field across the junction. This can be seen in Fig. 12a.

If a voltage is applied across this junction in a forward bias configuration (anode on p-side, cathode on n-side), it increases the electric field already present due to the space charge configuration in the depletion region. The majority carriers flow more freely, causing large currents (milliamps to amps) across the semiconductor without any radiation interactions. As the electron-hole pairs generated in radiation

interactions cause currents on the order of microamps, these large currents drown out interaction information. However, if a reverse bias configuration is used (anode at n-side, cathode at p-side), more residual free electrons from the p-side are pulled across the junction to the anode and more holes are pulled from the n-side across the junction to the cathode, creating more fixed space charges and increasing the size of the depletion region (i.e.: increasing the active volume of the detector). In this configuration, leakage currents are minimized because only the minority carriers are drawn across the junction. If radiation interacts inside the depletion region, holes are swept to the p-side and electrons are swept to the n-side and collected [70]. The reverse biasing configuration is shown in Fig. 12b.

The charges on either side of the depletion region also act as a capacitor, which is detrimental to the maximum pulse height possible to extract from the detector and thus detrimental to the signal-to-noise ratio. To reduce the capacitance, the distance between the two “plates” should be increased as much as possible via increasing applied bias, which in turn widens the depletion region. The width of the depletion region can in principle be increased to the point where nearly the entire silicon volume is active [71]. However, care must be taken to avoid increasing the bias voltage so high that the charges on either side of the junction have enough potential to freely cross the depletion region, which results in a breakdown of proportionality and can potentially damage the detector. Any volume of the semiconductor not within the depletion region is a dead volume that is not sensitive to radiation. As the outer surfaces of the detector are the locations of these dead volumes, they act as attenuators for incident radiation. These dead layers are detrimental to the spectroscopic capabilities and efficiency of the detector and should be minimized if possible.

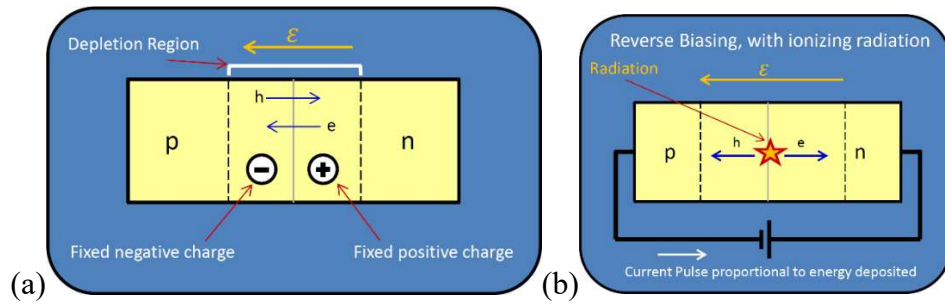


**Fig. 12.** (a) Depletion region in a p-n semiconductor, with no external bias applied; (b) reverse biasing configuration applied to improve the proportionality and performance of a semiconductor detector, with radiation creating an electron/hole pair in the depletion region. Note the increased width of the depletion region due to the reverse bias [67]

#### 2.2.2.2. Silicon Photomultipliers (SiPMs)

If reverse bias is increased past proportionality, but not to the point that the detector experiences damage, any electron-hole pair created in the active volume of the detector is accelerated to the point that it has enough energy to generate additional electron-hole pairs. These pairs go on to create still more pairs, and an avalanche of charge is generated, which continues until the behavior is quenched (typically via a quench resistor) [72]. Each avalanche results in roughly the same amount of liberated charge, and the current generated is orders of magnitude larger than the current from individual electron-hole pairs. A cross section sketch of a semiconductor detector undergoing an avalanche is depicted in Fig. 13.

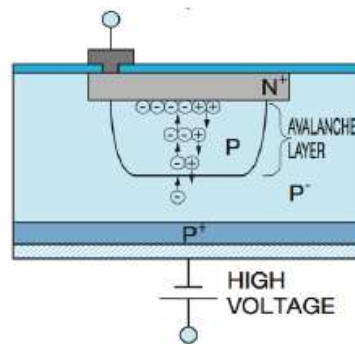


**Fig. 13.** Cross section of a Hamamatsu n-on-p photodiode experiencing an avalanche [73]



Under these biasing conditions, the silicon detector behaves as a pure counter, reminiscent to a Geiger-Müller tube, and as such is often called a Geiger-mode avalanche photodiode (G-APD or APD) [74]. If an array is formed using many thousands of extremely small APDs (on the order of tens of micrometers), the device is known as a silicon photomultiplier, or SiPM. The structure of an SiPM can be seen in Fig. 14.

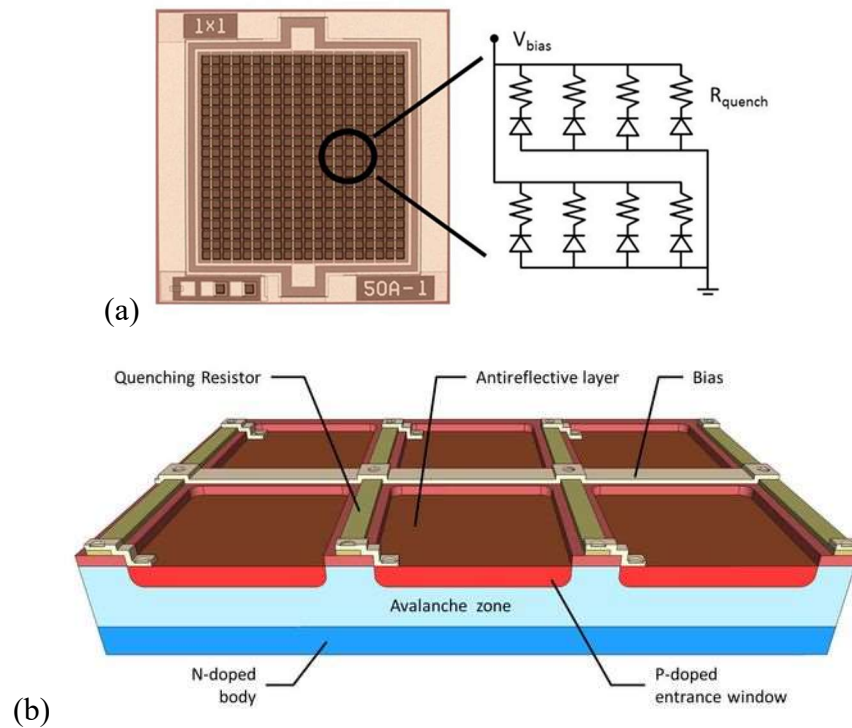


**Fig. 14.** (a) Physical layout of a 1x1 SiPM. Typical SiPMs are comprised of several thousand unique APDs connected in parallel [75]; (b) cross section of an SiPM [76]

The individual APDs, or pixels, of an SiPM can be triggered by visible light photons and are ideal for coupling to scintillators, where the number of pixels triggered is proportional to the amount of light generated in the scintillator. In this way SiPMs perform a similar function to photomultiplier tubes (PMTs). Like PMTs, SiPMs have higher sensitivities to certain wavelengths than to others, and so to for the best light collection efficiency the specific model of SiPM and type of scintillator should be selected to maximize agreement between the emission and absorption spectra.

SiPMs have many benefits over PMTs, including single-photon resolution, insensitivity to magnetic fields, low bias voltage, compactness, modularity, and ruggedness [77]. However, SiPMs are outperformed by PMTs in several respects. It can be costly to create large arrays of SiPMs, and large SiPMs are more susceptible to effects of cross talk. Moreover, increasing the number of SiPMs connected in parallel also increases parasitic capacitance, which is detrimental to signal-to-noise ratio. SiPMs experience significant sensitivity to temperature fluctuations, which is not as large of a concern for PMTs. PMTs are also a direct amplification of light output in a scintillator, meaning that the output signature from a PMT is a true representation of the scintillator timing performance [78]. Due to the semiconductor nature of the SiPM, additional complications are introduced. This makes simulating the output of an SiPM more difficult [79]–[81], and also influences the shape of the output signal [82]. However, for many applications, including small systems such as the detector that is the focus of this work, the advantages of SiPMs as light collection devices outweigh the disadvantages.

### 2.2.2.3. *PIPSBox*

The PIPSBox-2x1200-500A, manufactured by Canberra Industries [83], is a cylindrical gas cell and electron detector specially designed for radioxenon detection applications. Initially designed for utilization with NaI(Tl) crystals in a new generation beta-gamma coincidence detector using the SPALAX gas sampling system [84], the PIPSBox has been subject to significant study by several groups in the application of many different configurations for radioxenon detection [17], [22], [45], [85]–[87]. It consists of two Passivated Implanted Planar Silicon (PIPS) wafers in a parallel configuration and is held in place with an aluminum chassis, as can be seen in Fig. 15. These silicon wafers have a thickness of 500  $\mu\text{m}$  and circular active areas of  $\sim 1200 \text{ mm}^2$ , matching the dimensions of the internal gas volume ( $10.6 \text{ cm}^3$ ). When applying the recommended bias of -145 V, the depletion region amounts to roughly the entire volume of the detector and results in minimal dead layer [71]. This thickness is sufficient to completely absorb the energy of the electrons emitted from

the radioxenon isotopes of interest. The wafers are externally shielded by 650  $\mu\text{m}$  thick carbon windows which promote gas-tightness while also shielding the wafers from light and external charged particles. The PIPSBox can be brought down to a near-perfect vacuum without popping the carbon windows and ruining the gas tightness, so long as the pressure is decreased gradually. A thin metal tube is used to inject gas samples into the cell. The gas volume is almost entirely contained between the active areas of the silicon save for the tube itself, a small rectangular divot near the chip signal readouts, and several small and difficult to quantify dead volumes throughout the detector between the chassis, carbon windows, and silicon detectors. A cross section sketch of the PIPSBox can be seen in Fig. 16, and the specifications for the PIPSBox are listed in Table 4.

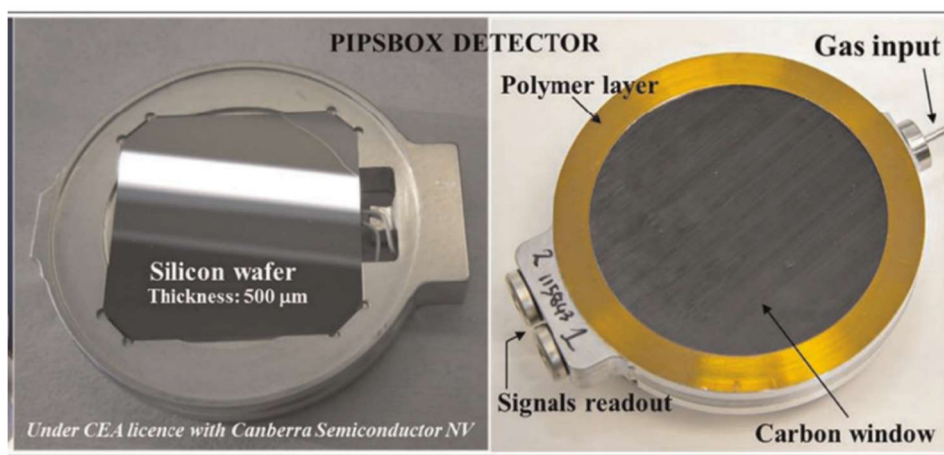


**Fig. 15.** PIPSBox detector: (left) silicon wafer detector in aluminum assembly, without carbon window; (right) fully assembled PIPSBox gas cell, with carbon window [17]

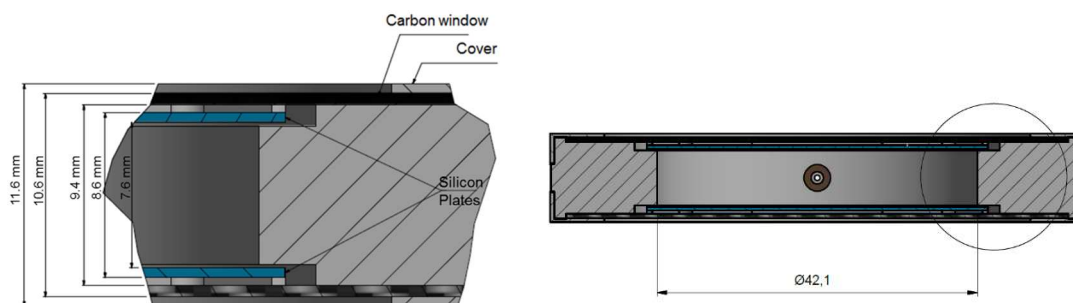


**Fig. 16.** Sketches indicating the PIPSBox dimensions and internal structure [71]

**Table 4.** Parameters for the PIPSBox-2×1200-500A [88]

Detector model	2 × PD1200-26-500
External dimensions (L × W × H)	84 × 70 × 12 mm <sup>3</sup>
Gas volume within PIPSBox	10.6 cm <sup>3</sup>
Active area (per silicon wafer)	1200 mm <sup>2</sup>
Chip thickness (per wafer)	500 μm
Carbon-epoxy window thickness	650 μm
Depletion depth (min - max)	475 – 515 μm
Operating voltage	100 – 150 V
Operating temperature	-20 – +40 °C
Leakage current (at +20 °C)	50 nA

The PIPSBox presents three key advantages over the commonly used plastic scintillators used in radioxenon detection systems: background, electron energy resolution, and memory effect. The low background materials involved in the construction of the PIPSBox as well as the shielding provided by the carbon windows and the aluminum chassis make the PIPSBox an inherently low background system in comparison to a plastic scintillator, reducing the chance of accidental triggers and coincidences. Electron energy resolution in the PIPSBox is significantly improved compared to plastics: a 7% FWHM has been measured with the PIPSBox for the 129 keV conversion electron from <sup>131m</sup>Xe [84], while the best energy resolution observed in plastic scintillators at this energy is ~23% FWHM [12], [89]. The significantly improved electron resolution allows for clearer separation between the closely-spaced conversion electron signatures of <sup>131m</sup>Xe (129 keV) and <sup>133m</sup>Xe (199 keV), reducing interference and improving MDC. As memory effect involves the persistence of signature from previous sample injections, the rate at which systems with strong memory effect (such as plastic scintillator-based systems) can evaluate new samples is significantly hampered. A memory effect of ~0.3% has been observed in the PIPSBox when subjected to a series of pump and flushes using a roughing pump, and still less (~0.1%) when a turbo pump is used to reach even lower pressures [17], [84], [86]. By comparison, a memory effect upwards of 5% has been observed in unmodified plastic scintillators under similar conditions [14], [90]. Though the aluminization of the inner surface of a plastic gas cell has been shown to reduce

memory effect by several orders of magnitude through the creation of a diffusion barrier [90], [91], such methods can be costly and difficult.

The PIPSBox, despite its advantages, is not without flaws. The PIPSBox has a solid angle of  $2.54\pi$  [45], a far cry from the  $4\pi$  solid angle approximated by the plastic scintillators typically used in radioxenon detection systems. This reduction in solid angle, and consequently efficiency, counterbalances the significant improvement in electron resolution and background. Attenuation of low energy photons is a significant concern—MCNP simulations indicate that 31 keV X-rays are attenuated by the PIPSBox at a rate of  $\sim 25\%$ . The PIPSBox is also quite noisy, making it difficult to achieve a noise threshold below about 60 keV when utilized in experiments with an AMPTEK A250F/NF [92]. However, when used with a preamplifier specially designed by Canberra (originally Mirion Technologies) for the PIPSBox, the detector is expected to achieve energy thresholds as low as 12 keV [93]. The PIPSBox experiences electron backscatter due to the high-Z of silicon, which is detrimental to spectroscopy and causes interference. However, provided the backscattered electron was detected in both PIPS, the full energy of the electron can be reconstructed by summing the signal from both PIPS [45]. A low noise threshold is advantageous in this, as backscattered electrons may not have enough energy to trigger the second silicon if a high noise threshold is used, particularly for lower energy electrons such as the 129 keV electrons from  $^{131\text{m}}\text{Xe}$ .

### ***2.2.3. Field Programmable Gate Arrays (FPGAs)***

The field programmable gate array, or FPGA, is an integrated circuit device that can be programmed by a user to perform various tasks. Unlike circuits designed on a printed circuit board (PCB) or application specific integrated circuits (ASICs), the design of an FPGA is not dictated at the time of manufacturing—instead, an FPGA has various configurable logical blocks that can be placed and rearranged at will by the user. The structure of an FPGA is reset every time the device is power cycled, allowing for rapid prototyping and on-the-fly changes and tests [94], [95].

The design of the FPGA is dictated using a hardware description language (HDL) such as VHDL or Verilog [96]. These description languages grant the user a degree of abstraction to aid in logic design without being hampered by minutia, similar to how programming languages such as Python abstract the user from machine-level processes described in languages such as Assembly so that the user may think more about what should be done with the code, rather than how to do it. For example, instead of designing an adding circuit, the user may use an HDL and write code describing the functionality of an adding circuit; when the code is compiled and the FPGA is programmed, the compiler will generate the circuit structure for the user. Components that may be defined in FPGAs include, but are not limited to, storage elements such as registers, flip-flops, and block RAMs, multiplexers, and state machines. The internal structure of the FPGA is communicated to the rest of a circuit through input/output (I/O) pins. Firmware is then used to communicate with these I/O pins, allowing the user to interact with the FPGA using a software application programming interface (API) [97]. A sketch of an FPGA is shown in Fig. 17.

It may seem at first glance that FPGAs fit a similar role as microcontrollers in electronic design. However, microcontrollers differ fundamentally in that they are sequential. Because the logic of an FPGA is defined on the hardware level, it can operate many processes in parallel [98]. FPGAs can make decisions in real time based on stimulus from multiple separate and concurrent inputs, which makes them ideal for applications that require monitoring several signals simultaneously.

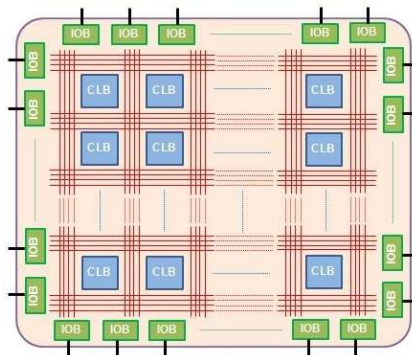


**Fig. 17.** The internal structure of an FPGA, with configurable logic blocks (CLBs) defining the internal logic and I/O Blocks (IOBs) providing means for the FPGA to communicate with the surrounding circuitry [98]

## 2.3. Algorithms and Calculations

Various algorithms and calculations, some already well-established in literature and some designed and improved during this research, are necessary for the development of a proper analysis framework. Discussed below is the radioxenon identification regimes currently employed, determination of minimum detectable concentrations for the radioxenon isotopes of interest, and various data processing procedures important to the completion of this work.

### *2.3.1. Radioxenon Identification- ROI Method*

The several means for coincident radioxenon identification can be broadly broken into two categories: region of interest (ROI) methods and statistical methods. Of these two, the ROI methods are the ones utilized by the CTBTO and the U.S. National Data Center [99]. To discern the radioxenon coincidence events from the background, one must define a range of energies for photons and for electrons, wherein one looks for coincidence events. These ROIs are defined as  $2\times$  the full-width at half-max (FWHM) of the peaks of interest [100], though have also been defined in other ways [101]. These ranges are typically visualized as boxes on a 2D histogram plot of the coincidence events, where gamma energies are plotted against electron energies. The most common number of defined ROIs is 7: one for  $^{214}\text{Pb}$  (a daughter of  $^{222}\text{Rn}$ ), one for  $^{135}\text{Xe}$ , one for  $^{133\text{m}}\text{Xe}$ , one for  $^{131\text{m}}\text{Xe}$ , and three for  $^{133}\text{Xe}$  (one for the gamma coincidence line, one for the X-ray coincidence line, and a third in the X-ray coincidence line that overlaps the metastable isotopes). However, in some cases 10 ROIs are used: six are the same as the first six detailed above, but instead of one ROI in accounting for the interference of  $^{133}\text{Xe}$  with the metastable isotopes, four ROIs are defined [102]. Examples of ROI definitions can be seen in Fig. 18.

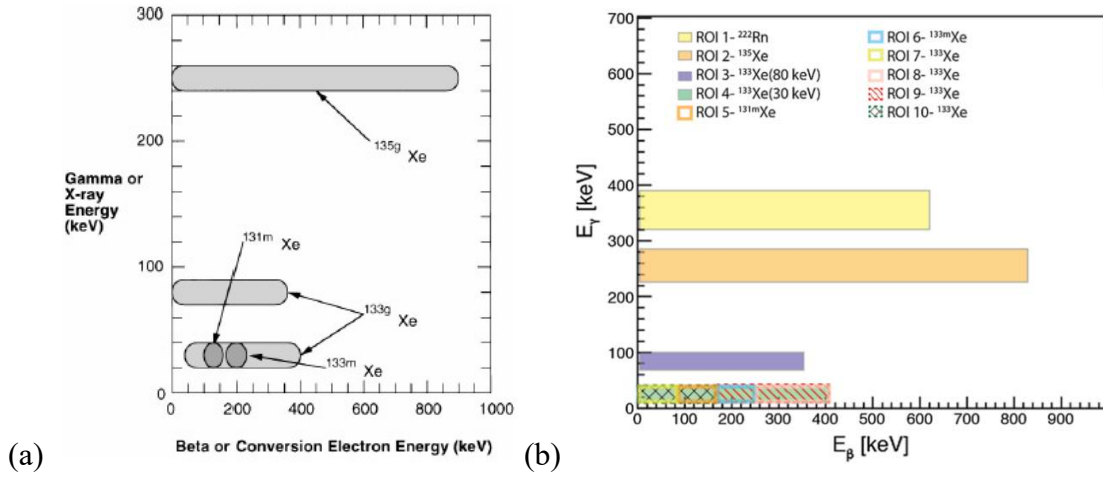


**Fig. 18.** (a) Regions of interest defined exclusively indicating the radioxenon isotope signatures on a 2D coincidence histogram plot [40]; (b) 10 regions of interest defined for the radioxenon isotopes of interest, plus  $^{214}\text{Pb}$  (the radon daughter), on a 2D coincidence histogram plot without background [102]

As the definition of ROIs comes directly from the FWHM of the photopeaks and electron peaks of interest, high resolution detectors yield smaller ROIs. The impact that improved energy resolution and small ROIs have on MDC can be quite significant [85]. A smaller window of energies reduces the range of energies wherein a background coincidence may be falsely defined as a true coincidence for all four nuclides in general. More specifically, for the two metastable isotopes a smaller ROI reduces the interference counts from the overlapping beta spectrum from  $^{133}\text{Xe}$ . As all photons are monoenergetic it is especially critical for photon detectors to have a good energy resolution, but electron energy resolution is also key for the monoenergetic electrons emitted by  $^{131\text{m}}\text{Xe}$  and  $^{133\text{m}}\text{Xe}$ .

### 2.3.2. Statistical Methods

Though the ROI method is the dominant method for radioxenon identification, other approaches have been investigated [99]. Extensive work has been conducted involving deconvolution methods for determining the contribution of several radioxenon isotope signatures to a single spectrum [19], [46], [103]–[106]. This involves solving an over defined linear system of equations of the form  $\underline{\mathbf{A}} * \underline{\mathbf{w}} = \underline{\mathbf{b}}$  to determine individual isotopic contributions to an experimental coincidence spectrum.



This technique has been implemented in the Spectral Deconvolution Analysis Tool (SDAT) software and has demonstrated impressive results in determining the percent contribution of each isotope to a mixed spectrum when compared to the ROI method.

The library of individual isotopic spectra can be taken via experimentation, or via simulation (e.g.: MCNP) provided that the detector to be utilized in experiments is accurately defined in the simulation and various physics concerns such as Compton backscatter are fully accounted for. Library spectra must be appropriately calibrated such that all spectral features between them and the experimental spectrum are in agreement. In all cases where this algorithm is utilized, the  $n \times m$  dimension 2D coincidence histogram for each library isotope as well as the experimental spectrum are decomposed into vectors of dimensions  $(n \times m) \times 1$ . The library isotopes are then placed, column by column, into the **A** matrix, and the experimental spectrum is placed into the **b** column vector. The system is solved to yield a column vector of spectrum weights **w**. This system can be seen in eqn. (1):

$$\begin{bmatrix} X & X & X & X & R & B \\ e & e & e & e & n & c \\ 1 & 1 & 1 & 1 & 2 & k \\ 3 & 3 & 3 & 3 & 2 & G \\ 1 & 3 & 3 & 5 & 2 & n \\ m & m & & & d \end{bmatrix} \begin{bmatrix} C_1 \\ C_2 \\ C_3 \\ C_4 \\ C_5 \\ C_6 \end{bmatrix} = \begin{bmatrix} S \\ a \\ m \\ p \\ l \\ e \end{bmatrix} \quad (1)$$

The technique can accommodate an arbitrarily large number of library spectra, but is typically used with either 4 ( $^{131\text{m}}\text{Xe}$ ,  $^{133\text{m}}\text{Xe}$ ,  $^{133}\text{Xe}$ , and  $^{135}\text{Xe}$ ), 5 (the four radioxenons and detector background), or 6 (the four radioxenons plus radon and its progeny and detector background). Compressing the spectrum (e.g.: from  $256 \times 256$  to  $64 \times 64$ ) for better statistics in each channel has been shown as effective in improving results, while binary masking techniques (where regions determined important are assigned a “1” and regions determined unimportant, such as high energy regions in the background where no relevant radioxenon information is located, are assigned a “0”) have achieved mixed results [105].

### 2.3.2.1. Statistical Methods- Least Squares

Least squares is a regression method for obtaining the best solution possible for a system of linear equations  $\underline{\underline{A}}^* \underline{\underline{w}} = \underline{\underline{b}}$  where discrepancies between the  $\underline{\underline{A}}$  matrix and  $\underline{\underline{b}}$  vector do not permit an exact solution for  $\underline{\underline{w}}$ . This often is the case with experimental data where noise (statistical or otherwise) does not allow  $\underline{\underline{w}}$  to perfectly satisfy trends defined by the linear system. It is a non-iterative method and is best applied in cases where the statistical distribution for each unique sample (in the case of spectroscopy, a sample is defined as the number of counts in a channel) is Gaussian [107].

The method of regression attempts to minimize the squared difference between a data point and a line of fit. The difference between the datum  $y_i$  and fit value  $\hat{y}_i$  is the residual  $r_i$ . The summed squares  $S$  of the residuals for  $n$  data points are then given by:

$$S = \sum_{i=1}^n r_i^2 = \sum_{i=1}^n (y_i - \hat{y}_i)^2 \quad (2)$$

By minimizing this summation, the optimal fit values can be derived [108]. In the context of spectroscopy and the linear system  $\underline{\underline{A}}^* \underline{\underline{w}} = \underline{\underline{b}}$ , the best fit can be determined by solving the eqn. (3) [109]:

$$\underline{\underline{w}} = (\underline{\underline{A}}^T \underline{\underline{A}})^{-1} \underline{\underline{A}}^T \underline{\underline{b}} \quad (3)$$

Many software packages and functions exist to that effectively conduct this to calculate the best fit, such as the simple backslash in MATLAB [108]. The SDAT software has primarily been implemented using a non-negative least-squares solver approach, with significant success [105].

### 2.3.2.2. Statistical Methods- Maximum Likelihood

Maximum likelihood is an attractive alternative to a least squares solve when the statistics associated with each sample are not Gaussian in nature (e.g.: Poisson statistics characteristic of low count rates) [107]. In general, maximum likelihood estimates differ from least squares estimates, particularly for data that are not normally distributed. As maximum likelihood methods attempt to use all the

information of the spectrum, they are particularly robust; nevertheless, they can fall victim to common issues involved in optimization problems such as local maxima [110].

A probability density function (pdf) involving  $\theta$ , a vector of unknown parameters, and  $y_1, \dots, y_n$ , the random variables yielded from the generating process governed by  $\theta$ , is denoted by  $f(y|\theta)$ . The joint density, or likelihood function  $L(\theta|\mathbf{y})$ , is the product of the individual densities of  $n$  variables:

$$f(y_1, \dots, y_n|\theta) = \prod_{i=1}^n f(y_i|\theta) = L(\theta|\mathbf{y}) \quad (4)$$

It is noteworthy that the likelihood function is written in the opposite form of the joint density pdf—the joint density pdf is written as a set of data conditioned on parameters, whereas the likelihood function is a set of parameters conditioned on the data. Though they are equivalent, it implies that the focus of the likelihood function is in the parameters based on observed data [111]. Maximum likelihood methods involve determining values for the parameters  $\theta$  that will maximize this likelihood function—in other words, it aims to determine the parameters most likely to have produced all the observed data. This is done by taking the derivative of the likelihood function and setting it equal to zero. Due to the relative simplicity of working with the derivatives of summations as opposed to products, by exploiting the properties of logarithms this maximization is often done on the log of the likelihood function:

$$\ln(L(\theta|\mathbf{y})) = \sum_{i=1}^n \ln(f(y_i|\theta)) \quad (5)$$

As the natural logarithm is a monotonic function, the values that maximize the likelihood function also maximize the natural log of that function, making this a useful simplification.

Spectral deconvolution using maximum likelihood has shown promise in radioxenon identification applications. A study on SDAT where maximum likelihood was used as a solver demonstrated impressive results, outperforming both the ROI

method and the least-squares method in low-count situations [112]. As low count rates are the most likely scenario for an atmospheric detection of radioxenon, maximum likelihood may be the ideal tool for the application. The log-likelihood function for the Poisson distribution in this case is defined as:

$$\ln(L) = \sum_{i=1}^N \left( - \sum_{k=1}^M W_k f_k(i) + S(i) \ln \left( \sum_{k=1}^M W_k f_k(i) \right) - \ln(S(i)!) \right) \quad (6)$$

where  $S(i)$  is the vectorized form of the experimental sample spectrum with channel numbers denoted by  $i$  ranging from 1 to  $N$ ,  $k$  denotes the spectral component ranging from 1 to the maximum  $M$  (4 or 6),  $f_k(i)$  is value of the normalized reference spectrum for the  $k$ th nuclide/spectral component at channel  $i$ , and  $W_k$  is the unknown weighting (activity) of the  $k$ th nuclide/spectral component to be solved for. The maximization of this quantity takes the form:

$$\sum_{i=1}^N \left( \frac{S(i) f_j(i)}{\sum_{k=1}^M W_k f_k(i)} - f_j(i) \right) = 0, j = 1, 2, \dots, M \quad (7)$$

Following and adapting previous literature [113], the system can be solved iteratively for  $W_k^q$ , where  $q$  is the iteration number, via:

$$\sum_{k=1}^M W_k \sum_{i=1}^N \frac{f_k(i) f_j(i)}{D_q(i)} = \sum_{i=1}^N \frac{S(i) f_j(i)}{D_q(i)} \quad (8)$$

$$D_q(i) = \begin{cases} \sum_{k=1}^M W_k^{q-1} f_k(i), & \text{if } q > 0 \\ S(i) + 1 & \text{if } q = 0 \end{cases} \quad (9)$$

where  $D_q(i)$  is the variance of the number of counts in each channel varying with each iteration  $q$ .

### 2.3.2.3. Hybrid and Other Methods

Bayesian methods have been applied to studies of composite gamma spectra [114], [115]. Using prior information gleaned from previous measurements as well as

current measurements, the Bayesian approach minimizes the error weighted least square difference between an overfitted linear system of equations representing the summation of weighted gamma spectra fits for each of the isotopes of interest and a full experimental spectrum. This method is used in radioxenon detection by examining the ratios between two or more isotopes of interest. Successful detection criterion is based on the probabilistic distributions of possible ratios between radioxenon isotopes based on the measurement and the priors. This method uses the full information of the gamma spectra, not just the regions of interest, and theoretically allows for more consistent decision making. However, at the time of writing no in depth study of this method has yet been conducted specifically for radioxenon application. Studies of Bayesian methods as applied to radioxenon measurements have shown that it is possible to achieve activity estimates for  $^{131\text{m}}\text{Xe}$  and  $^{133\text{m}}\text{Xe}$  that are well under conventionally defined critical limits by using anti-correlated Bayesian approaches with maximum likelihood [116].

Other methods include successive 1D Gaussian fitting and ROI simultaneous fitting [99]. 1D Gaussian fitting utilizes known peak locations and known detector resolutions to reduce interference in regions of interest. Constrained Gaussian fits are applied to the 1D electron and photon spectra where radioxenon signatures would appear were they present in the sample, and counts using the fitted Gaussians are used instead of the raw ROI counts, reducing noise. ROI simultaneous fitting is very similar to SDAT, but instead of using the entire spectrum for each vector only the counts in the ROIs are used as vectors. These vectors are all fit simultaneously using non-negative least squares. This approach ideally makes the algorithm more robust against noise and calibration drift when compared to either the traditional SDAT approach and the traditional ROI approach.

### ***2.3.3. MDC Calculation***

The minimum detectable concentration calculation was developed through the application of the statistical arguments on detection limits presented in the seminal paper by Currie in 1968 [117]. The critical level,  $L_c$ , is a count limit indicating the

number of counts (after subtracting background) necessary to determine that a source is present in the sample with a false positive rate  $\alpha$ . The detection level,  $L_d$ , is a count limit defined such that the probability distribution of possible outcomes (with  $\mu_{\text{sample}} = L_d$ ) intersects the critical level  $L_c$  such that the percentage  $\beta$ , indicating false negatives, falls below the  $L_c$ .  $L_c$  and  $L_d$  are determined based on the abscissa of the normal distribution. These levels are demonstrated in Fig. 19. Values of  $\alpha$  and  $\beta$  are defined by the experimentalist, though are in the case of radioxenon measurements typically both chosen to be 5% [118].

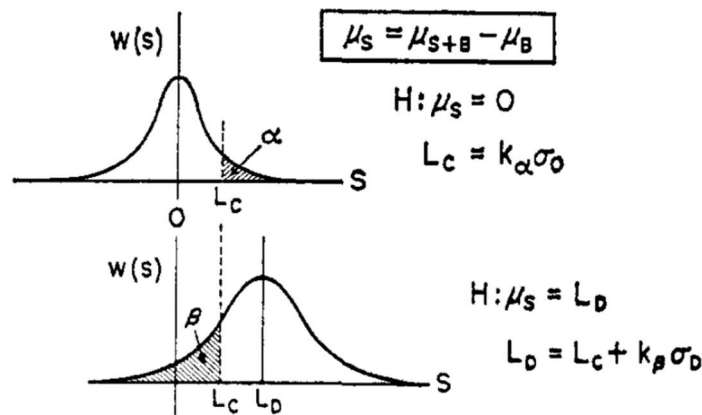


**Fig. 19.** The critical level  $L_c$  and the detection level  $L_d$ , with the acceptable amount of false positives denoted by  $\alpha$  and false negatives denoted by  $\beta$ .  $k$  are abscissa for the normal distribution,  $\mu$  is the mean for the source (S) and background (B),  $\sigma$  is the standard deviation of the normal distribution, and  $H$  is the hypothesis being presented. Note that  $\alpha$  and  $\beta$  do not have to be the same, as is the case here [117]

Applying these principles to radioxenon detection yields the minimum detectable concentration equation. A separate MDC value is calculated for each isotope of interest. The formula for these calculations is described in eqn. (10) [118].

$$MDC \left[ \frac{mBq}{m^3 \text{ air}} \right] = \left( \frac{2.71 + 3.29\sigma_0}{\varepsilon_{\beta\gamma} BR_{\beta\gamma}} \right) \left( \frac{\lambda^2}{(1 - \exp(-\lambda T_c)) \exp(-\lambda T_p) (1 - \exp(-\lambda T_A))} \right) \left( \frac{T_c * 1000}{V_{\text{air}}} \right) \quad (10)$$

The three subdivisions of the MDC equation effectively represent the influence of the different components of the radioxenon detection system [18]. The first term is related to the nuclear physics of the detector, with the terms representing:

- $\sigma_0: \sqrt{\frac{T_A}{T_B} BckCnt + \sigma_{BckCnt}^2 + InterferenceCnt + \sigma_{IntCnt}^2 + MemoryCnt + \sigma_{MemCnt}^2}$
- $\varepsilon_{\beta\gamma}$ : Efficiency for detection of a photon in  $SrI_2(Eu)$  and an electron in the PIPSTBox
- $BR_{\beta\gamma}$ : Emission intensity (branching ratio) of the coincident release of the photon and electron of interest (Table 2)

For the determination of the sigma term:

- $BckCnt$ : Summation of the total number of background counts observed in the ROI of interest
- $InterferenceCnt$ : Counts due to interferences from radon daughters,  $^{133}Xe$  in the metastable ROIs, electron backscatter interferences, and Compton scattering from higher energy photons into the lower energy ROIs
- $MemoryCnt$ : Counts due to memory effect
- $T_B$ : Background measuring time [s]

Radioxenon detection systems have a sample collection and gas processing unit. The second term of the MDC equation takes into account the radioactive decay of the particular nucleus being evaluated as it passes through this gas processing unit.

- $\lambda$ : Decay constant of isotope of interest (Table 2) [ $s^{-1}$ ]
- $T_c$ : Collection time of xenon sample [s]
- $T_p$ : Processing time of gas [s]
- $T_A$ : Counts acquisition time [s]

The third term takes into account the amount of air sampled by the gas processing unit to make the sample being evaluated and converts the result to the units of mBq/m<sup>3</sup>.

- $V_{air}$ : Sampled air volume [m<sup>3</sup>]

Excepting  $\lambda$ , the variables included in the second and third part of the equation are associated with the gas processing unit, not the detector itself nor the physics of the radioxenon of interest [18]. When calculating the MDC of a radioxenon detector without a specifically associated gas processing unit, it is not unusual to use values associated with other gas processing units [87] such as ARSA [14] or the new Xenon International system [9], [15].

Though for final reporting a unique MDC is determined for each isotope, the calculation is conducted on an ROI-by-ROI basis. This is an important distinction for  $^{133}\text{Xe}$ , where the two unique coincident decay paths result in two unique ROIs that must be accounted for. To determine the overall MDC for  $^{133}\text{Xe}$ , an MDC must be uniquely calculated for each ROI and the values must be combined using the equation shown in (11) [118]:

$$MDC_{^{133}\text{Xe}} \left( \frac{\text{mBq}}{\text{m}^3 \text{air}} \right) = \sqrt{\frac{1}{(MDC_{^{133}\text{Xe}}^{30 \text{ keV}})^{-2} + (MDC_{^{133}\text{Xe}}^{81 \text{ keV}})^{-2}}} \quad (11)$$

For the calculation of MDC for each isotope, *BckCnt* is simply the total number of counts falling into the ROI associated with that isotope during the background measurement. The background counts are scaled to the measurement time used for analyzing atmospheric samples and is typically defined to be 24 hours, in agreement with the measurement time used by ARSA. For photons and monoenergetic electrons the ROIs are defined based on the measured FWHM of each peak of interest, while for beta spectra the ROIs are determined by using the beta end point energies described in Table 2.

### 2.3.4. Signal Processing

Radiation does not loudly proclaim its existence—it is an inferred presence that is identified by inspection of secondary effects, such as changes in current or voltage in a measurement system. How this inspection is done is a question of signal processing, which is relevant from algorithmically identifying a radiation event to resolving pulse amplitude.

#### 2.3.4.1. Digital Filtering and Filter Design

Digital filtering is a technique of convolving a signal, each individual sample being denoted by  $x[n]$ , with a response function defined by filter coefficients  $h[n]$ , to yield the output signal  $y[n]$ . This process, mathematically, is defined as [119]:



$$y[n] = \sum_{k=0}^N h[k] * x[n - k] \quad (12)$$

where  $N+1$  is the number of filter coefficients in the response function. The response function can in theory have an arbitrarily large number of coefficients, but in practice is limited by implementation resources [120] and application considerations.

The convolution operation involves defining a form for a filter,  $h = h[0], h[1], \dots, h[N]$ . The filter is then reversed and then shifted across the input signal  $x$ . At each value of  $[n]$ , the coefficients of  $h$  are multiplied by the coefficients of  $x$  in the manner of  $h[0]x[n]$ ,  $h[1]x[n-1]$ ,  $h[2]x[n-2]$ , ...,  $h[N]x[n-N]$ . These products are then summed together to yield the value  $y[n]$ . The process is repeated for every  $n$ . Another way this procedure can be visualized is holding the position of the filter constant while the incoming data flows by. This operation is quite easily introduced in hardware via multiplication and summation circuits. A logical visualization of this process is shown in Fig. 20, while the hardware implementation is shown in Fig. 21.

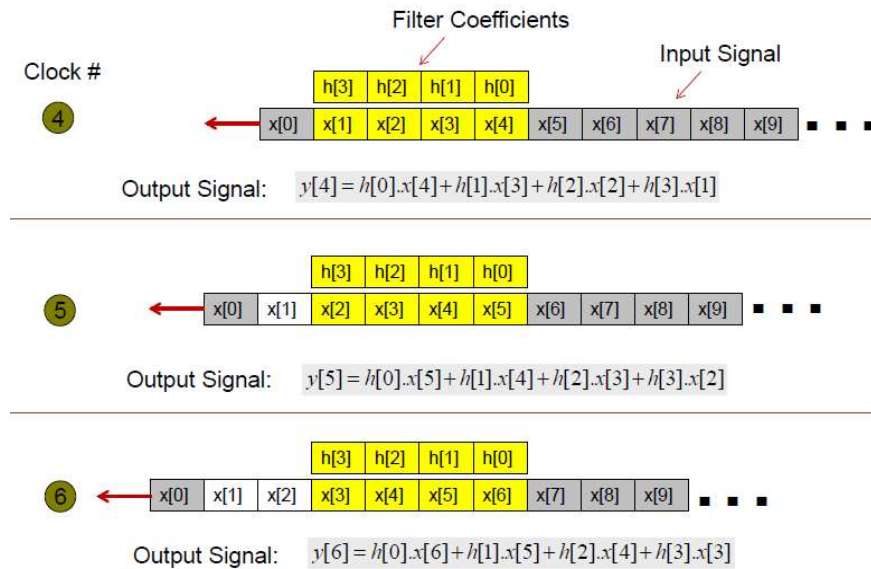


**Fig. 20.** Convolution process using a four-element filter on an incoming stream of data [119]

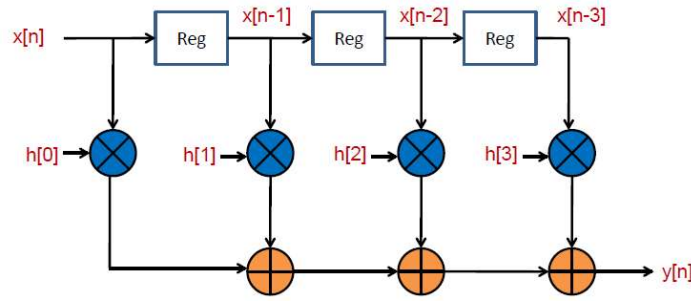


**Fig. 21.** Hardware implementation of a four-element filter. *Reg* indicates a shift register that delays the input signal by one clock cycle [119]

Filtering is particularly useful in noise reduction: by averaging many samples together, the impact of random fluctuations in signal noise can be minimized. A moving average filter is one such filter, designed by setting the coefficients in the response function of length  $N$  to be  $h[n] = 1/N$ . Triangular filters use response functions that are symmetric, where on the leading edge there are  $N/2$  samples with a value  $h[n] = +1$ , followed by  $N/2$  samples with a value  $h[n] = -1$ . The amount of time encompassed by these samples is known as the peaking time of the filter. The triangular filter sums the most recent samples, but then subtracts away an equal number of older samples. When exposed to an ideal baseline (i.e.: no radiation pulse) with noise, the triangular filter returns a value of 0. Triangular filters typically have a sharp peak, and as such they are ideal for use as an energy-level based triggering mechanism. When a pulse is observed, the triangular filter sums along the rising edge of the pulse while subtracting away the baseline, leading to a peak that (provided the size of the response function is appropriately chosen) is significantly shorter and more pronounced than the original pulse.

Trapezoidal filters are similar to triangular filters, save that they have a gap between the  $+1$  and  $-1$  portions of the response function where  $h[n] = 0$ , which is referred to as the flat top time. Trapezoidal filters are particularly useful for determining the amplitude of incoming pulses with more reliability than simply finding the peak value of the pulse, which could be obscured by noise. The flat top time is defined to be of a size roughly the size of the peaking time of the pulse. Defining the trapezoidal filter coefficients in this manner means the maximum values

at the top of the pulse are summed together while values on the baseline are subtracted away, resulting in the most distinct peak in the filtered signal and thus yielding the highest energy resolution possible.

#### 2.3.4.2. *Triggering*

As stated in the previous section, triangular filters are particularly useful as energy threshold-based triggers. This approach is called leading edge triggering. However, in situations when dealing with varying pulse amplitudes and timing is particularly important, this approach may present issues. For example: charge sensitive preamplifiers (CSPs) integrate incoming charge with a characteristic rise time based on the internal capacitance of the device [121]. Pulses coming from CSPs thus have a fixed rise time regardless of amplitude, meaning that pulses with different maximum pulse heights will cross an energy-based trigger threshold at different times. This is known as trigger walking, as exemplified in Fig. 22. Trigger walking can be very problematic for coincidence systems, particularly those which rely on coincidence timing windows with tight restrictions.

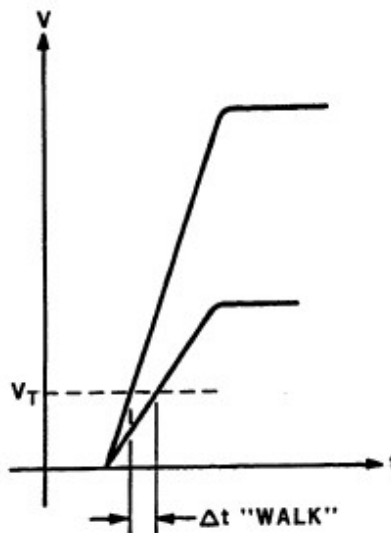


**Fig. 22.** Trigger walking, where using a leading edge trigger will result in different trigger times for pulses with a fixed rise time but different amplitudes [122]

Constant fraction discrimination (CFD) is an alternative approach to a leading edge trigger that reduces or eliminates trigger walking. Instead of triggering once the

pulse reaches a certain energy, the system triggers on an incident pulse at a certain fraction of the rise time. This is achieved by making a copy of the original pulse, scaling/shrinking the copy by a certain fraction, and then delaying the original pulse by some amount of time. The copied pulse is then subtracted from the original, but temporally shifted, pulse, creating a signal that crosses the zero value at a fixed percentage of the peak height. A depiction of the CFD method is shown in Fig. 23.

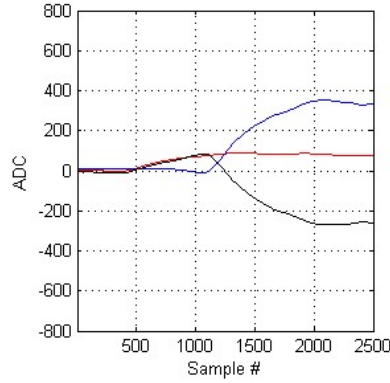


**Fig. 23.** A depiction of a constant fraction discriminator being used on a pulse from a charge sensitive preamplifier. The blue pulse is the original, but temporally shifted, pulse, the red is the copied and scaled pulse, and the black is the subtracted pulse

Assuming a linear rise time, the comparator should fire at a time:

$$t_0 = \frac{t_d}{1 - f} \quad (13)$$

where  $t_0$  is the comparator firing time,  $t_d$  is the delay time, and  $f$  is the fractional amplitude of the pulse. To make the trigger time independent of both amplitude and rise time of the pulse, the delay time should be less than  $(1-f) \times t_r$ , where  $t_r$  is the minimum rise time [122].

#### 2.3.4.3. Coincidence Identification

There are two primary ways whereby coincidence events may be identified: list-mode and real-time. List-mode is the dominant form of coincidence data collection and recording, both within and outside of radioxenon-specific applications [17], [123]–[129]. In brief: list-mode involves reading out each unique radiation interaction via analog or digital readout electronics and generating a list of data, with each entry

corresponding to an event and including such crucial information as energy and time of interaction. A script then reads through the data and identifies interactions that are in close proximity in time and flags them as coincidence events. This method is advantageous in that all data can be examined in post-processing at the leisure of the user. Real-time methods, as the name implies, aim to identify coincidence events as they occur, such that no post-processing is strictly necessary. This coincidence identification module can be implemented in an FPGA using triangular filters, a trigger threshold, and a coincidence timing window (CTW), all of which may be defined by the user in advance. Because processing via hardware is extremely fast (determined by trace length and by the frequency of an onboard oscillator clock), it is the transfer of data via USB to a PC user interface that typically is the cause for dead time in a system. By only transferring data of interest (i.e.: coincidence pulses) to the PC, dead-time can be significantly reduced while still accurately indicating coincidence count rates [21], [92], [130]. Following the initial programming of the FPGA, this coincidence identification and data transfer process can be entirely automated, a critical feature for IMS implementation. It should be noted that real-time methods can also generate list-mode data (and can be done quickly if utilizing onboard memory) but are often used instead for their ability to reject single event pulses outright.

## **2.4. Previous Noble Gas Detector Design Principles**

With the basic physics of radon, the working principles of radiation detectors, and the various approaches to radon identification having been discussed, it is appropriate to explore the previous technologies upon which this research has been built.

### ***2.4.1. Gas Processing Unit***

It must be noted that the radiation detector at each noble gas monitoring station is only one part of a larger system. This system involves three sections: xenon collection, gas purification, and the radiation detector with associated readout [10]. Though this research focuses on the third part of this chain, the gas processing that occurs in the

first two parts of the chain is critical to the operation of the noble gas stations and as such should be discussed in brief. An example schematic of the noble gas processing system is shown in Fig. 24. This particular schematic is specific to ARSA—however, the three components of trapping, purification, and quantification shown in the sketch are universal.

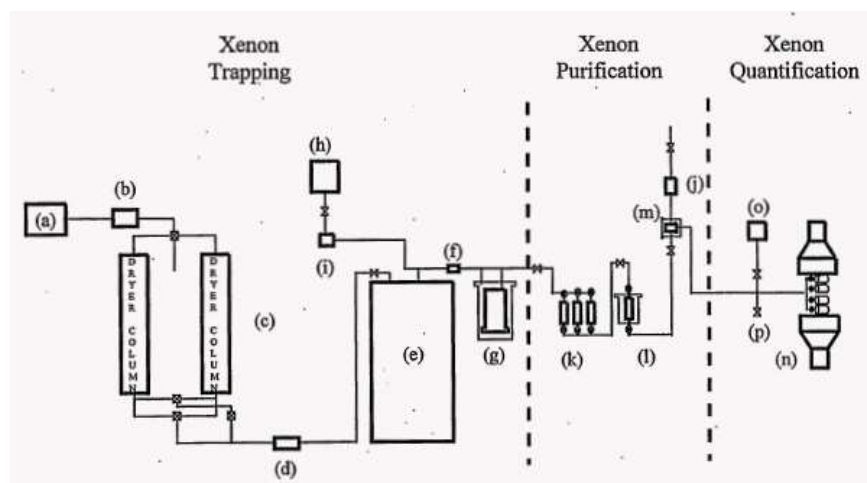


**Fig. 24.** Schematic exemplifying a full radioxenon detection system, from sampling to detection [10]; (a) piston compressor pump, (b) heat exchanger, (c) dual air drying/CO<sub>2</sub> removal columns, (d) mass-flow controller, (e) cryogenic air-chiller, (f) initial radon "pre-trap," (g) main charcoal trap for xenon trapping, (h) nitrogen bottle/generator, (i-j) mass flow controllers for nitrogen flow, (k) CO<sub>2</sub>-removal traps, (l) radon removal trap, (m) final charcoal trap for xenon transfer into counting system, (n) beta-gamma coincidence spectrometer, (o) residual gas analyzer, (p) path to archive bottles

With notable exceptions [17], [86], [131], much of the improvement in radioxenon detection over the past decades has been in the improvement of the gas sampling systems. Decreasing sampling time and increased sampling volume are both expected to substantially increase the sensitivity of noble gas stations [15], [84], [87].

#### **2.4.2. Beta-Gamma Coincidence**

As all radioxenon isotopes of interest decay via the coincident release of a photon and an electron, and as coincidence detection is such an effective means of reducing the impact of background, it is unsurprising that the radioxenon detection systems developed for and used by the IMS either currently make use of beta-gamma

coincidence or are beginning to utilize beta-gamma coincidence in next generation models. These beta-gamma coincidence systems are multi-material, with different volumes serving to detect different types of radiation. In most cases the gas cell serves as the electron detector and is constructed from a material that is well-suited for detecting electrons but has an intentionally poor photon efficiency. The most commonly used material is a plastic scintillator, coupled to a PMT. Photons pass through the walls of the plastic and deposit their energy in surrounding photon detectors. These photon detectors are chosen as high-Z materials, with the most common choice being an NaI(Tl) crystal coupled to a PMT. Coincidence decays are identified by correlating the interactions in these detectors.

#### *2.4.2.1. ARSA and the Xenon International*

Initially designed by PNNL in the mid and late 1990s, the Automated Radioxenon Sampler/Analyzer (ARSA) is in many ways the seminal radioxenon detection system [10], [40], [132], [133]. Various aspects of the system were further developed through the first decade of the 2000s, and though it has not itself been adopted into the IMS it has been adapted and has served a role in many studies on radioxenon detection [14], [26], [118], [134]–[141]. The original design consists of 4 gas cells made of BC-404 for electron detection. Each cell has walls 1.2 mm thick and an internal volume of 4.0 cm<sup>3</sup>, and presents near  $4\pi$  solid angle (98.5% [142]) to the gas volume. The cells are coupled to PMTs for light collection. These cells are held between 2 optically separated NaI(Tl) crystal plates, used for photon detection. These NaI(Tl) subtend a significant portion of the plastic scintillator, presenting a large solid angle to the gas source. Each plate is coupled to a pair of 3" PMTs for light collection. A sketch of the original ARSA system is shown in Fig. 25.

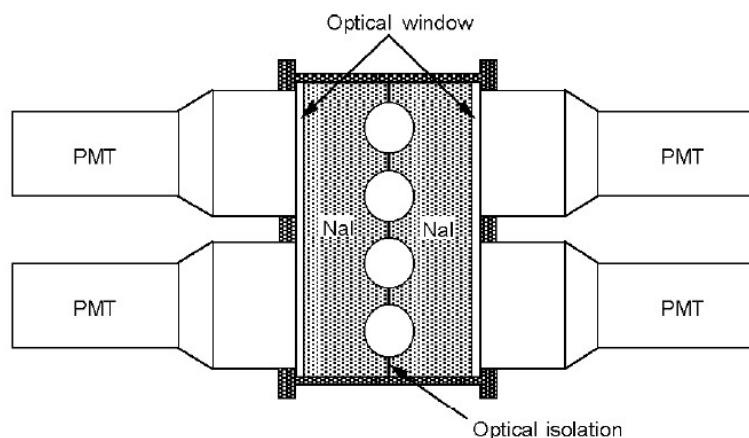


**Fig. 25.** A 2D sketch of the original ARSA detection system [14]

The gas processing component of the ARSA system utilizes two parallel atmospheric sampling units. The atmosphere is sampled for 8 hours, and the gas is then processed for an additional 5.45 hours to create a test sample. The sample is then injected into one of the four volumes, where it is measured for 24 hours. The cell is then pumped to low pressures and flushed with a neutral gas for 8 hours before a new sample is introduced. In this way the ARSA may continuously measure samples. ARSA has achieved MDCs of less than  $1 \text{ mBq/m}^3$  for the xenon isotopes of interest, with an MDC of  $0.15 \text{ mBq/m}^3$  for  $^{133}\text{Xe}$  [14].

The Xenon International is the successor system to ARSA, and is the result of a collaborative effort between PNNL and Teledyne Brown Engineering [143]. The Xenon International uses similar detector technology as ARSA, but significantly improves the sample generation methodology and sample frequency. Xenon International holds objective MDC requirements of  $0.15 \text{ mBq/m}^3$  for  $^{131\text{m}}\text{Xe}$ ,  $^{133\text{m}}\text{Xe}$ , and  $^{133}\text{Xe}$ , and  $0.5 \text{ mBq/m}^3$  for  $^{135}\text{Xe}$  [15]. The Xenon International system is shown in Fig. 26.



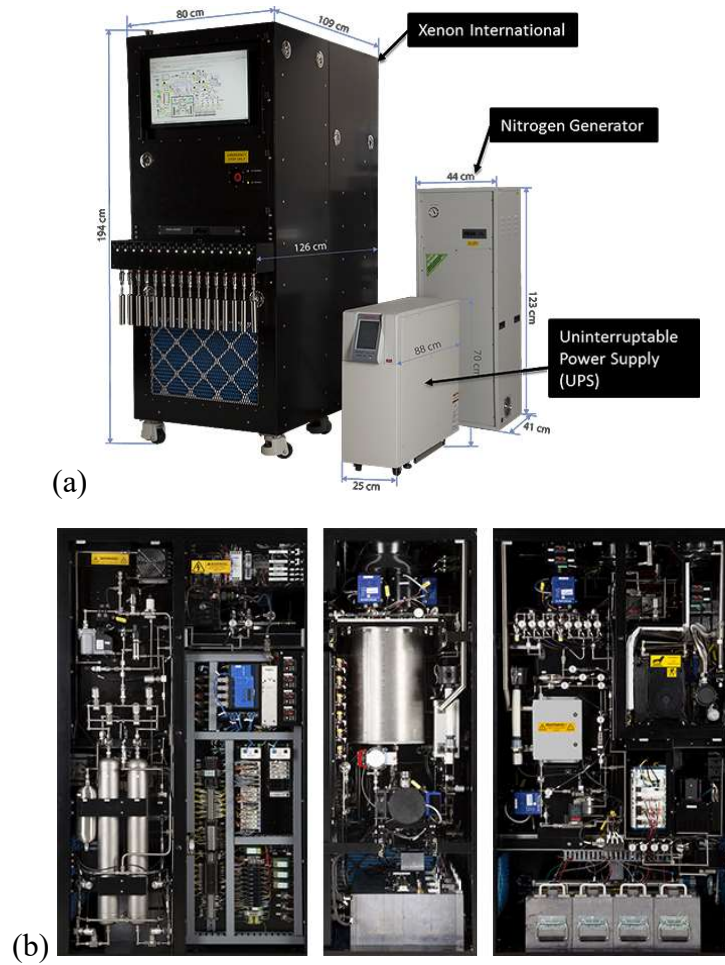


Fig. 26. The Xenon International system and required additional apparatuses; (a) external view; (b) internal view

#### 2.4.2.2. SAUNA

The Swedish Automatic Unit for Noble gas Acquisition (SAUNA) system was developed by the Swedish Defense Research Agency in 2003 [12], [144]. SAUNA has, like ARSA, played a key role in various radioxenon detection experiments [6], [8], [25], [145]–[148], but unlike ARSA SAUNA has been implemented in the IMS [11], [148]. Since its original conception the SAUNA has been updated to SAUNA II and then more recently to SAUNA III, with each iteration improving aspects of the previous such as time resolution for source localization, MDC, and operation costs [149]. A transportable version of the system, SAUNA TXL, has also been developed to expand the applicability of the system. In addition to various iterations of SAUNA

proper, the modular nature of SAUNA has motivated the development of various other specialized offshoot technologies.

The SAUNA system is fully automatic, requiring no day-to-day human intervention; the systems have demonstrated 99% uptime [150]. As of 2017, there are 36 operating SAUNA systems worldwide. Like ARSA, the SAUNA system uses NaI(Tl) for photon detectors and plastic scintillators for electron detection. The original SAUNA consisted of 2 gas cells made of BC-404 for beta and conversion electron detection, each with an internal volume of  $6.4 \text{ cm}^3$  and with 1 mm thick walls [12]. The ends of the beta cells are attached to PMTs. Each cell is placed inside a hole bored through the sides of one of two cylindrical NaI(Tl) crystal, each of which is attached to a single light guide and PMT. The inside of the hole is coated in a 0.2 mm layer of aluminum, in order to increase light collection efficiency in the plastic scintillators without absorbing a significant amount of low energy X-rays. A depiction of the detectors utilized by SAUNA is shown in Fig. 27.

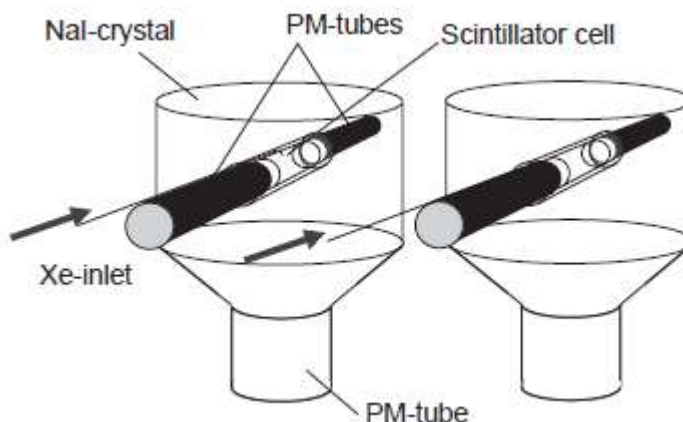


**Fig. 27.** A sketch of the original SAUNA detectors [12]

The stable xenon extraction capabilities have improved significantly from SAUNA to SAUNA III, going from  $0.5 \text{ cm}^3$  of xenon every 6 hours to  $3.25 \text{ cm}^3$  every 6 hours in SAUNA III. Initial versions of SAUNA experienced significant memory effect, particularly when subjected to particularly high activity samples: one study showed  $48 \text{ mBq/m}^3$  sample resulted in  $\sim 10\%$  of the xenon left in the cell during the next measurement [12]. Memory effect has improved significantly in the more recent

SAUNA systems, with SAUNA III claiming memory effect of  $\sim 0.06\%$ . The initial SAUNA achieved average MDCs of  $< 1 \text{ mBq/m}^3$  for the radioxenons of interest after a continuous 5 months of operation, and the newer models have further improved these results: SAUNA II and III have demonstrated MDCs of 0.2 and  $0.15 \text{ mBq/m}^3$  for  $^{133}\text{Xe}$ , respectively. The SAUNA III system can be seen in Fig. 28.



**Fig. 28.** The SAUNA III system [150]

#### 2.4.2.3. *ARIX*

Efforts towards the design of the Automatic Radioanalyzer for Isotopic Xenon (ARIX) began in 1999 during the Provisional Technical Secretariat Phase II readiness plan [26]. A field version was produced at the Khlopin Radium Institute in Russia in 2005 [13], [151] and a mobile version was introduced in 2007 [152]. ARIX is, along with SAUNA, one of the beta-gamma coincidence radioxenon detection systems employed in the IMS. Like SAUNA and ARSA, ARIX consists of an atmospheric sampling module, a sample-preparation module, and a detector/analyzer module. The sample preparation utilizes low-temperature adsorption on activated charcoal in order to extract xenon from the atmosphere, producing  $0.8 \text{ cm}^3$  of xenon every 4 hours. Samples are then measured in 10-hour increments.

Again in the same vein as ARSA and SAUNA, ARIX utilizes a plastic scintillator for the detection of electrons that is placed inside a well-type NaI(Tl) crystal for photon detection, with a PMT connected to each scintillator for light collection.

Unlike ARSA and SAUNA, however, the ARIX is a beta-gated system: the electron information is used only as a trigger for the photon detection, and spectroscopic information from the electron detector is not used. This allows the plastic scintillator to be very thin: 0.1 mm of polystyrene organic scintillator was found to be sufficient to produce an optical signal that could be correlated with the photon signal. The inner volume of this gas cell is  $7.3 \text{ cm}^3$  in the original design. A sketch of the ARIX detector module can be seen in Fig. 29. The ARIX system performs within CTBTO limits, with an MDC of  $0.9 \text{ mBq/m}^3$  for  $^{133}\text{Xe}$  determined from an 18-hour measurement.

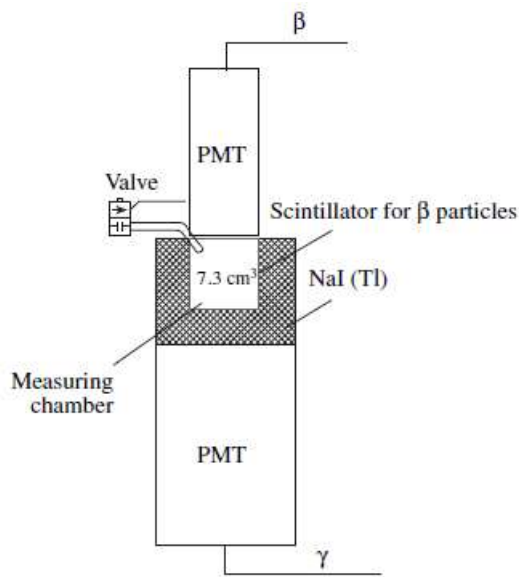


**Fig. 29.** A sketch of the detector unit for the ARIX radioxenon detection system [151]

#### 2.4.2.4. *Phoswich, and others*

Though the designs detailed above receive the most focus and active application for radioxenon detection, other radioxenon detection system designs have been investigated. The Phoswich, short for “phosphor-sandwich”, is a detector consisting of multiple materials coupled to a single PMT. Each material is specialized for the detection of a different type of radiation, and the pulses from the different scintillators can be distinguished via pulse shape analysis. In addition to beta-gamma coincidence, techniques such as Compton suppression can be applied to reduce background as well

as reduce interference and improve signal-to-noise ratios. Efforts have been made to implement real-time pulse discrimination in FPGAs for use with Phoswich detectors to great effect [153], [154]. The use of a single PMT allows for the simplification of hardware and calibration necessary for the system. Various materials have been investigated in many combinations for the Phoswich detector, including plastic scintillators such as BC-400 and BC-404, stilbene, NaI(Tl), CsI(Tl),  $\text{CaF}_2(\text{Eu})$ , yttrium aluminum perovskite (YAP), and bismuth germanate (BGO) [126], [155]–[166]. These designs can be quite sophisticated, with some employing  $\text{Al}_2\text{O}_3$  coatings to reduce memory effect in the gas cell [91].

A commercial off-the shelf form, PhosWatch, was designed, developed, and tested by XIA specifically for use in radioxenon monitoring [126], [165]–[168]. This all-in-one package includes a Phoswich detector encased in a copper shield and then further encased in lead shielding, readout electronics, and a Pixie-4 digital pulse processor for pulse shape analysis and beta-gamma coincidence detection. This PhosWatch design achieved MDC values of 0.5-0.6 mBq/m<sup>3</sup> for  $^{133}\text{Xe}$  [166].

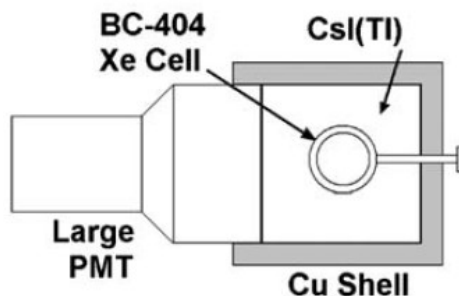


**Fig. 30.** Geometry of the PhosWatch detector [165]

#### 2.4.2.5. *Alternative Materials*

Utilizing exclusively silicon detectors has been investigated for radioxenon detection systems [169]. One manifestation of this technology was the 24-element Silicon PIN diode detector, developed in 2013 [127]. This compact device specifically aimed for improved energy resolution for X-rays and conversion electrons, while reducing background and eliminating memory effect. As with many solid state detection systems, leakage current and cross-talk introduced difficulties.

Nevertheless, the detector is estimated to achieve an MDC of  $0.1 \text{ mBq/m}^3$  for  $^{133}\text{Xe}$  when using a 24-hour sampling time. This device can be seen in Fig. 31.



**Fig. 31.** The 24-element silicon PIN detector during assembly. When completely assembled the silicon surrounds the gas volume on all 6 sides [127]

Another silicon PIN detector developed by the V. G. Khlopin Radium Institute and Lares Ltd. also demonstrated a low MDC of  $0.18 \text{ mBq/m}^3$  for  $^{133}\text{Xe}$  for a 24-hour count time [170]. A system was introduced by another group that utilized a silicon surface barrier detector as an electron detector, an HPGe as a photon detector, and a scintillator as a muon detector [124]. The study using this system found that using muon-gamma anti-coincidence could reduce background by a factor of  $\sim 2.5\times$ , and when combined with beta-gamma coincidence it could be reduced by nearly two orders of magnitude in the case of  $^{131\text{m}}\text{Xe}$ .

Conspicuously absent from this discussion of solid state radioxenon detectors are the PIPSTBox and CZT. An extended discussion of the history of the PIPSTBox and its role in radioxenon detection is presented in later sections, and the role of CZT is discussed in the section on previous work completed at Oregon State University.

In addition to solid state detectors, interest has been shown in stilbene as a possible alternative to plastic scintillator gas cells. Stilbene has been shown to have a high resistance to memory effect ( $\sim 2$  orders of magnitude reduction compared to plastic scintillators) and a better resolution for electrons than plastic scintillators [23], [131], [171], [172]. However, the crystalline structure of the material can make the cells fragile and prone to leaking if it is subjected to a vacuum of sufficiently high strength (on the order of torr to millitorr).

### 2.4.3. Gamma Spectroscopy

Beta-gamma coincidence is only one of the two methods for radioxenon detection. The other, gamma spectroscopy, makes use of the excellent resolution of high purity germanium detectors to identify radioxenon at low concentrations. These devices can be highly effective, but they need to be cooled to liquid nitrogen temperatures in order to function.

#### 2.4.3.1. SPALAX<sup>TM</sup>

The Système de Prélèvement d'air Automatique en Ligne avec l'Analyse des radio-Xénons, or SPALAX<sup>TM</sup>, is the third and last of the radioxenon detection systems implemented in the IMS. First designed in 2000 by the French atomic energy commission (CEA), it has been subjected to continuous study and application since the early 2000s [6], [16], [173]–[179]. The system is autonomous and monitors continuously, with less than 14 days annual downtime. SPALAX, like ARSA, SAUNA, and ARIX, is comprised of an atmospheric sampling unit, a gas processing unit, and an HPGe used for sample evaluation. SPALAX generates 7.5 cm<sup>3</sup> of xenon during a 24-hour sampling time. Despite being the less sensitive method of spectroscopy, radioxenon is identified in SPALAX using gamma spectroscopy instead of beta-gamma coincidence. Gamma spectroscopy allows for the direct detection of the four radioxenon isotopes of interest simultaneously, without intensive identification algorithms, and is a robust method well suited for use in-field. The HPGe, with its superior photon resolution, is particularly well-suited for this application—however, it does require liquid nitrogen cooling during operation, increasing resource demands. SPALAX uses the gamma rays emitted from <sup>133</sup>Xe and <sup>135</sup>Xe, and the K<sub>α</sub> X-rays and gamma rays emitted in anti-coincidence from the two metastable isotopes. [16] SPALAX has demonstrated an MDC of 0.15 mBq/m<sup>3</sup> for <sup>133</sup>Xe for a 24-hour measuring time.

The gas processing system and detection system in SPALAX have been further improved in recent years [17], [84], [180]–[182]. This new version of the system has a sampling frequency of 8 or 12 hours and an acquisition time of 10.3 hours to

produce a  $6.5 \text{ cm}^3$  xenon sample. The radiation detection system component of the SPALAX has been augmented from a system that purely uses gamma spectroscopy to an advanced beta-gamma detection system using an HPGe for photon detection and a PIPSBox for electron detection. The system is fully solid state, and yields high resolution detection for both photons and electrons compared to the traditionally used beta-gamma coincidence system materials of NaI(Tl) and plastic scintillators. Memory effect was also found to be on the order of 0.1% in the PIPSBox. This system has demonstrated triple coincidence for the rejection of non-metastable isotopes (which decay only in double coincidence), though issues with electron backscatter were found to make up a significant portion of triple coincidence events and cannot be neglected [17]. The system has successfully been operated continuously for at least 5 months and can achieve an MDC of  $0.1\text{-}0.3 \text{ mBq/m}^3$  for all radioxenon isotopes of interest.

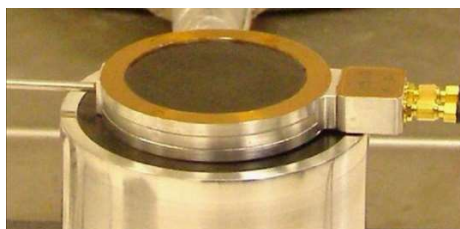


**Fig. 32.** The detector in SPALAX NG, or SPALAX New Generation, with a PIPSBox placed on an HPGe for both high resolution electron and photon detection [180]

#### **2.4.4. Non-Radioxenon Detectors**

Despite the difficulties presented for using  $^{37}\text{Ar}$  for underground nuclear explosion monitoring, efforts have been taken by some groups to evaluate its use for this application. The MARDS line, developed since 1999 through to the most recent version MARDS-II in 2013, are automatic field deployable gas processing and detection systems designed for on-site  $^{37}\text{Ar}$  identification [183]. The system can create one sample every two hours for evaluation. Though a definitive description of the detector could not be found, available information indicates that low-noise proportional counters with an anti-coincidence rejection system are used to identify the low-energy gamma ray released in  $^{37}\text{Ar}$  decay. The MARDS-II is capable of



achieving an MDC of 26 mBq/m<sup>3</sup> for <sup>37</sup>Ar after 10 hours of counting. MCNPX simulation indicates that the radioargon activity concentration at the surface 80 days after a 1 kT explosion ranges from 1×10<sup>3</sup> to 1×10<sup>6</sup> mBq/m<sup>3</sup> air, depending on the predominant rock material [184]. This implies that the MARDS-II system would be an effective tool in underground nuclear explosion monitoring, particularly when used to supplement radioxenon detection efforts.

#### ***2.4.5. Previous Oregon State University Detection Systems***

Several beta-gamma coincidence radioxenon detection systems have been developed at Oregon State University investigating novel material combinations as alternatives to the current state-of-the-art. As many of the design and operation aspects of these detectors have directly influenced or have been integrated into the design of the PIPS-SrI<sub>2</sub>(Eu), it is appropriate to discuss these designs here.

All these systems use digital pulse processing in an FPGA for real-time coincidence identification. Coplanar CZT serves as the photon detection medium in all of these previous systems owing to its high resolution, high density, room temperature operation, no PMT or similar light collection device, simple readout electronics (compared to pixelated detectors), and depth-of-interaction independence [185]–[188]. Despite these advantages to CZT issues such as leakage current, noise at low energies, slow charge carrier drift time in the crystal, and high cost in large volumes prevent CZT from being a universal improvement over currently used photon detectors such as NaI(Tl).

##### ***2.4.5.1. TECZT***

The Two-Element CZT (TECZT) system utilizes two coplanar CZT facing each other surrounding a 1 cm<sup>3</sup> gas cell [20], [44], [189]. The system can be seen in Fig. 33. In contrast to other beta-gamma coincidence detection systems where each detection volume is sensitive to a specific type of radiation, each volume in the TECZT is sensitive to both photons and electrons. By using only CZT, as opposed to a plastic scintillator, both high resolution electron and photon measurements could be

conducted. As it was a proof-of-concept design the prototype system was made use of only two CZT, providing sub-optimal solid angle. However, the system could easily be expanded to six CZT crystals for near  $4\pi$  coverage of the gas cell, substantially improving the MDC. CZT is expected to show resistance to memory effect in comparison to plastic scintillators, but as the prototype gas cell was made of a plastic holding material no measurement was ever explicitly conducted to quantify this.

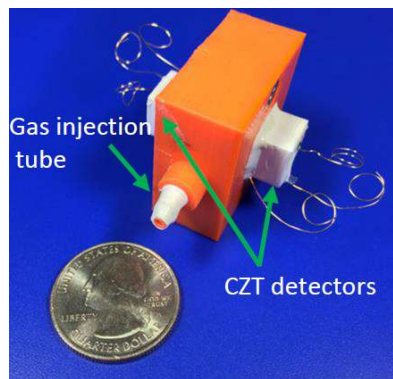


**Fig. 33.** The TECZT detector, with quarter for scale [44]

The TECZT showed mixed performance. When a background measurement was taken with the TECZT, the system rejected events at a rate of 98.2% due to successful implementation of coincidence identification inside an FPGA. High resolution was observed in the case of photons such as 250 keV (4.4% FWHM) and 81 keV (12.5% FWHM), but poor resolution was observed in the case of the 31 keV X-rays (42-48% FWHM) due to noise concerns at low energies. Excellent energy resolution was observed for 129 keV conversion electrons (10.1% FWHM). However, due to the high-Z nature of CZT, backscatter of conversion electrons was observed between the two detectors. The incomplete energy deposition from the backscattered conversion electrons results in a tailing effect in the spectrum, causing interference with other ROIs and degrading the MDC of the system. This backscatter can be seen in Fig. 34, which shows the 2D coincidence spectrum for  $^{131m}\text{Xe}$  as taken by the TECZT system.

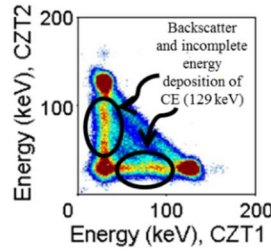


**Fig. 34.** 2D energy histogram of the TECZT detector in response to  $^{131m}\text{Xe}$  when running in coincidence mode. The lines between 31 keV and 129 keV are due to incomplete energy deposition from backscattered conversion electrons [20]

#### 2.4.5.2. CASP

To address the backscatter concerns of the TECZT system without abandoning the excellent results afforded by CZT, a second prototype utilizing a CZT crystal, an array of silicon photomultipliers (SiPMs), and a plastic scintillator (CASP) was developed [21], [89], [190]. This design returned to the design philosophy of having different materials dedicated to the detection of specific radiation: CZT for photon detection and plastic for electron detection. SiPMs were chosen over PMTs as light readout for the plastic scintillator to reduce system size and increase robustness. The detector was completely mounted on a fully custom PCB to reduce trace lengths, reducing noise and improving the low-energy performance of the CZT. The detector can be seen in Fig. 35.

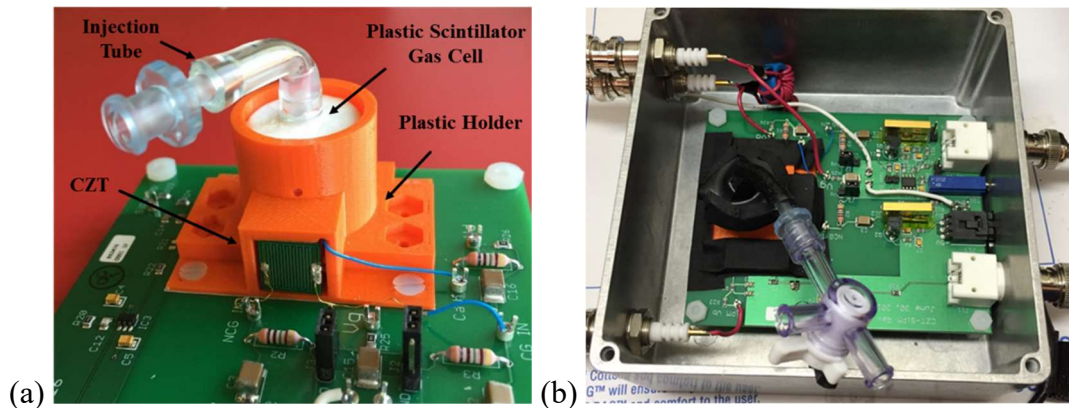


**Fig. 35.** (a) the CASP detector, with CZT and plastic scintillator visible. The plastic scintillator is mounted on the SiPM array, and as such the SiPM array is not visible; (b) the system assembled inside an aluminum box, to shield from light and other sources of electromagnetic interference [89]

Using the CASP eliminated the backscatter observed in the TECZT system and increased the solid angle for electrons without increasing the number of readout channels. Similar to the TECZT, the CASP could theoretically be expanded to accommodate up to four larger CZT for better solid angle coverage and improved sensitivity—such an expansion is expected to improve the sensitivity of the system by 4-12 $\times$ . The CASP system achieves a resolution of 30-36% FWHM at 31 keV, compared to the 42-48% observed in the TECZT. The system demonstrated a background rejection rate of 99.8%, significantly outperforming the TECZT as well as other state-of-the-art radioxenon detection systems. However, this system, like so many others that utilize plastic scintillators, had comparatively poor electron resolution (23.7% FWHM at 129 keV) and experienced significant memory effect.

#### 2.4.5.3. *Stilbene-CZT*

Directly succeeding the CASP system was the Stilbene-CZT system [23]. In effect a direct upgrade to the CASP, the Stilbene-CZT functioned using the same pulse processing technology and same PCB but with improved materials: a better CZT crystal was used, and the plastic scintillator was replaced with a stilbene crystal of nearly equal structure and dimensions. The system can be seen in Fig. 36.

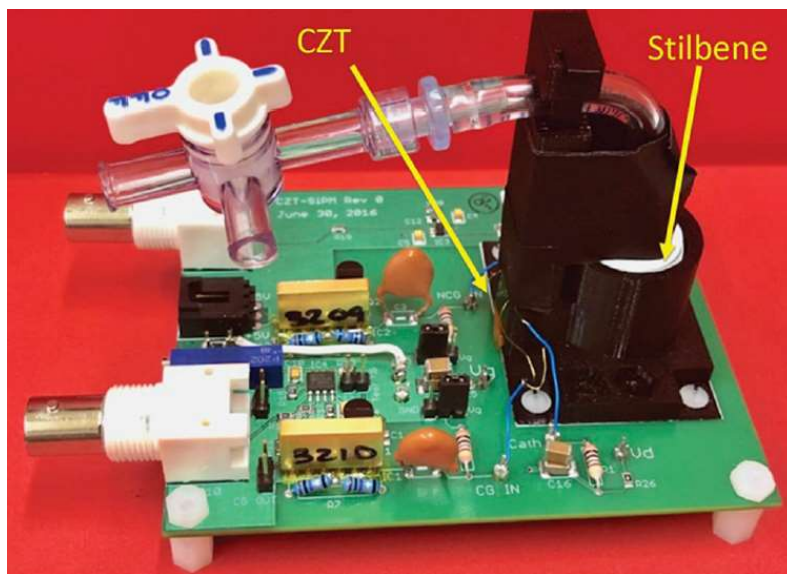


**Fig. 36.** The Stilbene-CZT, using the same board as was used for the CASP system. As in Fig. 35, the array of SiPMs is underneath the scintillator and is not visible [23]

The Redlen coplanar CZT crystal [191] used in this system proved to have higher resolution and lower noise than the CZT crystal used in the CASP system, with a 25.8% FWHM observed for 31 keV X-rays and 9.3% FWHM observed for 81 keV photons. Though only one CZT crystal was used in the prototype, like the CASP and the TECZT systems the number and size of CZT crystals used could be increased without significant difficulty. The electron energy resolution, 20.2% FWHM at 129 keV, was also improved when compared to measurements with the CASP system, though it did not outperform the resolution observed with the TECZT. The system demonstrated a background rejection rate of 99.85%. Using stilbene as a gas cell and electron detector also addresses the problem of memory effect that consistently plagues plastic scintillators. The stilbene crystal was measured to have a memory effect of  $0.045 \pm 0.017\%$ , an improvement of roughly two orders of magnitude compared to plastic scintillators [14], [90]. Like the CASP, the stilbene-CZT system does not experience electron backscatter like the TECZT. The stilbene cell used in this design was not perfectly airtight, and leakage was a concern during experiments. Though manufacturing imperfections in the specific cell used in the prototype cannot be ruled out, leakage in stilbene cells has been observed in other studies and may be a common shortcoming of pumping stilbene gas cells of this size to low pressures [171].

#### 2.4.5.4. *PIPS-CZT*

The PIPS-CZT marked a particularly significant shift from the previous radioxenon detector designs: instead of using a two-channel digital pulse processor with a single dedicated photon detection and single electron detection volume, a four-channel system was implemented with two photon detectors and two electron detectors [22], [45], [87]. This shift necessitated a shift in digital pulse processing system as well as a complete overhaul of the coincidence identification methodology from a “first triggering pair” approach to a pattern recognition approach. This coincidence identification regime is the same as that used in the PIPS-SrI<sub>2</sub>(Eu) and is discussed in detail in later sections. As the PIPS-CZT has much in common with the

PIPS-SrI<sub>2</sub>(Eu) detector, more space is dedicated to discussing its merits and shortcomings than previous OSU detectors.

The PIPS-CZT is a fully solid state detection system that is operational at room temperature. It utilizes the PIPSBox, discussed in earlier sections, as the two electron detectors, while using two coplanar CZT crystals mounted to the center of the PIPSBox outer faces as photon detectors. The detection system can be seen in Fig. 37. Inspiration to use the PIPSBox as an electron detector was taken from the SPALAX modification where a silicon-based PIPSBox gas cell was used as an electron detector in conjunction with a pair of HPGe detectors for photon detection to further improve the MDC of the system [17].

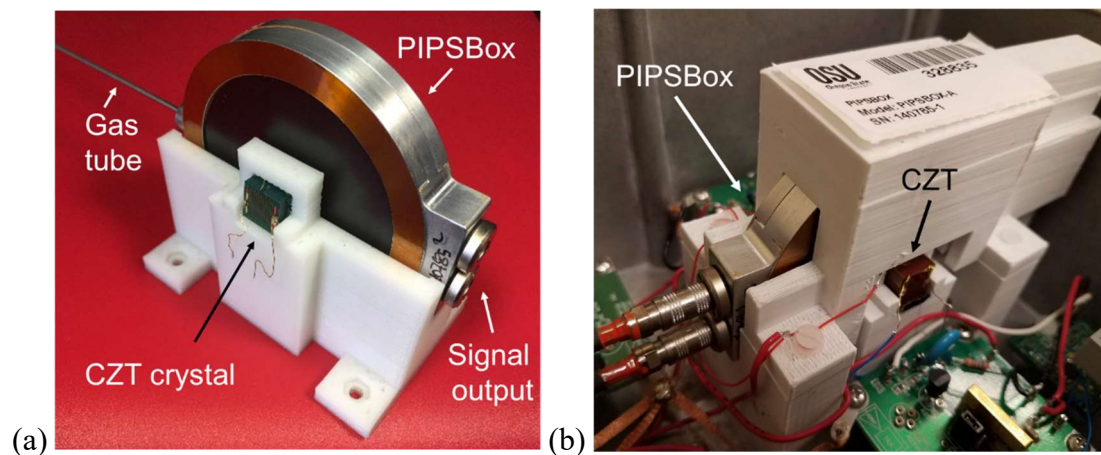


**Fig. 37.** The PIPS-CZT system shown (a) outside of [45] and (b) inside of [87] the aluminum box and with associated readout electronics

The poor solid angle ( $0.39\pi$ ) subtended by the CZT crystals is immediately apparent from Fig. 37, but as is the case for the other OSU systems the number and size of the CZT crystals could be increased to cover the entire active face of the PIPSBox. The CZT and readout electronics used in the PIPS-CZT achieved 35% FWHM for 31 keV X-rays and 11.8% FWHM for 81 keV photons, outperforming the TECZT albeit not the CASP and stilbene-CZT. Using commercial off-the-shelf preamplifiers, the PIPSBox demonstrated 12.5-14.3% FWHM for 129 keV conversion electrons, a significant improvement when compared to plastic scintillators. From a 45-hour background measurement with the system inside a lead

cave, the background rejection rate was found to be  $99.98 \pm 0.01\%$ , the best measured rejection rate of all the OSU radioxenon detection systems. Using a vacuum pump and several pump-and-flush procedures down to several torr, the memory effect of the PIPSBox was found to be  $0.256 \pm 0.034\%$ , a roughly  $20\times$  improvement over a plastic scintillator. There was difficulty in reducing the pressure in the PIPSBox to lower pressures than 4 torr, and it is expected that the memory effect would be reduced even further were a turbo pump used to achieve millitorr pressures. Optimistic MDC calculations predict that the PIPS-CZT meets the CTBTO requirements for MDC: when assuming a blank sample, negligible memory effect, neglecting interferences between radioxenons, and using gas processing parameters associated with Xenon International, the PIPS-CZT has an estimated MDC of  $0.61 \pm 0.15 \text{ mBq/m}^3$  for  $^{133}\text{Xe}$ . An MDC of  $0.31 \pm 0.11$  for  $^{133}\text{Xe}$  was estimated when simulating CZT coverage of the entire PIPSBox face using MCNP6.

The PIPS-CZT is not without fault. Issues such as cost, slow drift time, and subpar performance at low energies continue to mar the performance of CZT. It is not possible to expand the solid angle of the PIPSBox, which at  $2.54\pi$  compares unfavorably to the near- $4\pi$  solid angle of plastic scintillator gas cells. The noise threshold of the PIPSBox is between 45 and 65 keV, which is a significant detriment to the efficiency of the system. Electron backscatter is an issue in the PIPSBox due to the high  $Z$  of silicon. In cases where the electron backscatters and interacts in both PIPS detectors the signals can be summed together to reconstruct the full energy of the deposited electron, but the high noise threshold makes two interactions with enough energy to trigger the system unlikely. The silicon also attenuates  $\sim 25\%$  of X-rays emitted from the gas source (as simulated in MCNP6), reducing the absolute efficiency of the detector. Despite these shortcomings, the excellent electron resolution and the novelty of the detector makes the use of the PIPSBox in radioxenon detection systems worthy of continued investigation.

### 3. MATERIALS AND METHODS

The focus of this research is to explore alternative detector materials and identification methods for atmospheric radioxenon monitoring applications. The PIPS-SrI<sub>2</sub>(Eu) was designed using several guiding criteria and the combined experience gained from several iterations of detector design at OSU.

An ideal radioxenon detection system must above all be sensitive—the detectors used in the IMS must at least be capable of detecting <sup>133</sup>Xe at  $\leq 1$  mBq/m<sup>3</sup>, though because it is the ratios between the radioxenon isotopes that are key for identifying nuclear explosions, sensitivity to the other radioxenon isotopes of interest is also critical. In beta-gamma coincidence systems, reliable coincidence recognition and rejection of unwanted background are key to this effort. This is directly promoted by a narrow CTW, which is itself promoted by rapid detector response. Good energy resolution is an important contributing factor, particularly for photons but for electrons as well. High efficiency also plays a significant role, as the MDC of the detector is inversely proportional to overall beta-gamma efficiency. Memory effect should be as low as possible, minimizing interference from previous measurements and yielding minimal down time. Low noise is critical. For photon detectors, the 31 keV X-ray is an essential component for detecting 3 of the 4 isotopes. For electron detectors, high noise thresholds reduce the efficiency for the highest emission probability region of the beta spectra from <sup>133</sup>Xe and <sup>135</sup>Xe, as well as hampering the efficacy of summing the signals of multiple electron detectors to reduce the impact of backscatter. As the stations in the IMS are quite remote, a detector that is capable of long-term operation with little maintenance is also necessary, and in this vein, compactness and simplicity of implementation are also benefits.

The PIPS-SrI<sub>2</sub>(Eu) is a low-background, high-sensitivity detection system constructed using modern materials. It is comprised of a PIPSBox for high resolution electron detection and a pair of SrI<sub>2</sub>(Eu) crystals coupled to SiPMs for high resolution photon detection. It uses advanced pattern-based coincidence recognition between four independent detector volumes in real time in the digital domain. The PIPS-



$\text{SrI}_2(\text{Eu})$  has minimal memory effect when compared to the plastic scintillators used in most state-of-the-art beta-gamma radioxenon detection systems. Compared to the previous PIPS-based detection system designed at OSU, the PIPS-CZT, the PIPS- $\text{SrI}_2(\text{Eu})$  has improved efficiency, reduced noise, improved treatment of backscatter, reduced cost for photon detectors of equivalent dimensions, and theoretically faster detector response. A Solidworks model of the proposed detection system is shown in Fig. 38, and a cross sectional view indicating the several possible coincidence patterns are shown in Fig. 39.

In addition to the development of the detection system, an advanced radioxenon identification algorithm has been developed and implemented in a Python software package [192]. Based on the simultaneous deconvolution algorithms employed in SDAT, this method uses an iterative maximum likelihood solve on a set of 2D coincidence spectra to determine contributions from pure radioxenon isotopes to an unknown mixed experimental spectrum. The spectra are segmented into various regions wherein the counts in the histogram bins are summed together with the aim of improving statistics in key regions and hastening the convergence of the solve. This method is referred to as Regional Spectral Deconvolution (RSD).

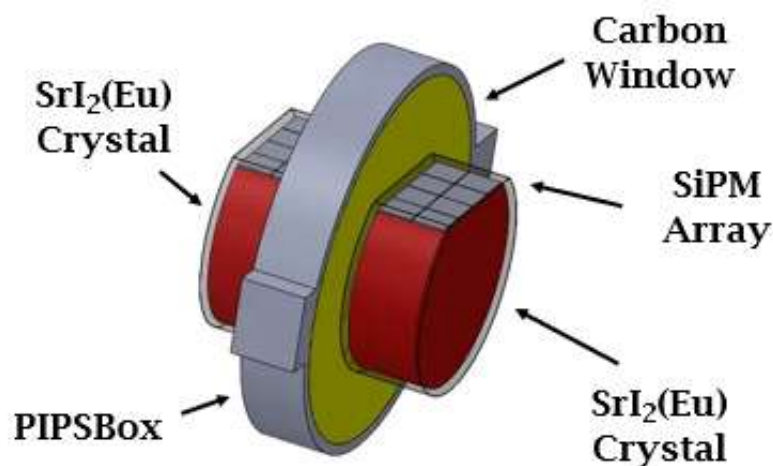


**Fig. 38.** The PIPS- $\text{SrI}_2(\text{Eu})$  detection system, sketched in Solidworks

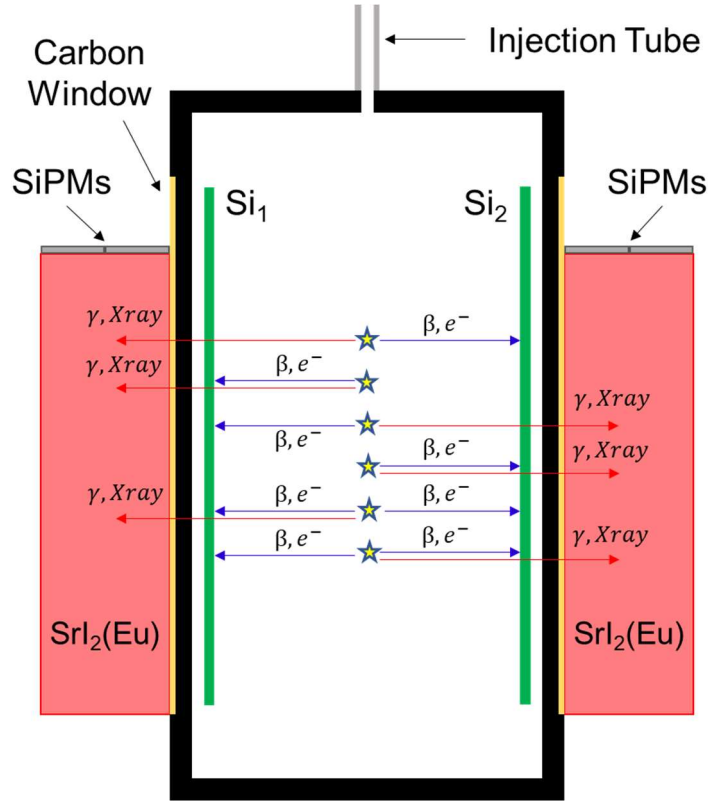


**Fig. 39.** Cross sectional view of the PIPS-SrI<sub>2</sub>(Eu) detector, showing the 6 possible coincidence patterns that might occur in the detector

### 3.1. Detector Infrastructure

#### 3.1.1. Photon Detector: SrI<sub>2</sub>(Eu)+SiPMs

The SrI<sub>2</sub>(Eu) crystals utilized in this work were grown and assembled by CapeSym Inc. [62], and are doped with Eu<sup>2+</sup> at 5%. SrI<sub>2</sub>(Eu) detectors were chosen for their exceptional brightness (and consequently high resolution for photons), high-Z number, high density, improved size-to-cost ratio in comparison to CZT, and absence of internal radiation that plagues other high resolution scintillators such as LaBr<sub>3</sub>(Ce). In marked contrast to coplanar CZT, where the time between radiation deposition and detector response can vary depending on the depth of interaction in the volume [187], the response of SrI<sub>2</sub>(Eu) to radiation occurs on the order of nanoseconds. Provided that the signal-to-noise threshold is high enough, the SrI<sub>2</sub>(Eu) has a much more consistent time between interaction and trigger than coplanar CZT. Downsides of SrI<sub>2</sub>(Eu) are minimized in application to radioxenon detection. SrI<sub>2</sub>(Eu)

does have issues with self-absorption, which can lead to lengthy decay time that is detrimental with large detectors and under high count rate circumstances. A photon detector used in conjunction with a PIPSBox does not need to be large, and so self-absorption is not a severe concern. Furthermore, as the count rates in the atmospheric samples being measured are never expected to be particularly high, pileup rarely presents itself outside of characterization experiments. The inconvenience of the hygroscopicity of  $\text{SrI}_2(\text{Eu})$  is minimized by the virtue of the detector being stationary—once it has been built and deployed, it is not likely to see frequent disturbance.

Radioxenon detection is a compact application, one where SiPMs are particularly well-suited as a light collection device. Thus, SiPMs were chosen for use with the  $\text{SrI}_2(\text{Eu})$  crystals. Conflicting results in the literature have been observed regarding coupling  $\text{SrI}_2(\text{Eu})$  to SiPMs—one study showed no resolution degradation due to using SiPMs instead of PMTs [193], while another showed a degradation from 3.4% to 4.4% for the 662 keV photopeak when using a cubic  $\text{SrI}_2(\text{Eu})$  crystal [194]. Though SiPMs can be saturated by excessive photon exposure and produce non-linearity, and though  $\text{SrI}_2(\text{Eu})$  is bright, the long decay time of  $\text{SrI}_2(\text{Eu})$  and the relatively low energies of the photons of interest ( $\leq 352$  keV) makes this oversaturation of minor concern.

To maximize the efficiency of the  $\text{SrI}_2(\text{Eu})$  each crystal should be at least as large as the active area of the PIPSBox:  $1200 \text{ mm}^2$ . The largest commercially available SiPM is  $6 \times 6 \text{ mm}^2$ . To cover the entire face of the  $\text{SrI}_2(\text{Eu})$ , at least 34 SiPMs would be necessary. SiPMs are in effect a capacitor and adding this many SiPMs in parallel causes excessive parasitic capacitance to the circuit. One option would be to eschew SiPMs and simply use a PMT instead. If SiPMs are to be used, however, the fewest SiPMs possible should be used to minimize capacitance and preserve a good signal-to-noise ratio while still allowing the full collection of scintillation light. This trade-off inspired the design for the  $\text{SrI}_2(\text{Eu})$  detector shown in Fig. 40: a disk detector with a lateral slice removed to create a flat surface to couple to an array of SiPMs. This D-shape was sized to allow for an array of eight SiPMs to completely cover one of the

surfaces. It was determined that this cut would result in a minimal reduction of photon solid angle- the total photon solid angle without the cut was found using MCNP6 to be  $1.86\pi$ , while with the cut was  $1.78\pi$ . It is not clear whether this exotic scintillator shape will significantly hamper the resolution of the detector, though research does seem to indicate that the presence of edges and corners that might act as light trapping locations do not significantly hamper the light collection and the resolution of the detector [195]. One study showed that  $1 \text{ cm}^3$  cubic  $\text{SrI}_2(\text{Eu})$  scintillators achieved a 3.6% resolution for 662 keV when coupled to SiPMs [196].

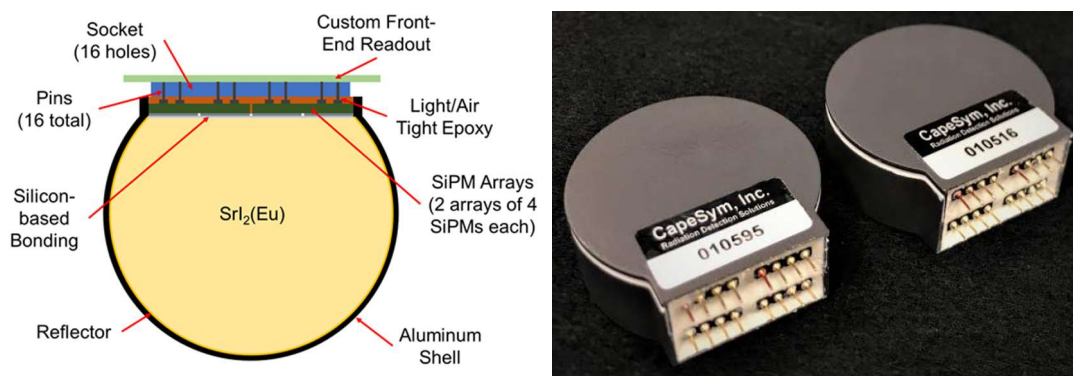


**Fig. 40.** (left) a sketch of the  $\text{SrI}_2(\text{Eu})$  detector; (right) the manufactured and packaged  $\text{SrI}_2(\text{Eu})$  detectors, completely assembled save for the front-end readout and socket

At the recommendation of engineers at CapeSym, two 4-SiPM SensL ArrayJ-60035-4P-PCB SiPM arrays [197] were directly and permanently mounted onto each crystal via a silicon-based bonding to maximize light collection efficiency and energy resolution. These SiPMs were chosen for their high packing factor and excellent agreement with the  $\text{SrI}_2(\text{Eu})$  photon emission spectrum (420 nm peak absorption efficiency for the SiPMs [198] and 420 nm peak emission for  $\text{SrI}_2(\text{Eu})$  [55]). Each  $\text{SrI}_2(\text{Eu})$  detector is 1.5" in diameter, chosen to match with the diameter of the active area of the PIPSBox, and 0.5" thick. The crystal is entirely covered in a reflector (save for the SiPM light collection window), encapsulated in a 0.5 mm thick aluminum shell to isolate it from moisture in the atmosphere, and sealed with an epoxy applied to the back of the SiPM arrays to create full air-tightness. Pins, one anode pin and one common cathode pin for each SiPM, protrude from the back of the

arrays and are exposed through the epoxy, which allows for the connection of external electronics for signal readout. This allows for maximum flexibility—by keeping the electronics outside of the aluminum shell, optimization can be made to the readout without disrupting the crystal itself. This configuration sufficiently shielded the SiPMs and  $\text{SrI}_2(\text{Eu})$  crystals from ambient light exposure such that the detector could be operated in a well-lit room without additional light shielding, though particularly luminous light (such as a flashlight) was found able to penetrate the epoxy layer and cause the SiPMs to trigger. A 9-pin female socket (8 anode and one cathode) is mounted to a custom front-end readout PCB, which is then outfitted with a BNC connector to be read to a digital pulse processor for further conditioning in the digital domain. Digital data acquisition allows for on-the-fly variation and optimization of data acquisition parameters such as trigger shape, and theoretically allows for pulse fitting to be applied in the FPGA for better trigger timing.

Two processing boards were investigated: one that allowed for digital integration, and one that utilized charge sensitive preamplifiers (CSPs) provided by Cremat Inc. [199]. These boards not only provide conditioning, but also include a LT8410 switching regulator to step up applied voltage, taking it from +5 V to +27.5 V to provide power to the SiPMs. Comparison of these boards, as well as to traditional analog conditioning, is discussed in later sections; however, the final version of the detector uses the Cremat CSPs for analog charge integration. The CSPs act as integrators, and if the characteristic decay time of the CSP is significantly longer than the decay time of the scintillator the rise time of the output pulse is largely dependent on the decay time of the CSP and is effectively constant regardless of pulse height. The rise time of the  $\text{SrI}_2(\text{Eu})$  pulses output from the Cremat preamplifier is approximately 11  $\mu\text{s}$ .

Compared to the photon detectors of the PIPS-CZT, the solid angle is improved nearly 5-fold. Despite the poor solid angle of the CZT crystals, the PIPS-CZT demonstrated high sensitivity. The relative increase in the solid angle for photon detection is expected to significantly increase the efficiency of the system, further reducing the MDC.

### 3.1.2. Electron Detector: *PIPSBox<sup>TM</sup>*

The PIPSBox, a cylindrical gas cell/silicon detector developed by Canberra, is a modern technology that has to date seen limited use. It was designed specifically for radioxenon detection systems to address problems associated with plastic scintillators, such as poor electron resolution and memory effect [17]. Downsides of the PIPSBox including high noise, attenuation of X-rays, electron backscatter, and reduced solid angle for electrons when compared to plastic scintillators, might suggest that the detector introduces more problems than it solves. However, the promising results in the PIPS-CZT imply that these shortcomings are sufficiently compensated for by the other performance characteristics such as low background and high resolution for electrons to still deliver a high sensitivity system. The exact PIPSBox model used in this research is shown in Fig. 41.

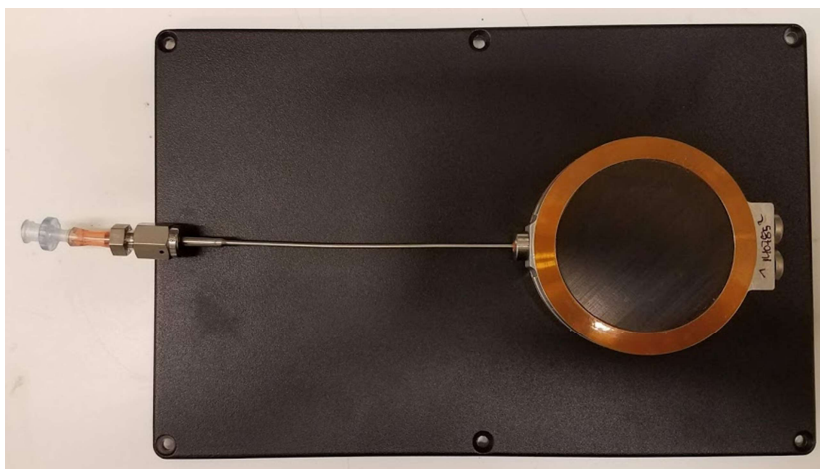


**Fig. 41.** The PIPSBox-2x1200-500A used in this research

Backscatter with the PIPSBox still presents an issue, but as mentioned previously the impact of this backscatter can be significantly reduced by summing the two signatures together. When using an energy threshold of about 50 keV the peak-to-backscatter ratio for the 129 keV conversion electron was improved from ~26% to ~62% [45]. Since the PIPS-CZT experiments, the custom Canberra preamplifier has been acquired [93], as shown in Fig. 42. The preamplifier is powered by  $\pm 12$  V supplied through a SUB-D connector. -145 V is supplied directly to the preamplifier

and is then carried to the PIPSBox via a pair of BNC-LEMO connectors. Though the use of this preamplifier increases the overall size of the detection system in comparison to using the A250F/NF preamplifiers as used in the PIPS-CZT system, the reduction in trigger threshold from 50-70 keV to 10-30 keV is expected to significantly improve the sensitivity of the system. Particularly important will be the impact on summing the two PIPS channels on the backscatter problem.

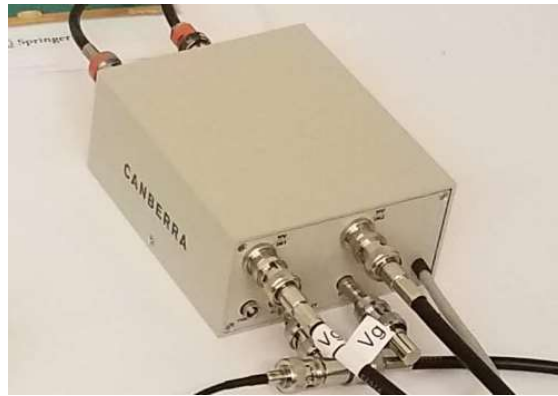


**Fig. 42.** The Canberra custom 2-channel preamplifier for use with the PIPSBox

### ***3.1.3. Eight-Channel Digital Pulse Processor (DPP8)***

A complete detection system requires not only the detectors themselves, but the readout and processing as well. To this end, a custom eight-channel digital pulse processor is utilized in this work.

#### ***3.1.3.1. Design and Function***

The digital pulse processor, the DPP8, was developed previously at Oregon State University for the simultaneous readout of arbitrarily many detectors, up to eight. The DPP8 can run in either singles mode, where only one channel is examined, or in coincidence mode, where all channels of interest are examined simultaneously. The processor is powered with a +5-+6 V voltage supply. The processor is comprised of two PCBs. The first is a custom in-house designed board devoted to simultaneously converting signals from up to eight detectors from analog to digital. This is done via an onboard 14-bit resolution, 125 MHz sampling rate, 8-channel analog-to-digital converter (ADC) that constantly samples the detector responses. Each channel has 2-

lane serial low-voltage differential signaling (LVDS) output, which provides high speeds at low power [200]. The second board is a commercial off-the-shelf board provided by Opal Kelly [201], on which a Xilinx Kintex-7 FPGA, cooling fan, and USB 3.0 port is mounted. This board utilizes the Opal Kelly FrontPanel® software development kit, which includes a VHDL-to-MATLAB interface through which MATLAB and the FPGA communicate [202]. The operation of FrontPanel is demonstrated in Fig. 43, and the DPP8 can be seen in Fig. 44.

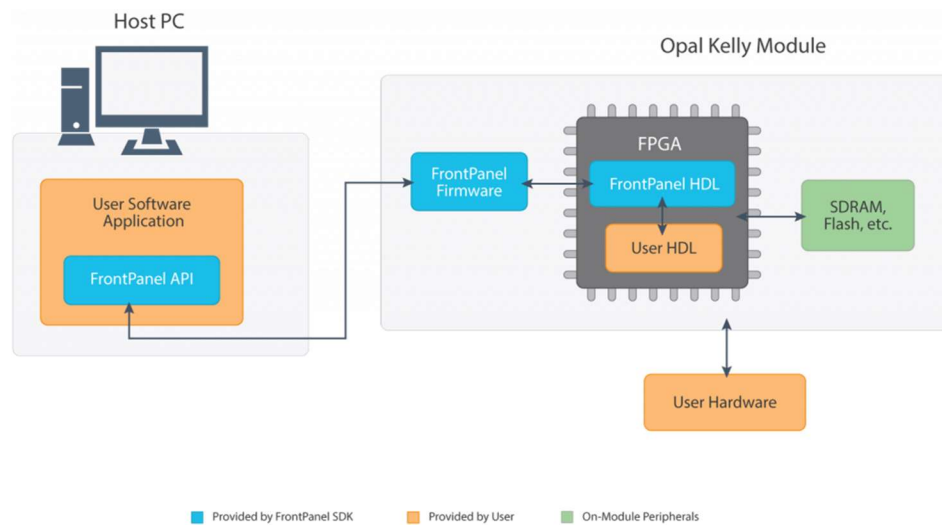


**Fig. 43.** A flow diagram demonstrating the application and utility of the FrontPanel software development kit [202]

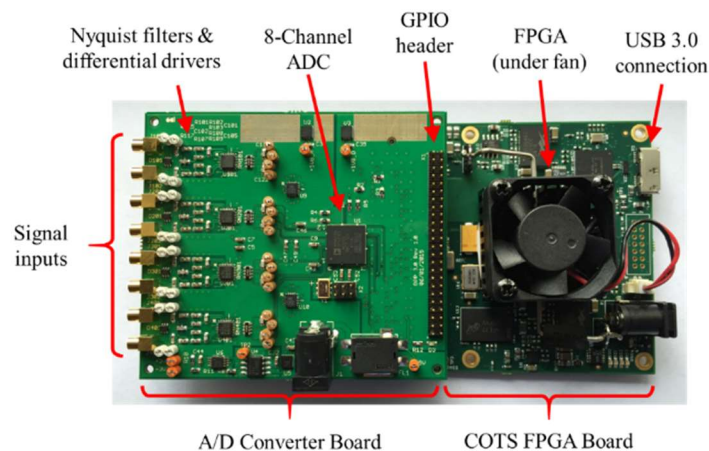


**Fig. 44.** The DPP8, an 8 channel, 14-bit, 125 MHz, FPGA-based digital pulse processor that can process coincidence pulses from up to 8 independent detecting bodies in hardware in real-time



Onboard the FPGA, a filter processes data output from the ADC. Initially designed using an FIR filter, limitations in the number of filter coefficients prompted the development of a trigger that uses a pair of block RAMs instead: one for peaking time and one for flat top time. The user may select one of 16 different peaking times and flat top times for the trigger filter, with a maximum size of 1000 samples for each. The minimum peaking time is 10 samples, but the minimum flat top time is set to zero samples to allow for a triangular trigger filter as well as a trapezoidal filter. A leading edge trigger produces a one-clock “high” signal if the filtered data exceeds a certain amplitude, at which point the FPGA captures the pulse data. To assure that the correct pulse data is transmitted, a delay of a user-specified number of clock cycles is introduced to incoming samples. When the trigger signal is set to “high”, the delayed pulse shape is written to a block RAM, which can then be read out to MATLAB. Based on user specifications, the trigger filter output shape and a version of the pulse passed through a moving average filter can also be recorded and sent to MATLAB. Various other data, such as real and live time counters, are recorded by the FPGA and can be accessed by the user. The FPGA determines trigger timings, records pulse shapes, transfers data, and conducts other actions using various state machines in communication with each other and with MATLAB [96].

Parameters that can be adjusted via user input include run mode, number of samples to record prior to a trigger, pileup rejection, noise threshold, filter parameters, coincidence patterns, CTW, and switches that indicate if the edge filter output and moving average pulse should be output to the PC. The operational flow of the FPGA functionality is indicated in Fig. 45.

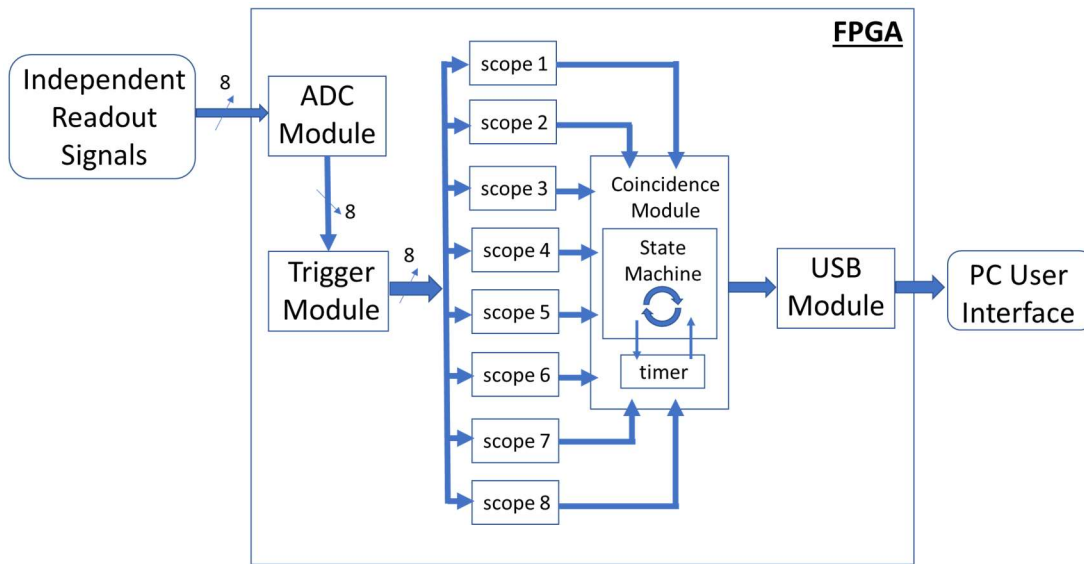


**Fig. 45.** The structure and workflow of the FPGA onboard the DPP8. The FPGA was designed using VHDL

### 3.1.3.2. Coincidence Module

Coincidence events are identified in the FPGA in real time via pattern recognition. The user defines a certain set of patterns in 8-bit binary, where a “1” means “triggered” and a “0” means “not triggered”. These patterns are usually set to reflect true coincidences (e.g.: the six permutations illustrated in Fig. 39); however, if the user is also attempting to record single events (such as with a background measurement), additional patterns may be defined to reflect individual channels triggering. If the FPGA receives a trigger signal from one channel, a coincidence timing counter begins to iterate and continues until a user-defined CTW has been exceeded. If at the end of the CTW the pattern of triggered channels is in agreement with a user-defined pattern, the system will register a coincidence event and the pulse data will be sent to the PC. As an example, if channel 1 triggers and starts the counter and channel 5 triggers before the CTW is exceeded, and the user has set one of the recognized coincidence patterns as “00010001”, then the system will register a coincidence event. If the coincidence counter finishes and the triggered channels do not match a coincidence pattern specified by the user, the FPGA will not identify the event as a coincidence and the pulse data will not be sent to the PC. As another example, the

user may communicate to the system to identify coincidences between channel 1 and channel 5 (“00010001”) as well as between channel 1, channel 5, and channel 6 (“00110001”). If channel 1 triggers and by the end of the CTW nothing else is triggered, the system rejects the event as a single interaction. If channel 1 triggers and channel 5 triggers within the CTW, the pulses will be considered in coincidence and will be sent to the PC. If channel 1 triggers and then both channel 3 and channel 5 trigger within the CTW, the pulses will not be considered in coincidence, because though the channel 1 and channel 5 coincidence was defined by the user the combination of channel 1 with channel 3 and channel 5 (“00010101”) was not. This eliminates the issue of the system potentially flagging events that are extremely unlikely to be in coincidence from a single decay, such as both two photon detectors triggering.

#### ***3.1.4. Power Supply***

Across all the radioxenon detector projects undertaken at OSU, ground loops have presented themselves as a persistent issue. Between the powering of the processors, the preamps, and the different detectors, multiple power supplies are virtually always necessary to conduct experiments. Because each power supply has its own ground, and because they are connected to each other through the detection system and pulse processor, there can exist a potential between the grounds and current can flow between them. This in turn produces oscillations and noise in the pulse signal. Ground loops have been mitigated to some degree in these past systems by connecting the grounds of several of the power supplies, but it has never been possible to connect them all. For the PIPS-SrI<sub>2</sub>(Eu), a “star ground”, or single ground to which all power supplies are connected, has been introduced.

A single HTAA-16W-AG power supply is used to supply all voltages. The power supply is placed inside a metal box, inside which all electrical connections are made. The box acts as a star ground for the system. This power supply outputs +/-12 V and +5: the +/-12 V is used to power the PIPSBox preamp, while the +5 V is used to power the DPP8 and the SiPM arrays for the SrI<sub>2</sub>(Eu). The +5 V supply also serves to

supply the -145 V needed to bias the PIPSBox. This is done using two inverting EMCO A02N proportional DC-DC converters, one for each silicon detector. These converters take in +5 V and output some voltage proportional to the input voltage. This proportionality is determined using a user set control voltage, controlled in this case by a potentiometer. Each EMCO has a trimmer of its own to adjust for proportionality and a regulator to maintain a very stable input voltage (resulting in a likewise stable output voltage). A small board, roughly 1"  $\times$  2", was designed using EAGLE software to accommodate these DC-DC converters, trimmers, regulators, and other associated electronics. The unpopulated and populated board is shown in Fig. 46a and Fig. 46b, respectively.

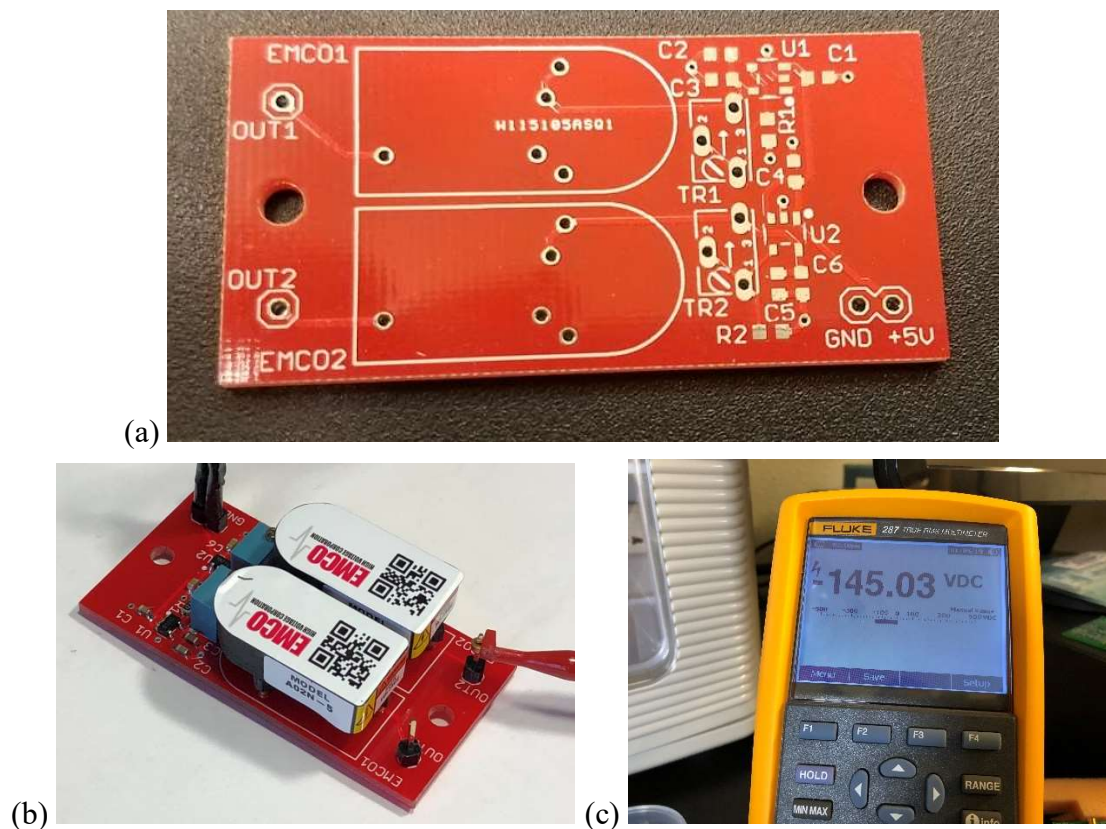


**Fig. 46.** (a) Unpopulated board; (b) populated board; (c) output voltage from the EMCO DC-DC converters

The EMCO board is placed on an inside wall of the box, as close as possible to the SHV connects that lead to the PIPS preamplifier. All devices are connected to the common ground along with their respective voltages, creating a common ground for

all devices. 5 banana plug sockets were also placed on the power supply box as a means of making the box more versatile for potential use in future experiments. A sketch of the electronic connections for the experimental setup is shown in Fig. 47a, and the assembled box is shown in Fig. 47b. Having all of these power supplies in the same box and with the same ground will reduce or eliminate the ground loop issues plaguing the systems developed in the past, but do not necessarily eliminate potential electromagnetic noise picked up by the box itself.

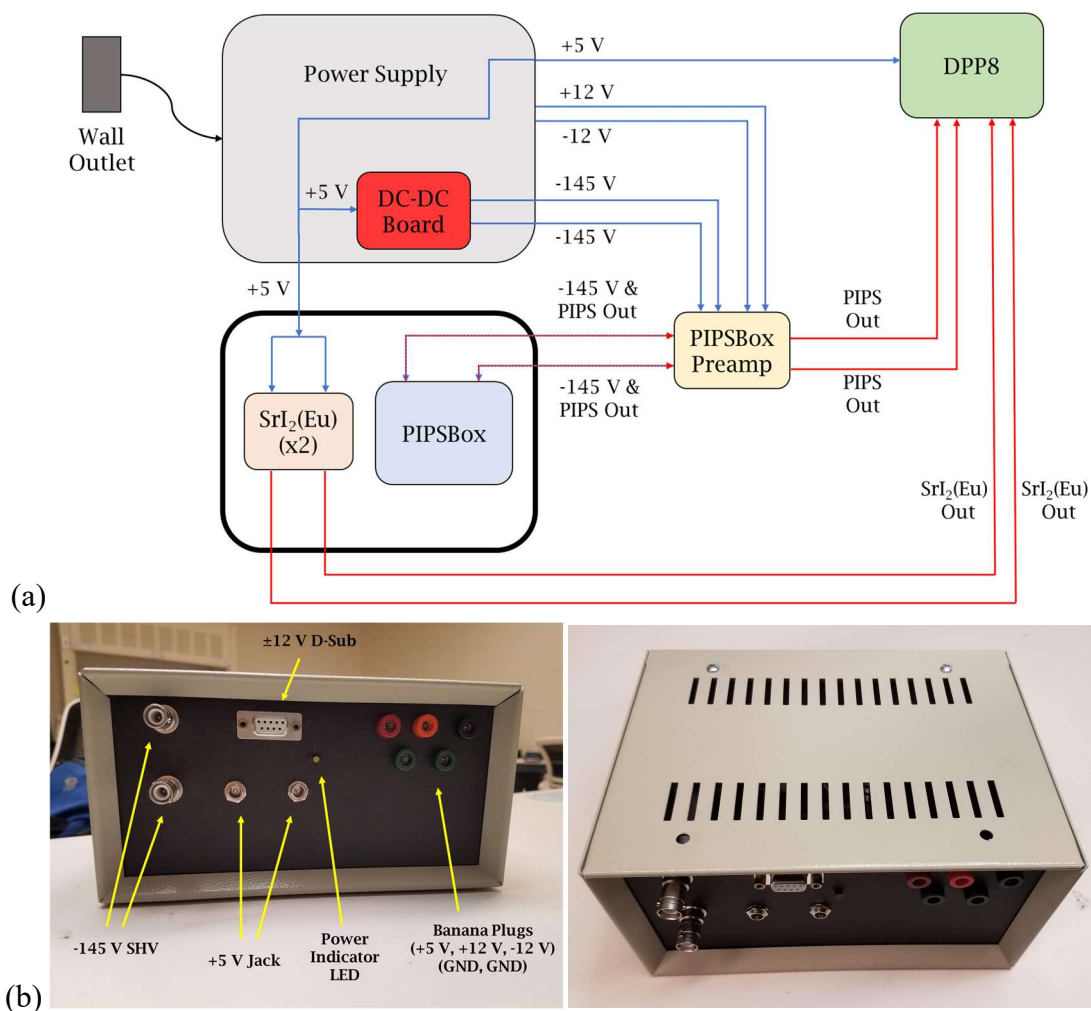


**Fig. 47.** (a) Sketch of power supply, indicating how the power is routed to all components of the experimental setup. Blue arrows indicate voltage being supplied, while red arrows indicate pulse signal; (b) assembled power supply box. The banana plugs are not used in this experiment, but are included on the box to provide easy accessibility in future experiments

### 3.1.5. Holder and Detector Setup

To hold the PIPS-SrI<sub>2</sub>(Eu) system stable during measurement and during possible movement of the system, a holder was designed in Solidworks and 3D printed using standard PLC. The holder was screwed into the bottom of an aluminum box such that it is held stationary. Openings in the holder exist where wires are to be attached, and the top parts are easily separable to allow for the detectors to be removed if necessary. The holder is shown in Fig. 48.

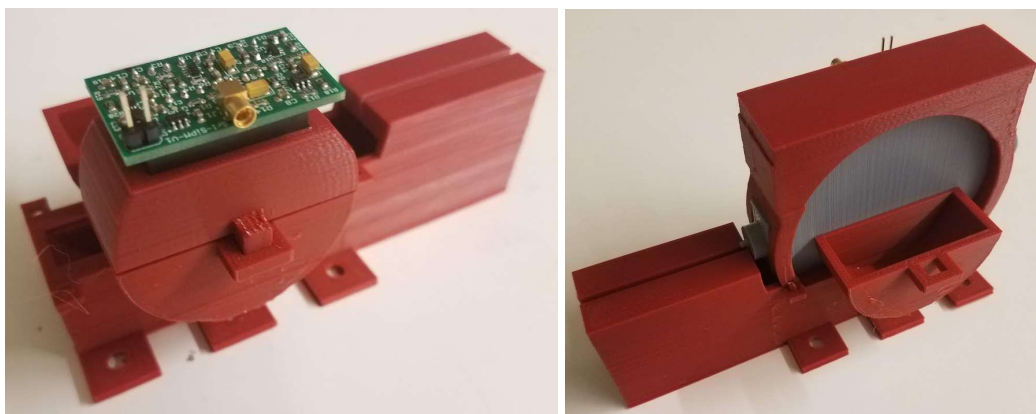


**Fig. 48.** The holder for the PIPS-SrI<sub>2</sub>(Eu) system, shown from two different angles. The two SrI<sub>2</sub>(Eu) crystals are held in place alongside the PIPSBox, which is itself held secure in the center. A long groove is in place to hold the injection tube steady. The grey PLC in the middle is a model of the PIPSBox for demonstration purposes

The entire detection system is held inside an aluminum box, chosen for additional electromagnetic shielding and for easy transport. The aluminum box also makes a convenient common ground for the system. The box was machined with custom holes to allow for the protrusion of the injection tube, which is held stationary with a rubber stopper, as well as BNC connectors (for signal readout and for voltage supply in the case of the PIPSBox) and a single jack to which +5 V is sourced and directed to each SrI<sub>2</sub>(Eu) board. Copper mesh is used to connect the grounds of the BNC connection to the aluminum box, maintaining a common ground for the system. The PIPSBox gas injection line was fitted with a Luer-compatible barb for easy gas evacuation and sample injection. The system inside the box is shown in Fig. 49.



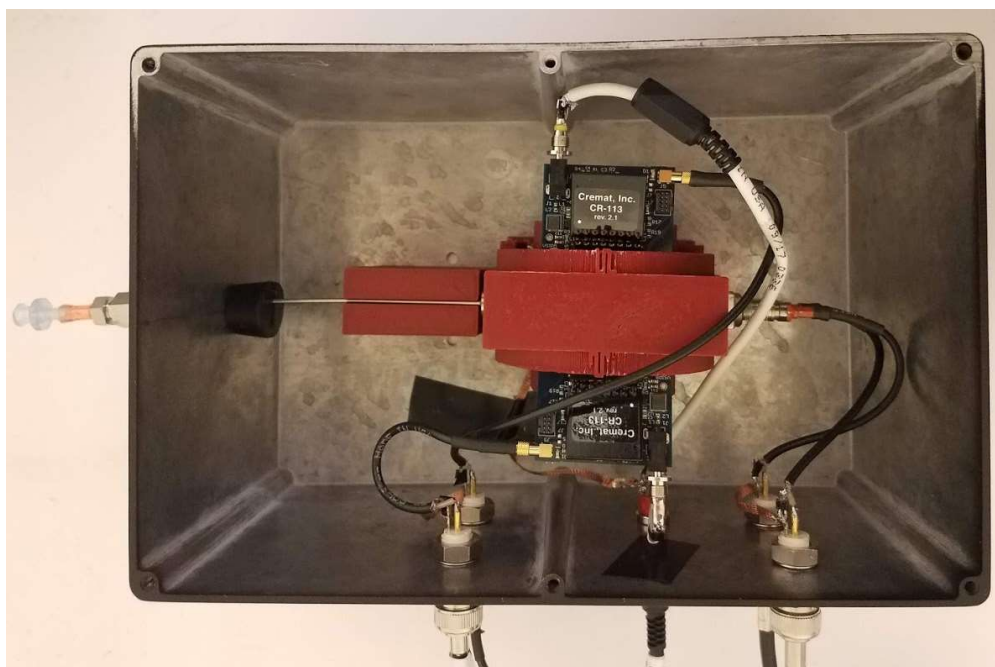


**Fig. 49.** The PIPS-SrI<sub>2</sub>(Eu) system inside the aluminum box, as seen from above. The PIPSB<sub>ox</sub> is powered and has signal read out via the two BNC connections to the bottom right, while the two SrI<sub>2</sub>(Eu) are powered by the single +5 V jack in the center and have their signal read out by the two BNC connections on the bottom left

The system is placed almost entirely in a lead cave, constructed using 2" thick bricks, during experiments to further reduce ambient background. The only gap in the lead cave is a roughly 2" × 8" rectangle near the front of the box (left side of Fig. 49) to allow access to the wiring and to the injection tube.

### 3.1.6. *Vacuum Pump*

Before radioxenon samples are injected into the system and after the samples are extracted, a vacuum is applied to the gas cell to clear out possible contaminating gas. This was initially done using a hand pump. However, when working with the PIPS-CZT unexpectedly intense memory effect was observed in the PIPSB<sub>ox</sub>. It was postulated that this was likely in part due to a weak vacuum being applied to the gas volume: a hand pump was being used that could only achieve 100 torr pressures, whereas experiments showing negligible memory effect achieved pressures on the order of millitorr using a turbopump [86]. Acquiring a vacuum pump capable of achieving ~1 torr or below pressures was ideal, and it was verified by Canberra

engineers that the PIPSBox could be taken to these pressures [71]. A Welch Duo-Seal 1400(B-01) pump, reportedly capable of pumping to 0.1 mtorr [203], was procured for this application. The vacuum pump was fitted with a Luer valve such that it could easily interface with the PIPSBox gas line.

There was no gauge onboard this vacuum pump, nor was there a way to control the rate of evacuation. Evacuating the cell too rapidly can result in rupture, and so the rate of evacuation was initially limited via the use of a very thin Luer-compatible needle connected to the vacuum pump connector. Few vacuum gauges are relatively affordable while still being able to accurately monitor gas pressures ranging from atmospheric pressure down to the mtorr level. A two-gauge system was employed as a cost-effective solution: a \$10 off-the-shelf analog gauge with relatively poor precision was used to monitor how rapidly the volume was evacuated down to pressures on the order of a dozen torr, at which point a sensitive \$120 TPI 605 digital vacuum gauge would display the pressure with a precision of 20 mtorr as it continued to drop from 12 torr down. This required a temporary setup that required several Luer connectors, but it quickly became clear that the gas was being evacuated slowly enough that a rupture was not a concern. At this point the analog gauge was removed from the system, simplifying the arrangement of gas lines and reducing the number of potential leakage sites. Exhaust is pumped into a fume hood using a clear rubber hose to assure that no radioxenon gas is expelled into the lab space upon evacuation. The pump, analog gauge, digital gauge, and Luer connections are shown in Fig. 50. The system has proven capable of pumping the PIPSBox down to 0.76 torr in a best case scenario, but during the measurements presented in this work the PIPSBox was commonly pumped down to ~4-5 torr. This reduction in efficacy of vacuum is attributed to leakages in the pump gas line, not the PIPSBox itself.



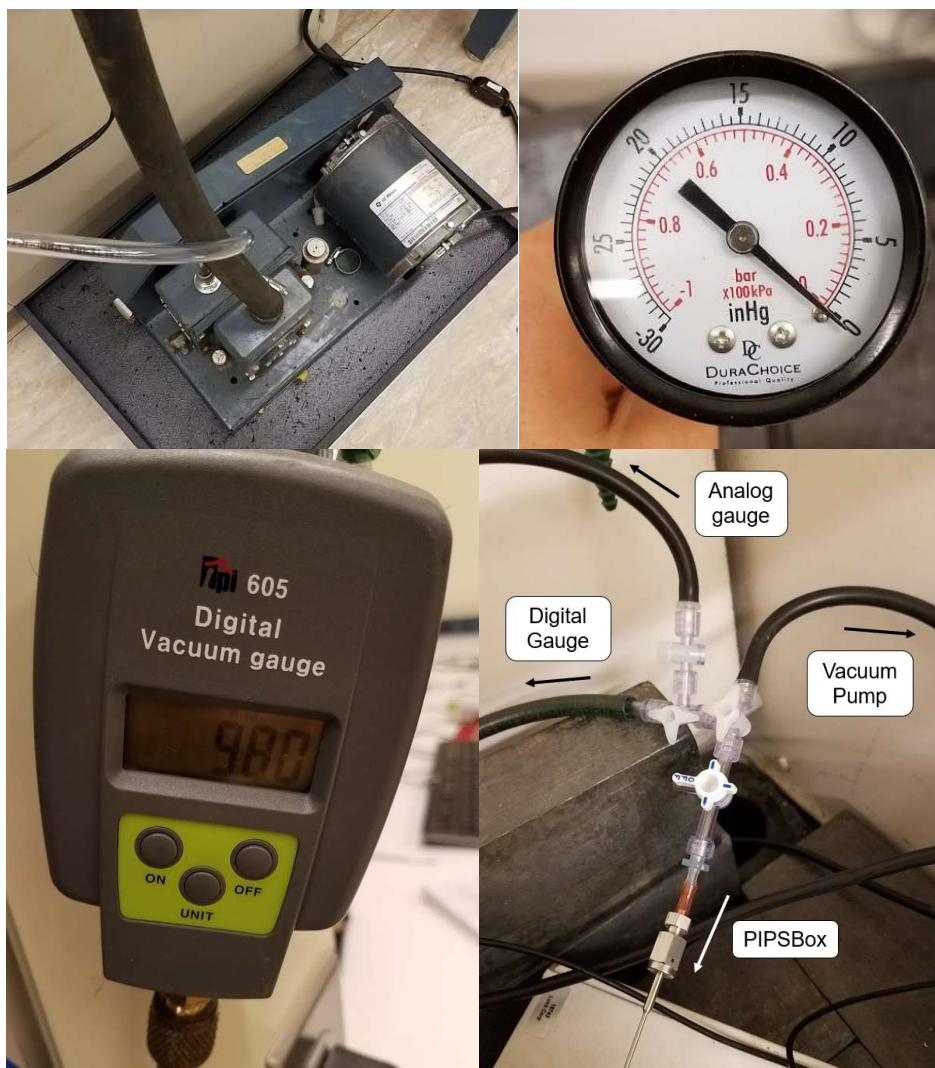


Fig. 50. (from left to right, top row then bottom row): Welch Duo-Seal 1400(B-01) pump, with clear exhaust tube; DuraChoice analog gauge for observing evacuation rates and vacuum strength far from 0 torr; TPI 605 digital vacuum gauge, for observing evacuation rate and vacuum strength below 12 torr; Luer system for evacuating the PIPSBBox of radioxenon gas

### 3.2. Simulation

Several qualities about the PIPS-SrI<sub>2</sub>(Eu) system would be difficult or impossible to investigate using practical experimental means. In these cases, simulations can be used to fill the void. Simulation was also instrumental in guiding the initial design choices for the system. MCNP6 was used for all simulation tasks. Solid angles were simulated for all detectors, and efficiencies were estimated.

### **3.2.1. PTRAC**

The ptrac card was particularly essential for generating the library spectra used in the statistical analyses discussed in the following section, as well as other valuable information such as backscatter rates. As such, it deserves special mention. The ptrac card prompts MCNP to track individual particle histories on a microscopic level, from generation until termination. The ptrac file output at the end of the simulation indicates the interactions each particle underwent through its history, the position of the particle at those interaction points, what volumes the interactions occurred in, what times they occurred, what direction the particle was traveling when they occurred, and the energy of the particle following the interaction.

A custom program was written to parse ptrac files. The program can easily be run in any Python work environment (e.g.: Spyder, PyCharm), so long as the NumPy, matplotlib, and pandas libraries are accessible in addition to the standard Python library. The program requires one or two ptrac files as input. It is critical that these ptrac files have been generated using an MCNP input file that allows particle tracking for all interaction types in all cells to guarantee correct results. Energy deposition can be tracked in up to 2 cell volumes per ptrac file. By correlating history numbers in individual runs, the code can affect coincidence events. For example, if a beta ptrac file has interactions in the electron detectors in histories 1, 4, 5, and 7, and a gamma ptrac file has interactions in the photon detectors in histories 2, 4, and 7, the program would identify two coincidences: history 4 and history 7.

## **3.3. Statistical Modeling**

### **3.3.1. Regional Spectral Deconvolution (RSD)**

A new statistical method, hereby referred to as Regional Spectral Deconvolution (RSD), is being investigated whereby the presence and ratios of radioxenon isotopes can be identified in an experimental spectrum using maximum likelihood methods. This method is an adaptation of the methods used in the SDAT code: it involves using a library spectrum for each of the radioxenon isotopes of interest (generated using

experimental data using isotopically pure samples or using simulated spectra sourced from MCNP), segmenting each of these spectra into many unique regions, summing the total counts within each of those regions, and creating a vector with each index representing one of those summed values. The relative intensities between the indices in each vector are characteristic to that specific isotope. Segmenting the spectra in such a way drastically improves computation time when compared to the traditional simultaneous deconvolution (SDAT) method (which simply forms the vectors based on the counts in each histogram bin of the 2D spectra) and aims to improve accuracy at low concentrations.

SDAT and RSD both inherently address situations such as backscatter in the PIPSBox: in the ROI method, counts falling outside of an ROI due to backscatter and into the ROI of another isotope act as nothing but a loss of counts in the first ROI and as interference in the second, while in this proposed method these backscatters are treated naively by the algorithm as simply an inherent part of the spectrum of that particular isotope. When determining the amount of a certain isotope in an experimental spectrum, the algorithm expects a certain amount of backscatter and these backscatters are not treated as lost. Take for example the  $^{131m}\text{Xe}$  signature of a 129 keV conversion electron (C.E.) in coincidence with a 31 keV X-ray (Fig. 51a). Backscatter of the C.E. can occur and create a tail, the severity of which can be particularly hard to discern when overlapping a  $\beta$ -spectrum generated from  $^{133}\text{Xe}$ . Traditional ROI approaches either draw a box around the peak region, neglecting the tail, or draw a larger box around the entire signature, including the tail, which could have a significantly detrimental effect on MDC. In very low count rate situations statistical approaches would also struggle—how would the statistical model determine if a sample spectrum has  $^{131m}\text{Xe}$  if the sample spectrum has such low counts that it does not well represent the shape of the isotope as generated in simulation and recorded in the isotope library? RSD would, instead of conducting a statistical approach where the whole spectrum is an evenly binned  $n \times m$  structure, break the spectrum into various larger regions and conduct a maximum likelihood analysis based on how many counts fall into each specific region for each isotope.

The dimensions of each region would be informed by the resolution of the detector as determined by experimental injection of the radioxenon isotopes of interest. This sectioning approach is meant to improve the statistics in areas with poor statistics. A demonstration of this sectioning can be seen in Fig. 51b. Note that the regions are not of equal size, nor are they all the same shape. Though all regions in Fig. 51b are rectangular, they do not necessarily have to be. This approach will likely involve significant optimization to determine the best region definitions for each isotope for this system, though such a study is beyond the scope of this work.

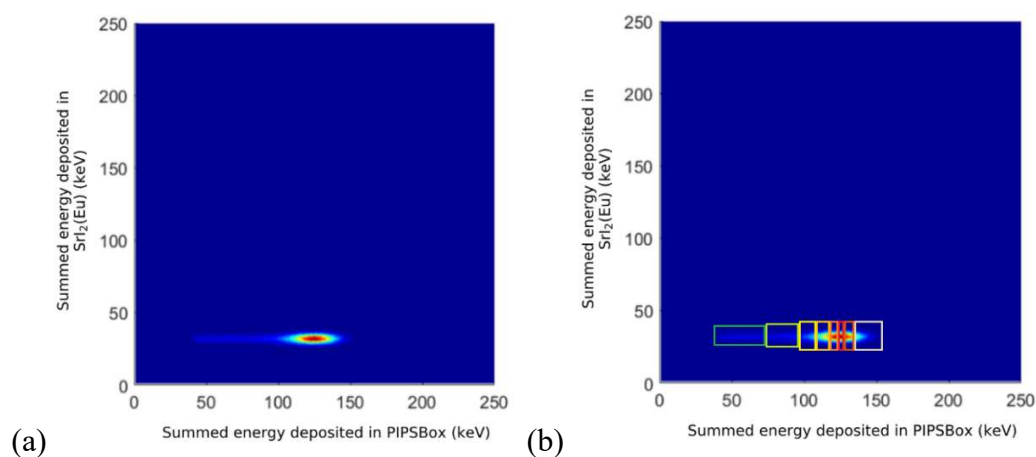


**Fig. 51.** (a) simulated  $^{131m}\text{Xe}$  signature in the PIPS-SrI<sub>2</sub>(Eu); (b) the same signature, with unequal region sectioning applied. All regions have roughly equal counts

The regions are determined for each isotope individually but are applied to all library spectra as well as the experimental spectrum. This is necessary to keep all the columns in the  $\underline{\underline{A}}$  matrix of equal length. The regions defined in Fig. 51b would all show zero (or nearly zero, depending on the extent of Compton down scatter) counts in the  $^{135}\text{Xe}$  coincidence spectrum, and vice versa; the regions defined to account for the 250 keV  $\gamma \times 0-910$  keV  $\beta$  coincidences would have zero counts in the  $^{131m}\text{Xe}$  column of the  $\underline{\underline{A}}$  matrix.

### 3.3.2. Python Package

Development of a Python package involved two phases. The first phase involved a proof-of-concept, where the methods outlined previously by Lowery and Biegalski

[112] were implemented directly. The matrices were entered into an  $\underline{A}$  matrix using the full  $m \times m$  2D coincidence spectra as is, where each matrix element is one indexed value in one of the 2D histograms. Background was not introduced in these initial tests. The 2D library spectra used in this work, as generated from MCNP6 and ptrac, are shown Fig. 52. Note that in practice, the  $^{133}\text{Xe}$  spectra that each represent a unique decay path are combined into one single spectrum based on branching ratios and efficiency. The second phase involved the implementation of the new regional sectioning methodology and introduction of background.

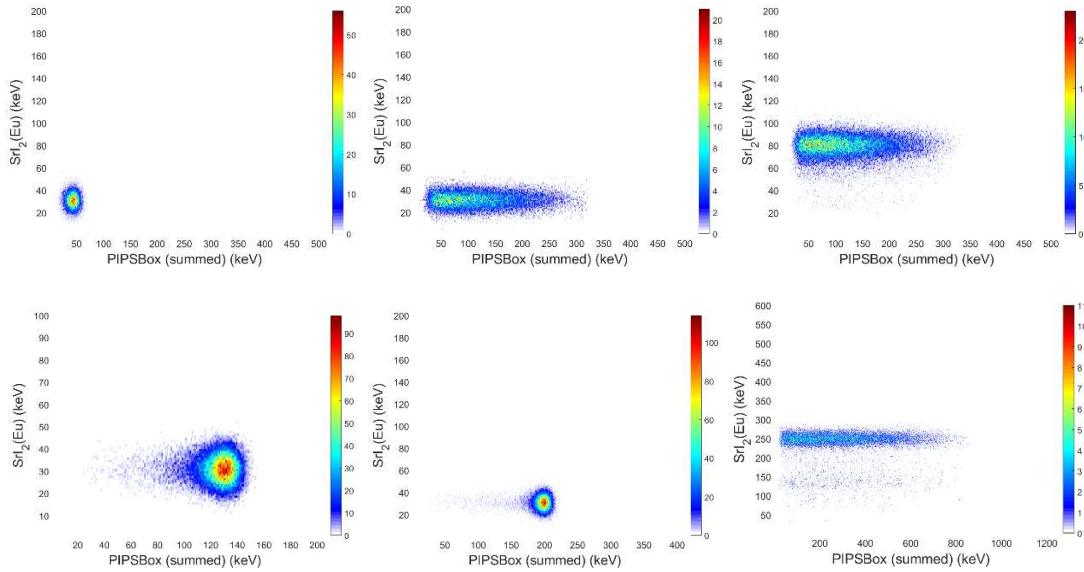


**Fig. 52.** 2D spectra generated in MCNP6 using ptrac for the PIPS-SrI<sub>2</sub>(Eu) system, with Gaussian broadening applied to the peaks in MATLAB to create a statistical spread. From top left to bottom right: 45 keV C.E. in coincidence with 31 keV X-rays, 0-346 keV  $\beta$  in coincidence with 31 keV X-rays, 0-346 keV  $\beta$  spectrum in coincidence with 81 keV  $\gamma$ -rays, 129 keV C.E. in coincidence with 31 keV X-rays, 0-199 keV C.E. in coincidence with 31 keV X-rays, 0-910 keV  $\beta$  spectrum in coincidence with 250 keV  $\gamma$ -rays

### 3.4. Experimentation

The experimental work for the SrI<sub>2</sub>(Eu) detector processed through several phases. Initial characterization work was done on the SrI<sub>2</sub>(Eu) and the PIPSBox individually using laboratory check sources. This allowed for proper calibration and optimization of the detectors without having to account for the short half-lives of the radioxenon

isotopes ( $^{137}\text{Cs}$ , for example, has a half-life of over 30 years, compared to the longest radioxenon isotope with a half-life of just over 11 days). Following this, background was measured, and the detector was evaluated with radioxenon samples.

#### ***3.4.1. Characterization of $\text{SrI}_2(\text{Eu})$***

$\text{SrI}_2(\text{Eu})$  investigations include:

- Crystal uniformity, brightness, and positional sensitivity
- Characterization of a digital integration board
- Characterization of an analog integration board
- Optimization of trigger (in FPGA) and peak detection (in MATLAB) filter shaping times
- Minimization of noise threshold
- Energy calibration and resolution with lab check sources
- Comparison of results using digital and analog pulse processing
- Coincidence verification using  $^{137}\text{Cs}$  and timing response
- Trigger walking
- Temperature shift

#### ***3.4.2. Characterization of PIPSBox***

PIPSBox investigations include:

- Noise thresholds with AMPTEK A250F/NF preamplifiers
- Noise thresholds with the Cremat preamplifier
- Optimization of trigger (in FPGA) and peak detection (in MATLAB) filter shaping times
- Energy calibration and resolution with lab check sources
- Response time using coincidence backscatter
- Reduction of backscatter via summation for both preamplifiers

### 3.4.3. Characterization of Full Detector

Characterization of the full detector includes the measurement of all radioxenon isotopes of interest, background, and memory effect using  $^{131\text{m}}\text{Xe}$ . During radioxenon measurements, resolution of all relevant photon and electron peaks are identified and efficiencies are experimentally determined in an absolute way.

#### 3.4.3.1. TRIGA and Sample Preparation

Radioxenon samples were prepared using  $^{130}\text{Xe}$ ,  $^{132}\text{Xe}$ , and  $^{134}\text{Xe}$  gas and irradiating them in the OSU TRIGA reactor. The xenon gases are contained in independent stainless steel containers, and at time of manufacture were at atmospheric pressure and 99.99% pure. However, over several years of use these canisters have dropped in pressure significantly, making ingress of small amounts of air or other impurities likely. Nevertheless, the gas in these canisters are sufficient to conduct preliminary characterization on the prototype detector.

The samples were prepared by using a vacuum hand pump to extract any air from a syringe and then drawing a sample of stable xenon gas into the syringe, as shown in Fig. 53. Following the preparation of the samples, the xenon samples were exposed to a neutron flux of  $2.51 \times 10^{11} \text{ cm}^{-2}\text{s}^{-1}$  in the thermal column of the OSU TRIGA reactor for varying amounts of time. Despite an effective live-time counter implemented in the FPGA, efforts were made to create small samples such that high activity would not introduce significant pileup. The samples were injected one by one into the gas cell.



**Fig. 53.** Generation of individual samples of xenon gas, where 99.99% pure xenon gas of a certain isotope is drawn into a syringe for irradiation in the TRIGA reactor

### 3.4.3.2. Efficiency

The determination of the Minimum Detectable Concentration (MDC) for each radioxenon of interest requires that the beta-gamma coincidence detection efficiency be known for the detection system. One way this can be determined is through MCNP simulations, where either the efficiency of the electrons/betas and the X-rays/gammas of interest are determined individually and multiplied or the coincidence efficiency is determined directly using ptrac. However, it has been shown that experimentally observed efficiencies and efficiencies obtained from simulation can vary significantly [45], [162], in part due to an incomplete knowledge of the internal layout of the PIPSBox components and the properties of the source distribution. As such, the efficiency of the PIPS-SrI2(Eu) system should be determined in an absolute fashion. Because the flux of the TRIGA reactor used to create the sample of radioxenon is not precisely known, the precise activity of the creates sample cannot be determined. One possible avenue would be to determine the efficiency in a relative way [204]. In this case two samples of the same composition would be created, with one sample injected into a well-characterized detector and the other injected into the detector with unknown efficiency. Precise knowledge of the relative sizes and compositions of the samples is mandatory, and without a refined and highly controlled sample creation system this is difficult to achieve reliably.

A third way to calculate efficiency, this time in an absolute manner, was described in detail by Cooper et. al. [204]. This method only requires one sample to be created and does not require a knowledge of the activity of the source *a priori*. The count rates of the beta singles and gamma singles to the coincidence count rates of the system in order to determine the efficiencies for each electron or photon of interest individually, though it does require some simplifications by assuming certain things about the efficiencies for low energy or low importance decay paths (such as the 25 keV C.E. released by the decay of  $^{133}\text{Xe}$ ). The equations are:

$$A_T = \frac{C_{\beta\gamma}}{BR_{\beta\gamma}\epsilon_{\beta\gamma}} = \frac{C_{\beta\gamma}}{BR_{\gamma}\epsilon_{\beta\gamma}} = \frac{C_{\beta\gamma}}{BR_{\gamma}\epsilon_{\beta}\epsilon_{\gamma}} \quad (14)$$



$$A_T = \frac{C_\gamma}{BR_\gamma \epsilon_\gamma} \quad (15)$$

$$A_T = \frac{C_\beta}{1 - (1 - \epsilon_\beta)(1 - \epsilon_{CE_i} BR_{CE_i})} \quad (16)$$

with  $C$  being counts,  $BR$  being branching ratio, and  $\epsilon$  being efficiency for the radiation of interest. In all cases where a beta decay is possible it occurs with a virtually 100% branching ratio, so  $BR_\beta$  is defined as 100% and  $BR_{\beta\gamma} = BR_\gamma$ . Eqn. (14) can be solved with respect to eqn. (15) to yield  $\epsilon_\beta$  using only the known gamma singles rate and coincidence count rate.  $\epsilon_\gamma$  is more difficult to determine due to having to account for the multiple decay paths and are accounted for by determining the probability that any one decay mechanism is detected. As no means were available to verify the precise quality of relative samples, this absolute method was used to determine all experimental efficiencies.

## 4. RESULTS

### 4.1. Simulation

#### 4.1.1. Model

The PIPS-SrI<sub>2</sub>(Eu) was modeled closely to the geometry of the physical detector. All parts of the detection system itself, including the silicon detectors, carbon windows, aluminum chassis, internal gas cell, SrI<sub>2</sub>(Eu) crystals, aluminum shells for holding the SrI<sub>2</sub>(Eu), aluminum box, and lead cave. The gas cell was modeled as a mixture of 70% xenon gas and 30% nitrogen with the density calculated for STP conditions, to roughly reflect the sample. The PLC holder, injection tube, and front-end circuitry were not modeled. Exact measurements for the SrI<sub>2</sub>(Eu) made it possible to recreate the detector in the model with high precision and accuracy, but incomplete knowledge of the internals of the PIPSBox necessitated some inference. The model is shown in Fig. 54.

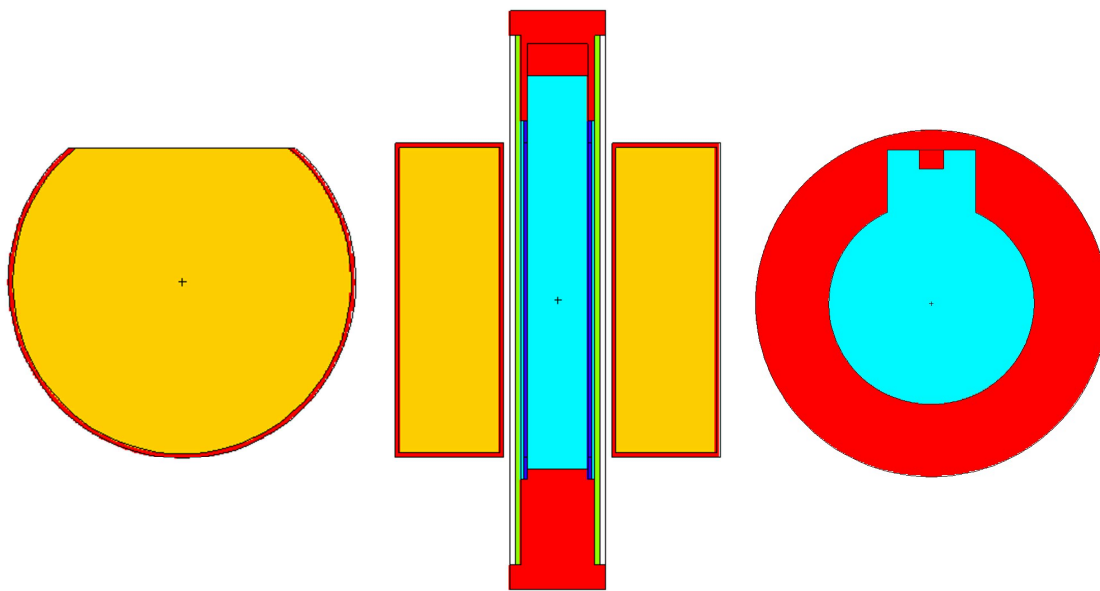


**Fig. 54.** The model of the PIPS-SrI<sub>2</sub>(Eu) as visualized using MCNPX VisEd, showing the SrI<sub>2</sub>(Eu) crystal in aluminum shell (left), PIPSBox with aluminum chassis and gas cell (right), and the entire system collectively (center). Red is aluminum, gold is SrI<sub>2</sub>(Eu), carbon windows are green, silicon detectors are dark blue, and the gas cell is light blue

#### 4.1.2. Solid Angle

Solid angle directly informs efficiency, and so simulating solid angle was important during the initial design phase for giving a sense of efficiency improvement or reduction compared to previous designs. Solid angle was simulated by setting all volumes to vacuum and simulating an isotropic volume source of arbitrary energy filling the entire gas cell. The solid angle was the fraction of the radiation quanta passing into the volumes of interest. In this way, the solid angle of the PIPSBBox was determined to be  $2.54\pi$ . This simulation also informed the losses that would be experienced due to the cut applied to the  $\text{SrI}_2(\text{Eu})$ . The  $\text{SrI}_2(\text{Eu})$  without cut was  $1.86\pi$ , while with the cut was  $1.78\pi$ . Both of these  $\text{SrI}_2(\text{Eu})$  solid angles are significant improvements over the  $1 \text{ cm}^3$  coplanar CZT used in the PIPS-CZT work, which had a total solid angle of  $0.39\pi$ .

#### ***4.1.3. Spectra***

Each of the radiations of interest were simulated in turn. These simulations were used for preliminary estimations for the efficiencies of the system, as well as roughly how much backscatter was expected in the PIPSBBox and how much summing the two silicon detector signals would be able to reduce it. The simulations used ptrac to track particles in the silicon and the  $\text{SrI}_2(\text{Eu})$  crystals. These data were used in the calculation of simulated efficiency, as well as for evaluation of the spectral deconvolution method. Spectra obtained from these simulations are shown in Fig. 55. In all cases,  $2 \times 10^5$  instances were run.

It is worth noting that these spectra indicate profound differences with the experimental results in interesting ways. Even when using Gaussian broadening in MCNP, the photopeak-to-total ratio of the spectra are significantly higher in the simulated spectra than in the experimental spectra—roughly  $2.25\times$  higher in the case of the 250 keV photopeak for  $^{135}\text{Xe}$ . These results appear both when using an F8 tally and when using ptrac. The differences between the simulated and experimental spectrum shapes serve to partially explain the differences between simulated and experimental efficiency, as a larger portion of counts falling into the photopeak (i.e.:

the ROI) results in overestimation. A more complete discussion of this difference can be found later in the paper.

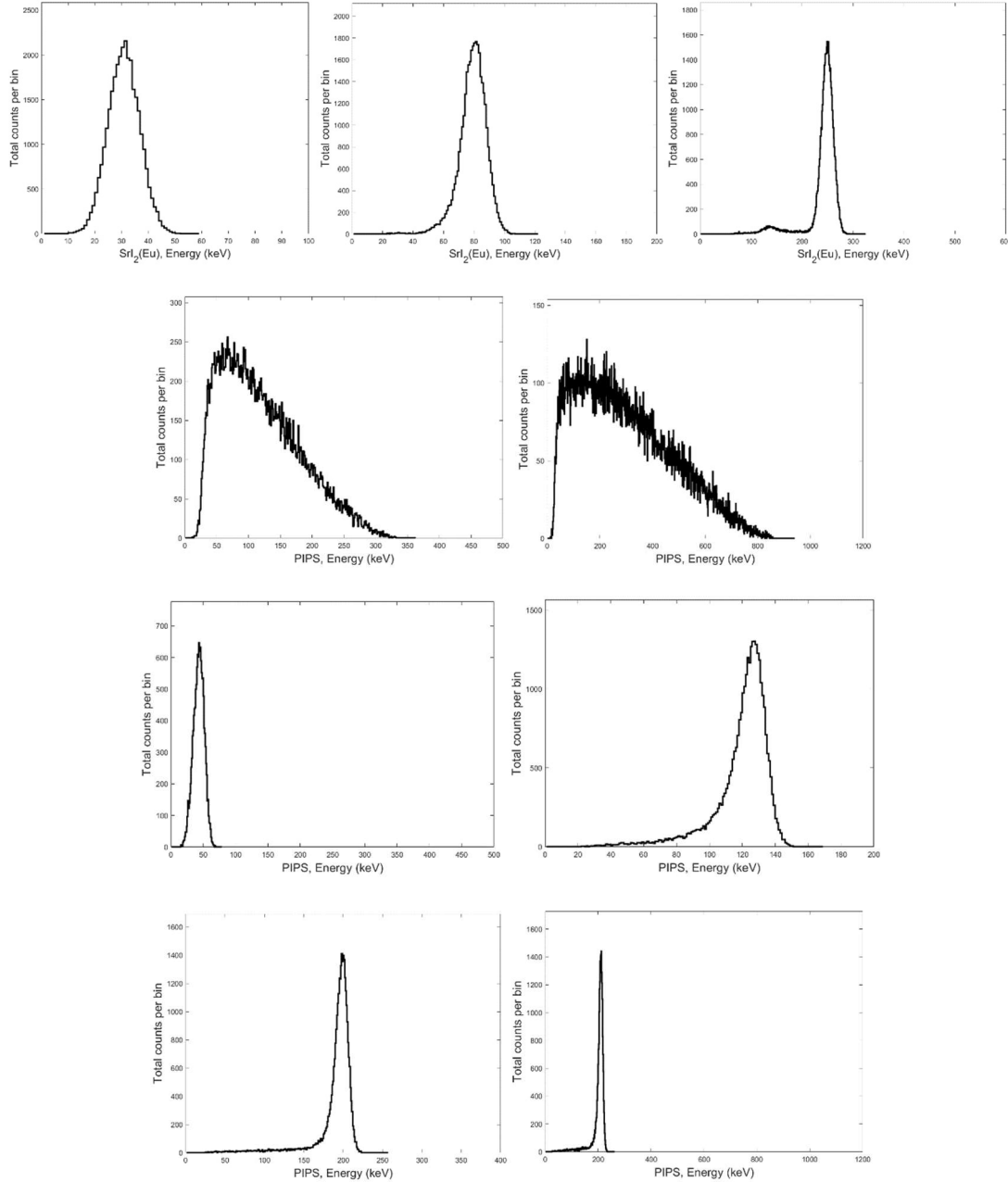


**Fig. 55.** Simulated spectra, in order, for 31 keV, 81 keV, and 250 keV photons in  $\text{SrI}_2(\text{Eu})$  and spectra for the 0-346 keV beta, 0-910 keV beta, and the 45 keV, 129 keV, 199 keV, and 214 keV C.E.s in the PIPSBox. Doppler broadening was applied in MATLAB. Axes were chosen to agree with the axes chosen in the experimental presentations shown later in this work

Though not shown in Fig. 55, the peaks in the electron simulations downshifted in energy depending on the initial energy of the electron and the spectrum had to be recalibrated to account for this. This effect was not as extreme in the case of the higher energy electrons; for example, the peak from 199 keV C.E.s was observed to shift 1-2 keV. However, low energy C.E.s such as the 45 keV C.E. shifted significantly, up to 8 keV. These shifts are a consequence of electron attenuation in the gas, which is included in the simulation. Possible non-linearity of the PIPSBox was not experimentally quantified in this research, but it is nevertheless an important aspect of the system that should be investigated in the future to optimize results.

#### *4.1.3.1. Backscatter Reduction*

Using the ptrac files generated for the spectra simulations, by identifying coincidences between the two silicon detectors it was possible to estimate the significance of backscatter in the PIPSBox. The gas was not neglected in the simulation and did result in non-negligible attenuation of the electrons, particularly in the 45 keV electron. Various energy cuts were defined. The percent of coincidence events that involve an electron depositing energy in both silicon detectors that exceeded an energy cut is shown in Fig. 56. It can be seen from this plot that the backscatter percentage is significant. This implies that modest gains are achievable by summing the two silicon detectors, with performance improving further as the detector threshold is reduced. Backscatter reduction via summation is demonstrated in Fig. 57 for the 129 keV C.E. from  $^{131\text{m}}\text{Xe}$  using ptrac. In this case  $2 \times 10^6$  histories were run. An energy threshold of 28 keV was used, and Gaussian broadening was applied in MATLAB.

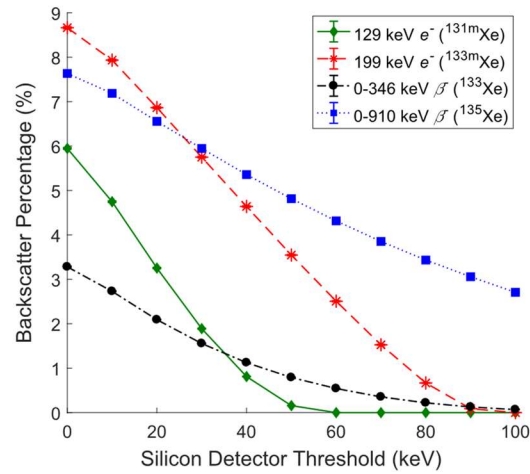


**Fig. 56.** Percentage of total electron histories modeled in MCNP6 that deposit enough energy to trigger both silicon detectors, as a function of energy threshold. Due to attenuation in the sample gas, 45 keV electrons from  $^{133}\text{Xe}$  experienced negligible ( $<0.01\%$ ) multi-volume energy depositions and are not included in this plot [45]

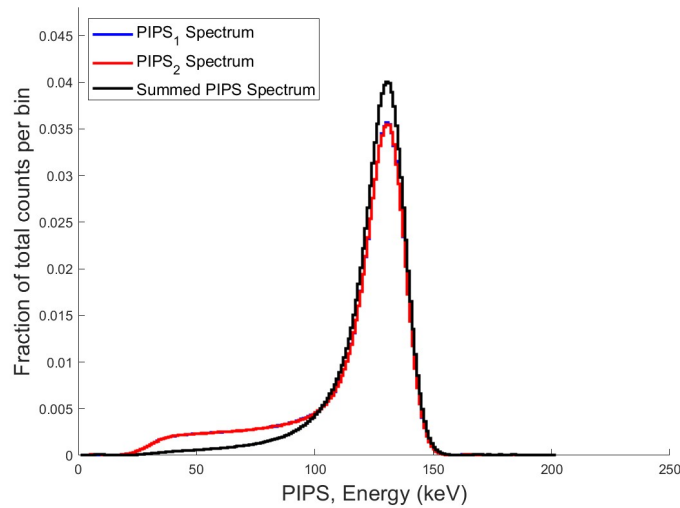


**Fig. 57.** Histogram of simulated results from 129 keV C.E.s interacting in the PIPSBBox

Fig. 57 demonstrates two things. The first is that tailing cannot be done away with completely using summation; it is in part caused by attenuation in the gaseous sample between the silicon detectors and cannot be eliminated. However, the second thing demonstrated by this figure is that significant tailing reduction can be observed via summation; this simulation predicts that a tail-to-total ratio is increased from 78.7% in the individual cases to 89.3% in the summed case.

#### 4.1.3.2. Efficiency

Efficiencies were calculated by using ptrac to identify interactions occurring in a given volume. The efficiencies are determined only for the regions of interest: i.e.: the efficiency quoted for the 250 keV photon from  $^{135}\text{Xe}$  only accounts for the coincidences in the photopeak. The sizes of the ROIs were determined via the experimental peak resolutions indicated in later sections. The coincidence efficiency was determined by simply multiplying the efficiencies of each individual efficiency together. Energy thresholds were experimentally determined and were later applied to the data.  $2 \times 10^5$  histories were run in each case. These results are shown in Table 5.

**Table 5.** Efficiencies determined via MCNP6 simulation for different ROIs, as determined using ptrac and thresholds of 15 keV and 28 keV for photons and electrons, respectively

ROI	$\epsilon_{\beta, PIPS}$	$\epsilon_{\gamma, SrI_2(Eu)}$	$\epsilon_{\beta\gamma, PIPS-SrI_2(Eu)}$
$^{131m}\text{Xe}$	$55.2 \pm 0.5\%$	$24.9 \pm 0.2\%$	$13.7 \pm 0.2\%$
$^{133m}\text{Xe}$	$59.7 \pm 0.5\%$	$24.9 \pm 0.2\%$	$14.9 \pm 0.2\%$
$^{133}\text{Xe}$ , 81 keV $\gamma \times$ 0-346 keV $\beta$	$44.0 \pm 0.4\%$	$41.8 \pm 0.3\%$	$18.4 \pm 0.2\%$
$^{133}\text{Xe}$ , 31 keV X-ray $\times$ 0-346 keV $\beta$	$44.0 \pm 0.5\%$	$24.9 \pm 0.2\%$	$11.0 \pm 0.2\%$
$^{133}\text{Xe}$ , 31 keV X-ray $\times$ 45 keV C.E.	$25.8 \pm 0.3\%$	$24.9 \pm 0.2\%$	$6.4 \pm 0.1\%$
$^{135}\text{Xe}$ , 31 keV X-ray $\times$ 214 keV C.E.	$60.7 \pm 0.5\%$	$24.9 \pm 0.2\%$	$15.1 \pm 0.2\%$
$^{135}\text{Xe}$ , 250 keV $\gamma \times$ 0-910 keV $\beta$	$61.7 \pm 0.4\%$	$39.4 \pm 0.3\%$	$24.3 \pm 0.2\%$

When compared to experimental results demonstrated later in this work, the MCNP results seem to significantly overpredict the efficiency of the  $\text{SrI}_2(\text{Eu})$ , by roughly a factor of 1.8-3, whereas the simulations are within a few percent in the case of the PIPSTBox (excepting the 45 keV C.E., which is significantly underpredicted in simulation). This significant overprediction of efficiency is believed to be due to the underprediction of Compton scatter by MCNP, as discussed in the previous sections.

## **4.2. $\text{SrI}_2(\text{Eu})$ +SiPM Characterization**

In this section, discussion involving characterizations that are particularly isolated to the  $\text{SrI}_2(\text{Eu})$  crystals, independent of the PIPSTBox, are detailed. Discussion of measurements conducted with radioxenon isotopes is reserved for the coincidence characterizations in Section 4.4.

### ***4.2.1. Digital Integrating Board***

Two front end readout boards were designed for use with the  $\text{SrI}_2(\text{Eu})$ +SiPM detectors. The first of these was a board that was based on digital charge integration, where charge is integrated digitally to create a pulse as opposed to in analog electronics such as a charge sensitive preamplifier. Though this board was eventually set aside in favor of an analog integration based board, it holds value in the initial characterization of the  $\text{SrI}_2(\text{Eu})$  detectors and as such deserves mention.

#### ***4.2.1.1. Design***

Due to the flexibility offered by digital charge integration, the first readout board for the  $\text{SrI}_2(\text{Eu})$  was designed without charge sensitive preamplification. Other than the minimal charge integration that is inherent to the operation of the SiPMs, there is no analog charge integration that occurs on this board. The PCB was designed in EAGLE. It is a two-layer 35 mm  $\times$  20 mm board with an 8x2 2.54 mm-pitch socket for connecting to the SiPM array, a two-pin header for applying the main voltage, and a MMCX jack for the output signal. The top view of the PCB, as shown in EAGLE, is shown in Fig. 58. The board needs only a single voltage source, somewhere between +3.5 V and +5.5 V. This voltage is converted to about +27.5 V to bias the SiPM array.



The same voltage also used to produce a +3.3 V regulated voltage to power the on-board voltage-sensitive preamplifiers. The circuit was designed using two separate SiPM readouts, one for each 2x2 SiPM array, to lower the overall capacitance and improve the signal-to-noise ratio. The two signals are summed using a low-noise op-amp to produce the output signal (MMCX connector). Though the board was designed for use with the two SiPM array setup used in the  $\text{SrI}_2(\text{Eu})+\text{SiPM}$  detectors, an arbitrary amount of SiPMs (up to 8) can be accommodated.

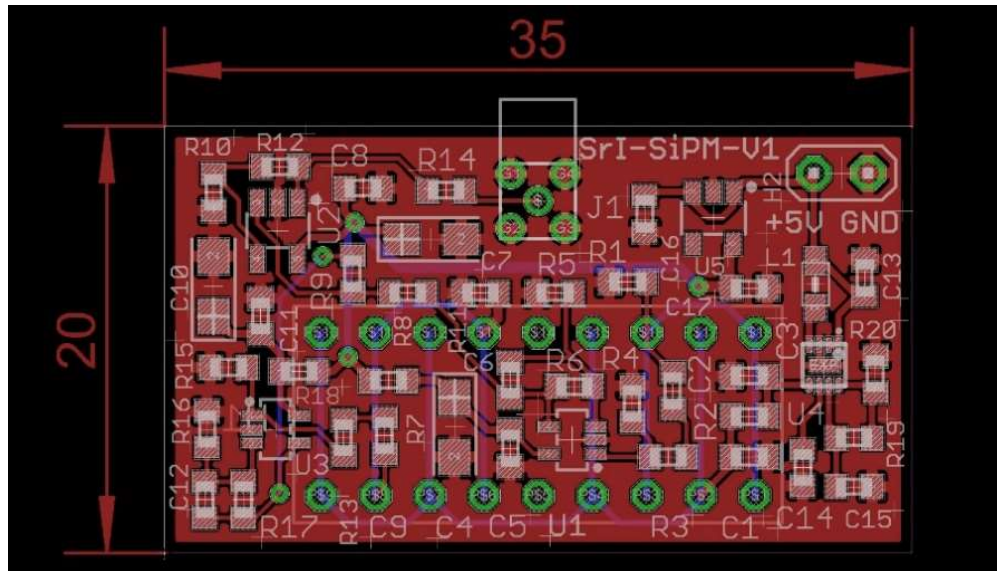


**Fig. 58.** Top view of the front-end readout PCB designed and fabricated for  $\text{SrI}_2(\text{Eu})+\text{SiPM}$  detector

#### 4.2.1.2. *Temperature Study*

Though SiPMs have many advantages over traditional PMTs, one drawback is sensitivity to temperature. In ideal conditions an SiPM runs at a fixed overvoltage, which supplies a fixed gain. However, as temperature shifts so too does the conductivity of silicon, with rising temperatures resulting in higher breakdown voltages. Fluctuations in temperature are thus accompanied by a varying overvoltage, resulting in a varying signal gain and shifting of photopeaks in spectra. If a measurement is taken during a very short period, this shift can be easily corrected for in post processing—however, if the measurement is long, a shifting photopeak will present itself as a poor resolution. The radioxenon detection systems used in the IMS

are expected to take measurements ranging from several hours to days and are likely to experience significant temperature shifts when deployed in the field, and as such this shift is an important factor that must be considered.

As the overvoltage shift in the SiPMs is assumed to be the same for a given model of SiPM regardless of the coupled crystal, the temperature-based photopeak shift was evaluated using a CsI(Tl) crystal coupled to a 2x2 SensL J-Series SiPM array (the same model used for the SrI<sub>2</sub>(Eu) detectors). A fixed biasing voltage was applied to the SiPMs and the detector was brought to various temperatures using an adiabatic temperature chamber. Once the detector reached equilibrium temperature with the chamber, it was exposed to a <sup>137</sup>Cs check source and a spectrum was taken. Spectra were taken at 11 temperatures ranging from 12° C to 32° C, a range that the detector might experience during deployment in the field. The significance of the variation can be seen in Fig. 59, where the collected pulses are reduced to 70% of their initial pulse height when the temperature increases by 20° C.

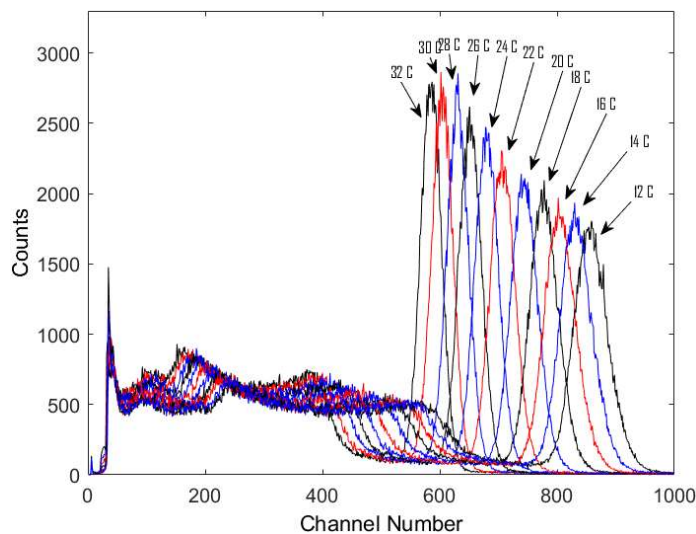


**Fig. 59.** Response of a 2x2 J-Series SiPM array coupled to a CsI(Tl) crystal to <sup>137</sup>Cs at various temperatures with a fixed biasing voltage (~27 V). Higher temperatures result in lower gains due to lower over-voltages

It should be noted that the SrI<sub>2</sub>(Eu)+SiPM detectors are not evaluated in a temperature-controlled setting for the experiments constituting this research. As such

the photopeaks determined from long measurements may suffer from these temperature fluctuations.

#### 4.2.1.3. Initial Characterization of the $\text{SrI}_2(\text{Eu})$ Crystals

$^{137}\text{Cs}$  energy spectra were taken for each  $\text{SrI}_2(\text{Eu})$  using the RX1200 digital pulse processor and the boards discussed above, with the results shown in Fig. 60. No spectral or pulse-shape corrections were applied in the measurements. The energy of each voltage pulse was determined not using digital integration but instead by using a digital trapezoidal filter with 10  $\mu\text{s}$  peaking time implemented in the RX1200 FPGA.

The baselines of the incoming pulses were found to be highly stable over at least several microseconds. These measurements indicated that the pulse heights of detector #010516 (4.4% FWHM), henceforth referred to as the brighter  $\text{SrI}_2(\text{Eu})$ , are  $\sim 30\%$  greater than those collected in detector #010596 (5.1% FWHM), henceforth referred to as the dimmer  $\text{SrI}_2(\text{Eu})$ . Possible causes of this reduced pulse height and reduced photopeak resolution could be attributed to a poorer quality crystal or worse light collection efficiency.

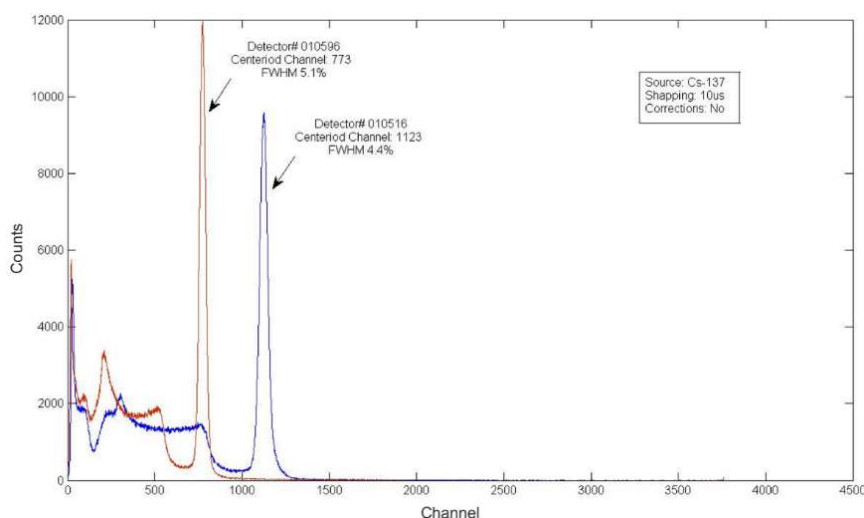


**Fig. 60.**  $^{137}\text{Cs}$  energy spectra collected from the two  $\text{SrI}_2(\text{Eu})$ +SiPM detectors using the RX1200

Unless otherwise mentioned, all subsequent measurements that involve a single  $\text{SrI}_2(\text{Eu})$  use the brighter crystal.

#### 4.2.1.4. *Pulse Shape Investigation*

To inspect the pulse shape, both the preamplifier output and the SiPM output were routed out to an oscilloscope. Using a  $^{137}\text{Cs}$  source with the  $\text{SrI}_2(\text{Eu})$ , the peak of the SiPM pulse was found to be 40 mV and the amplified pulse was about 900 mV. Both pulses had the same rise time of about 2  $\mu\text{s}$ , and a decay constant of  $\tau \approx 7 \mu\text{s}$ . As this decay constant is present in both the amplified and the unamplified pulses, it can be inferred that the  $\text{SrI}_2(\text{Eu}) + \text{SiPM}$  detector time constant is 7  $\mu\text{s}$ . This time constant is longer than the values quoted in the literature; this may be due to variable quantities of  $\text{Eu}^{2+}$  doping and/or due to the use of SiPMs instead of PMTs, which is known to have an effect on output pulse shape [82].

An unexpected “lip,” or a rapid rise and rapid decay on the rising edge of the pulse before the main body of the pulse begins to rise, was observed in the results from  $\text{SrI}_2(\text{Eu})$ . This “lip” can be seen in the pulses shown in Fig. 61. In this example readout at the end of the front end electronics chain (yellow) is compared to readout from a direct wire connection to the output of the SiPMs (blue). The peak of the lip is reached in roughly 80 ns, at which point the signal starts to decay. After decaying for roughly 40 ns, the signal begins to rise again, this time much slower, forming the true  $\text{SrI}_2(\text{Eu})$  signal. The lip feature was not present on all pulses but occurred much more frequently in the case of high energy incident radiation. The feature occurred in both  $\text{SrI}_2(\text{Eu})$  crystals, with both boards, and occurs regardless of position, source, local signal interference (such as nearby cell phones), ambient light, or if an oscilloscope or the DPP8 was used. Digital integration of the lip (as opposed to the full pulse) resulted in a somewhat recognizable spectrum extremely poor energy resolution, indicating some correlation between the net charge in the lip and source energy. The unpredictable nature of this feature does pose a problem for the reliability of timing between the scintillators as well as and optimizing filters to achieve the best energy resolution, and as such should be done away with if at all possible. It is also unknown if, or to what degree, ignoring the lip in post-processing during digital integration would improve or degrade the results.

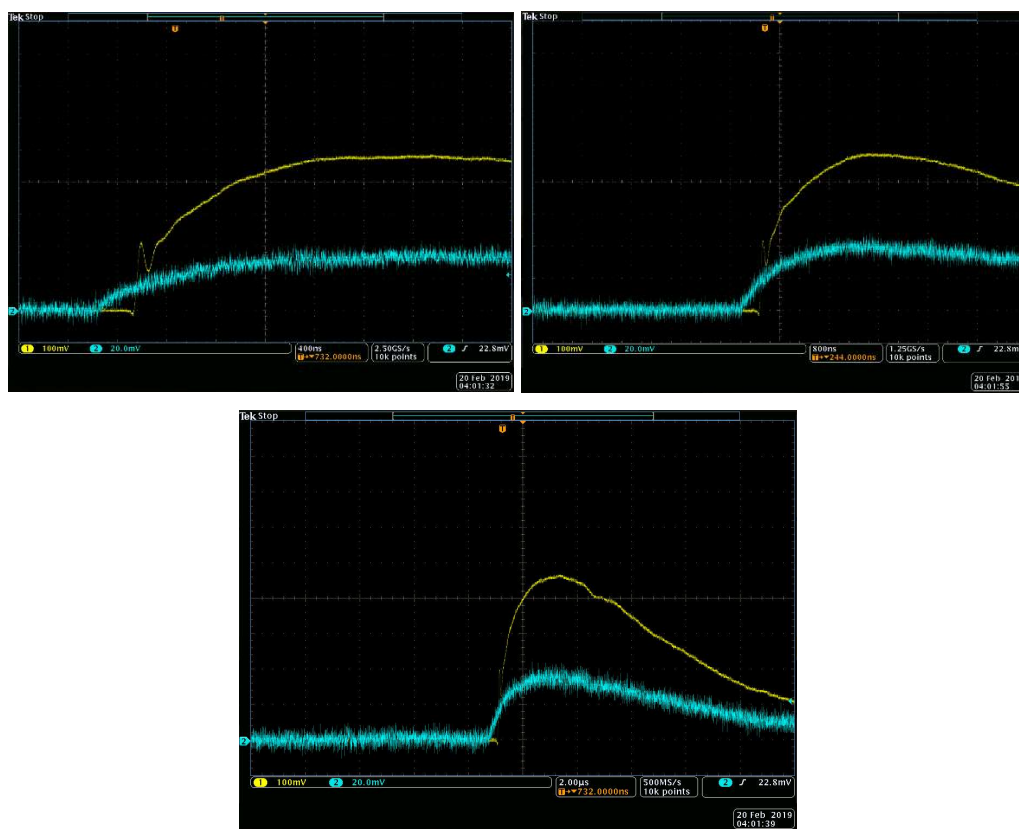


**Fig. 61.** Measurement of  $^{137}\text{Cs}$  using the  $\text{SrI}_2(\text{Eu})$  crystal, showing the fast rise time “lip” from the same event at three different time scales. The yellow signal is sourced from the output of the readout circuit board (post-voltage sensitive preamplifier), while the blue signal is sourced from the output of the SiPMs

Nothing in the literature indicates that this is due to some mechanism in the scintillator.  $\text{SrI}_2(\text{Eu})$  has a single primary decay component [60], with some variations in shape due to reabsorption and reemission by the  $\text{Eu}^{2+}$ . However, the decay and reabsorptions both occur on the order of microseconds; nothing in the literature supports behavior on the order of 80 ns, as is seen here. More likely this is a phenomenon related to the electronics. The lip is in all cases immediately preceded by a small dip in the baseline before rapidly peaking and then just as rapidly dropping and is possibly due to a sort of charge-discharge behavior. It could be caused by circuitry related to the voltage preamplifier, or it could be related to the SiPMs themselves. This feature was observed in simulated and experimental results taken by SensL to characterize the J-Series SiPMs, though a non-disclosure agreement between Oregon State University and SensL regarding these results bars the inclusion

of a pictorial comparison between those results and the results observed here. The agreement does not guarantee that this feature is entirely due to the SiPMs—indeed, it is interesting that this feature does not present itself when examining the direct SiPM signal but only when examining the preamplifier signal. This could be due to the feature being washed out by the poor signal-to-noise ratio of the pure SiPM signal. It is nevertheless unclear if the electronics are the culprits at all: when testing the same circuit with a CsI(Tl) crystal, with the only change being that 4 SiPMs were used instead of 8, the lip was not observed. This experiment cast further uncertainty on the situation. As shall be discussed in subsequent sections, this was one among several reasons why the digital integration board was eventually set aside in favor of the CSP-based boards.

#### *4.2.1.5. Digital Integration Methodology*

No trapezoidal filter was used when investigating the efficacy of digital integration. Instead, the magnitude of each sample in the pulse was strictly summed over a certain range of samples. The digital integration was conducted in MATLAB. The peak of the resulting integrated pulse shape was used to determine the total energy deposited during an event. In the current design the maximum length of the pulse that the DPP8 can output is 4096 samples, or  $\sim 32.8 \mu\text{s}$ . Due to the long decay constant of  $\text{SrI}_2(\text{Eu})$  of 1-5  $\mu\text{s}$ , it was hypothesized and later confirmed via experimentation that integrating over long times, on the order of 17-25  $\mu\text{s}$ , results in the best resolutions. Pulses from low energy radiation, such as 31 keV X-rays, settle at negligibly close to the baselines much earlier (on the order of 10-15  $\mu\text{s}$ ), but due to the stability of the baseline integrating over long times was found to not be significantly determinantal to resolutions of these lower energy photons.

#### *4.2.1.6. Positional Dependence and $^{137}\text{Cs}$ Spectrum*

Positional dependency is a very serious concern for the PIPS- $\text{SrI}_2(\text{Eu})$  detector; as a radioxenon source injected into the PIPSBox would be effectively distributed across the entire surface of the  $\text{SrI}_2(\text{Eu})$  crystal, finding that the detector observed significant depth dependence would be a grave setback. Interactions that occur near the light

collection device will often create photons that must traverse the entire length of the scintillator twice, allowing more opportunities for self-absorption. It has been shown in literature that the self-absorption and subsequent reemission of light photons by  $\text{Eu}^{2+}$  can in large crystals result in incomplete charge integration even when using long integration times [59].

To test for this a  $^{137}\text{Cs}$  source, collimated using 2" thick lead bricks with a 2 mm gap in between, was placed in 9 positions about the crystal, starting from position 1 at the top of the detector (closest to the SiPMs) and processing by increments of  $\pi/8$  to position 9 at the bottom of the detector (furthest from the SiPMs). At each position, 250,000 counts were taken, and energies were determined using an integration window of 24  $\mu\text{s}$ . It was discovered that angular position of the  $^{137}\text{Cs}$  was not at all significantly correlated to the position of the photopeak, though it was significantly correlated with energy resolution. As the source was moved towards the far end of the crystal (away from the SiPMs) the resolution in general tended to improve. This is no doubt due to the self-absorption, albeit not as extreme as described in literature due to the comparatively small size of this crystal. Most gamma interactions occur shortly after the radiation enters the medium, and many of the scintillation light photons generated in an interaction close to the SiPMs must transverse the entire length of the crystal before being reflected and collected by the SiPM. During this travel the scintillation photon has some chance of being reabsorbed and re-emitted, reducing the chance that it will fall into the integration window and reducing the overall resolution of the photopeak. The resolution in relation to angle is shown in Fig. 62a. The best resolution obtained in these measurements was  $\sim 3.55\%$  FWHM, with the spectrum shown in Fig. 62b.

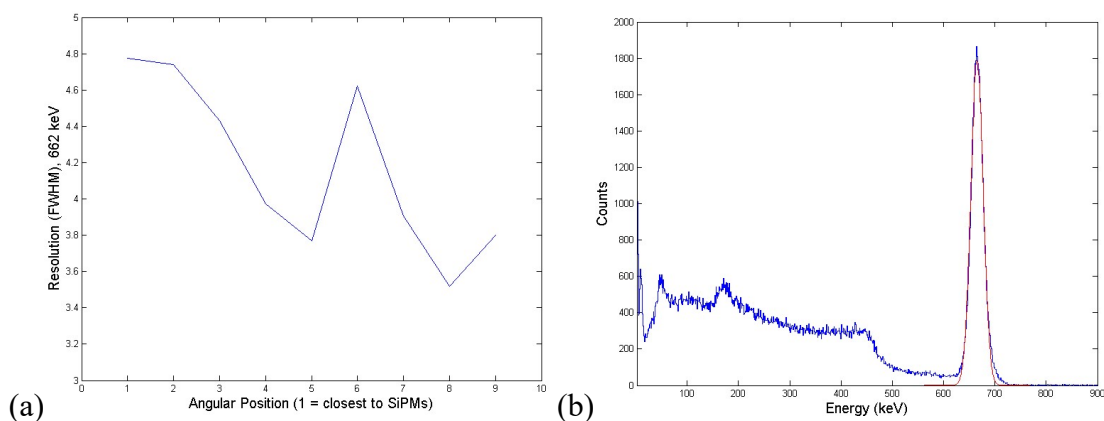


**Fig. 62.** (a) Angular dependence of energy resolution for 662 keV in the  $\text{SrI}_2(\text{Eu})$  detector. A general trend of improving resolution as the source moves further from the SiPMs can be seen. The cause of the large increase in FWHM at position 6 is unclear, but might be a statistical aberration; (b) Spectrum of  $^{137}\text{Cs}$  taken at position 8 (furthest from the SiPMs)


A very important element of the  $^{137}\text{Cs}$  spectrum is absent in both Fig. 60 and Fig. 62b: the 31 keV photopeak from X-rays. This peak is absolutely critical in radioxenon detection, as three of the four radioxenon isotopes of interest are wholly or partially dependent on it for identification. Various approaches were taken to detect the 31 keV X-rays, including changes to the parameters of the trigger module, adjusting the amplitude identification, modifying the values of the passive circuit components on the signal processing board, and drawing the signal from different parts of the processing chain (including directly from the SiPMs themselves sans amplification). None of these methods resulted in a discernable X-ray peak. The baseline in the  $\text{SrI}_2(\text{Eu})$  was largely flat (Fig. 61), so noisiness was not likely the reason for this lack of photopeak and thus further efforts to reduce noise were likely to be ineffective. Instead the photon spectrum was found to be decidedly nonlinear, with low energy signatures appearing at lower energies in the gamma spectrum than expected. This caused the X-ray signatures to blend with noise to the point where they were indistinguishable. This non-linearity was first verified using two features in the Compton continuum of  $^{137}\text{Cs}$ , as shown in Fig. 62b: the Compton edge ( $\sim 478$  keV) and the photon recoil energy from Compton backscatter ( $\sim 184$  keV). Both of these features are located at the appropriate energies in the spectrum. However, the lead excitation X-ray peak, expected to be at  $\sim 75$  keV, is roughly 20 keV lower than



expected, at 55 keV. This indicates that above  $\sim 184$  keV (and possibly lower) the  $\text{SrI}_2(\text{Eu})$  detectors using the digital integrating board function linearly, but below this energy nonlinearity begins to present itself.

This nonlinearity was reverified using an  $^{241}\text{Am}$  variable X-ray source, seen in Fig. 63. At first the Tb foil was used: the peak from the  $\sim 46$ -50 keV Tb X-rays could be seen, but it was inseparable from the 59 keV photon emitted from the decay of  $^{241}\text{Am}$ . Moreover, the X-rays were located at roughly 20 keV in the spectrum. Ba, with X-rays at the 32-36 keV range, could only be seen blending into the noise peak (which occurred around 14 keV in the spectrum). This was the case no matter what hardware, software, or firmware adjustments were attempted.

Target	Energy (keV)		Photon Yield
Selected	K_alpha	K_beta	(#/sec/steradian)
Cu	8.04	8.91	2,500
Rb	13.37	14.97	8,800
Mo	17.44	19.63	24,000
Ag	22.10	24.99	38,000
Ba	32.06	36.55	46,000
Tb	44.23	50.65	76,000



**Fig. 63.** The  $^{241}\text{Am}$  variable X-ray source, with X-rays emitted from 6 foils at energies given in the adjacent table

#### 4.2.2. Analog Integrating Board

The importance of observing 31 keV X-rays demanded that an alternative approach to the digital integration board be taken. Before directly modifying the board to pursue digital integration methods further, it was decided that analog integration methods should be investigated. The CR-113 charge sensitive preamplifier, designed by Cremat Inc. [199], was selected for the task. These preamplifiers comply with the compact design paradigm of the  $\text{SrI}_2(\text{Eu})$ : they are roughly 1 square inch in area, and on the order of a few of millimeters thick. These Cremat preamplifiers have

a 50  $\mu$ s time constant, which was believed to be adequate to capture the full pulse shape of the  $\text{SrI}_2(\text{Eu})$ .

For preliminary evaluation a test board provided by Cremat Inc. was used. Signal was drawn from the SiPMs using the digital integration test board, but with the SiPM anode signal routed directly to the output. The SiPMs were biased differently than those typically used with the board, and the board was slightly modified to suit our detector and biasing setup. Due to the inherent gain provided by the SiPM arrays and the high gain provided by the preamplifier, a voltage divider was added at the output to avoid signal clipping from large signals exceeding the dynamic range of the evaluation equipment. The board and preamplifier are shown in Fig. 64. The system was initially tested using  $^{137}\text{Cs}$ , and a representative pulse taken from this experiment is shown in Fig. 65 at various time scales.

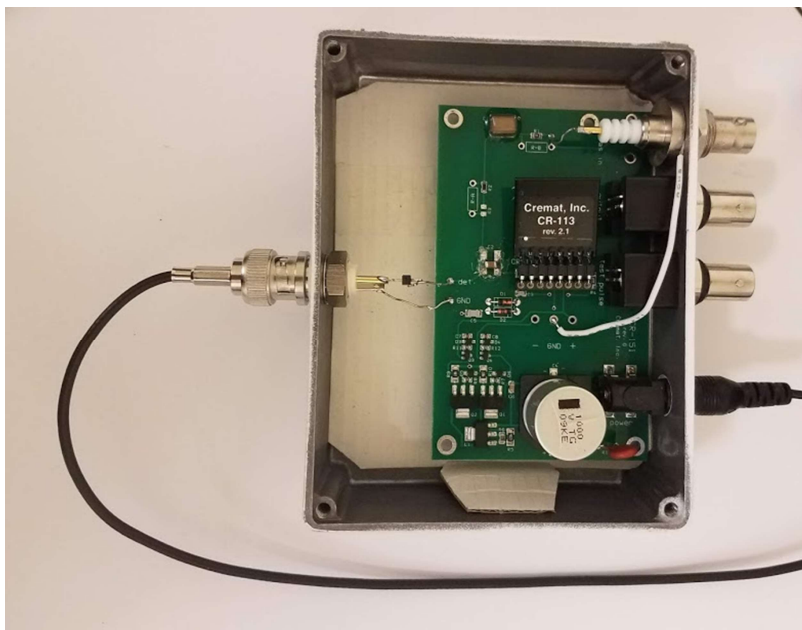


**Fig. 64.** The Cremat charge sensitive preamplifier mounted on the test board (detector not pictured)

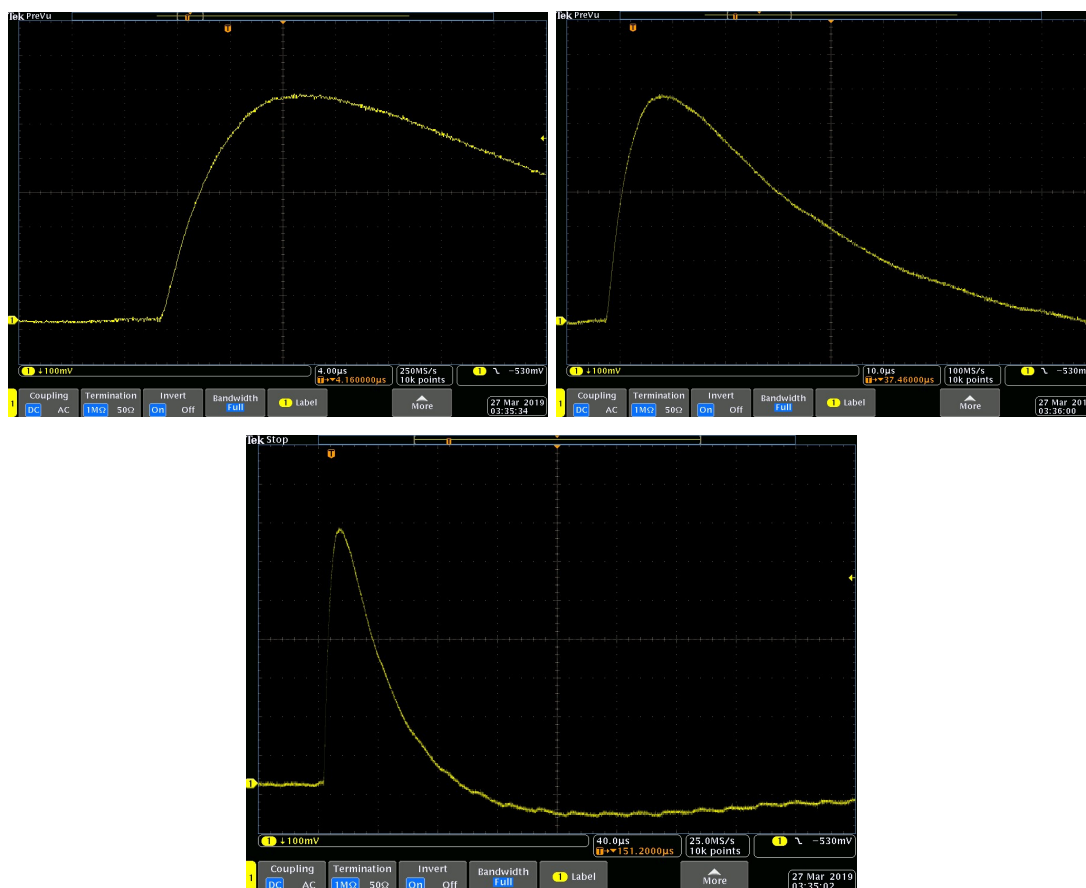


**Fig. 65.** A single pulse from  $^{137}\text{Cs}$  taken from the  $\text{SrI}_2(\text{Eu})$  detector using the Cremat preamplifier and test board. All three images show the same pulse at different time scales

Immediately apparent when comparing the pulses in Fig. 65 to those in Fig. 61 is the much longer time constant when using the Cremat preamplifier and test board. This lengthy time constant might be significant in high count-rate situations but is particularly well suited for the detection of radioxenon with the  $\text{SrI}_2(\text{Eu})$  due to low count rates, somewhat unpredictable pulse shapes (due to trapping), and long detector time constants of  $\tau \approx 7 \mu\text{s}$ . Also noteworthy is the undershoot—this is an unavoidable consequence of the preamplifier being AC coupled to the detector. DC coupling could serve as a potential alternative to eliminate this undershoot, but this has been discouraged by the preamplifier manufacturer. Furthermore, because the count rates in atmospheric radioxenon detection tend to be low the undershoot is likely inconsequential. The lip as observed in Fig. 61 is also completely absent in these

measurements. There is a small oscillation on the baseline of the pulse, caused by the inductor used in the LT8410 switching regulator used in the digital integration board to supply bias to the SiPMs. As the alternative to a switching regulator would be either a dedicated separate power supply (introducing potential ground loop issues) or a linear regulator (bulky and heat-intensive), the oscillation from this regulator is unavoidable in virtually all possible board designs. This oscillation was muted in the original measurements with the digital integration board due to the comparatively small gain provided by the voltage sensitive preamplifiers.

The trigger and MATLAB filter parameters were optimized using  $^{137}\text{Cs}$  to judge the improvement that the basic test board setup provided over the original digital integration board. For the trigger, a triangular filter with a  $2.4\ \mu\text{s}$  peaking time resulted in the lowest energy threshold. Using this, it was possible to see the X-rays emitted by  $^{137}\text{Cs}$ . The capability to measure low energy X-rays was verified using both the Mo foil and the Ag foil in the  $^{241}\text{Am}$  source, and it was determined that photons could be resolved against noise at a threshold of 17-19 keV. This noise threshold was later further reduced to 13 keV during radioxenon measurements. For the MATLAB trapezoidal filter, a flat top time of  $10\ \mu\text{s}$  (to match with the  $\sim 10\ \mu\text{s}$  rise time of the pulses) and peaking time of  $8.8\ \mu\text{s}$  (chosen to account for the majority of the highest part of the 662 keV pulse shape) were used. These values produced the best energy resolutions for 662 keV and 31 keV, with a resolution of 4.2% and 28.4% respectively. A peak detection method without any sort of digital filter was also investigated—however, the results were significantly poorer than those results obtained when using a filter, on the order of several percent for 662 keV and nearly 50% FWHM for 31 keV. As such, this approach was rejected in favor of the filter-based approach. Though the 662 keV resolution was not quite as high as that measured with the custom board, it is far outweighed by the fact that it was possible to set the noise threshold such that the  $\sim 31\ \text{keV}$  X-rays of interest could be observed. The preamplifier is linear, with key features (662 keV, 31 keV, the Compton edge, etc.) at the expected energies when using a linear calibration. The spectrum taken

from the  $^{137}\text{Cs}$  measurement, with fits, is shown in Fig. 66, and results from the Mo and Ag foil measurements are shown in Fig. 67.

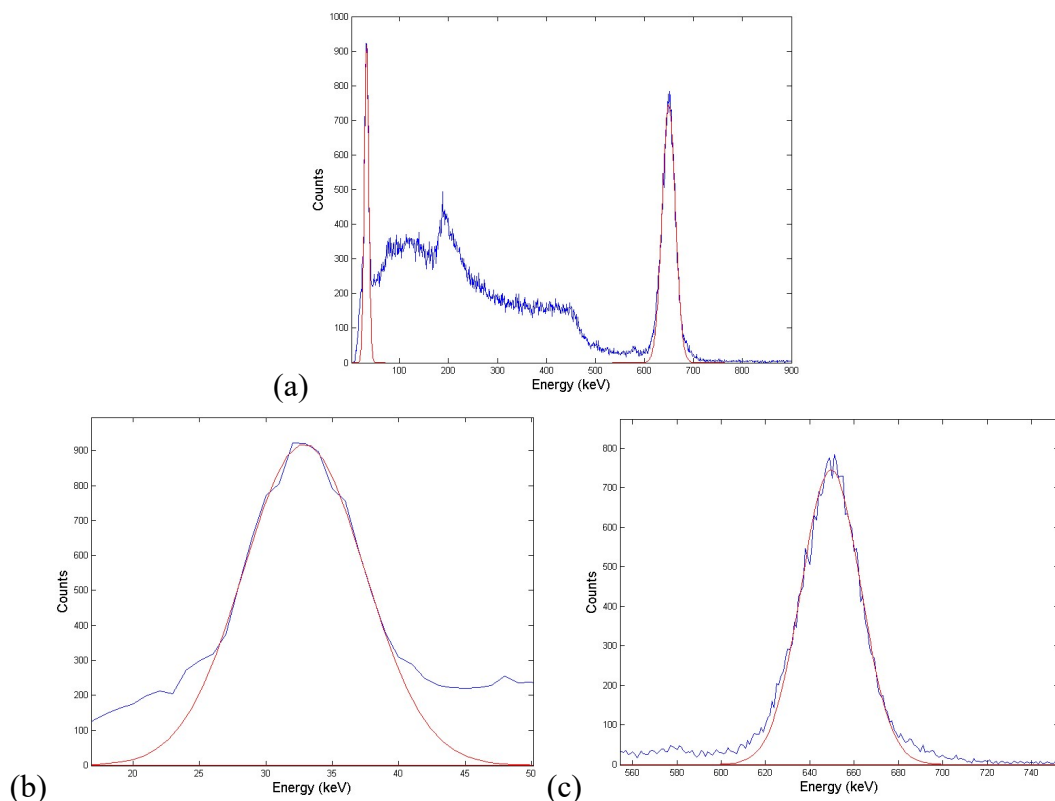


**Fig. 66.**  $^{135}\text{Xe}$  as measured by the  $\text{SrI}_2(\text{Eu})$  with the Cremat preamplifier and test board. (a) shows the full spectrum, while (b) and (c) show the 31 keV and 662 keV photopeaks, respectively. Note the very slight tailing effect in the 662 keV photopeak

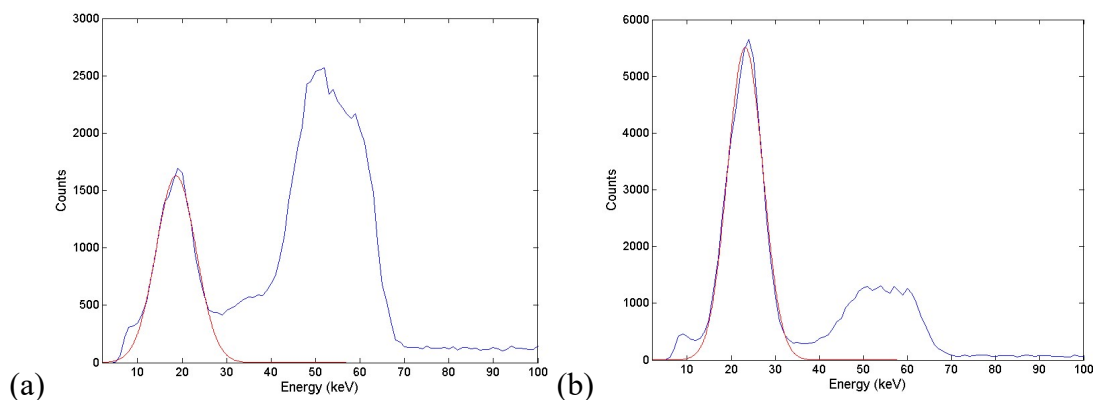


**Fig. 67.** Results from the (a) Mo and (b) Ag foil from the  $^{241}\text{Am}$  source. The resolutions were 49% and 35% FWHM, respectively. Note the symmetry of the photopeaks

There was a very slight degree of low energy tailing at the 662 keV peak that was not possible to eliminate through varying the MATLAB filter. This tail did not perceptibly occur in the 31 keV peak, nor was it seen in the X-rays emitted from the Mo and Ag foils. This is possibly due to the self-absorption discussed previously: the sources were placed at the bottom of the crystal, so only the higher energy photons would be able to pass through the scintillator far enough for trapping to become significant.

#### 4.2.2.1. *Preamplifier Board Design*

Due to the relatively large size of the Cremat characterization board, the circuit was adapted from the test board onto a new custom SiPM readout board. In keeping with this compact design philosophy, this version board is  $40 \times 35 \text{ mm}^2$  in size. The anode signal from the 8 SiPM pins are summed in parallel and routed to the input of the Cremat preamplifier, the output of which can then be read out to the DPP8 via MMCX. All the components on the board are powered by a single supply (originally +12 V, later +5 V) sourced from the multi-purpose power supply shown in Fig. 47. This voltage is stepped up to +27.5 V using a LT8410 switching regulator to bias the SiPMs. A location is dedicated on the board for a temperature sensitive microcontroller which, when populated, allows for automatic adjustment of the overvoltage to provide a stable SiPM gain; however, it should be noted that this location was left unpopulated during the characterization studies presented here and as such the temperature stabilization capabilities of the board have not been explored. An LED is used to indicate the operational state of the detector. The preamplifier is plugged into 8 right-angle sockets, such that it is held above and nearly parallel to the main circuitry plane of the board. The board can be seen in Fig. 68. As this board was modelled from the circuit employed in the Cremat characterization board, no lip was present in any measurements taken with these boards.



**Fig. 68.** The analog integrating preamplifier board. Right angle sockets hold the CR-113 charge sensitive preamplifier slightly above, and parallel to, the main circuitry of the board, allowing for an unobtrusive design. The board interfaces directly with the SiPM readout of the  $\text{SrI}_2(\text{Eu})$  detectors.

#### 4.2.2.2. *Pulse Shape and Oscillations*

Of immediate concern was the continued presence of the oscillations in the amplified output signals from the board, which can be seen in Fig. 69a. When powering the board with a +12 V voltage the amplitude of the oscillations could be quite large, particularly when dealing with low energy pulses: in the case of measuring 31 keV X-rays, the oscillations were on the order of a third to a half the base to peak height of the pulses. This can have a significant impact on pulse height determination and increase trigger walking.

The oscillations observed when using the Cremat test board were caused by the switching regulator used in the design, and it was this same cause that produced the oscillation in the revised board. This conclusion is reinforced by the data sheet LT8410, which indicates oscillation at a fixed period at a given current load [205]. The frequency of the oscillations observed in the output signal from the revised board was between that found in a “no load” and a “0.5 mA load” cases reported in the LT8410 data sheet. In Fig. 69 these cases are compared to a 31 keV X-ray pulse taken with the  $\text{SrI}_2(\text{Eu}) + \text{SiPMs}$  detector using the revised board.

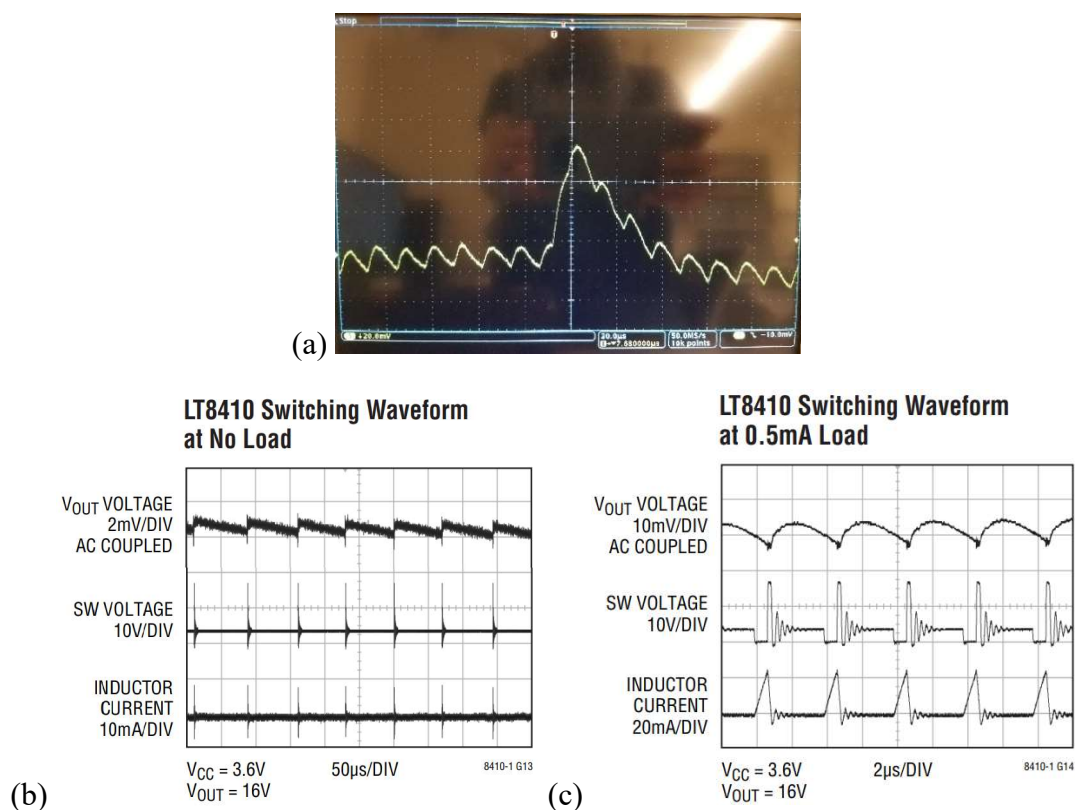


**Fig. 69.** (a) Oscillatory behavior due to the switching regulator, as seen riding on a 31 keV pulse; (b, c) plots of the performance of the LT8410 switching regulator [205], causing ripple very similar to those observed in this signal

The amplitude and period of the oscillations were found to have a positive linear correlation with the voltage applied to the board. A +6 V minimum power supply voltage was recommended in the Cremat application guide [199], but no +6 V power supply was readily available in the combined power supply. To test to see if this recommendation was a hard minimum, a separate linear voltage power supply was used to apply +4-13 V to the board while observing the output pulse shapes. These experiments indicated that +5 V, one of the voltages readily available in the combined power supply, was an adequate voltage to produce the expected gain while minimizing the oscillations.

The impact of oscillations can be mitigated to some degree by clever selection of amplitude filters. When using a +5 V voltage supply, oscillations were observed with a period of  $\sim 4.8 \mu$ s. To reduce the impact of the oscillations, parameters of the trapezoidal amplitude identification filter were set to closely agree with this period.



The peaking time of the trapezoidal filter was set to 4.8  $\mu\text{s}$ , and the flat top time, chosen to be as close to the  $\sim 11$   $\mu\text{s}$  average rise time of the pulses while still being some multiple of the oscillation period, was set to 9.6  $\mu\text{s}$ .

### ***4.2.3. CSP Time Constant Comparison***

If the time constant of the charge integration approach is too short, the reabsorption/reemission behavior of the  $\text{SrI}_2(\text{Eu})$  material can have a detrimental effect on the energy resolution. The Cremat preamplifiers in the studies up to this point had an RC time constant of 50  $\mu\text{s}$ , and it was of interest if the energy resolution of the detector could be further improved if a longer RC constant was used to do the charge integration. A custom Cremat preamplifier with an RC time constant of 100  $\mu\text{s}$  was procured to compare against the 50  $\mu\text{s}$  preamplifier. A  $^{137}\text{Cs}$  source was chosen for the comparison study.

#### ***4.2.3.1. Comparison Using Digital Equipment***

Tests were conducted for both the brighter and the dimmer  $\text{SrI}_2(\text{Eu})$  across various peaking time and flat top time settings for the trapezoidal peak filter. The dimmer  $\text{SrI}_2(\text{Eu})$  achieved a better 662 keV gamma ray resolution, while the brighter  $\text{SrI}_2(\text{Eu})$  achieved a better 31 keV X-ray resolution. One possible reason for the non-uniform trend in resolution is that the larger amplitude of the 662 keV pulses in the brighter crystal results in a greater slope on the leading edge in order to reach the peak in the same rise time ( $\sim 10$   $\mu\text{s}$ ). This could result in more variability in the brighter crystal over the samples of the trapezoidal filter peaking time range, which could in turn result in more variation in the final results of the brighter crystal. The reason why the brighter crystal would have a better resolution for the lower energy signals is that the oscillations due to the switching regulator are relatively more pronounced compared to peak amplitude for the dimmer crystal, resulting in a higher variability in the results for the dimmer crystals.

In Fig. 70, the product of the average 662 keV and 31 keV resolutions across all pkts at a given fit (left column) and across all fits at a given pkt (right column) are

given for both preamplifiers for brighter  $\text{SrI}_2(\text{Eu})$  (top row) and dimmer (bottom row). It is clear in both cases from the values shown on the y-axis that the difference across the peaking times and flat top time selection is very small, on the order of tenths to hundredths of a percent. This difference could quite easily be attributed to varying the Gaussian fitting parameters used to determine the photopeak resolutions. In lieu of the minimal variability of these results, the logic noted in the previous section guided the decision to maintain a peaking time of 4.8  $\mu\text{s}$  and a flat top time 9.6  $\mu\text{s}$ .

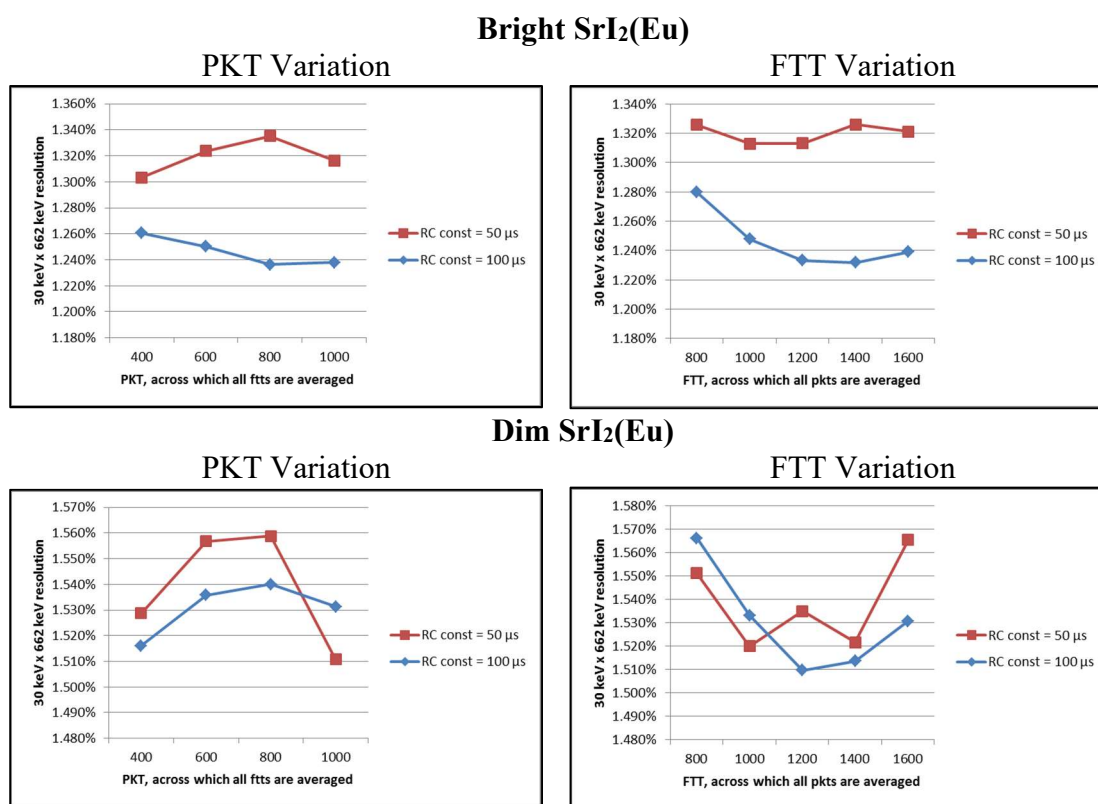


**Fig. 70.** A comparison of the two Cremat boards in terms of impact of resolution of the 31 keV and 662 keV photons across various peaking times and flat top times (1 sample = 8 ns). The resolutions of the two photopeaks, in terms of % FWHM, are multiplied together to give a “squared” FWHM resolution. Note the small range of the y-axes in all plots

It was difficult to get a consistent dataset across both crystals to conduct this comparison, as during the data acquisition the Willamette valley was experiencing an intense heat wave. As the day progressed the temperature fluctuations could have affected the SiPMs, which could in turn cause photopeak drifting and result in small

resolution fluctuations that make the sets of measurements difficult to compare. The brighter crystal experiments were taken on subsequent days, with the  $\tau = 50 \mu\text{s}$  data taken on a significantly hotter day than the  $\tau = 100 \mu\text{s}$  preamp. As the performance of SiPMs is dependent on the overvoltage, which is in turn dependent on temperature, it is not surprising that the  $50 \mu\text{s}$  preamplifier would perform worse. The dimmer crystal experiments were taken much closer together in time, and so are more representative of true difference in performance between the two preamplifiers. In this case, the results between the two preamplifiers are nearly the same. From this, it can be concluded that the impact of the reabsorption/reemission in the  $\text{SrI}_2(\text{Eu})$  crystals is not enough to see a significant improvement in results when using preamplifier with a decay time longer than  $50 \mu\text{s}$ . In the interest of insuring against higher count rates during the characterization procedure, where the long tail from the preamplifier would become significant, the  $50 \mu\text{s}$  decay time preamplifier was chosen for continued use.

Optimum results, taken using the settings at the minimum points in each of the plots above, the best resolutions are given in Table 6. This table is illustrative of the nearly negligible difference between the two amplifiers and should not be interpreted as indicative of the possible results from the system; better results were obtained for both photopeaks when experiments were conducted in more stable weather, where photopeak drifting was reduced. It must again be noted that this photopeak drifting should be minimized via the SiPM gain stabilization offered by the placing of the temperature-sensitive microcontroller on the preamplifier board, which was not placed during these tests.

**Table 6.** Best resolutions achieved with each of the  $\text{SrI}_2(\text{Eu})$  crystals using digital pulse processing. Preamplifiers with  $\tau = 50 \mu\text{s}$  and  $\tau = 100 \mu\text{s}$  were evaluated

Detector	$\text{SrI}_2(\text{Eu})\_1$	$\text{SrI}_2(\text{Eu})\_2$
30 keV, ( $\tau = 50 \mu\text{s}$ )	22.66%	29.08%
30 keV, ( $\tau = 100 \mu\text{s}$ )	22.54%	29.22%
662 keV, ( $\tau = 50 \mu\text{s}$ )	5.61%	5.04%
662 keV, ( $\tau = 100 \mu\text{s}$ )	5.46%	5.04%

#### 4.2.3.2. Comparison Using Analog Equipment

The various benefits offered by digital pulse processing (flexibility, simple data processing and recording, compact, cost) motivated the use of digital equipment for the characterization of the detection system thus far. To verify the correctness of the digital approach, as well as to ascertain that no significant performance loss would be introduced through use of digital pulse processing as opposed to traditional analog processing, it was prudent to evaluate the detection system using these traditional analog systems.

This evaluation was done under the context of comparing the  $50 \mu\text{s}$  and the  $100 \mu\text{s}$  preamplifiers with respect to energy resolution of the 31 keV and 662 keV photopeaks from  $^{137}\text{Cs}$  using the brighter  $\text{SrI}_2(\text{Eu})$  crystal. An analog shaping amplifier and MCA in a NIM bin were used to acquire spectra. The multi-purpose power supply was used to power the preamplification boards and bias the SiPMs, and the grounds of the NIM bin and the power supply were connected through the aluminum housing of the detector. The results of these experiments for both preamplifiers, using various amplifier shaping times, are given in Fig. 71. The optimal results obtained using these analog procedures are essentially the same as those obtained using digital analysis. This not only validates the correctness of the results obtained via the digital approach, but also shows that the use of a shaping amplifier is unnecessary to achieve optimal performance.

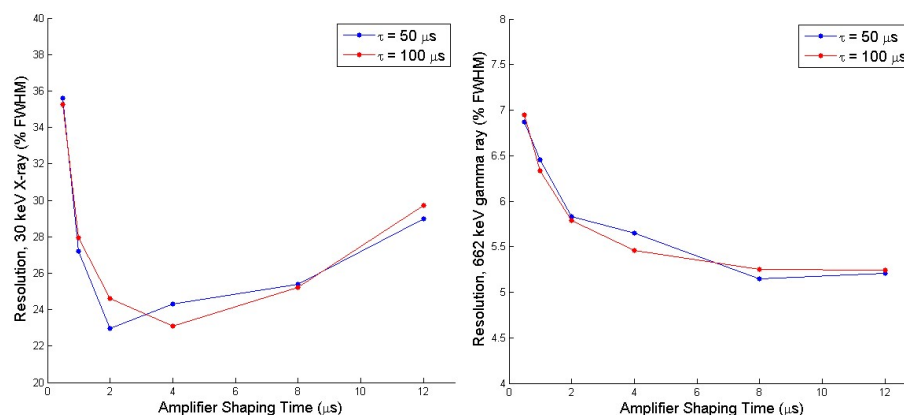


**Fig. 71.** Resolution for the 31 keV and 662 keV photopeak from  $^{137}\text{Cs}$  determined using an analog amplification circuit with shaping times of 0.5, 1, 2, 4, 8, and 12  $\mu\text{s}$

#### 4.2.4. Coincidence Timing Analysis

The behavior of the  $\text{SrI}_2(\text{Eu})$  detectors for measuring coincidences was of key concern. The two scintillators were placed in the holder without the PIPSBox in place, and a  $^{137}\text{Cs}$  source was placed in between the scintillators. A coincidence timing window of 1  $\mu\text{s}$  was used. The results of this measurement are shown in Fig. 72.

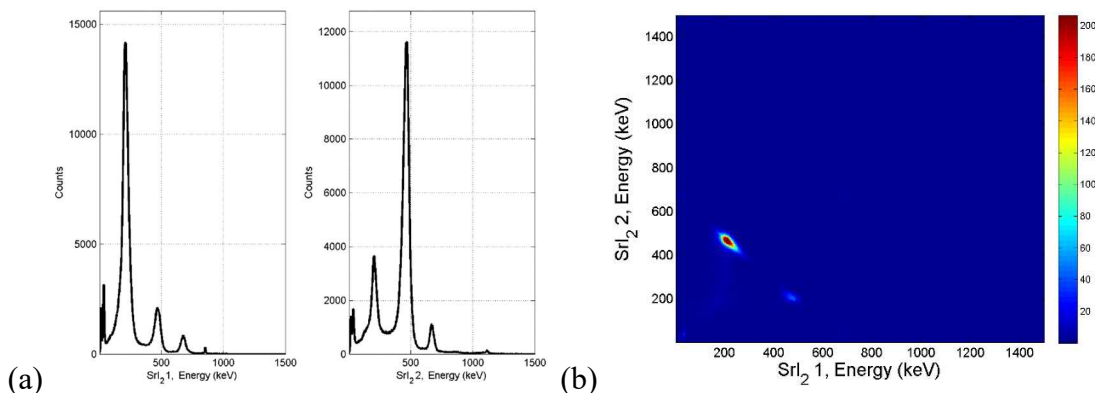


**Fig. 72.** (left) the output of each individual  $\text{SrI}_2(\text{Eu})$  crystal when run in coincidence mode measuring  $^{137}\text{Cs}$ ; (right) 2D coincidence histogram of the data.  $\text{SrI}_2(\text{Eu})_1$  is the brighter crystal, and  $\text{SrI}_2(\text{Eu})_2$  is the dimmer. Note the predominance of high-energy triggers in the dimmer crystal

The Compton backscatter line seen here does indicate expected behavior for a working coincidence module. That the line is clearly dominated by the two points at the extreme ends of the  $^{137}\text{Cs}$  is typical, but the fact that one region has strong dominance over the other is not. The dimmer  $\text{SrI}_2(\text{Eu})$  crystal consistently had a

larger incidence of interactions at the high-energy end of the Compton spectrum, while the brighter  $\text{SrI}_2(\text{Eu})$  has a correspondingly higher incidence of lower-energy triggers. This impact occurred regardless of which scintillator was connected to which channel, if the preamplifier units or readout boards were switched, if the crystal positions within the experimental setup were exchanged, etc. The only things that did cause the regions to become more normalized is by either reduction of trigger threshold on the dimmer crystal or by increasing the coincidence timing window.

The most likely cause of this issue is the failure of the dimmer crystal to reliably trigger in coincidence with the brighter crystal unless it had a larger leading edge slope. The brighter crystal triggers in coincidence every time it experiences either a low-energy or high-energy Compton interaction, due to having a larger peak brightness and thus a larger  $dV/dt$  (where  $V$  is voltage) on the rising edge than the dimmer crystal. The dimmer  $\text{SrI}_2(\text{Eu})$  on the other hand triggers in coincidence for most/all high-energy depositions but only sometimes triggers from lower-energy depositions, due to the smaller  $dV/dt$  requiring a larger time to trigger. This results in missing many coincidence events and is an example of trigger walking. To fully remove any concerns of these spectral features, the coincidence timing window was increased to  $4.4\ \mu\text{s}$  for all subsequent coincidence measurements.

### **4.3. PIPSBox Characterization**

As in the case of the  $\text{SrI}_2(\text{Eu})+\text{SiPM}$  detectors, discussion of the PIPSBox in this section will be dedicated to characterizing the PIPSBox without consideration of the  $\text{SrI}_2(\text{Eu})+\text{SiPM}$  detectors or radioxenon.

#### ***4.3.1. Preamplifier and Noise Threshold***

As noted in Section 2.2.2.3, initial work done at Oregon State University involving the PIPSBox necessitated a high noise threshold due to an unstable baseline. The custom PIPSBox preamplifier made by Canberra and the multi-purpose power supply were expected to largely rectify this problem. A representative pulse from the PIPSBox preamplifier when exposed to an electron source is shown in Fig. 73.

Despite the new specialized preamplifier, it is clear that the PIPSBox signal is quite noisy. Though the impact of this noisiness on triggering and on amplitude determination can largely be mitigated through triangular and trapezoidal filtering, it can still be detrimental to timing performance. In particular, the high signal noise in the PIPSBox makes direct implementation of a constant fraction discrimination-based coincidence triggering mechanism impossible.

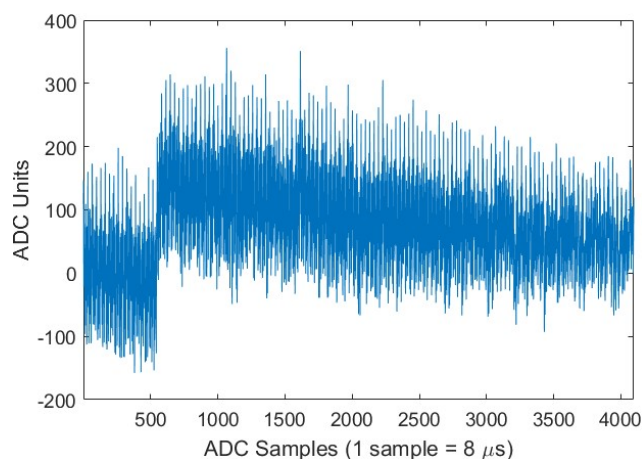


**Fig. 73.** A pulse from one of the PIPSBox channels as triggered by an electron

It was found that the stability of the baseline was significantly improved using the preamplifier when compared to when used with the AMPTEK A250F/NF, though some periodic baseline oscillations can still be seen in the PIPSBox signal that are believed to be the manifestation of a ground loop. The common ground of the power supply makes the power supply itself an unlikely culprit for this ground loop, which means that they can likely be attributed to the unknown internals of the preamplifier. Regardless of origin, these oscillations were of such a frequency that they could be well-mitigated through the use of a triangular trigger filter in the FPGA.

Before any characterizations were done, it was necessary to confirm that the preamplifier could be used in coincidence measurements.  $^{90}\text{Sr}$  decays into  $^{90}\text{Y}$ , which subsequently releases a beta with an endpoint energy of 2.28 MeV. This high energy electron is enough to penetrate the carbon window and trigger both silicon detectors in the PIPSBox, and so was chosen for this test. The PIPSBox was placed flat on the surface of a table on top of a stack of papers for additional electronic and vibrational

isolation, and the  $^{90}\text{Sr}$  source was placed in the center of the carbon window. The simultaneous triggering of the two channels was verified using a two-channel oscilloscope, demonstrating that the PIPS preamplifier could be used for coincidence measurements.

After the detector and preamplifier was confirmed to be in working order, the two most important things to investigate were the noise threshold when using the preamplifier and the resolution of peaks. Because of the carbon window, it is impossible to observe well-resolved low energy monoenergetic electron signatures (of particular interest due to the monoenergetic electron emissions of  $^{131\text{m}}\text{Xe}$  and  $^{133\text{m}}\text{Xe}$ ) in the PIPSBox without injecting a gaseous sample into the detector. As these initial studies were done before the irradiation of xenon, the only options readily available were to use high energy electron sources and low energy X-ray sources. The  $^{90}\text{Sr}$  source was useless for determining resolution due to the continuous nature of the energy of the beta emissions, and due to the electron inability to penetrate the carbon window at low energies any external electron sources would prove to be useless as well. Instead, a  $^{137}\text{Cs}$  and a  $^{109}\text{Cd}$  source were used for the  $\sim 31$  keV X-ray emitted by  $^{137}\text{Cs}$  and 22 keV X-ray emitted by  $^{109}\text{Cd}$ . These energies were enough to penetrate the carbon window and have an appreciable chance of depositing their energy in one of the silicon detectors. These sources were sufficient to roughly calibrate the PIPSBox, which was then further refined upon injection of the radioxenon isotopes.

The  $^{137}\text{Cs}$  source was investigated first, using various peaking times and flat top times for the peak detecting trapezoidal filter. The experimental configuration was the same as that used for the  $^{90}\text{Sr}$  evaluation. Fig. 74 shows the 31 keV peak from  $^{137}\text{Cs}$  well separated from the noise threshold using several different flat top times and a fixed peaking time of 400 samples (3.2  $\mu\text{s}$ ). It was determined from this test that, so long as a peaking time reasonably near this length is used, a very small flat top time (0-200 ns) should be used for the best resolution. Having little-to-no flat top time produces separation between the 31 keV X-ray signature and noise such that they are distinct peaks. This is somewhat counterintuitive—typically some flat top in the trapezoidal filter will produce the best results, as the flat top time is meant to account



for the rise time of the pulse. One possibility for this is that the beginning (rising edge and region about the peak) of the pulses may be the most consistent part of the pulse shape from pulse to pulse, and that by neglecting that part using a large flat top more variation is introduced into the amplitude evaluation. The best FWHM resolution achievable for the X-rays were  $\sim 31\%$  in  $\text{Si}_1$  and  $\sim 32\%$  in  $\text{Si}_2$ .

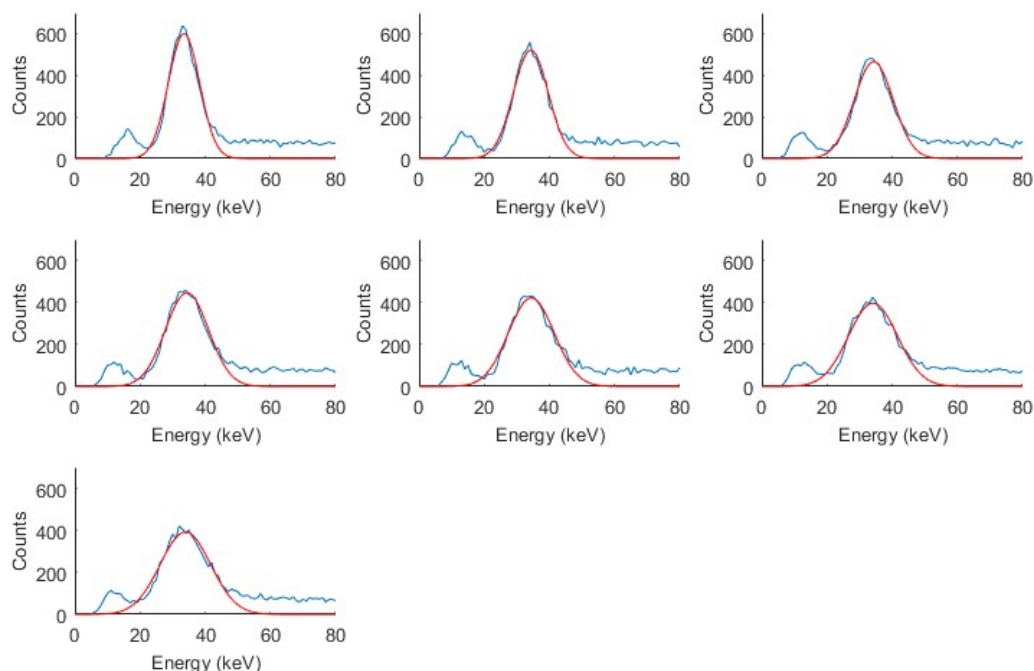


**Fig. 74.** X-rays from  $^{137}\text{Cs}$  in  $\text{Si}_1$ . All measurements use a  $3.2\ \mu\text{s}$  peaking time for amplitude identification filter. The flat top times for each plot range from 0 to  $4.8\ \mu\text{s}$ , in increments of 80 ns

It was also worth investigating if the 22 keV peak from  $^{109}\text{Cd}$  and the 31 keV peak from  $^{137}\text{Cs}$  were distinguishable from each other. As the 22 keV is even lower energy, it provides another opportunity to determine the best flat top time for noise separation and resolution. Again, using the same experimental configuration, a stack of 6  $^{109}\text{Cd}$  sources, totaling  $0.15\ \mu\text{Ci}$ , were stacked at the center of the carbon window of the PIPSBox, with a  $0.85\ \mu\text{Ci}$   $^{137}\text{Cs}$  source placed at the top (farthest away so that it would not overwhelm the much weaker  $^{109}\text{Cd}$  signature). Four measurements were taken, all with  $3.2\ \mu\text{s}$  peaking time and each with either a 0, 200, 400, and 600 ns flat top time. As it was established in the previous measurement, lower flat top times are better, but conducting a finer examination with smaller differences between the flat

top times tested should yield better results yet. The results of this measurement can be seen in Fig. 75. It is clear from the spectra shown in this figure that the two X-ray peaks are indistinguishable from each other. However, finer variation of flat top time shows that when using a zero flat top time the noise becomes blended with the photopeaks, whereas when using a longer flat top time the photopeaks and the noise are separable with a noise threshold of  $\sim 17$  keV. The best resolution of 44.5% FWHM for the combined peaks was achieved using a flat top time of 200 ns. As such, a peaking time of  $3.2 \mu\text{s}$  and a flat top time of 200 ns were used for all subsequent measurements with the PIPSBox.

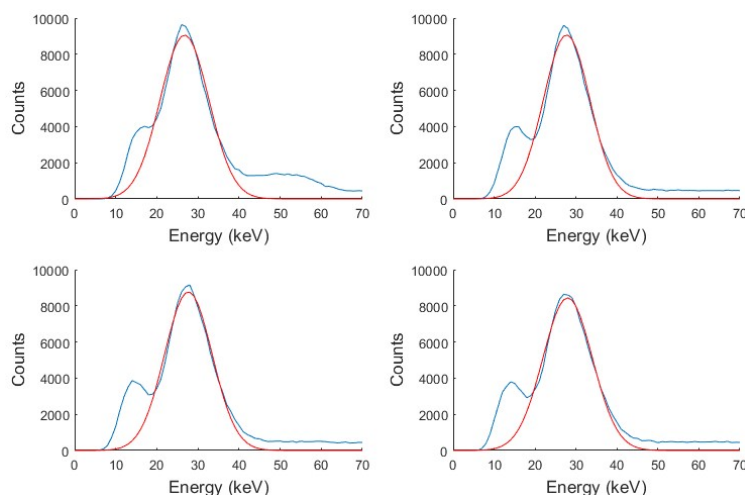


**Fig. 75.** The combined 22 keV X-ray from  $^{109}\text{Cd}$  and 31 keV X-ray from  $^{137}\text{Cs}$ , using a peaking time of  $3.2 \mu\text{s}$  and flat top times of (from top left to bottom right) 0, 200 ns, 400 ns, and 600 ns. The best resolution for the combined peak was 44.5%, achieved using 200 ns flat top time. Note that the x-axis of these plots are miscalibrated by roughly 25%, and that the photopeak should occur at 22 keV.

The ability to reliably detect radiation at low energies improves the efficacy of the PIPS summation, further reducing the tailing effect seen in monoenergetic electron sources. Detecting such low energies introduces the potential issue of misattributing X-rays emitted from radioxenon decays as electron events. However, this misattribution would only present itself in singles counting: the pattern recognition used in the FPGA necessitates a coincident photon trigger to occur in one of the  $\text{SrI}_2(\text{Eu})$  detectors for a coincidence event to be valid, something that would not be possible if the photon deposited all of its energy in a PIPS channel.

## 4.4. Evaluation of Full Detector

In this section the characterization of the detector using radioxenon samples and background is discussed. In terms of experimental order, background was measured first, followed by  $^{133/133m}\text{Xe}$ , then  $^{131m}\text{Xe}$ , and finally  $^{135}\text{Xe}$ . In this discussion,  $^{131m}\text{Xe}$  is discussed before  $^{133/133m}\text{Xe}$  due to the monoenergetic electron released by  $^{131m}\text{Xe}$  allowing for important studies on PIPSBox performance.

### 4.4.1. Background

The background measurement was taken prior to any of the radioxenon experiments to minimize any possible minor memory effect and produce the most reliable results possible. Note that this background is not taken using an IMS gas injection system, but instead is taken under a partial vacuum ( $\sim 5$  torr) after being exposed to ambient air. The measurement was taken over 48 hours, accepting both singles and coincidences.  $316,600 \pm 600$  valid triggers (i.e.: not noise) were measured, with  $13,100 \pm 100$  being coincidences. This yields a background rejection rate of  $95.85 \pm 0.04\%$ . This coincidence background is significantly higher than previous experiments with the PIPS-CZT, which achieved a rejection rate of  $99.98 \pm 0.01\%$  [87]. Though this can be attributed to the increased solid angle of the photon detector, likely more significant is the wide coincidence timing window necessitated by the trigger walking of the photon detector. If this coincidence timing window could be reduced, the background would likely be reduced significantly as well. Another possible way to reduce background would be by lining the inner walls of the lead cave with thin layer of copper to shield K-shell X-rays from lead. The background is shown in Fig. 76.

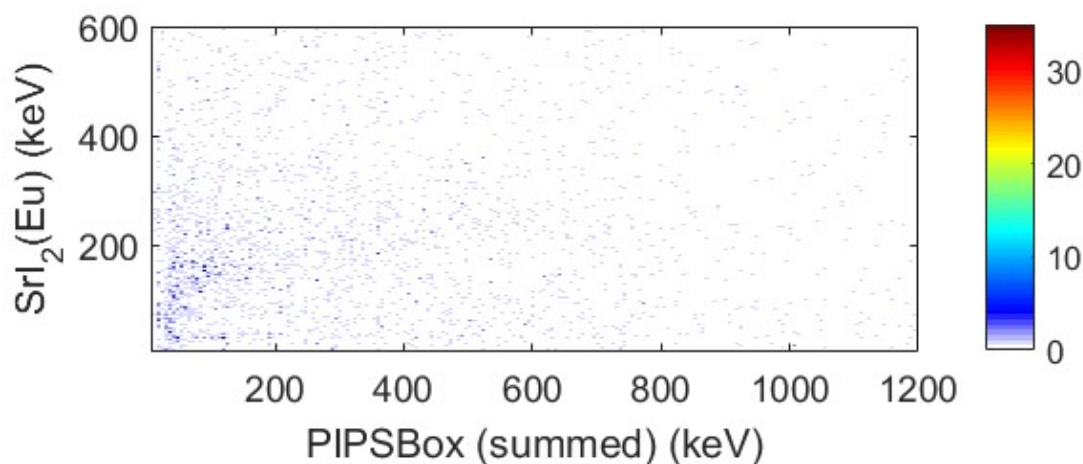


**Fig. 76.** 48-hour background measurement taken with the PIPS-SrI<sub>2</sub>(Eu) detector

#### 4.4.2. *Radi Xenon Measurements: <sup>131m</sup>Xe*

The unique decay behaviors of <sup>131m</sup>Xe amongst radioxenon isotopes of interest make it particularly useful for characterization of the system. <sup>131m</sup>Xe decays via the coincident release of an X-ray and a monoenergetic conversion electron, with the only competing decay path with significant intensity (>5% branching ratio) being the release of another monoenergetic conversion electron. The two monoenergetic conversion electrons give an easy way to calibrate the detector, and as they are only ~30 keV removed from one another also provide insight into the capabilities of the PIPSBox for electron detection with high energy resolution. Furthermore, the absence of an obscuring beta spectrum simplifies the study of electron backscatter.

A 1 mL sample of <sup>130</sup>Xe was irradiated for 4 hours to produce <sup>131m</sup>Xe, and several weeks were allowed to pass before <sup>131m</sup>Xe was injected while other experiments involving <sup>133/133m</sup>Xe (created from <sup>132</sup>Xe during the same irradiation) were conducted.

##### 4.4.2.1. *Coincidence Measurement*

The <sup>131m</sup>Xe isotope releases ~31 keV X-rays in coincidence with a conversion electron with energy of 129 keV. Fig. 77a shows the 2D coincidence histogram, and Fig. 77b shows the 1D histograms from each individual detector. 1,490,000 pulses were recorded.

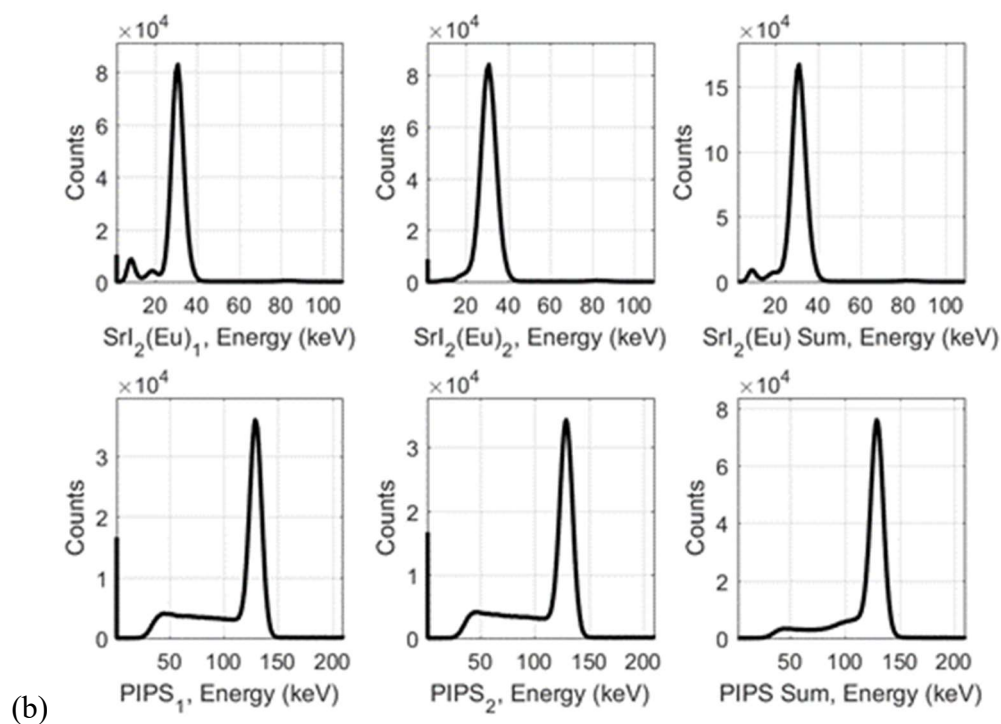
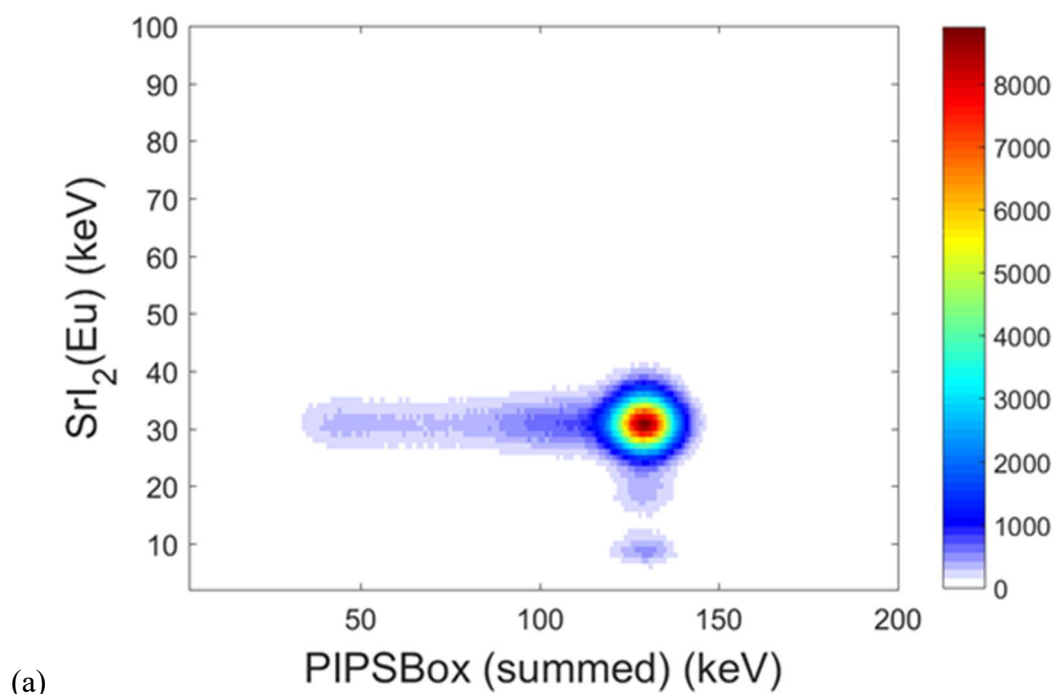


**Fig. 77.** (a) 2D coincidence histogram spectrum for  $^{131\text{m}}\text{Xe}$ ; (b) 1D histogram for each detecting body individually, as well as the combination of the two  $\text{Srl}_2(\text{Eu})$  spectra and the summation of the signal from the two PIPS channels

The 129 keV conversion electron is clear in the PIPSBox spectra, with a summed energy resolution of 9.6% FWHM. The resolution of the X-ray in the brighter  $\text{SrI}_2(\text{Eu})$  detector ( $\text{SrI}_2(\text{Eu})_1$ ) and the dimmer  $\text{SrI}_2(\text{Eu})$  detector ( $\text{SrI}_2(\text{Eu})_2$ ) 21.0% and 26.9% FWHM, respectively. The difference in resolution between the two crystals is unsurprising at these low energies due to the brightness and the oscillations discussed previously, though this trend is observed to reverse at higher energies. The brighter scintillator improves upon even the best results observed with coplanar CZT for radioxenon applications (25.8% FWHM) [23].

Some tailing is observed in both the photon and the electron spectra. Most of the photon tailing occurs in  $\text{SrI}_2(\text{Eu})_1$ , which is believed to be due to imperfect light sealing causing the already brighter crystal to produce light noise of sufficient amplitude to trigger the system. The tailing in the PIPSBox is discussed in the following section.

Using the methodologies outlined in eqns. (14)-(16) and in Cooper et. al. [204], efficiencies were determined experimentally and absolutely without knowledge of the activity of the sample. Using the count rates in the 31 keV X-ray region of the  $\text{SrI}_2(\text{Eu})$  singles spectra and comparing them to the count rates in the 31 keV X-ray  $\times$  129 keV C.E. in the coincidence spectrum, the efficiency for the 129 keV C.E. was determined using eqns. (14) and (15). Using known branching ratios and net count rates in the electron singles spectrum, the efficiency of the 159 keV C.E. was also determined. This allowed for the use of eqn. (16) to determine the X-ray efficiency and subsequently the  $\varepsilon_{\beta\gamma}$  for the ROI. These efficiencies are listed in Table 7. Note that these efficiencies are for the peaks. The unusually high efficiency for the 159 keV C.E. can be attributed to the torturous path that electrons take through a volume, and that 159 keV C.E. are likely to penetrate more deeply into the silicon and less likely to escape via backscatter.

**Table 7.** Experimental absolute efficiency from  $^{131\text{m}}\text{Xe}$  measurements

Detector	Radiation	Absolute Efficiency
PIPS	129 keV C.E.	$62.6 \pm 0.4\%$
	159 keV C.E.	$77.6 \pm 1.6\%$
$\text{SrI}_2(\text{Eu})$	31 keV X-ray	$11.0 \pm 0.4\%$
31 keV X-ray $\times$ 129 keV C.E.		$6.9 \pm 0.2\%$

#### 4.4.2.2. *PIPSBox Backscatter*

As the 199 keV conversion electron from  $^{133\text{m}}\text{Xe}$  can only experimentally be seen when obscured by the  $^{133}\text{Xe}$  beta spectrum, the backscatter reduction in the PIPSBox can be most easily observed and compared to the simulated results using the 129 keV C.E. from  $^{131\text{m}}\text{Xe}$ . The normalized energy histogram from each individual PIPS channel is shown superimposed onto the summed histogram in Fig. 78. As expected, the PIPSBox preamplifier has aided in the reduction of the tailing in the PIPSBox by summing the two channels when compared to the PIPS-CZT work [45]. The peak-to-total ratio before summation was 66.26% for PIPS<sub>1</sub> and 66.53% for PIPS<sub>2</sub>, and was 80.45% when the two were summed.

The experimental results do not perfectly match the simulated model shown in Fig. 57. The MCNP model underestimates the impact of gas attenuation which in the experiments, when combined with the  $< 4\pi$  solid angle presented by the PIPSBox, results in an unavoidable tail.

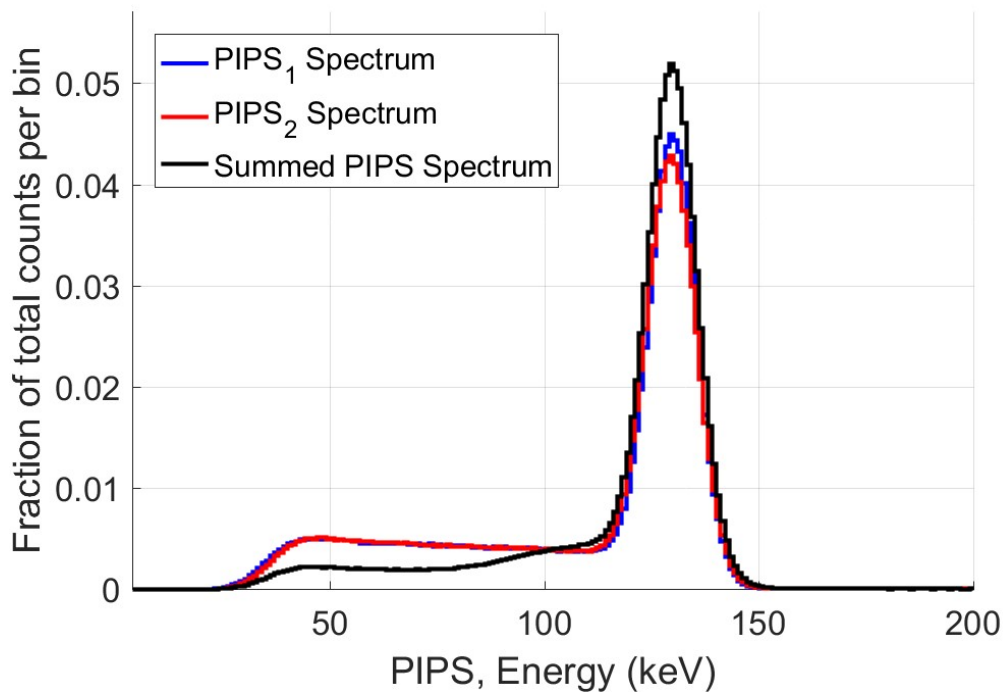


**Fig. 78.** Reduction of the backscatter in the PIPSBox (each spectrum normalized)

#### 4.4.2.3. *PIPSBox Timing Response*

It was experimentally verified during work on the PIPS-CZT that the response time of the PIPSBox was not the limiting factor in minimizing the coincidence timing window. The response time of the PIPSBox is not dependent on the photon detectors, and so the study done for the PIPS-CZT is directly relevant to the PIPS-SrI<sub>2</sub>(Eu) system as well. The study is quoted directly from the PIPS-CZT work [45]:

The performance of the PIPSBox had to be isolated. A coincidence pattern searching for only coincidences between two silicon detectors was defined. The coincidence timing window was set to 1 sample (8 ns) and slowly increased in 3 sample iterations, with the goal of determining the count rate at each CTW. 1000 coincidences were recorded for each measurement. It was found that after 16 samples (128 ns), increasing the coincidence timing window further did not significantly increase the rate of coincidences observed ([Fig. 79]). This indicates that the PIPSBox response is significantly faster than that of the [photon] detectors and is not the limiting factor in the length of the CTW.



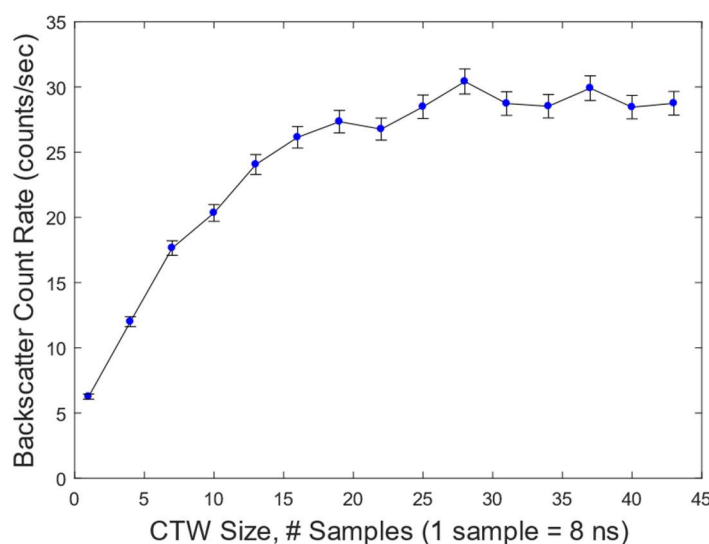


**Fig. 79.** Coincidence count rate between  $\text{Si}_1$  and  $\text{Si}_2$  with a varying coincidence timing windows [45]

#### 4.4.3. Radioxenon Measurements: $^{133/133\text{m}}\text{Xe}$

Of the three radioxenon samples,  $^{133/133\text{m}}\text{Xe}$  is the most complex sample to measure for multiple reasons. For one, the sample is a combination of both  $^{133}\text{Xe}$  and  $^{133\text{m}}\text{Xe}$ . Though  $^{133}\text{Xe}$  can be measured separately by allowing the  $^{133\text{m}}\text{Xe}$  to decay, no such luxury exists for the measurement of  $^{133\text{m}}\text{Xe}$ .  $^{133}\text{Xe}$  has multiple significant coincidence decay paths, which means that a separate beta-gamma efficiency must be determined for each ROI. This effort is frustrated by the multiple more complex decay modes. A decay model for  $^{133}\text{Xe}$ , taken from Cooper et. al. [204], illustrates this and is shown in Fig. 80. These modes must be taken into account when attempting to understand the spectra as well as when determining the efficiency of the system.

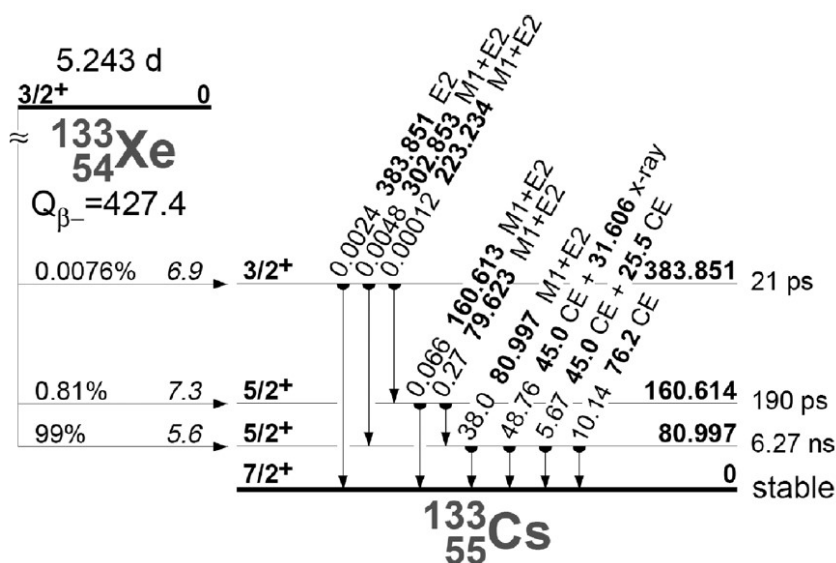


**Fig. 80.** A decay model showing branching ratios and energies of several important decay paths for  $^{133}\text{Xe}$

A 1.5 mL sample of  $^{132}\text{Xe}$  was irradiated for 4 hours to produce  $^{133/133\text{m}}\text{Xe}$ , and roughly 16 hours were allowed to pass before the sample was injected.

#### 4.4.3.1. Coincidence Measurement

The  $^{133}\text{Xe}$  isotope releases  $\sim 31$  keV X-rays in coincidence with a 0-346 keV  $\beta$  and a 45 keV conversion electron in competition with an 81 keV gamma in coincidence with the 0-346 keV  $\beta$ .  $^{133\text{m}}\text{Xe}$  releases a  $\sim 31$  keV X-ray in coincidence with a 199 keV conversion electron. Fig. 81a shows the 2D coincidence histogram, and Fig. 81b shows the 1D histograms from each individual detector. Fig. 82a and Fig. 82b show the same measurements on the same sample as Fig. 81, but taken roughly two weeks later such that only an insignificant amount of  $^{133\text{m}}\text{Xe}$  remained. 10,000,000 pulses were recorded for the first measurement, and 100,000 were recorded for the second.

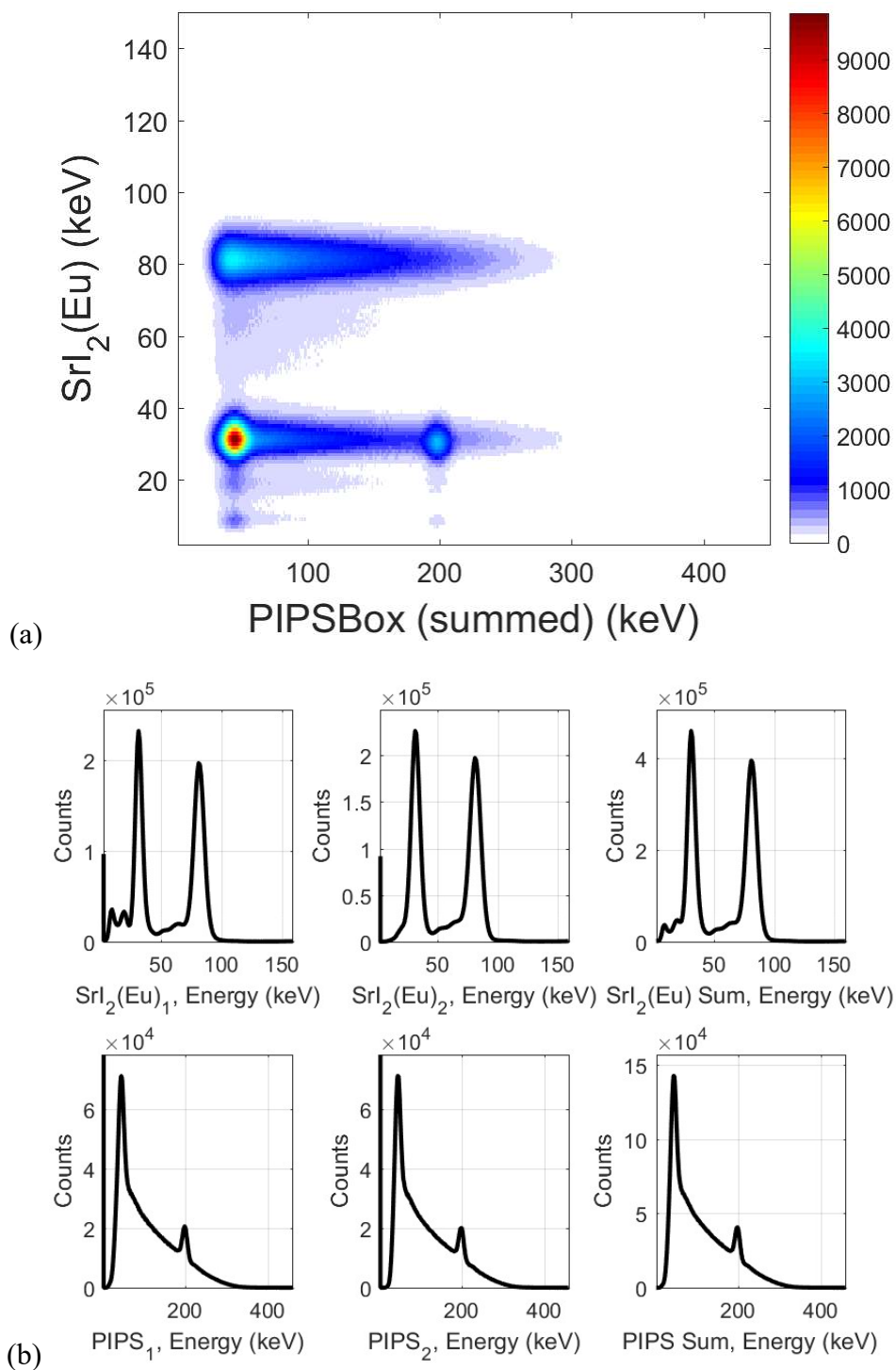


**Fig. 81.** (a) 2D coincidence histogram spectrum for  $^{133}\text{Xe}$  and  $^{133\text{m}}\text{Xe}$ ; (b) 1D histogram for each detecting body individually, as well as the combination of the two  $\text{Srl}_2(\text{Eu})$  spectra and the summation of the signal from the two PIPS channels

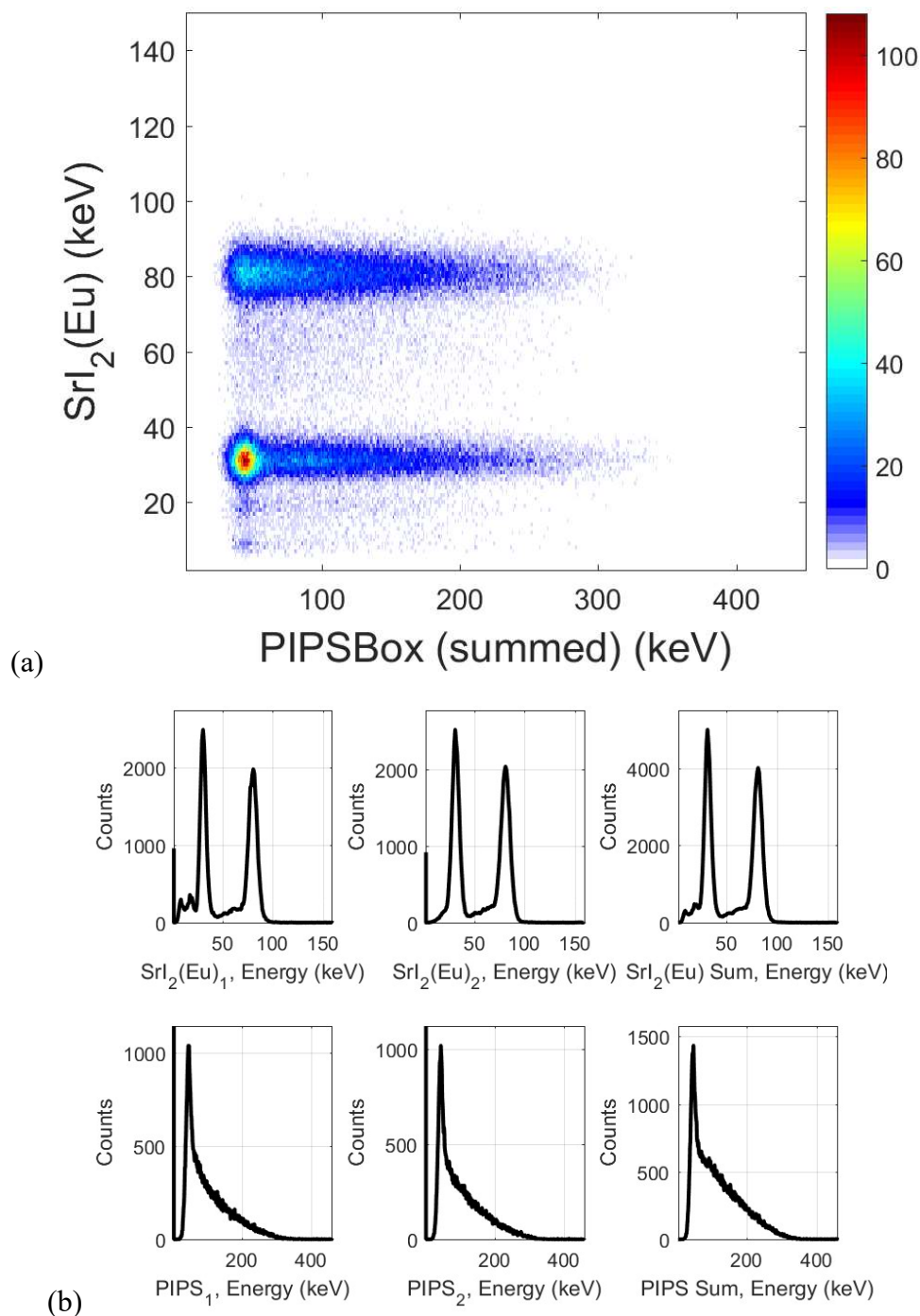


**Fig. 82.** (a) 2D coincidence histogram spectrum for  $^{133}\text{Xe}$ , after  $^{133\text{m}}\text{Xe}$  has decayed; (b) 1D histogram for each detecting body individually, as well as the combination of the two  $\text{SrI}_2(\text{Eu})$  spectra and the summation of the signal from the two PIPS channels

It should be noted that the 31 keV peak in ratio to the 81 keV peak should be larger in Fig. 81 compared to Fig. 82 due to the additional decays of  $^{133\text{m}}\text{Xe}$  with the C.E.s in coincidence with X-rays. However, the pattern recognition settings for the first measurement were incorrectly defined: triple coincidences were not set as a recognized pattern. Not only does no PIPS summation and backscatter reduction occur in the first measurement, all double coincidence events are also rejected. As 199 keV conversion electrons have a higher likelihood of backscattering than the betas ( $E_{\text{avg},\beta} = 100.4 \text{ keV}$  [206]) and the 31 keV X-ray is released in coincidence with two electrons (the beta and the 45 keV C.E.), the coincidences with the X-ray have a higher probability of experiencing a triple coincidence than coincidences with the gamma ray. In the second measurement the backscatter pattern is correctly defined, yielding a slightly higher X-ray to gamma ratio despite  $^{133\text{m}}\text{Xe}$  not contributing. A separate study was conducted for each injection where only triple coincidences were examined. Fig. 83a shows the results of triple coincidences with  $\text{SrI}_2(\text{Eu})_1$  from the first experiment, and Fig. 83b shows the same results from the second experiment. It can be seen that the X-ray to gamma ratio is significantly higher in the first set of experiments due to the presence of  $^{133\text{m}}\text{Xe}$ , which reinforces the conclusion that the reason why the X-ray to gamma ratio is higher in the second set of experiments is due to the ill-defined coincidence patterns in the first set of experiments.

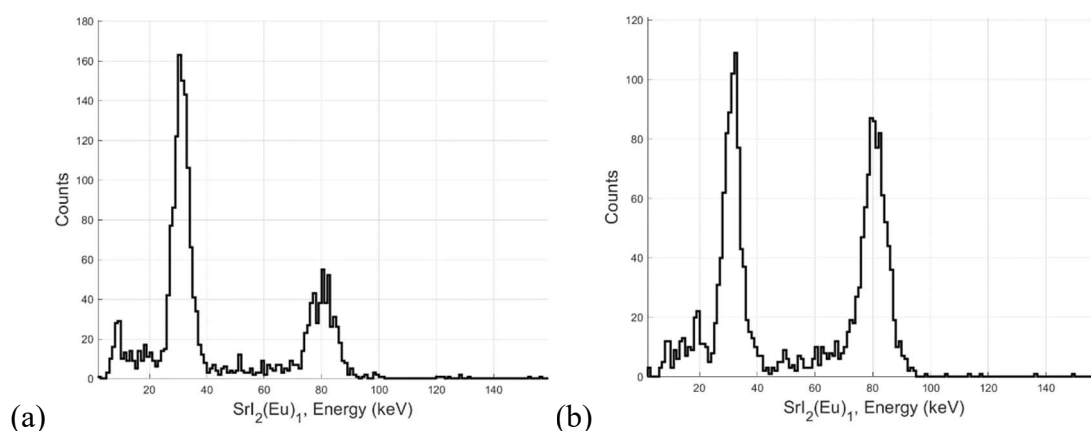


**Fig. 83.**  $\text{SrI}_2(\text{Eu})_1$  histogram of photons observed in triple coincidence, from (a) the first measurement, with  $^{133\text{m}}\text{Xe}$ , and (b) the second measurement, with no  $^{133\text{m}}\text{Xe}$ . Note the higher incidence of X-ray triple coincidences compared to gamma triple coincidences in the first experiment

Because betas are emitted with a lower limit of 0 keV, the beta spectrum taken in these measurements indicate a noise threshold of  $\sim 28$  keV. It was found that when the experiments were conducted outside of the lead cave the noise threshold returned to the previous level of  $\sim 17$  keV as determined during the  $^{109}\text{Cd}$  characterizations. This increase in noise in the PIPSBox when the system is in the lead cave is not observed in the  $\text{SrI}_2(\text{Eu})$  signals (in fact, the noise threshold is observed to be reduced from  $\sim 18$  keV to  $\sim 13$  keV when the system is inside the lead cave), which implies that the noise is isolated to either the PIPSBox or the preamplifier. One possibility is that the ground of the PIPSBox preamplifier was not sufficiently isolated, and that stray EM signals are picked up by the preamplifier when placed inside the imperfectly electromagnetically isolated lead cave; however, the true cause of this increase in noise threshold was not definitively determined. The reduction in background provided by the lead cave is believed to outweigh the increase in PIPSBox noise, and as such the system remained in the lead cave throughout the characterization process.

The 199 keV C.E. can clearly be seen in Fig. 81, with a summed energy resolution of 6.6% FWHM. This is in stark contrast to the resolution of the 199 keV peak in plastic scintillators or even stilbene, which is demonstrated in Fig. 84. The 45 keV C.E. is observed with a resolution of 34.3% FWHM and is clearly discriminated from noise. The 81 keV gamma ray was observed with an energy resolution of 12.7% FWHM in  $\text{SrI}_2(\text{Eu})_1$  and 13.0% FWHM in  $\text{SrI}_2(\text{Eu})_2$ .

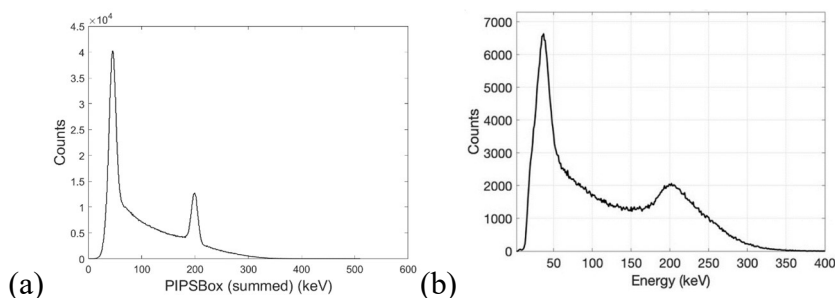


**Fig. 84.** X-ray gated spectrum of  $^{133}/^{133\text{m}}\text{Xe}$  taken with (a) PIPS- $\text{SrI}_2(\text{Eu})$  and (b) stilbene-CZT [23]. A resolution of 19.1% FWHM was reported for the stilbene-CZT (itself an improvement upon plastic scintillators [89]), compared to 6.6% FWHM for the PIPS- $\text{SrI}_2(\text{Eu})$

Due to the relative simplicity of the second experiment (one isotope instead of two) and the incorporation of all coincidences (including triple coincidences), the second data set was used to calculate the efficiencies for  $^{133}\text{Xe}$ . Using the count rates in the 81 keV gamma region of the  $\text{SrI}_2(\text{Eu})$  singles spectra and comparing them to the count rates in the 81 keV  $\gamma \times 0\text{--}346$  keV  $\beta$  in the coincidence spectrum, the efficiency for the beta was determined using eqns. (14) and (15). This ROI was used to determine the efficiency of the beta due to no interfering conversion electrons in the ROI. When conducting this same procedure for the 31 keV X-ray region, an overall efficiency for the 31 keV X-ray  $\times 0\text{--}346$  keV  $\beta + 45$  keV C.E. is determined. Using the calculated beta efficiency, the total efficiency for this ROI, and by making some assumptions (76 keV electrons are not detected in coincidence with betas,  $\epsilon_{CE25} = 0$  due to being below the energy threshold), the 45 keV C.E. efficiency can be determined using the equation:

$$\epsilon_{\beta+C.E \times Xray} = \epsilon_{\beta \times \gamma} + \epsilon_{CE \times Xray} - \epsilon_{\beta \times \gamma} \epsilon_{CE \times Xray} \quad (17)$$

Using these solved values, known branching ratios, and by making the assumption that  $\epsilon_{CE76} = \epsilon_{CE45}$  and  $\epsilon_{CE25} = 0$ , eqn. (18) can be used to solve for the X-ray and gamma ray efficiencies. These values are then used to solve for the  $\epsilon_{\beta\gamma}$  for each ROI.

$$\epsilon_{\gamma_i} = \frac{C_{\beta\gamma_i} * \left( \frac{1 - (1 - BR_{\beta} \epsilon_{beta}) * [1 - BR_{CE76} \epsilon_{CE76} - BR_{Xray} \epsilon_{CE45} - BR_{CE25} \epsilon_{CE45}] - BR_{CE25} \epsilon_{CE25} - BR_{CE25} \epsilon_{CE25} \epsilon_{CE45}}{C_{\beta} BR_{\gamma_i} \epsilon_{\beta ROI}} \right)}{C_{\beta} BR_{\gamma_i} \epsilon_{\beta ROI}} \quad (18)$$

To determine the  $^{133m}\text{Xe}$  efficiencies, a linear interpolation was done between the 159 keV C.E. efficiency from  $^{131m}\text{Xe}$  and the 214 keV C.E. from  $^{135}\text{Xe}$  (discussed in the next section). The X-ray efficiency was simply an average of the three different X-ray efficiencies as calculated for the other isotopes. These X-ray efficiencies differed from each other by less than 0.2%, well within error. The efficiencies for  $^{133/133m}\text{Xe}$  are listed in Table 8. As before, these efficiencies are for the peaks, not for total detection probability.

**Table 8.** Experimental absolute efficiency from  $^{133/133m}\text{Xe}$  measurements

Detector	Radiation	Absolute Efficiency
PIPS	45 keV C.E.	$45.3 \pm 2.0\%$
	0-346 keV $\beta$	$47.5 \pm 0.7\%$
	199 keV C.E. ( $^{133m}\text{Xe}$ )*	$64.5 \pm 16.7\%^*$
$\text{SrI}_2(\text{Eu})$	31 keV X-ray	$11.2 \pm 0.5\%$
	81 keV $\gamma$ -ray	$23.7 \pm 0.9\%$
31 keV X-ray $\times$ 45 keV C.E. + 0-346 $\beta$		$8.0 \pm 0.4\%$
81 keV $\gamma$ -ray $\times$ 0-346 $\beta$		$11.3 \pm 0.5\%$
31 keV X-ray $\times$ 199 keV C.E. ( $^{133m}\text{Xe}$ )*		$7.1 \pm 2.1\%$

\*These C.E. efficiency for  $^{133m}\text{Xe}$  is calculated via linear interpolation from other C.E. efficiencies, and the X-ray efficiency for  $^{133m}\text{Xe}$  is calculated by averaging the X-ray efficiencies calculated for the other radioxenon isotopes

#### 4.4.3.2. Memory Effect Evaluation

Memory effect was measured using the 81 keV  $\gamma \times$  0-346 keV  $\beta$  ROI of  $^{133}\text{Xe}$ . A before measurement of 25,000 pulses was taken over 23 minutes, with a count rate in the ROI of  $7.710 \pm 0.074$  cps. The system was then pumped and flushed several times down to 2.5 torr. Following this, 1150 pulses were then taken over a period of 116 minutes with a count rate in the ROI of  $0.025 \pm 0.002$ . This indicates a memory effect of  $0.318 \pm 0.026\%$ , which matches reasonably closely to the previous results from the PIPS-CZT evaluation of  $0.256 \pm 0.034\%$  [45]. The most likely reason for the worse memory effect when compared to the PIPS-CZT measurement is the extended period that the  $^{133}\text{Xe}$  sample was inside the detector. Though the 81 keV  $\gamma \times$  0-346 keV  $\beta$  ROI of  $^{133}\text{Xe}$  is significantly larger than the 31 keV X-ray  $\times$  129 keV C.E. ROI of  $^{131m}\text{Xe}$ , background count rates are less than the error associated with the count rates



discussed here ( $0.00064 \pm 0.00006$  in the  $81 \text{ keV } \gamma \times 0\text{-}346 \text{ keV } \beta$  ROI, based on the experiment shown in Fig. 76) and as such should have negligible impact on the memory effect measurement.

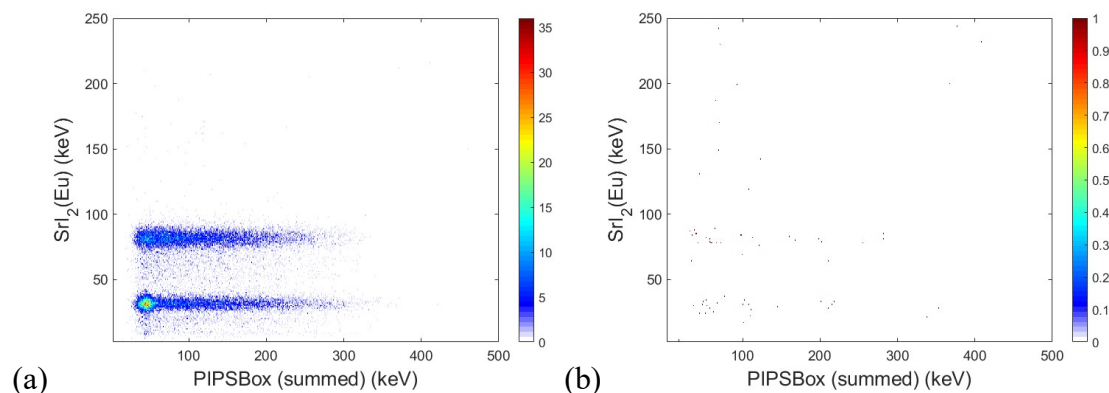


**Fig. 85.** Memory effect in the PIPS-SrI<sub>2</sub>(Eu) system after being exposed to <sup>133</sup>Xe for several weeks; (a) before extraction; (b) after extraction

#### 4.4.4. Radioxenon Measurements: <sup>135</sup>Xe

A 1 mL sample of <sup>134</sup>Xe was irradiated for 1.4 hours to produce <sup>135</sup>Xe, and roughly 16 hours were allowed to pass before the sample was injected.

##### 4.4.4.1. Coincidence Measurement

The <sup>135</sup>Xe isotope releases 250 keV gamma rays in coincidence with a  $\beta$  with an energy of 0-910 keV. In addition, a coincidence of  $\sim 31 \text{ keV}$  X-rays, a 214 keV conversion electron, and the 0-910 keV  $\beta$  is observed with a low, but not insignificant, branching ratio (5.7%). Though this signature is typically not used in MDC calculations due to the relatively low branching ratio, obfuscation from <sup>133</sup>/<sup>133m</sup>Xe, and short half-life of <sup>135</sup>Xe, the signature still appears in spectra and should be noted. Fig. 86a shows the 2D coincidence histogram, and Fig. 86b shows the 1D histograms from each individual detector. 2,000,000 pulses were recorded.

All of the spectral features stated above are clearly visible in both the 1D and 2D spectra. The 250 keV gamma ray is observed with an energy resolution of 8.6% and 7.5% FWHM for the brighter and dimmer SrI<sub>2</sub>(Eu), respectively. The 214 keV C.E. is observed with a 6.1% FWHM. Also present in the spectrum is the Compton scatter

line of the 250 keV gamma ray fully depositing its energy between both the  $\text{SrI}_2(\text{Eu})$  and the PIPSBox, as well as a Compton backscatter peak at around 140 keV in the gamma spectrum.

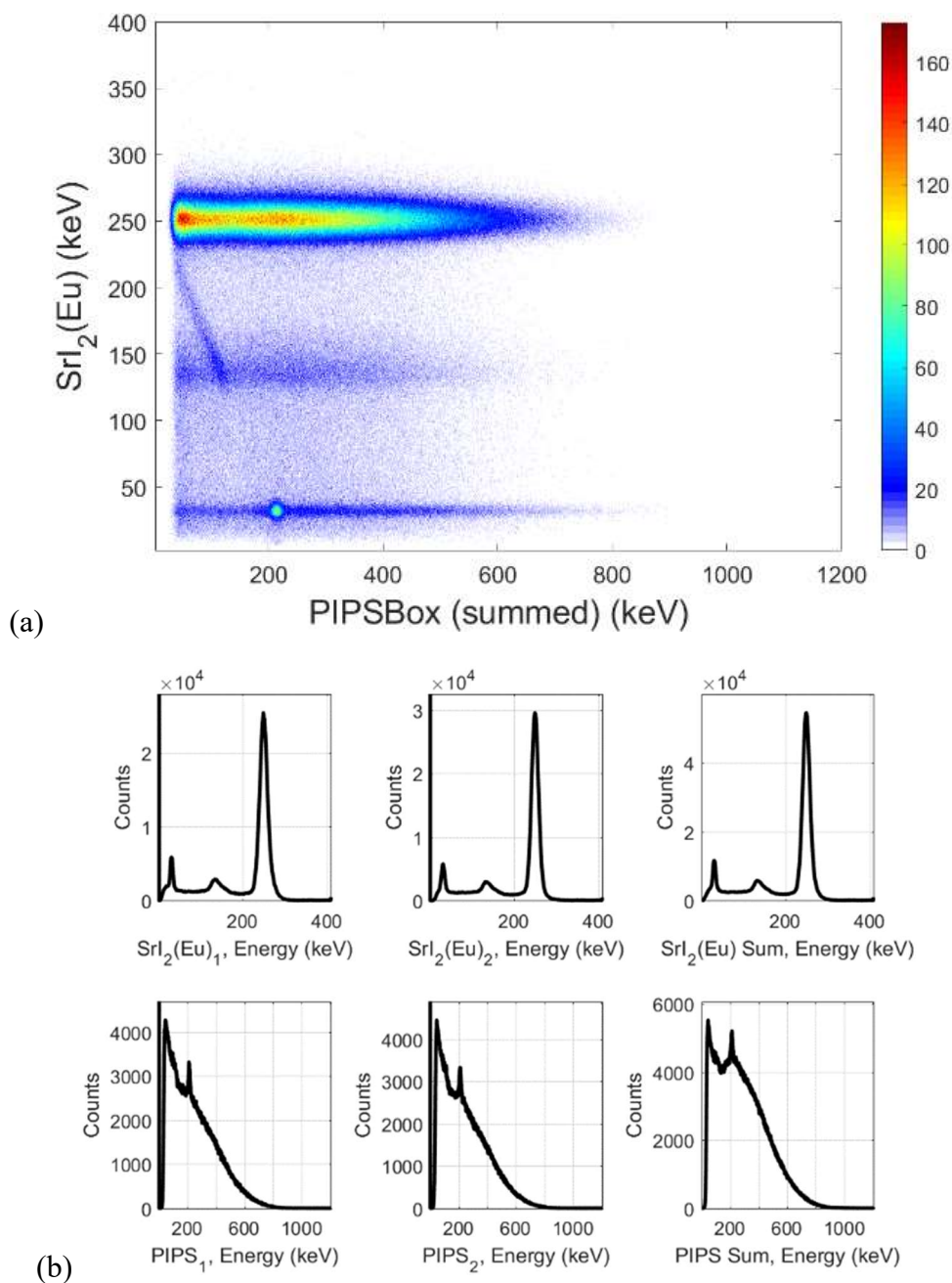


**Fig. 86.** (a) 2D coincidence histogram spectrum for  $^{135}\text{Xe}$ ; (b) 1D histogram for each detecting body individually, as well as the combination of the two  $\text{SrI}_2(\text{Eu})$  spectra and the summation of the signal from the two PIPS channels

Using the count rates in the 250 keV gamma region of the SrI<sub>2</sub>(Eu) singles spectra and comparing them to the count rates in the 250 keV  $\gamma \times 0-910$  keV  $\beta$  in the coincidence spectrum, the efficiency for the beta was determined using eqns. (14) and (15). By comparing the net count rates in the 31 keV X-ray region and the net count rates in the 31 keV X-ray  $\times 0-910$   $\beta$  and 214 keV C.E. ROI and comparing the efficiencies of this region to that of the beta spectra already determined, the efficiency of the 214 keV C.E. was determined. Eqn. (16) was then used to determine the both the gamma ray and X-ray efficiency and the  $\varepsilon_{\beta\gamma}$  for the ROI as well as the X-ray  $\times$  C.E. coincidence region. These efficiencies are listed in Table 9. As is the case for the other isotopes these efficiencies are for the peaks, not for total detection probability. The high errors associated with the C.E. and X-ray are due to the low count rates in those regions.

**Table 9.** Experimental absolute efficiency from <sup>135</sup>Xe measurements

Detector	Radiation	Absolute Efficiency
PIPS	0-910 keV $\beta$	$61.9 \pm 0.4\%$
	214 keV C.E.	$59.6 \pm 22.3\%$
SrI <sub>2</sub> (Eu)	31 keV X-ray	$11.0 \pm 4.5\%$
	250 keV $\gamma$ -ray	$14.2 \pm 0.9\%$
250 keV $\gamma$ -ray $\times 0-910$ keV $\beta$		$8.8 \pm 0.6\%$
31 keV X-ray $\times 0-910$ keV $\beta + 214$ keV C.E.		$6.6 \pm 3.7\%$

#### 4.4.5. Constant Fraction Discriminator

The lengthy coincidence timing window necessitated by the SrI<sub>2</sub>(Eu) contributes to the high background count rejection rate, which reduces the sensitivity of the system. It would thus be beneficial in the long term to implement a constant fraction

discriminator trigger, limiting the trigger walking seen in the leading edge trigger approach. Though a full implementation is beyond the scope of this work, several steps were taken to facilitate an eventual implementation. These included a proof-of-concept study in MATLAB, as well as the implementation of variable-length moving average filters and signal scaling, delay, and subtraction infrastructure in the FPGA.

Due to its comparatively simple implementation and straightforward visualization, CFD was first demonstrated in MATLAB on previously saved pulses. The DPP8 was designed to store the signal from a given channel starting from some set number of samples before the trigger point for that channel. In the case of the data being examined during the proof-of-concept, the pre-sample setting was 400 samples: thus, data sent to MATLAB from both  $\text{SrI}_2(\text{Eu})$  and the PIPS channels start at exactly 400 samples prior to the trigger point of that channel, regardless of how much time occurred in between the triggers in real time. This prevented a direct comparison between the efficacy of the leading edge trigger and CFD but was pedagogical in the sense of shining light on some difficulties that might manifest in an FPGA implementation.

CFD requires the scaling of the incoming signal, with the ideal scaling fraction for scintillator applications suggested as  $\sim 0.2\text{-}0.4$  of the original pulse height [207]. Due to simplicity of implementation of division by bit-shifting in an FPGA, a scaling of 0.25 was used in the MATLAB demonstration. Using less scaling (e.g.: 0.5) was likely to increase variability in crossing time and using a larger scaling (e.g.: 0.125) introduced accidental crossings due to noise. The top-left two plots of Fig. 87 shows the CFD using this scaling factor and a delay of 700 samples ( $5.6\ \mu\text{s}$ ), while the bottom-left two plots indicate the leading edge trigger of the original (blue) pulses. The MATLAB implementation drew attention to three difficulties that would arise in VHDL implementation: significant noisiness in the PIPSBox signal, oversaturation of zero crossings due to the random nature of noise cancelling itself out, and the issue of identifying the correct crossing point.

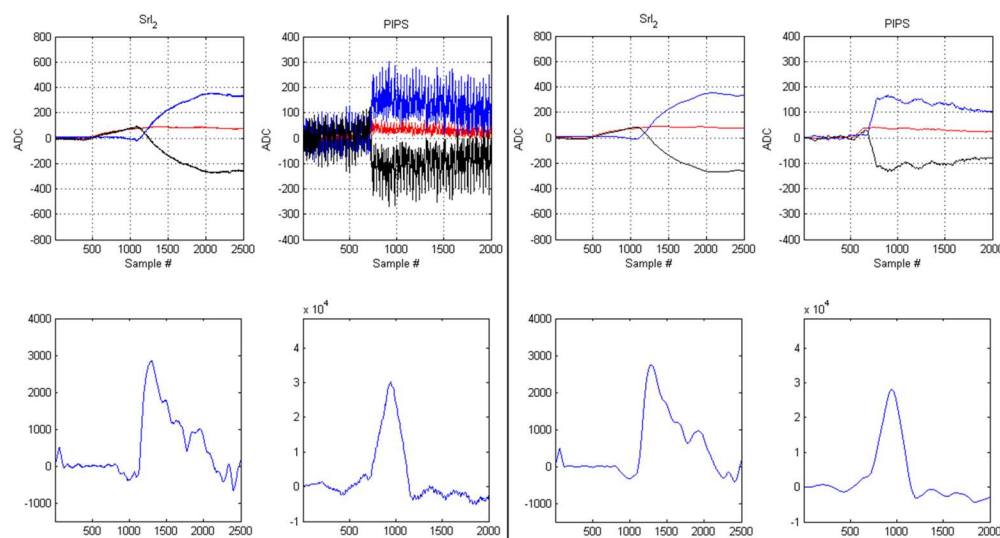


**Fig. 87.** The CFD for the  $\text{SrI}_2(\text{Eu})$  and PIPS channels in coincidence for  $^{131\text{m}}\text{Xe}$  data (top row) and the leading edge triggers (bottom row). The scaled signal is in red, the original delayed signal to be subtracted is in blue, and the zero-crossing subtracted signal is in black. The leftmost four plots are using a moving average filter of 0 samples, while the four plots on the right use a moving average filter is 51 samples

The first issue was directly addressed through the implementation of a moving average filter in VHDL, the length of which can be set by the user via MATLAB. The effect of this moving average filter was demonstrated in MATLAB on the right side of Fig. 87, which is simply the left side of Fig. 87 but with the moving average filter applied. This optional feature has been fully implemented in the FPGA and can be toggled on and off as well as have its length set via MATLAB. An FIR filter was ineffective in this particular case, as the number of coefficients necessary was too large and resource intensive. Thus, like the leading edge triangular trigger filter, BRAMs were used. To improve latency and avoid the necessity of using a divider IP core, the user is restricted to defining the moving average filter length  $L$  in factors of 2. This allows for division to be conducted by a bit shift, the amount of which determined by the length of the moving average filter. The filter is universal across channels, i.e.: the user may not define a different filter size for each channel.

The moving average filter signals are kept independent of the original signal. The FPGA bases the leading edge trigger off the original signal, which is delayed by half of the length of the moving average filter (i.e.:  $L/2$ ) using a shift register. In this way,

the moving average signal at any given time is representative of the values  $L/2$  before the delayed original signal and the  $L/2$  values following that sample of the delayed original signal. The moving average filter is in effect averaging “around” a given point, as opposed to “behind” a given point. The moving average value is determined by adding a new sample to its value at every clock while at the same time subtracting off an old value, while dividing the total value by the total number of samples in the moving average filter via a bit shift. All processes are clocked via the onboard ADC clock save for a state machine used to recognize a reset signal from the user, which is clocked with the Opal Kelly host clock.

This is perhaps best visualized in a simulation, where a square wave with amplitude 100 is read in from the ADC. This simulation is shown in Fig. 88. *dina* is the original ADC data, *dly\_q* is the delayed ADC data that is passed out of the module and goes to serve as the leading edge trigger data, *mavg\_data* is the moving average value of the square wave, shown to go from 0 to 100 to 0. *mavg\_length* is the width of the moving average filter and is set by the user with the selection of 6 (*mavg\_length\_sel*,  $2^6 = 64$ ). *acc\_b* is the accumulator for the moving average filter, and *acc\_q* is the total value of all the summed points. The experimental moving average pulses output from the DPP8 behave precisely as expected in terms of pulse shape and timing, and are identical to the moving average results as implemented in MATLAB.

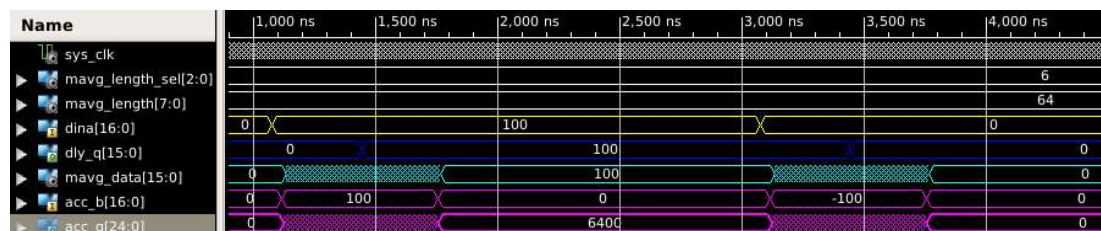


**Fig. 88.** Simulation of the moving average filter with a square wave

The accidental zero crossings from baseline fluctuations are significantly reduced by using leading edge triggers as a gate for the zero crossing filter. This at first seems counterintuitive, as coincidences between CFD triggers are meant to have finer time resolution than those from leading edge triggers. Finer time resolution using leading

edge trigger gating is possible in VHDL with a delay line and a zero crossing window. The original data stream is delayed by some amount of time  $d$  (consistent across all channels), chosen to account for half of the uncertainty  $\sigma$  in the leading edge trigger time such that  $d = \sigma/2$ . When a leading edge trigger is observed in the original data, a counter is started where the zero crossing must be identified in the delayed data within the time  $\sigma$ . The timings are recorded with respect to the original leading edge crossing of the first leading edge trigger. Once the leading edge coincidence timing counter plus any additionally triggered CFD counters are finished, the minimum time difference between the CFD triggers in the various channels is identified. A large coincidence window is set limiting the possible time between the leading edge triggers (e.g.: 4.4  $\mu\text{s}$  in the case of this work), and a smaller window set between the zero crossing triggers that act as an additional check that must be passed before the coincidence is confirmed by the FPGA. Though the leading edge triggering remains real time, the CFD approach identifies coincidences after they occur. However, the delay is small, on the order of 2-3  $\sigma$  in time—significantly less than the data transfer time of even a single pulse to the PC for post-processing list-mode-based identification. If the events fail the zero crossing trigger check using the finer timing window, the coincidence is discarded.

This delayed method of identification makes a solution to the third issue, that of multiple genuine (i.e.: not based on baseline noise) zero crossings due to signal fluctuations on the leading edge of the pulse, relatively straightforward. As additional zero crossings in a given channel are unlikely to occur far from the rising edge of the pulse shape, and as the uncertainty in the leading edge trigger is inherently limited by the rise time of the pulse, the zero crossing for a channel is defined as the last zero crossing that occurs within the time window  $\sigma$ . This approach should resolve crossings due to any oscillations on the leading edge of the pulses that would result in uncertainty in the CFD triggers.

Some infrastructure discussed above regarding the identification of these zero crossings and the difference between the times of the triggers has been designed in VHDL, but complete implementation necessitates future work. It is worth noting that

the CFD approach is in practice likely to increase the absolute time between the triggers of the  $\text{SrI}_2(\text{Eu})$  and the PIPS due to the longer rise time of the CSPs used with the  $\text{SrI}_2(\text{Eu})$  as well as due to the signal delays that must be introduced to produce the subtraction signal. However, one of the advantages of  $\text{SrI}_2(\text{Eu})$  when compared to coplanar CZT is its improved consistency between radiation interaction and signal generation. Owing to the fixed rise time of the CSPs and the fixed signal delays, the increase in absolute time between triggers is essentially constant across all situations. This can easily be accounted for by utilizing a shift-register in the FPGA to delay the signals of the PIPS by some amount to account for this temporal offset.

#### 4.5. MDC Calculations

MDCs were calculated based on the equations provided in Section 2.3.3. The calculation of the  $\sigma_0$  term in the MDC equation is simplified in several ways. Memory effect in the PIPSBox is already  $\sim 15\text{-}20\times$  lower than plastic scintillators and it has been demonstrated that applying stronger vacuums reduces the effect further. By assuming that the vacuum pump available at an IMS station (e.g.: a turbo pump) would be stronger than that available in the lab and used in this characterization, memory effect is expected to be very low and so memory effect counts, and the associated error, are ignored in the calculation. The error of the background counts is assumed to be exclusively due to statistical fluctuations, which are assumed to be Poisson in nature. Thus,  $\sigma_{BckCnts}$  is defined as simply the square root of the scaled background counts. When a new detector is established, a long ambient background measurement with good counting statistics is taken, which is then subtracted from all subsequent background measurements which occur immediately before sample injection. The MDC calculation done here is based on the background measurement discussed in Section 4.4.1, and assumes that these measured background counts are net background counts (i.e.: the amount of constant quantifiable present background that can be reliably subtracted out is zero).

A radon generator was not available during the period of this research and so the radon daughter interference could not be experimentally determined [18]. Instead, the



ratios describing the interferences in the  $^{135}\text{Xe}$  and  $^{133}\text{Xe}$  ROIs were calculated using tabulated branching ratios [206], in a procedure outlined in the work previously done at OSU on the PIPS-CZT (where a radon generator was also not available) [87]. For completeness, the method and consequences are quoted here in full, with relevant numbers changed to reflect the data from the simulations for the PIPS-SrI<sub>2</sub>(Eu) system:

In the ROI defined for the decay of  $^{214}\text{Pb}$ , defined as 352 keV  $\gamma \times 0\text{--}710$  keV  $\beta$ , the  $\varepsilon_\beta$  was assumed to be the same as for the  $^{135}\text{Xe}$   $\beta$  spectrum. The  $\varepsilon_{\beta\gamma}$  was then determined by simulating 250 keV and 352 keV photons in MCNP6 and then scaling the  $\varepsilon_{\beta\gamma}$  of the  $^{135}\text{Xe}$  ROI by the ratio of the two simulated gamma efficiencies. The number of 242 keV photons that fall into the 250 keV ROI of  $^{135}\text{Xe}$  was also accounted for, assuming the same FWHM for both photon peaks. This resulted in an interference ratio of [49.9%] in the  $^{135}\text{Xe}$  ROI. A similar procedure was used to determine the efficiency for detecting the interfering decay of the radon daughters in the  $^{133}\text{Xe}$  ROI, while also accounting for the offset of the beta spectrum due to the release of a conversion electron. The interference ratio for  $^{133}\text{Xe}$  was determined to be [83.4%]. The interferences from  $^{133}\text{Xe}$  were calculated experimentally using the data shown in [Fig. 82]. Compton scattering of photons from higher energy gammas into the 81 keV gamma region of  $^{133}\text{Xe}$  and the X-ray regions of  $^{133}\text{Xe}$  and the metastables were not considered, nor were the electron backscatter effects between  $^{133}\text{Xe}$  and the metastables. These simplifications make the MDC calculation an optimistic one, a fact that should be kept in mind when comparing evaluating the MDC of this system against others. Considering these adjustments, the  $\sigma_0$  term may be simplified to:

$$\sigma_0 = \sqrt{2 \left( \frac{T_A}{T_B} BckCnt_{ROI_0} \right) + \left( \frac{BckCnt_{ROI_0}}{BckCnt_{ROI_{interfering}}} * \sigma_{ROI_{interfering}} \right)^2} \quad ([19])$$

where the first term accounts for background counts in the ROI of the isotope being examined and the second term accounts for interferences, with the

$\sigma_{ROI_{interfering}}$  term simply being the square root of the background counts in the interfering ROI (e.g.: for the  $^{135}\text{Xe}$  calculation, the  $BckCnt_{ROI_{interfering}}$  is in reference to the  $^{214}\text{Pb}$  352 keV  $\gamma \times 0\text{-}710$  keV  $\beta$  ROI, and  $BckCnt_{ROI_0}$  refers to the  $^{135}\text{Xe}$  ROI).

Using the efficiencies and calculated in the previous sections, ROIs defined as  $2\times$  the FWHM based on the resolutions of the peaks of interest, and the background spectrum shown in Fig. 76, the MDCs were calculated using parameters from both the ARSA and the Xenon International gas processing systems. These results are shown in Table 10, with a comparison to the PIPS-CZT as taken from experimental data extrapolated to a pair of  $2\times 2\times 1$  cm<sup>3</sup> CZT crystals.

**Table 10.** MDCs for the PIPS-SrI<sub>2</sub>(Eu) system and the PIPS-CZT system, using ARSA gas processing parameters and Xenon International gas processing parameters

Isotope	MDC (mBq/m <sup>3</sup> ) PIPS-SrI <sub>2</sub> (Eu)		MDC (mBq/m <sup>3</sup> ) PIPS-CZT [87] ( $2\times 2\times 1$ cm <sup>3</sup> CZT, simulated)
	ARSA gas processing parameters	Xenon Int. gas processing parameters	Xenon Int. gas processing parameters
$^{131\text{m}}\text{Xe}$	$0.21 \pm 0.06$	$0.12 \pm 0.03$	$0.42 \pm 0.33$
$^{133\text{m}}\text{Xe}$	$0.27 \pm 0.09$	$0.15 \pm 0.05$	$0.44 \pm 0.36$
$^{133}\text{Xe}$	$0.48 \pm 0.03$	$0.26 \pm 0.02$	$0.31 \pm 0.11$
$^{135}\text{Xe}$	$1.92 \pm 0.16$	$1.00 \pm 0.08$	$1.00 \pm 0.28$

The results from the prototype, though optimistic, are nevertheless compelling. When using the ARSA gas processing unit and using the simplifications outlined above, three of the four radioxenon isotopes are expected to be below 1 mBq/m<sup>3</sup> sensitivity, in agreement with the MDC requirement set by the CTBTO of  $\leq 1$  mBq/m<sup>3</sup> for  $^{133}\text{Xe}$ . When using the Xenon International gas processing unit all four isotopes are expected to be below the CTBTO limit (with  $^{135}\text{Xe}$  meeting the limit

within error) as well as meeting the Xenon International threshold MDCs ( $\leq 0.3$  mBq/m<sup>3</sup> for <sup>131m</sup>Xe, <sup>133m</sup>Xe, and <sup>133</sup>Xe, and  $\leq 1.0$  mBq/m<sup>3</sup> for <sup>135</sup>Xe). The PIPS-SrI<sub>2</sub>(Eu) either equals or outperforms the expanded version of the PIPS-CZT for all four radioxenon isotopes of interest. The MDCs are expected to decrease further still if the coincidence timing window is decreased and background can be reduced.

It should be noted that detector background differs based on where the detector is located on the earth, as well as which gas processing system is used to sample the atmosphere and provide a background sample. As such, MDCs are subject to some variation depending on these factors.

## 4.6. Statistical Methods

### 4.6.1. Code Structure

Before discussing the investigations conducted using the statistical approach, the actual structuring of the Python package should be addressed. A main file, *ml\_rxe.py*, is used to control various settings and the operating of the code. These include selection of library spectra, which experimental spectra to deconvolve, if the new RSD method is to be used, and how many sections to use. If the new method is not use, the code defaults to using the traditional SDAT solve using maximum likelihood. The library spectra are generated in advance using MCNP6, ptrac, and the parsing script written in Python which identifies energy deposition in volumes of interest in the ptrac file. MATLAB was used to synthesize synthetic experimental spectra based on these simulated spectra and the real background spectrum shown in Fig. 76. These experimental spectra were created by randomly selecting points sourced from the library spectra in certain quantities defined by the user. In these tests, <sup>214</sup>Pb was not used and its implementation is left to future study. A few sample spectra, with sectioning superimposed, are shown in Fig. 89.

In this implementation of the code, large sections are defined based on a user-provided text file indicating the outer limits of each section. These large sections are broken up into some number of smaller sections, equally spaced in the x-axis. In the initial testing done with the code, some of these regions overlapped in the <sup>133</sup>Xe X-ray

region. Though nothing strictly prohibits overlapping, it does make the indices of the simulation matrix correlated and has the effect of applying heavier statistical weight to certain regions of the spectrum. The potential benefits or downsides to this approach is not thoroughly investigated in this work but is worth noting nevertheless.

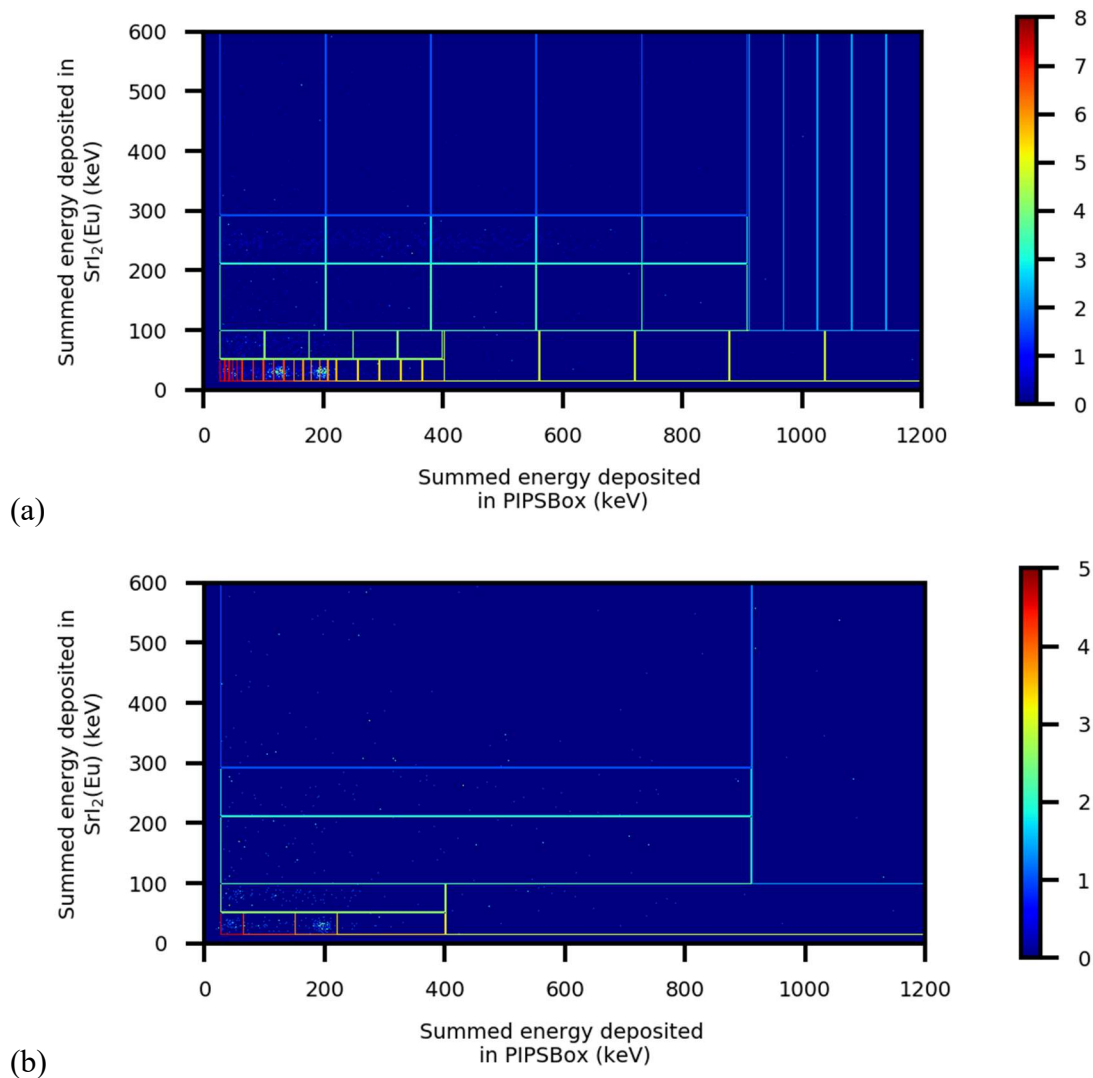


**Fig. 89.** Synthetic experimental spectra generated using the Python package, with different sectioning superimposed. In (a), the four radioxenon isotopes and background each have 1000 events contributing to the spectrum. The spectrum is divided into 50 subregions. In (b),  $^{131m}\text{Xe}$  contributes 300 events,  $^{133}\text{Xe}$  contributes 500 events, and background contributes 1000 events. The spectrum is here divided into 10 subregions

Once the spectra are generated, counts in the regions are summed. The resulting sums are converted to vectors, normalized, and placed into the linear system

described in eqn. (1). The system is then solved iteratively using maximum likelihood and relative weights are determined. Iterations halt when all isotopes are converged to within some error between current and previous iteration, which is set by the user.

#### ***4.6.2. Initial Investigations***

The first phase of investigation involved simple region definitions that closely mirrored the traditional ROIs as shown in Fig. 18; i.e.: much of the spectrum was entirely neglected in the solve, including a large part of the Compton region of  $^{135}\text{Xe}$ . Several synthetic experimental spectra were generated using different percentages of the independent radioxenon isotopes, with varying success rates in terms of convergence and accurate results. All trials used a  $< 1\%$  difference between the current and the previous iteration for estimated contribution of each radioxenon isotope as a convergence condition. In these initial trials, the X-ray decay path and the gamma decay path from  $^{133}\text{Xe}$  was considered, for the sake of the solve, to be separate entities. This was later dropped in favor of using the full  $^{133}\text{Xe}$  spectrum as one single unit. The 45 keV C.E. signature is also not included for  $^{133}\text{Xe}$ . Background was not considered.

Solves were attempted in a handful of cases, with one particularly elucidating case chosen for discussion. To make this experimental spectrum 90 interactions from  $^{135}\text{Xe}$ , 90 from  $^{131\text{m}}\text{Xe}$ , 90 from  $^{133\text{m}}\text{Xe}$ , 45 from the gamma region of  $^{133}\text{Xe}$ , and 45 from the X-ray region of  $^{133}\text{Xe}$  were randomly selected from the library simulation files and concatenated together. This dataset can be seen in Fig. 90, with the results from the solves using no sub-sectioning, 7-region sub-sectioning, and the standard SDAT method using a maximum likelihood solver, shown in Table 11. Note that there are some events from  $^{135}\text{Xe}$  that fall outside the user defined large region, meaning that they are effectively ignored with this initial implementation (which only looks at events inside the boxes). The fact that results quite close to the true values implies some robustness to the method.

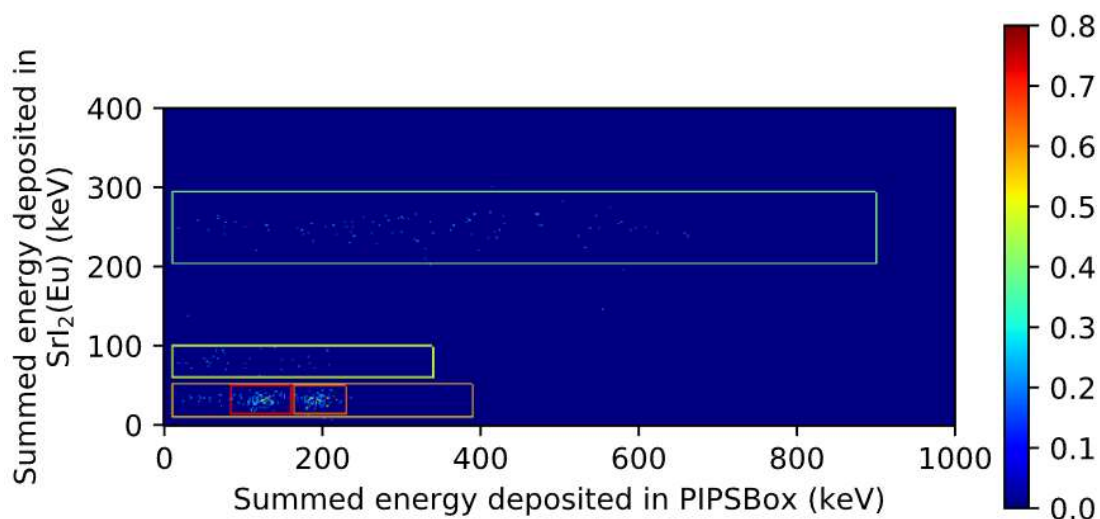


**Fig. 90.** Experimental spectrum for a low count rate scenario. The results of the solves for this data set are shown in Table 11

**Table 11.** Results of a few different trials of the dataset shown in Fig. 90. Note that exact run times vary based on the computer conducting the solve

Isotope	Real percentage	1 subregion/ROI	7 subregions/ROI	Maximum Likelihood SDAT implementation
$^{131\text{m}}\text{Xe}$	25 %	24.86%	24.41%	25.26%
$^{133\text{m}}\text{Xe}$	25 %	24.43%	25.14%	24.43%
$^{135}\text{Xe}$	25 %	25.1%	25.10%	25.01%
$^{133}\text{Xe}$ (gamma region)	12.5%	12.66%	12.66%	12.60%
$^{133}\text{Xe}$ (X-ray region)	12.5%	12.95%	12.70%	12.71%
Run Time	-	$0.63 \pm 0.02$ s	$0.65 \pm 0.03$ s	$18.1 \pm 0.1$ s

The new method is observed to perform competitively with the traditional SDAT solve, at a fraction of the time, though these early studies do not address the toxic effects of background. Aside from improvement in runtime, this study did not indicate superior performance using the new method.

Another solve was conducted to see when the algorithm would “break.” An experimental spectrum was generated using only 1 count from each of the 5 library spectra. As expected, the results were not correct—however, even in these extremely small count rate situations, when using 7 subregions/ROI the algorithm indicated ~20% for  $^{131\text{m}}\text{Xe}$ ,  $^{135}\text{Xe}$ , and  $^{133}\text{Xe}$  (gamma), 0% for  $^{133\text{m}}\text{Xe}$ , and 40% for  $^{133}\text{Xe}$  (X-ray). Though this study did not indicate what impact background may have in this situation, it is worth noting that by comparison the standard SDAT method did not converge at all. This again demonstrates robustness to the method, albeit with simplified cases.

### ***4.6.3. Involved Investigations***

A battery of tests was conducted using synthetic experimental spectra composed of all the radioxenon isotopes (with all decay paths of  $^{133}\text{Xe}$  combined for the single isotope) and background in various ratios with each other. The different combinations of radioxenon isotopes comprising the synthetic experimental spectra in these trials are shown in Table 12. Two investigations were conducted: the first, where regions were modeled after those shown in Fig. 89, with 1 to 10 subregions in each larger region defined in an unfocused and evenly distributed way (e.g.: Fig. 89a), and the second, where the regions were more finely segmented along the ROI regions with high counting statistics and more coarsely segmented in the background regions and in the low counting statistics ROI regions. This focused segmentation pattern is shown in Fig. 91. In this plot, the segmentation in the key high-statistics regions of interest is so fine (with each section accounting for  $1\text{ keV}^2 - 9\text{ keV}^2$ ) that the individual segments are indistinguishable from each other. In addition to this, a minor qualitative examination was conducted where the broad ROI sectioning indicated in Fig. 90 were included as additional sections superimposed onto the sections shown in Fig. 91. This study was done to get a sense of possible benefits from using broadly defined additional statistical weighting in addition to fine region sectioning in key areas.

Due to the highly localized background spectrum, using the same background as a base to take samples to create the synthetic experimental spectrum and as the library background spectrum gave an unfair advantage to the traditional SDAT method, as the background bins lined up exactly. If the background is shifted in its entirety up in energy by one bin, the traditional SDAT method shows awful performance due to the background having no bins in common with the background utilized in the synthetic experimental spectrum. The work around to this was to use a Gaussian broadening filter on the library background spectrum to give the background some statistical spread. The spectrum was broadened five times, with each iteration using the previous broadened spectrum as an input. Synthetic experimental spectra that involve background were created using randomly sampled counts taken from this broadened library background. To improve the rigor of future results, the background spectrum should be taken over much longer periods to ascertain high statistics.

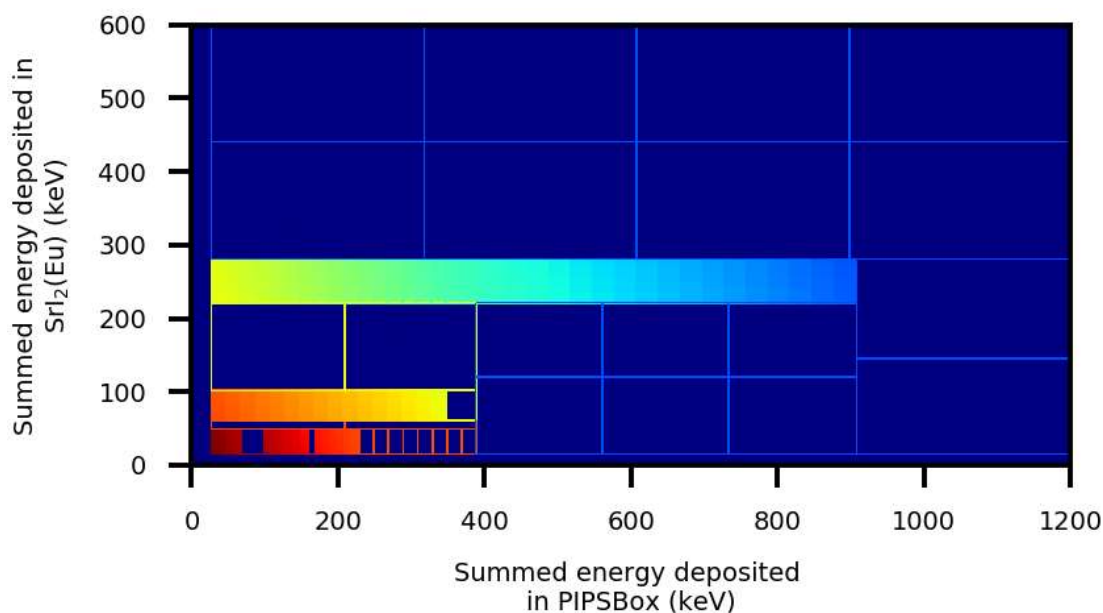


**Fig. 91.** Highly localized segmentation based on the high statistics regions of the traditional ROIs. The segmentation in these regions is very fine, and are indistinguishable from each other in this plot



**Table 12.** A list of different combinations of the library isotopes used to create various synthetic spectra

	Counts sampled from each library spectrum to make the synthetic experimental spectrum				
Trial	$^{131m}\text{Xe}$	$^{131m}\text{Xe}$	$^{131}\text{Xe}$	$^{135}\text{Xe}$	Background
1	0	0	100	500	100
2	0	0	100	500	1000
3	0	0	0	500	1000
4	0	0	0	100	1000
5	0	500	500	0	0
6	0	50	500	0	0
7	0	100	500	0	0
8	0	200	500	0	0
9	0	300	500	0	0
10	0	300	500	0	1000
11	100	100	0	0	1000
12	10	0	0	0	1000
13	0	0	0	100	500
14	0	0	100	0	500
15	0	100	0	0	500
16	100	0	0	0	500
17	0	0	0	0	20
18	0	0	0	20	0
19	0	0	20	0	0
20	0	20	0	0	0
21	20	0	0	0	0
22	0	0	0	0	1000
23	0	0	0	1000	0
24	0	0	1000	0	0
25	0	1000	0	0	0
26	1000	0	0	0	0
27	1000	500	500	500	0

The data for these solves are somewhat involved, are included in completeness in the Appendix for the unfocused and focused sectioning cases. Results from the overlapping case were universally unconvincing, indicating no improvements over the non-overlapping cases in any configuration, and as such their inclusion in the appendix was deemed unnecessary. The results in the appendix include the number of subregions per large region (for the unfocused cases), runtime (in seconds), iterations,

estimated contribution, true contribution, the difference between the estimated and the true, the average absolute value of those differences, and the average of the squared differences. Some key conclusions from these trials are enumerated below:

- In most cases, RSD does converge to contribution ratios that are close to the true ratios, usually within  $\pm 1\%$
- The RSD method significantly outperforms the SDAT method in terms of speed in all cases
- The SDAT method outperformed the RSD method in the majority of cases in terms of accuracy between the estimated and true percent contributions
- In no case did the SDAT method fail to converge. This was not the case in the RSD method, which failed to converge within 50 iterations in some select cases. However, this failure to converge did not inherently imply inaccuracy in the solution; in fact, in one case the solution that did not converge was the most accurate of all attempted solves (trial 6)
- The RSD method performs worst in comparison to the SDAT approach when dealing with experimental spectra with a low number of counts sourced from isotopes spread over large regions with and with large interfering background, such as in trials 13 and 14
- No universal trend existed between accuracy of results and the number of sections used when using unfocused sectioning (Fig. 89a)
- Accuracy was improved in the case when focused sectioning was used (Fig. 91) compared to the unfocused sectioning most clearly in cases when single isotopes were being observed (trials 22-26), while in single isotope cases with very low counts the relationship is less obvious (trials 17-21)
- There is no observable correlation between the number of regions and the speed of convergence ranging between 9 and 90 regions when using the unfocused sectioning (Fig. 89)
- Focused sectioning tends to significantly outperform unfocused sectioning when background is present, though SDAT usually outperforms both

From these trials, the RSD approach provides little improvement over the SDAT method except in terms of the computation time of the solve. The fact that RSD performs the most poorly relative to SDAT when background is included in the synthetic experimental spectrum could be due to the correlation between the library background spectrum and the synthetic spectrum giving an edge to SDAT. Another reason RSD could be outperformed due to SDAT could be poor statistics in the library spectra, as only  $2 \times 10^5$  particles were run for each isotope. Improving the robustness of the statistics in these library spectra could reduce bias in sampling for creating synthetic experimental spectra, bias which could overinflate the performance of the SDAT approach. In that vein, it is unclear if the performance of the algorithm in comparison to SDAT is due to poor performance from the RSD method or due to SDAT performance being bolstered due to bias.

This investigation of the RSD method has not been an exhaustive one. One avenue that was not investigated was non-rectangular sectioning: for example, combining many of the background sections into one single section having more than four sides, such as an “L” shape or a “C” shape. This approach would correlate the counts in various background regions of the spectrum that would otherwise not be correlated if using the purely rectangular sectioning approach. Another approach would be to size the sections around the traditional ROIs in ring-like shapes around the traditional peaks, representing the 2D gaussian shapes of said peaks. Additionally, an exhaustive optimization study could be beneficial: various sectioning approaches could be tested and compared to the ground truth, and an algorithm could adjust the sectioning to converge to the best, or one of the best, possible sectioning regimes. Such a study could be undertaken using unsupervised machine learning or other optimization techniques.

## 5. CONCLUSIONS AND FUTURE WORK

A prototype radioxenon detection system for treaty verification and threat reduction, comprised of  $\text{SrI}_2(\text{Eu})$ +SiPMs and a PIPSBox, was designed, constructed, and characterized using lab check sources and radioxenon gas samples. Coincidence events were identified in real-time using a custom 8-channel digital pulse processor with pattern recognition. Improving upon the PIPS-CZT system in terms of low energy resolution and efficiency, the PIPS- $\text{SrI}_2(\text{Eu})$  system utilizes novel D-shaped ultrabright  $\text{SrI}_2(\text{Eu})$  scintillators coupled to an array of SiPMs for photon detection and a PIPSBox for electron detection. The system is high resolution with small ROIs, and improves significantly upon the energy resolutions of common materials used in state-of-the-art radioxenon detection systems such as  $\text{NaI}(\text{Tl})$  and plastic scintillators. Memory effect is  $\sim 15\times$  reduced compared to plastic scintillators, with further improvements expected using better vacuum pumping equipment. Trigger walking in the photon detectors necessitate long time coincidence timing windows, which may be reduced through the implementation of a constant fraction discriminator trigger. When assuming a blank sample, neglecting memory effect, neglecting backscatter from  $^{133}\text{Xe}$  into the metastable ROIs, and estimating radon interference based on simulated and tabulated data, MDCs calculated using parameters from the Xenon International gas processing unit are well in agreement with CTBTO requirements of  $\leq 1 \text{ mBq/m}^3$  for  $^{133}\text{Xe}$  as well as in the objectives of the Xenon International system. Key future improvements to this work include:

- Implementation of a constant fraction discriminator trigger to reduce background count rates
- Application of a copper lining to the inner walls of the lead cave to shield against lead X-rays
- Rigorous characterization of the system using a radon generator
- Introduction of the temperature-sensitive microcontroller
- Mixed sample characterization
- Field testing at an IMS station

In addition to the experimental characterization of the PIPS-SrI<sub>2</sub>(Eu), a new spectral deconvolution approach based on regional sectioning was formulated. This approach uses regional sectioning to improve statistics in count-starved areas and maximum likelihood solve for spectral deconvolution. A Python package, `radioxenon_ml`, was written to accomplish this task. Tests were conducted using library spectra generated in MCNP and synthetic experimental spectra generated from randomly sampling these library spectra. This new method outperforms the traditional spectral deconvolution methods significantly in terms of execution time, but consistent improvement in the accuracy of determining relative library contributions to an experimental spectrum was not observed. No clear trends presented themselves in terms of number of regions selected and accuracy of results. This lackluster performance could be due to low statistics in the library spectra providing an edge to traditional fine spectral deconvolution methods. Future improvements to these efforts include different regional sectioning regimes or possibly automatic optimization of sectioning (e.g.: using machine learning) and general improvements to the readability and user-friendliness of the code for more general distribution.

## Bibliography

- [1] “The Treaty: CTBTO Preparatory Commission.” [Online]. Available: <https://www.ctbto.org/the-treaty/>. [Accessed: 28-Aug-2019].
- [2] CTBTO Preparatory Commission, “Overview of the Verification Regime,” 2012. [Online]. Available: <https://www.ctbto.org/verification-regime/monitoring-technologies-how-they-work/radionuclide-monitoring/>. [Accessed: 05-Jul-2016].
- [3] R. W. Perkins and L. A. Casey, “Radioxenons: Their role in monitoring a Comprehensive Test Ban Treaty,” DOE/RL--96-51, PNNL-SA--27750, 266641, Jun. 1996.
- [4] M. B. Kalinowski and C. Pistner, “Isotopic signature of atmospheric xenon released from light water reactors,” *J. Environ. Radioact.*, vol. 88, no. 3, pp. 215–235, Jan. 2006.
- [5] M. B. Kalinowski and M. P. Tuma, “Global radioxenon emission inventory based on nuclear power reactor reports,” *J. Environ. Radioact.*, vol. 100, no. 1, pp. 58–70, Jan. 2009.
- [6] M. B. Kalinowski *et al.*, “Discrimination of Nuclear Explosions against Civilian Sources Based on Atmospheric Xenon Isotopic Activity Ratios,” *Pure Appl. Geophys.*, vol. 167, no. 4–5, pp. 517–539, May 2010.
- [7] P. Burnard, Ed., *The Noble Gases as Geochemical Tracers*. Berlin, Heidelberg: Springer Berlin Heidelberg, 2013.
- [8] K. B. Olsen *et al.*, “Noble gas migration experiment to support the detection of underground nuclear explosions,” *J. Radioanal. Nucl. Chem.*, vol. 307, no. 3, pp. 2603–2610, Mar. 2016.
- [9] D. A. Haas *et al.*, “Improved performance comparisons of radioxenon systems for low level releases in nuclear explosion monitoring,” *J. Environ. Radioact.*, vol. 178–179, pp. 127–135, Nov. 2017.
- [10] T. W. Bowyer, K. H. Abel, and W. K. Hensley, “Automatic radioxenon analyzer for CTBT monitoring,” PNNL--11424, 431123, Dec. 1996.

- [11] M. Auer, T. Kumberg, H. Sartorius, B. Wernsperger, and C. Schlosser, “Ten Years of Development of Equipment for Measurement of Atmospheric Radioactive Xenon for the Verification of the CTBT,” *Pure Appl. Geophys.*, vol. 167, no. 4–5, pp. 471–486, May 2010.
- [12] A. Ringbom, T. Larson, A. Axelsson, K. Elmgren, and C. Johansson, “SAUNA—a system for automatic sampling, processing, and analysis of radioactive xenon,” *Nucl. Instrum. Methods Phys. Res. Sect. Accel. Spectrometers Detect. Assoc. Equip.*, vol. 508, no. 3, pp. 542–553, Aug. 2003.
- [13] Y. V. Dubasov *et al.*, “The АРИКC-01 Automatic Facility for Measuring Concentrations of Radioactive Xenon Isotopes in the Atmosphere,” *Instrum. Exp. Tech.*, vol. 48, no. 3, pp. 373–379, 2005.
- [14] J. McIntyre *et al.*, “Measurements of ambient radioxenon levels using the automated radioxenon sampler/analyzer (ARSA),” *J. Radioanal. Nucl. Chem.*, vol. 248, no. 3, pp. 629–635, 2001.
- [15] J. C. Hayes, “Requirements for Xenon International: Revision 1,” Pacific Northwest National Laboratory (PNNL), Richland, WA (US), PNNL-22227 (Rev 1), Dec. 2015.
- [16] J.-P. Fontaine, F. Pointurier, X. Blanchard, and T. Taffary, “Atmospheric xenon radioactive isotope monitoring,” *J. Environ. Radioact.*, vol. 72, no. 1–2, pp. 129–135, Jan. 2004.
- [17] G. Le Petit *et al.*, “Spalax<sup>TM</sup> new generation: A sensitive and selective noble gas system for nuclear explosion monitoring,” *Appl. Radiat. Isot.*, vol. 103, pp. 102–114, Sep. 2015.
- [18] M. W. Cooper, J. C. Hayes, B. T. Schrom, J. I. McIntyre, and J. H. Ely, “Minimum Detectable Concentration and Concentration Calculations,” PNNL-25418, 1526738, May 2016.
- [19] S. Biegalski, A. Flory, D. Haas, J. Ely, and M. Cooper, “SDAT implementation for the analysis of radioxenon  $\beta$ - $\gamma$  Coincidence spectra,” *J. Radioanal. Nucl. Chem.*, no. 296, pp. 471–476, Sep. 2012.

- [20] L. Ranjbar, “A Two-element CZT-based Radioxenon Detection System for Nuclear Weapon Test Monitoring,” PhD Dissertation, Oregon State University, Corvallis, OR, 2016.
- [21] S. A. Czyz, “A Compact Radioxenon Detection System Using CZT, an Array of SiPMs, and a Plastic Scintillator,” Master’s Thesis, Oregon State University, Corvallis, OR, 2016.
- [22] A. M. Alhawsawi, “Development of a CZT-Silicon Detection System in Support of the Comprehensive Nuclear-Test-Ban Treaty,” PhD Dissertation, Oregon State University, Corvallis, OR, 2017.
- [23] H. R. Gadey, A. T. Farsoni, S. A. Czyz, and K. D. McGee, “A stilbene - CdZnTe based radioxenon detection system,” *J. Environ. Radioact.*, vol. 204, pp. 117–124, Aug. 2019.
- [24] C. J. Werner (editor), “MCNP Users Manual - Code Version 6.2,” Los Alamos National Laboratory, Los Alamos, NM, LA-UR-17-29981, 2017.
- [25] J. H. Ely, M. W. Cooper, J. C. Hayes, T. R. Heimbigner, J. I. McIntyre, and B. T. Schrom, “Final Technical Report on Radioxenon Event Analysis,” PNNL-22308, 1088637, Mar. 2013.
- [26] T. R. Heimbigner, J. I. McIntyre, T. W. Bowyer, J. C. Hayes, and M. E. Panisko, “Environmental monitoring of radioxenon in support of the radionuclide measurement system of the International Monitoring System,” in *Proceedings of the 24th Seismic Research Review—Nuclear Explosion Monitoring: Innovation and Integration*, 2002, pp. 694–700.
- [27] P. R. J. Saey, “The influence of radiopharmaceutical isotope production on the global radioxenon background,” *J. Environ. Radioact.*, vol. 100, no. 5, pp. 396–406, May 2009.
- [28] IAEA, “Nuclear Data for Safeguards- C-3. Cumulative Fission Yields.” [Online]. Available: <https://www-nds.iaea.org/sgnucdat/c3.htm>. [Accessed: 02-Sep-2019].



- [29] T. W. Bowyer, K. H. Abel, W. K. Hensley, M. E. Panisko, and R. W. Perkins, “Ambient  $^{133}\text{Xe}$  levels in the Northeast US,” *J. Environ. Radioact.*, vol. 37, no. 2, pp. 143–153, Jan. 1997.
- [30] F. J. Klingberg, S. R. Biegalski, A. Prinke, D. A. Haas, and J. D. Lowrey, “Analysis of  $^{125}\text{Xe}$  electron–photon coincidence decay,” *J. Radioanal. Nucl. Chem.*, vol. 307, no. 3, pp. 1933–1939, Mar. 2016.
- [31] F. J. Klingberg, S. R. Biegalski, D. Haas, and A. Prinke, “ $^{127}\text{Xe}$  coincidence decay analysis in support of CTBT verification,” *J. Radioanal. Nucl. Chem.*, vol. 305, no. 1, pp. 225–232, Jul. 2015.
- [32] J. I. McIntyre *et al.*, “Measurements of Argon-39 at the U20az underground nuclear explosion site,” *J. Environ. Radioact.*, vol. 178–179, pp. 28–35, Nov. 2017.
- [33] C. R. Carrigan, R. A. Heinle, G. B. Hudson, J. J. Nitao, and J. J. Zucca, “Trace gas emissions on geological faults as indicators of underground nuclear testing,” *Nature*, vol. 382, no. 6591, pp. 528–531, Aug. 1996.
- [34] M. B. Kalinowski, “Characterisation of prompt and delayed atmospheric radioactivity releases from underground nuclear tests at Nevada as a function of release time,” *J. Environ. Radioact.*, vol. 102, no. 9, pp. 824–836, Sep. 2011.
- [35] C. R. Carrigan, Y. Sun, and M. D. Simpson, “The characteristic release of noble gases from an underground nuclear explosion,” *J. Environ. Radioact.*, vol. 196, pp. 91–97, Jan. 2019.
- [36] I. Pisso *et al.*, “The Lagrangian particle dispersion model FLEXPART version 10.3,” *Geosci. Model Dev. Discuss.*, pp. 1–67, Jan. 2019.
- [37] Y. Hao, “Overview of NUFT: A Versatile Numerical Model for Simulating Flow and Reactive Transport in Porous Media,” in *Groundwater Reactive Transport Models*, F. Zhang, G.-T. (George) Yeh, and J. C. Parker, Eds. BENTHAM SCIENCE PUBLISHERS, 2012, pp. 212–239.

- [38] Kenneth Krane, “12.8: Nuclear Structure and Radioactivity- Beta Decay,” in *Modern Physics*, Second Ed., Oregon State University, Corvallis, OR: John Wiley & Sons, Inc.
- [39] G. F. Knoll, “Radiation Sources,” in *Radiation Detection and Measurement*, 4th ed., John Wiley & Sons, Inc., 2000, p. 4.
- [40] P. L. Reeder and T. W. Bowyer, “Xe isotope detection and discrimination using beta spectroscopy with coincident gamma spectroscopy,” *Nucl. Instrum. Methods Phys. Res. Sect. Accel. Spectrometers Detect. Assoc. Equip.*, vol. 408, no. 2–3, pp. 582–590, May 1998.
- [41] Mirion Technologies, “Gamma-Ray Coincidence Counting Techniques.” [Online]. Available: <https://www.mirion.com/learning-center/lab-experiments/gamma-ray-coincidence-counting-techniques-lab-experiment>. [Accessed: 03-Sep-2019].
- [42] Robert N. Cherry, Jr., “Chapter 48 - Radiation: Ionizing,” *Encyclopaedia of Occupational Health and Safety, Fourth Edition*. [Online]. Available: <http://www.ilocis.org/documents/chpt48e.htm>. [Accessed: 03-Sep-2019].
- [43] “National Nuclear Data Center.” [Online]. Available: <http://www.nndc.bnl.gov/>. [Accessed: 09-Oct-2018].
- [44] L. Ranjbar, A. T. Farsoni, and E. M. Becker, “A CZT-based radioxenon detection system in support of the Comprehensive Nuclear-Test-Ban Treaty,” *J. Radioanal. Nucl. Chem.*, vol. 310, no. 3, pp. 969–978, Dec. 2016.
- [45] S. A. Czyz *et al.*, “A radioxenon detection system using PIPS and CZT,” *J. Radioanal. Nucl. Chem.*, vol. 319, no. 3, pp. 703–715, Mar. 2019.
- [46] K. M. Foltz Biegalski and S. R. Biegalski, “Deconvolution of three-dimensional beta-gamma coincidence spectra from xenon sampling and measurement units,” *J. Radioanal. Nucl. Chem.*, vol. 263, no. 1, pp. 259–265, Jan. 2005.
- [47] G. F. Knoll, “Scintillation Detector Principles,” in *Radiation Detection and Measurement*, 4th ed., John Wiley & Sons, Inc., 2000, pp. 220–224.

- [48] A. T. Farsoni, “Scintillation Detectors,” Oregon State University, 2015.
- [49] Inrad Optics, “Scintinel Stilbene Single Crystals,” Inrad Optics, 181 Legrand Avenue Northvale, NJ 07647, Data Sheet.
- [50] L. Bläckberg *et al.*, “Investigations of surface coatings to reduce memory effect in plastic scintillator detectors used for radioxenon detection,” *Nucl. Instrum. Methods Phys. Res. Sect. Accel. Spectrometers Detect. Assoc. Equip.*, vol. 656, no. 1, pp. 84–91, Nov. 2011.
- [51] E. Garutti, “Scintillation Detectors- Particle Detection via Luminescence,” University of Hamburg, 30-Apr-2012.
- [52] R. Hofstadter, “Europium Activated Strontium Iodide Scintillators,” US3373279A, 12-Mar-1968.
- [53] N. J. Cherepy *et al.*, “Strontium and barium iodide high light yield scintillators,” *Appl. Phys. Lett.*, vol. 92, no. 8, p. 083508, Feb. 2008.
- [54] N. Cherepy *et al.*, “Prospects for High Energy Resolution Gamma Ray Spectroscopy with Europium-Doped Strontium Iodide,” *MRS Proc.*, vol. 1164, Jan. 2009.
- [55] N. J. Cherepy *et al.*, “Performance of europium-doped strontium iodide, transparent ceramics and bismuth-loaded polymer scintillators,” 2011, p. 81420W.
- [56] N. J. Cherepy *et al.*, “Instrument Development and Gamma Spectroscopy With Strontium Iodide,” *IEEE Trans. Nucl. Sci.*, vol. 60, no. 2, pp. 955–958, Apr. 2013.
- [57] N. J. Cherepy *et al.*, “History and current status of strontium iodide scintillators,” in *Hard X-Ray, Gamma-Ray, and Neutron Detector Physics XIX*, San Diego, United States, 2017, p. 1.
- [58] P. R. Beck *et al.*, “Advancements in Gamma Spectrometers Based on Europium-doped Strontium Iodide and Characterization of its Gamma and Electron Response,” p. 4, Aug. 2014.

- [59] P. R. Beck *et al.*, “Strontium iodide instrument development for gamma spectroscopy and radioisotope identification,” presented at the SPIE Optical Engineering + Applications, San Diego, California, United States, 2014, p. 92130N.
- [60] C. M. Wilson *et al.*, “Strontium iodide scintillators for high energy resolution gamma ray spectroscopy,” presented at the Optical Engineering + Applications, San Diego, California, USA, 2008, p. 707917.
- [61] R. S. Perea *et al.*, “Scintillation properties of strontium iodide doped with europium for high-energy astrophysical detectors: nonproportionality as a function of temperature and at high gamma-ray energies,” *J. Astron. Telesc. Instrum. Syst.*, vol. 1, no. 1, p. 016002, Oct. 2014.
- [62] CapeSym, “SrI2(Eu) Developer Kit,” CapeSym, Inc, 6 Huron Dr. Suite 1B Natick, MA 01760, Data Sheet, 2017.
- [63] Saint-Gobain Crystals, “LYSO Scintillation Material,” Saint-Gobain Crystals, Data Sheet.
- [64] M. S. Alekhin, J. T. M. de Haas, K. W. Kramer, I. V. Khodyuk, L. de Vries, and P. Dorenbos, “Scintillation properties and self absorption in SrI2:Eu<sup>2+</sup>,” in *IEEE Nuclear Science Symposium & Medical Imaging Conference*, Knoxville, TN, 2010, pp. 1589–1599.
- [65] T. Huang, Q. Fu, S. Lin, and B. Wang, “NaI(Tl) scintillator read out with SiPM array for gamma spectrometer,” *Nucl. Instrum. Methods Phys. Res. Sect. Accel. Spectrometers Detect. Assoc. Equip.*, vol. 851, pp. 118–124, Apr. 2017.
- [66] G. Baldwin, “Uranium Enrichment Determination with Commercial CZT Detectors and a Non-proprietary analysis Algorithm,” Y-12 National Security Complex, 18-Jul-2013.
- [67] A. T. Farsoni, “Solid State Detectors,” Oregon State University, 2015.
- [68] G. F. Knoll, “Semiconductor Diode Detectors,” in *Radiation Detection and Measurement*, 4th ed., John Wiley & Sons, Inc., 2000.

- [69] G. F. Knoll, "Germanium Gamma-Ray Detectors," in *Radiation Detection and Measurement*, 4th ed., John Wiley & Sons, Inc., 2000.
- [70] V. Saveliev, "Silicon Photomultiplier - New Era of Photon Detection," in *Advances in Optical and Photonic Devices*, K. Young, Ed. InTech, 2010.
- [71] H. Shepard and S. Czyz, "Case #18058 CANBERRA Services Contact Form - U.S.," 06-Feb-2018.
- [72] SensL, "Introduction to the SiPM- Technical Note," SensL, Cork, Ireland, Technical Note, Feb. 2017.
- [73] S. Krishnamoorthy, "(2011) (Krishnamoorthy) A Light-Sharing Approach to High-Resolution 3D Gamma-Ray Detection for Positron Emission Tomography.pdf," Dissertation, Stony Brook University, Stony Brook, NY, 2012.
- [74] D. Renker, "Geiger-mode avalanche photodiodes, history, properties and problems," *Nucl. Instrum. Methods Phys. Res. Sect. Accel. Spectrometers Detect. Assoc. Equip.*, vol. 567, no. 1, pp. 48–56, Nov. 2006.
- [75] KETEK, "SiPM WORKING PRINCIPLE," *KETEK GmbH*. [Online]. Available: <https://www.ketek.net/sipm/technology/working-principle/>. [Accessed: 22-Aug-2018].
- [76] KETEK, "Microcell Construction." 2016.
- [77] KETEK, "Silicon photomultipliers (SiPM)," *KETEK GmbH*. [Online]. Available: <https://www.ketek.net/sipm/>. [Accessed: 05-Sep-2019].
- [78] Hamamatsu Photonics, "Photomultiplier Tubes Construction and Operating Characteristics Connections to External Circuits." HAMAMATSU PHOTONICS K.K., Electron Tube Center, Jan-1998.
- [79] S. Seifert *et al.*, "Simulation of Silicon Photomultiplier Signals," *IEEE Trans. Nucl. Sci.*, vol. 56, no. 6, pp. 3726–3733, Dec. 2009.
- [80] D. Marano *et al.*, "Improved SPICE electrical model of silicon photomultipliers," *Nucl. Instrum. Methods Phys. Res. Sect. Accel. Spectrometers Detect. Assoc. Equip.*, vol. 726, pp. 1–7, Oct. 2013.

- [81] F. Villa, Y. Zou, A. Dalla Mora, A. Tosi, and F. Zappa, “SPICE Electrical Models and Simulations of Silicon Photomultipliers,” *IEEE Trans. Nucl. Sci.*, vol. 62, no. 5, pp. 1950–1960, Oct. 2015.
- [82] McGee, Kacey D., “Silicon Photomultiplier Modeling of CsI(Tl) with Front End Electronics using a Monte Carlo Model.pdf,” Master’s Thesis, Oregon State University, Corvallis, OR, 2019.
- [83] “CANBERRA Industries - Worldwide Leader in Radiation Detectors & Nuclear Measurement.” [Online]. Available: <http://www.canberra.com/#2>. [Accessed: 08-Jun-2018].
- [84] G. Le Petit *et al.*, “Innovative concept for a major breakthrough in atmospheric radioactive xenon detection for nuclear explosion monitoring,” *J. Radioanal. Nucl. Chem.*, vol. 298, no. 2, pp. 1159–1169, Nov. 2013.
- [85] M. P. Foxe, B. W. Miller, R. Suarez, and J. C. Hayes, “A Figure-of-Merit for Beta Cell Detector Characterization,” PNNL--24760, 1258732, Sep. 2015.
- [86] M. P. Foxe, J. C. Hayes, M. F. Mayer, J. I. McIntyre, C. B. Sivals, and R. Suarez, “Characterization of a Commercial Silicon Beta Cell,” Pacific Northwest National Lab (PNNL), Richland, WA (US), PNNL--25297, 2016.
- [87] S. A. Czyz, A. T. Farsoni, and H. R. Gadey, “Evaluation of a semiconductor-based atmospheric radioxenon detection system,” *Nucl. Instrum. Methods Phys. Res. Sect. Accel. Spectrometers Detect. Assoc. Equip.*, p. 162614, Aug. 2019.
- [88] Mirion Technologies, “PIPS specification sheet, Series CD, Model PIPSBOX-2x1200-500A,” Canberra Industries, Meriden, CT, Data Sheet.
- [89] S. A. Czyz, A. T. Farsoni, and L. Ranjbar, “A prototype detection system for atmospheric monitoring of xenon radioisotopes,” *Nucl. Instrum. Methods Phys. Res. Sect. Accel. Spectrometers Detect. Assoc. Equip.*, vol. 884, pp. 64–69, Mar. 2018.
- [90] L. Bläckberg *et al.*, “Memory effect, resolution, and efficiency measurements of an Al<sub>2</sub>O<sub>3</sub> coated plastic scintillator used for radioxenon detection,” *Nucl.*

- Instrum. Methods Phys. Res. Sect. Accel. Spectrometers Detect. Assoc. Equip.*, vol. 714, pp. 128–135, Jun. 2013.
- [91] W. Warburton, W. Hennig, J. Bertrand, S. George, S. Biegalski, and P. BAA10, “Alpha-Al<sub>2</sub>O<sub>3</sub> diffusion barriers to eliminate the radioxenon memory effect in phoswich detectors,” in *34rd Monitoring Research Review*, 2012, pp. 731–740.
- [92] S. A. Czyz, A. T. Farsoni, H. R. Gadey, M. A. Mannino, L. Ranjbar, and A. M. Alhawsawi, “PIPS-CZT: A Compact, Low-Cost Atmospheric Radioxenon Detection System,” presented at the SORMA XVII Conference, University of Michigan, 14-Jun-2018.
- [93] Mirion Technologies, “PIPSBOX-2x1200-500PA Detectors,” Canberra, Data Sheet OPS-309, Jun. 2018.
- [94] “What is an FPGA? Field Programmable Gate Array.” [Online]. Available: <https://www.xilinx.com/products/silicon-devices/fpga/what-is-an-fpga.html>. [Accessed: 12-Sep-2019].
- [95] “What is an FPGA? Programming and FPGA Basics - INTEL® FPGAS,” *Intel*. [Online]. Available: <https://www.intel.com/content/www/us/en/products/programmable/fpga/new-to-fpgas/resource-center/overview.html>. [Accessed: 12-Sep-2019].
- [96] D. M. Harris and S. L. Harris, *Digital Design and Computer Architecture*, 2nd ed. Morgan Kaufmann, 2012.
- [97] “What is an API? (Application Programming Interface),” *MuleSoft*, 07-Dec-2016. [Online]. Available: <https://www.mulesoft.com/resources/api/what-is-an-api>. [Accessed: 12-Sep-2019].
- [98] “What Is an FPGA? An Introduction to Programmable Logic.” [Online]. Available: <https://www.allaboutcircuits.com/technical-articles/what-is-an-fpga-introduction-to-programmable-logic-fpga-vs-microcontroller/>. [Accessed: 12-Sep-2019].

- [99] N. Deshmukh, A. Prinke, B. Miller, and J. McIntyre, "Comparison of new and existing algorithms for the analysis of 2D radioxenon beta gamma spectra," *J. Radioanal. Nucl. Chem.*, vol. 311, no. 3, pp. 1849–1857, Mar. 2017.
- [100] W. Hennig *et al.*, "Study of silicon detectors for high resolution radioxenon measurements," presented at the 2011 Monitoring Research Review, 2011, vol. 296, pp. 695–707.
- [101] J. Schulze, M. Auer, and R. Werzi, "Low level radioactivity measurement in support of the CTBTO," *Appl. Radiat. Isot.*, vol. 53, no. 1–2, pp. 23–30, Jul. 2000.
- [102] M. W. Cooper *et al.*, "Radioxenon net count calculations revisited," *J. Radioanal. Nucl. Chem.*, vol. 321, no. 2, pp. 369–382, Aug. 2019.
- [103] K. M. F. Biegalski, S. R. Biegalski, and D. A. Haas, "Further Development of the Spectral Deconvolution Analysis Tool (SDAT) to Improve Counting Statistics," in *28th Seismic Research Review: Ground-Based Nuclear Explosion Monitoring Technologies*, 2006.
- [104] K. M. Foltz Biegalski and S. R. Biegalski, "Determining detection limits and minimum detectable concentrations for noble gas detectors utilizing beta-gamma coincidence systems," *J. Radioanal. Nucl. Chem.*, vol. 248, no. 3, pp. 673–682, Jun. 2001.
- [105] K. M. Foltz Biegalski, S. R. Biegalski, and D. A. Haas, "Performance evaluation of spectral deconvolution analysis tool (SDAT) software used for nuclear explosion radionuclide measurements," *J. Radioanal. Nucl. Chem.*, vol. 276, no. 2, pp. 407–413, May 2008.
- [106] S. R. F. Biegalski, K. M. Foltz Biegalski, and D. A. Haas, "SDAT: analysis of  $^{131}\text{mXe}$  with  $^{133}\text{Xe}$  interference," *J. Radioanal. Nucl. Chem.*, vol. 282, no. 3, pp. 715–719, Dec. 2009.
- [107] V. A. Muravsky, S. A. Tolstov, and A. L. Kholmetskii, "Comparison of the least squares and the maximum likelihood estimators for gamma-spectrometry," *Nucl. Instrum. Methods Phys. Res. Sect. B Beam Interact. Mater. At.*, vol. 145, no. 4, pp. 573–577, Dec. 1998.



- [108] “Least-Squares Fitting - MATLAB & Simulink.” [Online]. Available: <https://www.mathworks.com/help/curvefit/least-squares-fitting.html>. [Accessed: 13-Sep-2019].
- [109] A. C. Ph.D, “The Linear Algebra View of Least-Squares Regression,” *Medium*, 22-Dec-2016. [Online]. Available: <https://medium.com/@andrew.chamberlain/the-linear-algebra-view-of-least-squares-regression-f67044b7f39b>. [Accessed: 15-Sep-2019].
- [110] I. J. Myung, “Tutorial on maximum likelihood estimation,” *J. Math. Psychol.*, vol. 47, no. 1, pp. 90–100, Feb. 2003.
- [111] William H. Greene, “Maximum Likelihood Estimation,” in *Econometric Analysis*, 6th ed., Prentice Hall, 2007.
- [112] J. D. Lowrey and S. R. F. Biegalski, “Comparison of least-squares vs. maximum likelihood estimation for standard spectrum technique of  $\beta$ - $\gamma$  coincidence spectrum analysis,” *Nucl. Instrum. Methods Phys. Res. Sect. B Beam Interact. Mater. At.*, vol. 270, pp. 116–119, Jan. 2012.
- [113] L. Jánosy, *Theory and Practice of the Evaluation of Measurements*. Hungarian Academy of Sciences, Budapest, Hungary: Oxford University Press, 1965.
- [114] M. Zähringer and G. Kirchner, “Nuclide ratios and source identification from high-resolution gamma-ray spectra with Bayesian decision methods,” *Nucl. Instrum. Methods Phys. Res. Sect. Accel. Spectrometers Detect. Assoc. Equip.*, vol. 594, no. 3, pp. 400–406, Sep. 2008.
- [115] G. Kirchner, M. Steiner, and M. Zähringer, “A new approach to estimate nuclide ratios from measurements with activities close to background,” *J. Environ. Radioact.*, vol. 100, no. 6, pp. 484–488, Jun. 2009.
- [116] A. Vivier, G. Le Petit, B. Pigeon, and X. Blanchard, “Probabilistic assessment for a sample to be radioactive or not: application to radioxenon analysis,” *J. Radioanal. Nucl. Chem.*, vol. 282, no. 3, pp. 743–748, Dec. 2009.

- [117] L. A. Currie, “Limits for qualitative detection and quantitative determination,” *Anal. Chem.*, vol. 40, no. 3, pp. 586–593, 1968.
- [118] J. I. McIntyre, T. W. Bowyer, and P. L. Reeder, “Calculation of minimum-detectable-concentration levels of radioxenon isotopes using the PNNL ARSA system,” Pacific Northwest National Laboratory (PNNL), Richland, WA (US), PNNL-13102, Mar. 2006.
- [119] A. T. Farsoni, “Digital Filters in Radiation Detection and Spectroscopy (NE 537),” Oregon State University, Corvallis, OR, Jan-2015.
- [120] Xilinx Inc., “LogiCORE IP FIR Compiler v7.0 Product Guide for Vivado Design Suite,” Xilinx Inc., San Jose, CA, Data Sheet, Mar. 2013.
- [121] “Why use charge sensitive preamplifiers? – Cremat Inc.” .
- [122] H. Spieler, “Introduction to Radiation Detectors and Electronics V.5. Timing Measurements,” p. 20, 1998.
- [123] S. A. Czyz, “Preliminary Evaluation of Two Beta-Gamma Radioxenon Detection Systems,” presented at the CVT Workshop 2017, Ann Arbor, MI, 27-Nov-2017.
- [124] T. Schroettner, I. Schraick, T. Furch, and P. Kindl, “A high-resolution, multi-parameter,  $\beta$ - $\gamma$  coincidence,  $\mu$ - $\gamma$  anticoincidence system for radioxenon measurement,” *Nucl. Instrum. Methods Phys. Res. Sect. Accel. Spectrometers Detect. Assoc. Equip.*, vol. 621, no. 1–3, pp. 478–488, Sep. 2010.
- [125] M. E. Keillor *et al.*, “CASCADES: An Ultra-Low-Background Germanium Crystal Array at Pacific Northwest National Laboratory,” presented at the APPLICATIONS OF NUCLEAR TECHNIQUES: Eleventh International Conference, Crete, (Greece), 2011, pp. 208–215.
- [126] W. Hennig *et al.*, “Development of a COTS radioxenon detector system using Phoswich detectors and pulse shape analysis,” presented at the 2008 Monitoring Research Review, 2008.

- [127] C. E. Cox *et al.*, “A 24-element Silicon PIN diode detector for high resolution radioxenon measurements using simultaneous X-ray and electron spectroscopy,” in *Nuclear Science Symposium and Medical Imaging Conference (NSS/MIC), 2013 IEEE*, 2013, pp. 1–7.
- [128] M. Shetty and D. Şahin, “Data acquisition and analysis software for gamma coincidence spectrometry,” *J. Radioanal. Nucl. Chem.*, vol. 309, no. 1, pp. 243–247, Jul. 2016.
- [129] N. Marković, P. Roos, and S. P. Nielsen, “Digital gamma-gamma coincidence HPGe system for environmental analysis,” *Appl. Radiat. Isot.*, vol. 126, pp. 194–196, Aug. 2017.
- [130] E. M. Becker, “Eight-Channel Digital Spectrometer for Coincidence Measurements in Multi-element Detectors,” presented at the CVT Workshop 2016, Ann Arbor, MI, 2016.
- [131] C. B. Sivels *et al.*, “Stilbene cell development to improve radioxenon detection,” *Nucl. Instrum. Methods Phys. Res. Sect. Accel. Spectrometers Detect. Assoc. Equip.*, vol. 923, pp. 72–78, Apr. 2019.
- [132] T. W. Bowyer *et al.*, “Automated separation and measurement of radioxenon for the Comprehensive Test Ban Treaty,” *J. Radioanal. Nucl. Chem.*, vol. 235, no. 1–2, pp. 77–82, Sep. 1998.
- [133] J. C. Hayes *et al.*, “Operations of the Automated Radioxenon Sampler-Analyzer- ARSA,” in *21st Seismic Research Symposium: Technologies for Monitoring The Comprehensive Nuclear-Test-Ban Treaty*, Las Vegas, Nevada, 1999, pp. 249–260.
- [134] T. R. Heimbigner *et al.*, “The DOE Automated Radioxenon Sampler-Analyzer (ARSA) Beta-Gamma Coincidence Spectrometer Data Analyzer,” in *Proceedings of the 22nd Annual DoD/DOE Seismic Research Symposium, Planning for Verification of and Compliance with the Comprehensive Nuclear-Test-Ban Treaty (CTBT)*, 2000.

- [135] P. E. Dresel and S. R. Waichler, “Evaluation of Xenon Gas Detection as a Means for Identifying Buried Transuranic Waste at the Radioactive Waste Management Complex, Idaho National Environmental and Engineering Laboratory,” PNNL-14617, 15010628, Apr. 2004.
- [136] P. L. Reeder, T. W. Bowyer, J. I. McIntyre, W. K. Pitts, A. Ringbom, and C. Johansson, “Gain calibration of a  $\beta/\gamma$  coincidence spectrometer for automated radioxenon analysis,” *Nucl. Instrum. Methods Phys. Res. Sect. Accel. Spectrometers Detect. Assoc. Equip.*, vol. 521, no. 2–3, pp. 586–599, Apr. 2004.
- [137] M. W. Cooper *et al.*, “Improved  $\beta$ - $\gamma$  coincidence detector for radioxenon detection,” *Proc. 27th Seism. Res. Rev. Ground-Based Nucl. Explos. Monit. Technol.*, pp. 779–786, 2005.
- [138] C. E. Seifert *et al.*, “Mitigation of memory effects in beta scintillation cells for radioactive gas detection,” *Proc. 27th Seism. Res. Rev. Ground-Based Nucl. Explos. Monit. Technol.*, pp. 804–814, 2005.
- [139] M. W. Cooper *et al.*, “Automated QA/QC Check for Beta-Gamma Coincidence Detector,” presented at the 29th Monitoring Research Review, 2007, pp. 739–746.
- [140] M. W. Cooper *et al.*, “Redesigned  $\beta$ - $\gamma$  radioxenon detector,” *Nucl. Instrum. Methods Phys. Res. Sect. Accel. Spectrometers Detect. Assoc. Equip.*, vol. 579, no. 1, pp. 426–430, Aug. 2007.
- [141] D. A. Haas, S. R. Biegalski, and K. M. Foltz Biegalski, “Modeling  $\beta$ - $\gamma$  coincidence spectra of  $^{131}\text{mXe}$ ,  $^{133}\text{Xe}$ ,  $^{133}\text{mXe}$ , and  $^{135}\text{Xe}$ ,” *J. Radioanal. Nucl. Chem.*, vol. 277, no. 3, pp. 561–565, Sep. 2008.
- [142] J. I. McIntyre *et al.*, “Concentration independent calibration of  $\beta$ - $\gamma$  coincidence detector using  $^{131}\text{mXe}$  and  $^{133}\text{Xe}$ ,” *J. Radioanal. Nucl. Chem.*, vol. 282, no. 3, pp. 755–759, Dec. 2009.
- [143] “Xenon International | Teledyne Brown Engineering.” [Online]. Available: <https://tbe.com/energy/xenon-international>. [Accessed: 24-Sep-2019].

- [144] A. Ringbom, R. C. Haight, M. B. Chadwick, T. Kawano, and P. Talou, “Verifying the Comprehensive Nuclear-Test-Ban Treaty by Radioxenon Monitoring,” in *AIP Conference Proceedings*, 2005, vol. 769, pp. 1693–1697.
- [145] A. Axelsson and A. Ringbom, “Xenon air activity concentration analysis from coincidence data,” FOI- Swedish Defense Research Agency, Stockholm, Sweden, User Report FOI-R-0913-SE, 2003.
- [146] F. Postelt, “Capability to detect and categorise real and hypothetical atmospheric concentrations of radioxenon for Comprehensive Nuclear- Test-Ban Treaty verification,” Diploma Thesis, University of Hamburg, Hamburg, Germany, 2013.
- [147] T. W. Bowyer *et al.*, “Measurements of Worldwide Radioxenon Backgrounds - The ‘EU’ Project,” Technical Report PNNL-18783, 1134003, Sep. 2009.
- [148] A. Ringbom *et al.*, “Radioxenon detections in the CTBT international monitoring system likely related to the announced nuclear test in North Korea on February 12, 2013,” *J. Environ. Radioact.*, vol. 128, pp. 47–63, Feb. 2014.
- [149] “Product Range - The SAUNA concept.” [Online]. Available: <https://www.sensorsystems.se/3/our-products>. [Accessed: 24-Sep-2019].
- [150] Scienta Sensor Systems, “SAUNA-III- A fully automated radionuclide continuous monitoring system,” Scienta Sensor Systems AB, Uppsala, Sweden, Data Sheet, 2017.
- [151] Y. S. Popov, N. Kazarinov, V. Y. Popov, Y. M. Rykov, and N. Skirda, “Measuring low activities of fission-product xenon isotopes using the  $\beta$ - $\gamma$  coincidence method,” *Instrum. Exp. Tech.*, vol. 48, no. 3, pp. 380–386, 2005.
- [152] V. V. Prelovskii, N. M. Kazarinov, A. Yu. Donets, V. Yu. Popov, I. Yu. Popov, and N. V. Skirda, “The ARIX-03F mobile semiautomatic facility for measuring low concentrations of radioactive xenon isotopes in air and subsoil gas,” *Instrum. Exp. Tech.*, vol. 50, no. 3, pp. 393–397, May 2007.
- [153] A. T. Farsoni, B. Alemayehu, A. Alhawsawi, and E. M. Becker, “Real-time pulse-shape discrimination and beta–gamma coincidence detection in field-

- programmable gate array,” *Nucl. Instrum. Methods Phys. Res. Sect. Accel. Spectrometers Detect. Assoc. Equip.*, vol. 712, pp. 75–82, Jun. 2013.
- [154] B. Alemayehu, “Real-time Radioxenon Measurement using a Compton-suppressed Well-type Phoswich Detector for Nuclear Explosion Monitoring,” PhD Dissertation, Oregon State University, Corvallis, OR, 2013.
- [155] J. H. Ely *et al.*, “Novel beta-gamma coincidence measurements using phoswich detectors,” in *25th Seismic Research Review*, 2005, pp. 533–541.
- [156] A. T. Farsoni and D. M. Hamby, “MCNP analysis of a multilayer phoswich detector for  $\beta$ -particle dosimetry and spectroscopy,” *Nucl. Instrum. Methods Phys. Res. Sect. Accel. Spectrometers Detect. Assoc. Equip.*, vol. 555, no. 1–2, pp. 225–230, Dec. 2005.
- [157] J. I. McIntyre *et al.*, “Beta-Gamma Coincidence Counting Using an Yttrium Aluminum Perovskite and Bismuth Germanate Phoswich Scintillator,” 2005, vol. 3, pp. 1301–1304.
- [158] W. Hennig, H. Tan, A. Fallu-Labruyere, W. K. Warburton, J. I. McIntyre, and A. Gleyzer, “Design of a phoswich well detector for radioxenon monitoring,” *Proc. 28th Seism. Res. Rev. Ground Based Nucl. Explos. Monit. Technol.*, pp. 801–810, 2006.
- [159] A. U. Lopez, “Determination of Phoswich detector response using MCNP analysis to enhance Radioxenon measurement,” 2006.
- [160] A. T. Farsoni, D. M. Hamby, K. D. Roop, and S. E. Jones, “A Two-Channel Phoswich Detector for Dual and Triple Coincidence Measurements of Radioxenon Isotopes,” in *Proceedings of the 29th Monitoring Research Review: Ground-Based Nuclear Explosion Monitoring Technologies*, Denver, CO, 2007.
- [161] A. T. Farsoni, B. Alemayehu, A. Alhawsawi, and E. M. Becker, “A Phoswich Detector With Compton Suppression Capability for Radioxenon Measurements,” *IEEE Trans. Nucl. Sci.*, vol. 60, no. 1, pp. 456–464, Feb. 2013.

- [162] B. Alemayehu, A. T. Farsoni, L. Ranjbar, and E. M. Becker, “A Well-Type Phoswich Detector for Nuclear Explosion Monitoring,” *J. Radioanal. Nucl. Chem.*, vol. 301, no. 2, pp. 323–332, Aug. 2014.
- [163] W. Hennig, S. J. Asztalos, W. K. Warburton, A. Fallu-Labruyere, A. Samie, and P. Mekarski, “Development of a Phoswich Detector for Radioxenon Field Measurements,” *IEEE Trans. Nucl. Sci.*, vol. 61, no. 5, pp. 2778–2785, Oct. 2014.
- [164] W. Hennig, “Development of a phoswich detector for radioxenon field measurements,” 2014.
- [165] P. Mekarski, W. Zhang, K. Ungar, M. Bean, and E. Korpach, “Monte Carlo simulation of a PhosWatch detector using Geant4 for xenon isotope beta–gamma coincidence spectrum profile and detection efficiency calculations,” *Appl. Radiat. Isot.*, vol. 67, no. 10, pp. 1957–1963, Oct. 2009.
- [166] W. Hennig *et al.*, “Radioxenon measurements with the Phoswatch detector system,” *Proc. 2009 Monit. Res. Rev. Ground-Based Nucl. Explos. Monit. Technol. UR-09-05276*, vol. 2, pp. 641–652, 2009.
- [167] W. Hennig, Hui Tan, W. K. Warburton, and J. I. McIntyre, “Single-channel beta-gamma coincidence detection of radioactive xenon using digital pulse shape analysis of phoswich detector signals,” *IEEE Trans. Nucl. Sci.*, vol. 53, no. 2, pp. 620–624, Apr. 2006.
- [168] W. Hennig, H. Tan, W. K. Warburton, and J. I. McIntyre, “Single Channel Beta-Gamma Coincidence Detection of Radioactive Xenon Using Digital Pulse Shape Analysis of Phoswich Detector Signals,” p. 5.
- [169] W. Hennig *et al.*, “Study of silicon detectors for high resolution radioxenon measurements,” *J. Radioanal. Nucl. Chem.*, vol. 296, no. 2, pp. 675–681, May 2013.
- [170] M. P. Foxe and J. I. McIntyre, “Testing of the KRI-developed Silicon PIN Radioxenon Detector,” PNNL--23995, 1258733, Jan. 2015.
- [171] C. B. Sivals, “Development of an Advanced Radioxenon Detector for Nuclear Explosion Monitoring,” University of Michigan, Ann Arbor, MI, 2018.

- [172] W. K. Warburton and W. Hennig, “Stilbene Research to Support a Portable b/g Scintillation Detector with Improved Radioxenon MDCs,” XIA LLC, 2014.
- [173] G. Le Petit, C. Jutier, P. Gross, and V. Greiner, “Low-level activity measurement of  $^{131}\text{Xe}$ ,  $^{133}\text{Xe}$ ,  $^{135}\text{Xe}$  and  $^{133}\text{Xe}$  in atmospheric air samples using high-resolution dual X- $\gamma$  spectrometry,” *Appl. Radiat. Isot.*, vol. 64, no. 10–11, pp. 1307–1312, Oct. 2006.
- [174] G. Le Petit *et al.*, “Contribution to the development of atmospheric radioxenon monitoring,” *J. Radioanal. Nucl. Chem.*, vol. 276, no. 2, pp. 391–398, May 2008.
- [175] T. J. Stocki *et al.*, “Automated radioxenon monitoring for the comprehensive nuclear-test-ban treaty in two distinctive locations: Ottawa and Tahiti,” *J. Environ. Radioact.*, vol. 80, no. 3, pp. 305–326, Jan. 2005.
- [176] T. J. Stocki *et al.*, “Low level noble gas measurements in the field and laboratory in support of the Comprehensive Nuclear-Test-Ban Treaty,” *Appl. Radiat. Isot.*, vol. 61, no. 2–3, pp. 231–235, Aug. 2004.
- [177] T. J. Stocki *et al.*, “Measurement and modelling of radioxenon plumes in the Ottawa Valley,” *J. Environ. Radioact.*, vol. 99, no. 11, pp. 1775–1788, Nov. 2008.
- [178] P. R. J. Saey and L.-E. De Geer, “Notes on radioxenon measurements for CTBT verification purposes,” *Appl. Radiat. Isot.*, vol. 63, no. 5–6, pp. 765–773, Nov. 2005.
- [179] P. R. J. Saey *et al.*, “A long distance measurement of radioxenon in Yellowknife, Canada, in late October 2006,” *Geophys. Res. Lett.*, vol. 34, no. 20, Oct. 2007.
- [180] A. Cagniant, G. Le Petit, P. Gross, G. Douysset, H. Richard-Bressand, and J.-P. Fontaine, “Improvements of low-level radioxenon detection sensitivity by a state-of-the art coincidence setup,” *Appl. Radiat. Isot.*, vol. 87, pp. 48–52, May 2014.



- [181] G. Le Petit *et al.*, “High Resolution Electron-Photon Detection System A Major Breakthrough for Radioxenon Monitoring,” presented at the 2015 CTBT Science & Technology Conference, Vienna, Austria, 22-Jun-2015.
- [182] A. Cagniant *et al.*, “SPALAX NG: A breakthrough in radioxenon field measurement,” *Appl. Radiat. Isot.*, vol. 134, pp. 461–465, Apr. 2018.
- [183] W. Li, “Latest Development on MARDS- an Argon-37 Detection System.pdf,” presented at the SnT 2015, Vienna, Austria, Jun-2015.
- [184] D. A. Haas *et al.*, “The science case for  $^{37}\text{Ar}$  as a monitor for underground nuclear explosions,” PNNL-19458, 992009, Jun. 2010.
- [185] P. N. Luke, “Single-polarity charge sensing in ionization detectors using coplanar electrodes,” *Appl. Phys. Lett.*, vol. 65, no. 22, pp. 2884–2886, Nov. 1994.
- [186] M. Amman and P. F. Luke, “Coplanar-grid detector with single-electrode readout,” in *Hard X-Ray and Gamma-Ray Detector Physics, Optics, and Applications*, 1997, vol. 3115, p. 205.
- [187] Z. He, “Review of the Shockley–Ramo theorem and its application in semiconductor gamma-ray detectors,” *Nucl. Instrum. Methods Phys. Res. Sect. Accel. Spectrometers Detect. Assoc. Equip.*, vol. 463, no. 1, pp. 250–267, 2001.
- [188] Kromek, Inc., “About CZT,” 2017. [Online]. Available: <http://www.kromek.com/index.php/technology-main-menu/about-czt>. [Accessed: 21-Jul-2017].
- [189] L. Ranjbar, A. T. Farsoni, and E. M. Becker, “ $^{135}\text{Xe}$  measurements with a two-element CZT-based radioxenon detector for nuclear explosion monitoring,” *J. Environ. Radioact.*, vol. 169–170, pp. 221–228, Apr. 2017.
- [190] S. A. Czyz and A. T. Farsoni, “A radioxenon detection system using CdZnTe, an array of SiPMs, and a plastic scintillator,” *J. Radioanal. Nucl. Chem.*, vol. 313, no. 1, pp. 131–140, Jul. 2017.
- [191] “Redlen Technologies.”.
- [192] S. Czyz, *radioxenon\_ml*. 2018.

- [193] L. J. Mitchell and B. Philips, “Characterization of strontium iodide scintillators with silicon photomultipliers,” *Nucl. Instrum. Methods Phys. Res. Sect. Accel. Spectrometers Detect. Assoc. Equip.*, vol. 820, pp. 95–101, Jun. 2016.
- [194] K. Shimazoe, A. Koyama, H. Takahashi, S. Sakuragi, and Y. Yamasaki, “Fabrication and characterization of rectangular strontium iodide scintillator coupled to TSV-MPPC array,” *Nucl. Instrum. Methods Phys. Res. Sect. Accel. Spectrometers Detect. Assoc. Equip.*, vol. 845, pp. 503–506, Feb. 2017.
- [195] F. A. Danevich *et al.*, “Impact of geometry on light collection efficiency of scintillation detectors for cryogenic rare event searches,” *Nucl. Instrum. Methods Phys. Res. Sect. B Beam Interact. Mater. At.*, vol. 336, pp. 26–30, Oct. 2014.
- [196] K. Shimazoe, A. Koyama, H. Takahashi, S. Sakuragi, and Y. Yamasaki, “Fabrication and characterization of cubic SrI 2 (Eu) scintillators for use in array detectors,” *Nucl. Instrum. Methods Phys. Res. Sect. Accel. Spectrometers Detect. Assoc. Equip.*, vol. 810, pp. 59–62, Feb. 2016.
- [197] SensL, “ArrayJ User Manual,” SensL, Cork, Ireland, User Manual, Mar. 2018.
- [198] SensL, “J-Series High PDE and Timing Resolution, TSV Package Datasheet,” SensL, Cork, Ireland, Data Sheet, Nov. 2016.
- [199] Cremat Inc., “CR-113-R2.1 charge sensitive preamplifier Application Guide,” Cremat Inc., Data Sheet, Oct. 2018.
- [200] M. Mannino, “Real-Time Temporal Gamma Spectroscopy in a Field-Programmable Gate Array,” presented at the 2017 IEEE Nuclear Science Symposium & Medical Imaging Conference, Atlanta, GA, 23-Oct-2017.
- [201] “OpalKelly - Xilinx and Altera FPGA Integration Modules.” [Online]. Available: <https://opalkelly.com/>. [Accessed: 08-Oct-2018].
- [202] opalkelly.com, “FrontPanel®,” *Opal Kelly*. [Online]. Available: <https://opalkelly.com/products/frontpanel/>. [Accessed: 12-Sep-2019].

- [203] Welch-Ilmvac, “Owner’s Manual for Duoseal Vacuum Pump Models: 1400B-01 & 3Z654,” 5621 W. Howard Street Niles, IL 60714, User Manual Part No. 67-2065 R1.0.
- [204] M. W. Cooper *et al.*, “Absolute Efficiency Calibration of a Beta-Gamma Detector,” *IEEE Trans. Nucl. Sci.*, vol. 60, no. 2, pp. 676–680, Apr. 2013.
- [205] Linear Technology Corporation, “LT8410/LT8410-1 - Ultralow Power Boost Converter with Output Disconnect,” Linear Technology Corporation, 1630 McCarthy Blvd., Milpitas, CA, Data Sheet, 2008.
- [206] E. Browne and R. B. Firestone, *Table of Radioactive Isotopes*. Lawrence Berkeley Laboratory, University of California: John Wiley & Sons, Inc., 1986.
- [207] ORTEC Inc, “Fast-Timing Discriminator Introduction,” AMETEK Advanced Measurement Technology, 801 South Illinois Ave., Oak Ridge, TN 37831-0895 U.S.A., Technical Note and Introduction.

## Appendix

The tables listed below reflect the trials as indicated in Table 12. Red highlights indicate worst performance, while green highlights indicate best performance. Columns highlighted completely in red indicate situations that did not converge within 50 iterations.

Trial 1	Subregions	1	2	3	4	5	6	7	8	9	10	Focus	SDAT
	Runtime (sec)	2.86	3.1	2.95	3.31	2.93	3.1	3.47	3.41	3.38	3.3	3.52	155.99
Estimates	Iterations	3	3	3	5	3	3	3	3	3	3	3	2
	Xe131m	0.54	0.51	0.39	0.45	0.44	0.44	0.55	0.48	0.47	0.57	0	0
	Xe133m	0	0	0	0	0	0	0	0	0	0	0	0
	Xe133	12.49	12.56	12.73	12.75	12.97	12.73	12.81	12.89	12.88	12.75	14.74	14.37
	Xe135	71.12	71.16	71.06	71.08	70.74	70.91	70.99	70.7	70.88	71.05	71.54	71.44
	Background	15.85	15.76	15.81	15.72	15.85	15.92	15.65	15.94	15.77	15.63	13.72	14.19
True Percent	Xe131m	0	0	0	0	0	0	0	0	0	0	0	0
	Xe133m	0	0	0	0	0	0	0	0	0	0	0	0
	Xe133	14.29	14.29	14.29	14.29	14.29	14.29	14.29	14.29	14.29	14.29	14.29	14.29
	Xe135	71.43	71.43	71.43	71.43	71.43	71.43	71.43	71.43	71.43	71.43	71.43	71.43
	Background	14.29	14.29	14.29	14.29	14.29	14.29	14.29	14.29	14.29	14.29	14.29	14.29
	Background	14.29	14.29	14.29	14.29	14.29	14.29	14.29	14.29	14.29	14.29	14.29	14.29
Difference (Est-True)	Xe131m	0.54	0.51	0.39	0.45	0.44	0.44	0.55	0.48	0.47	0.57	0	0
	Xe133m	0	0	0	0	0	0	0	0	0	0	0	0
	Xe133	-1.8	-1.73	-1.56	-1.54	-1.32	-1.56	-1.48	-1.4	-1.41	-1.54	0.45	0.08
	Xe135	-0.31	-0.27	-0.37	-0.35	-0.69	-0.52	-0.44	-0.73	-0.55	-0.38	0.11	0.01
	Background	1.56	1.47	1.52	1.43	1.56	1.63	1.36	1.65	1.48	1.34	-0.57	-0.1
	Background	1.56	1.47	1.52	1.43	1.56	1.63	1.36	1.65	1.48	1.34	-0.57	-0.1
ABS(diff.)	Xe131m	0.54	0.51	0.39	0.45	0.44	0.44	0.55	0.48	0.47	0.57	0	0
	Xe133m	0	0	0	0	0	0	0	0	0	0	0	0
	Xe133	1.8	1.73	1.56	1.54	1.32	1.56	1.48	1.4	1.41	1.54	0.45	0.08
	Xe135	0.31	0.27	0.37	0.35	0.69	0.52	0.44	0.73	0.55	0.38	0.11	0.01
	Background	1.56	1.47	1.52	1.43	1.56	1.63	1.36	1.65	1.48	1.34	0.57	0.1
	Background	1.56	1.47	1.52	1.43	1.56	1.63	1.36	1.65	1.48	1.34	0.57	0.1
AVG(ABS(diff.))		0.842	0.796	0.768	0.754	0.802	0.83	0.766	0.852	0.782	0.766	0.226	0.038
(diff)^2	Xe131m	0.2916	0.2601	0.1521	0.2025	0.1936	0.1936	0.3025	0.2304	0.2209	0.3249	0	0
	Xe133m	0	0	0	0	0	0	0	0	0	0	0	0
	Xe133	3.24	2.9929	2.4336	2.3716	1.7424	2.4336	2.1904	1.96	1.9881	2.3716	0.2025	0.0064
	Xe135	0.0961	0.0729	0.1369	0.1225	0.4761	0.2704	0.1936	0.5329	0.3025	0.1444	0.0121	0.0001
	Background	2.4336	2.1609	2.3104	2.0449	2.4336	2.6569	1.8496	2.7225	2.1904	1.7956	0.3249	0.01
	Background	2.4336	2.1609	2.3104	2.0449	2.4336	2.6569	1.8496	2.7225	2.1904	1.7956	0.3249	0.01
AVG((diff.)^2)		1.21226	1.09736	1.0066	0.9483	0.96914	1.1109	0.90722	1.08916	0.94038	0.9273	0.1079	0.0033

Trial 2	Subregions	1	2	3	4	5	6	7	8	9	10	Focus	SDAT
	Runtime (sec)	3.15	2.99	3.12	3.06	3.15	3.6	3.43	2.97	2.94	3.18	3.81	212.94
Estimates	Iterations	2	2	2	2	2	3	3	3	3	3	3	3
	Xe131m	0.41	0.05	0.04	0	0.15	0.12	0.02	0.02	0.06	0.01	0.23	0
	Xe133m	0.51	0.52	0.35	0.5	0.44	0.46	0.46	0.39	0.39	0.41	0	0
	Xe133	4.97	5.25	5.67	5.41	5.57	5.44	5.56	5.2	5.48	5.59	6.55	6.4
	Xe135	30.8	30.73	30.58	30.48	30.44	30.43	30.35	30.43	30.42	30.28	30.56	31.13
	Background	63.31	63.46	63.36	63.61	63.4	63.56	63.62	63.96	63.65	63.72	62.66	62.47
True Percent	Xe131m	0	0	0	0	0	0	0	0	0	0	0	0
	Xe133m	0	0	0	0	0	0	0	0	0	0	0	0
	Xe133	6.25	6.25	6.25	6.25	6.25	6.25	6.25	6.25	6.25	6.25	6.25	6.25
	Xe135	31.25	31.25	31.25	31.25	31.25	31.25	31.25	31.25	31.25	31.25	31.25	31.25
	Background	62.5	62.5	62.5	62.5	62.5	62.5	62.5	62.5	62.5	62.5	62.5	62.5
	Background	62.5	62.5	62.5	62.5	62.5	62.5	62.5	62.5	62.5	62.5	62.5	62.5
Difference (Est-True)	Xe131m	0.41	0.05	0.04	0	0.15	0.12	0.02	0.02	0.06	0.01	0.23	0
	Xe133m	0.51	0.52	0.35	0.5	0.44	0.46	0.46	0.39	0.39	0.41	0	0
	Xe133	-1.28	-1	-0.58	-0.84	-0.68	-0.81	-0.69	-1.05	-0.77	-0.66	0.3	0.15
	Xe135	-0.45	-0.52	-0.67	-0.77	-0.81	-0.82	-0.9	-0.82	-0.83	-0.97	-0.69	-0.12
	Background	0.81	0.96	0.86	1.11	0.9	1.06	1.12	1.46	1.15	1.22	0.16	-0.03
	Background	0.81	0.96	0.86	1.11	0.9	1.06	1.12	1.46	1.15	1.22	0.16	-0.03
ABS(diff.)	Xe131m	0.41	0.05	0.04	0	0.15	0.12	0.02	0.02	0.06	0.01	0.23	0
	Xe133m	0.51	0.52	0.35	0.5	0.44	0.46	0.46	0.39	0.39	0.41	0	0
	Xe133	1.28	1	0.58	0.84	0.68	0.81	0.69	1.05	0.77	0.66	0.3	0.15
	Xe135	0.45	0.52	0.67	0.77	0.81	0.82	0.9	0.82	0.83	0.97	0.69	0.12
	Background	0.81	0.96	0.86	1.11	0.9	1.06	1.12	1.46	1.15	1.22	0.16	0.03
	Background	0.81	0.96	0.86	1.11	0.9	1.06	1.12	1.46	1.15	1.22	0.16	0.03
AVG(ABS(diff.))		0.692	0.61	0.5	0.644	0.596	0.654	0.638	0.748	0.64	0.654	0.276	0.06
(diff)^2	Xe131m	0.1681	0.0025	0.0016	0	0.0225	0.0144	0.0004	0.0004	0.0036	0.0001	0.0529	0
	Xe133m	0.2601	0.2704	0.1225	0.25	0.1936	0.2116	0.2116	0.1521	0.1521	0.1681	0	0
	Xe133	1.6384	1	0.3364	0.7056	0.4624	0.6561	0.4761	1.1025	0.5929	0.4356	0.09	0.0225
	Xe135	0.2025	0.2704	0.4489	0.5929	0.6561	0.6724	0.81	0.6724	0.6889	0.9409	0.4761	0.0144
	Background	0.6561	0.9216	0.7396	1.2321	0.81	1.1236	1.2544	2.1316	1.3225	1.4884	0.0256	0.0009
	Background	0.6561	0.9216	0.7396	1.2321	0.81	1.1236	1.2544	2.1316	1.3225	1.4884	0.0256	0.0009
AVG((diff.)^2)		0.58504	0.49298	0.3298	0.55612	0.42892	0.53562	0.5505	0.8118	0.552	0.60662	0.12892	0.00756

Trial 3	Subregions	1	2	3	4	5	6	7	8	9	10	Focus	SDAT
	Runtime (sec)	3.33	3.29	3.17	2.83	3.1	3.58	3.26	3.42	3.33	3.67	3.62	159.15
	Iterations	1	2	3	3	3	3	2	3	3	3	2	2
Estimates	Xe131m	0	0	0	0	0	0	0	0	0	0	0	0
	Xe133m	0	0	0	0	0.04	0	0	0.02	0.02	0.02	0	0
	Xe133	1.18	0.92	0.62	0.66	0.33	0.08	0	0.04	0	0.29	0	0
	Xe135	32.82	32.7	32.42	32.64	32.67	32.29	32.15	32.33	32.3	32.44	32.98	32.46
	Background	66	66.38	66.97	66.69	66.96	67.63	67.85	67.61	67.68	67.25	67.02	67.54
True Percent	Xe131m	0	0	0	0	0	0	0	0	0	0	0	0
	Xe133m	0	0	0	0	0	0	0	0	0	0	0	0
	Xe133	0	0	0	0	0	0	0	0	0	0	0	0
	Xe135	33.33	33.33	33.33	33.33	33.33	33.33	33.33	33.33	33.33	33.33	33.33	33.33
	Background	66.67	66.67	66.67	66.67	66.67	66.67	66.67	66.67	66.67	66.67	66.67	66.67
Difference (Est-True)	Xe131m	0	0	0	0	0	0	0	0	0	0	0	0
	Xe133m	0	0	0	0	0.04	0	0	0.02	0.02	0.02	0	0
	Xe133	1.18	0.92	0.62	0.66	0.33	0.08	0	0.04	0	0.29	0	0
	Xe135	-0.51	-0.63	-0.91	-0.69	-0.66	-1.04	-1.18	-1	-1.03	-0.89	-0.35	-0.87
	Background	-0.67	-0.29	0.3	0.02	0.29	0.96	1.18	0.94	1.01	0.58	0.35	0.87
ABS(diff.)	Xe131m	0	0	0	0	0	0	0	0	0	0	0	0
	Xe133m	0	0	0	0	0.04	0	0	0.02	0.02	0.02	0	0
	Xe133	1.18	0.92	0.62	0.66	0.33	0.08	0	0.04	0	0.29	0	0
	Xe135	0.51	0.63	0.91	0.69	0.66	1.04	1.18	1	1.03	0.89	0.35	0.87
	Background	0.67	0.29	0.3	0.02	0.29	0.96	1.18	0.94	1.01	0.58	0.35	0.87
AVG(ABS(diff.))		0.472	0.368	0.366	0.274	0.264	0.416	0.472	0.4	0.412	0.356	0.14	0.348
(diff)^2	Xe131m	0	0	0	0	0	0	0	0	0	0	0	0
	Xe133m	0	0	0	0	0.0016	0	0	0.0004	0.0004	0.0004	0	0
	Xe133	1.3924	0.8464	0.3844	0.4356	0.1089	0.0064	0	0.0016	0	0.0841	0	0
	Xe135	0.2601	0.3969	0.8281	0.4761	0.4356	1.0816	1.3924	1	1.0609	0.7921	0.1225	0.7569
	Background	0.4489	0.0841	0.09	0.0004	0.0841	0.9216	1.3924	0.8836	1.0201	0.3364	0.1225	0.7569
AVG((diff.)^2)		0.42028	0.26548	0.2605	0.18242	0.12604	0.40192	0.55696	0.37712	0.41628	0.2426	0.049	0.30276

Trial 4	Subregions	1	2	3	4	5	6	7	8	9	10	Focus	SDAT
	Runtime (sec)	3.12	2.88	2.87	3.5	3.69	3.33	3.19	3.45	3.4	3.05	3.55	210.52
	Iterations	3	2	2	3	3	3	3	3	3	3	3	3
Estimates	Xe131m	0.05	0	0	0	0	0	0	0	0	0	0	0
	Xe133m	0	0.1	0.08	0.04	0.22	0.17	0.06	0.27	0.27	0.19	0	0.02
	Xe133	2.47	2.45	2.31	2.5	2.56	2.53	2.52	2.43	2.71	2.42	0	0
	Xe135	9.75	9.84	9.57	9.59	9.12	9.02	8.85	9.27	9.31	9.1	8.01	8.51
	Background	87.74	87.61	88.05	87.88	88.1	88.28	88.56	88.03	87.71	88.29	91.99	91.47
True Percent	Xe131m	0	0	0	0	0	0	0	0	0	0	0	0
	Xe133m	0	0	0	0	0	0	0	0	0	0	0	0
	Xe133	0	0	0	0	0	0	0	0	0	0	0	0
	Xe135	9.09	9.09	9.09	9.09	9.09	9.09	9.09	9.09	9.09	9.09	9.09	9.09
	Background	90.91	90.91	90.91	90.91	90.91	90.91	90.91	90.91	90.91	90.91	90.91	90.91
Difference (Est-True)	Xe131m	0.05	0	0	0	0	0	0	0	0	0	0	0
	Xe133m	0	0.1	0.08	0.04	0.22	0.17	0.06	0.27	0.27	0.19	0	0.02
	Xe133	2.47	2.45	2.31	2.5	2.56	2.53	2.52	2.43	2.71	2.42	0	0
	Xe135	0.66	0.75	0.48	0.5	0.03	-0.07	-0.24	0.18	0.22	0.01	-1.08	-0.58
	Background	-3.17	-3.3	-2.86	-3.03	-2.81	-2.63	-2.35	-2.88	-3.2	-2.62	1.08	0.56
ABS(diff.)	Xe131m	0.05	0	0	0	0	0	0	0	0	0	0	0
	Xe133m	0	0.1	0.08	0.04	0.22	0.17	0.06	0.27	0.27	0.19	0	0.02
	Xe133	2.47	2.45	2.31	2.5	2.56	2.53	2.52	2.43	2.71	2.42	0	0
	Xe135	0.66	0.75	0.48	0.5	0.03	0.07	0.24	0.18	0.22	0.01	1.08	0.58
	Background	3.17	3.3	2.86	3.03	2.81	2.63	2.35	2.88	3.2	2.62	1.08	0.56
AVG(ABS(diff.))		1.27	1.32	1.146	1.214	1.124	1.08	1.034	1.152	1.28	1.048	0.432	0.232
(diff)^2	Xe131m	0.0025	0	0	0	0	0	0	0	0	0	0	0
	Xe133m	0	0.01	0.0064	0.0016	0.0484	0.0289	0.0036	0.0729	0.0729	0.0361	0	0.0004
	Xe133	6.1009	6.0025	5.3361	6.25	6.5536	6.4009	6.3504	5.9049	7.3441	5.8564	0	0
	Xe135	0.4356	0.5625	0.2304	0.25	0.0009	0.0049	0.0576	0.0324	0.0484	0.0001	1.1664	0.3364
	Background	10.0489	10.89	8.1796	9.1809	7.8961	6.9169	5.5225	8.2944	10.24	6.8644	1.1664	0.3136
AVG((diff.)^2)		3.31758	3.493	2.7505	3.1365	2.8998	2.67032	2.38682	2.86092	3.54108	2.5514	0.46656	0.13008

Trial 5	Subregions	1	2	3	4	5	6	7	8	9	10	Focus	SDAT
	Runtime (sec)	3.52	3.35	3.09	2.89	3.31	3.36	3.35	2.87	3	2.9	3.6	211.32
	Iterations	3	3	3	3	3	3	3	3	3	3	2	3
Estimates	Xe131m	0	0	0	0	0	0	0	0	0	0	0	0
	Xe133m	51.1	51.26	51.53	51.58	51.48	51.48	51.38	51.41	51.36	51.44	50.92	50.73
	Xe133	48.9	48.74	48.47	48.42	48.51	48.52	48.62	48.59	48.63	48.56	49.08	49.27
	Xe135	0	0	0	0	0	0	0	0	0	0	0	0
	Background	0.01	0.01	0	0	0	0	0	0	0	0	0	0
True Percent	Xe131m	0	0	0	0	0	0	0	0	0	0	0	0
	Xe133m	50	50	50	50	50	50	50	50	50	50	50	50
	Xe133	50	50	50	50	50	50	50	50	50	50	50	50
	Xe135	0	0	0	0	0	0	0	0	0	0	0	0
	Background	0	0	0	0	0	0	0	0	0	0	0	0
Difference (Est-True)	Xe131m	0	0	0	0	0	0	0	0	0	0	0	0
	Xe133m	1.1	1.26	1.53	1.58	1.48	1.48	1.38	1.41	1.36	1.44	0.92	0.73
	Xe133	-1.1	-1.26	-1.53	-1.58	-1.49	-1.48	-1.38	-1.41	-1.37	-1.44	-0.92	-0.73
	Xe135	0	0	0	0	0	0	0	0	0	0	0	0
	Background	0.01	0.01	0	0	0	0	0	0	0	0	0	0
ABS(diff.)	Xe131m	0	0	0	0	0	0	0	0	0	0	0	0
	Xe133m	1.1	1.26	1.53	1.58	1.48	1.48	1.38	1.41	1.36	1.44	0.92	0.73
	Xe133	1.1	1.26	1.53	1.58	1.49	1.48	1.38	1.41	1.37	1.44	0.92	0.73
	Xe135	0	0	0	0	0	0	0	0	0	0	0	0
	Background	0.01	0.01	0	0	0	0	0	0	0	0	0	0
AVG(ABS(diff.))		0.442	0.506	0.612	0.632	0.594	0.592	0.552	0.564	0.546	0.576	0.368	0.292
(diff)^2	Xe131m	0	0	0	0	0	0	0	0	0	0	0	0
	Xe133m	1.21	1.5876	2.3409	2.4964	2.1904	2.1904	1.9044	1.9881	1.8496	2.0736	0.8464	0.5329
	Xe133	1.21	1.5876	2.3409	2.4964	2.2201	2.1904	1.9044	1.9881	1.8769	2.0736	0.8464	0.5329
	Xe135	0	0	0	0	0	0	0	0	0	0	0	0
	Background	0.0001	0.0001	0	0	0	0	0	0	0	0	0	0
AVG((diff.)^2)		0.48402	0.63506	0.93636	0.99856	0.8821	0.87616	0.76176	0.79524	0.7453	0.82944	0.33856	0.21316

Trial 6	Subregions	1	2	3	4	5	6	7	8	9	10	Focus	SDAT
	Runtime (sec)	2.97	3.19	3.18	3.46	3.57	3	3.17	3.37	3.16	3.42	9.88	160.04
	Iterations	4	4	4	4	3	4	3	4	4	4	50	2
Estimates	Xe131m	0	0	0	0	0	0	0	0	0	0	0	0
	Xe133m	10.24	10.63	10.49	10.41	10.17	9.89	9.65	9.94	9.99	9.76	8.96	8.64
	Xe133	89.74	89.35	89.51	89.59	89.82	90.11	90.35	90.06	90.01	90.23	91.04	91.36
	Xe135	0	0	0	0	0	0	0	0	0	0	0	0
	Background	0.01	0.02	0	0	0	0	0	0	0	0	0	0
True Percent	Xe131m	0	0	0	0	0	0	0	0	0	0	0	0
	Xe133m	9.09	9.09	9.09	9.09	9.09	9.09	9.09	9.09	9.09	9.09	9.09	9.09
	Xe133	90.91	90.91	90.91	90.91	90.91	90.91	90.91	90.91	90.91	90.91	90.91	90.91
	Xe135	0	0	0	0	0	0	0	0	0	0	0	0
	Background	0	0	0	0	0	0	0	0	0	0	0	0
Difference (Est-True)	Xe131m	0	0	0	0	0	0	0	0	0	0	0	0
	Xe133m	1.15	1.54	1.4	1.32	1.08	0.8	0.56	0.85	0.9	0.67	-0.13	-0.45
	Xe133	-1.17	-1.56	-1.4	-1.32	-1.09	-0.8	-0.56	-0.85	-0.9	-0.68	0.13	0.45
	Xe135	0	0	0	0	0	0	0	0	0	0	0	0
	Background	0.01	0.02	0	0	0	0	0	0	0	0	0	0
ABS(diff.)	Xe131m	0	0	0	0	0	0	0	0	0	0	0	0
	Xe133m	1.15	1.54	1.4	1.32	1.08	0.8	0.56	0.85	0.9	0.67	0.13	0.45
	Xe133	1.17	1.56	1.4	1.32	1.09	0.8	0.56	0.85	0.9	0.68	0.13	0.45
	Xe135	0	0	0	0	0	0	0	0	0	0	0	0
	Background	0.01	0.02	0	0	0	0	0	0	0	0	0	0
AVG(ABS(diff.))		0.466	0.624	0.56	0.528	0.434	0.32	0.224	0.34	0.36	0.27	0.052	0.18
(diff)^2	Xe131m	0	0	0	0	0	0	0	0	0	0	0	0
	Xe133m	1.3225	2.3716	1.96	1.7424	1.1664	0.64	0.3136	0.7225	0.81	0.4489	0.0169	0.2025
	Xe133	1.3689	2.4336	1.96	1.7424	1.1881	0.64	0.3136	0.7225	0.81	0.4624	0.0169	0.2025
	Xe135	0	0	0	0	0	0	0	0	0	0	0	0
	Background	0.0001	0.0004	0	0	0	0	0	0	0	0	0	0
AVG((diff.)^2)		0.5383	0.96112	0.784	0.69696	0.4709	0.256	0.12544	0.289	0.324	0.18226	0.00676	0.081

Trial 7	Subregions	1	2	3	4	5	6	7	8	9	10	Focus	SDAT
	Runtime (sec)	3.29	3.52	2.75	3.49	3.29	3.35	2.94	2.9	3.17	3.35	9.59	157.74
	Iterations	3	3	3	3	3	3	3	3	4	4	58	2
Estimates	Xe131m	0	0	0	0	0	0	0	0	0	0	0	0
	Xe133m	17.16	17.23	17.08	17.18	17.26	16.93	17	16.81	16.84	17.04	18.47	17.64
	Xe133	82.83	82.77	82.91	82.82	82.73	83.06	83	83.19	83.16	82.96	81.53	82.36
	Xe135	0	0	0	0	0	0	0	0	0	0	0	0
	Background	0.01	0.01	0.01	0	0	0	0	0	0	0	0	0
True Percent	Xe131m	0	0	0	0	0	0	0	0	0	0	0	0
	Xe133m	16.67	16.67	16.67	16.67	16.67	16.67	16.67	16.67	16.67	16.67	16.67	16.67
	Xe133	83.33	83.33	83.33	83.33	83.33	83.33	83.33	83.33	83.33	83.33	83.33	83.33
	Xe135	0	0	0	0	0	0	0	0	0	0	0	0
	Background	0	0	0	0	0	0	0	0	0	0	0	0
Difference (Est-True)	Xe131m	0	0	0	0	0	0	0	0	0	0	0	0
	Xe133m	0.49	0.56	0.41	0.51	0.59	0.26	0.33	0.14	0.17	0.37	1.8	0.97
	Xe133	-0.5	-0.56	-0.42	-0.51	-0.6	-0.27	-0.33	-0.14	-0.17	-0.37	-1.8	-0.97
	Xe135	0	0	0	0	0	0	0	0	0	0	0	0
	Background	0.01	0.01	0.01	0	0	0	0	0	0	0	0	0
ABS(diff.)	Xe131m	0	0	0	0	0	0	0	0	0	0	0	0
	Xe133m	0.49	0.56	0.41	0.51	0.59	0.26	0.33	0.14	0.17	0.37	1.8	0.97
	Xe133	0.5	0.56	0.42	0.51	0.6	0.27	0.33	0.14	0.17	0.37	1.8	0.97
	Xe135	0	0	0	0	0	0	0	0	0	0	0	0
	Background	0.01	0.01	0.01	0	0	0	0	0	0	0	0	0
AVG(ABS(diff.))		0.2	0.226	0.168	0.204	0.238	0.106	0.132	0.056	0.068	0.148	0.72	0.388
(diff)^2	Xe131m	0	0	0	0	0	0	0	0	0	0	0	0
	Xe133m	0.2401	0.3136	0.1681	0.2601	0.3481	0.0676	0.1089	0.0196	0.0289	0.1369	3.24	0.9409
	Xe133	0.25	0.3136	0.1764	0.2601	0.36	0.0729	0.1089	0.0196	0.0289	0.1369	3.24	0.9409
	Xe135	0	0	0	0	0	0	0	0	0	0	0	0
	Background	0.0001	0.0001	0.0001	0	0	0	0	0	0	0	0	0
AVG((diff.)^2)		0.09804	0.12546	0.06892	0.10404	0.14162	0.0281	0.04356	0.00784	0.01156	0.05476	1.296	0.37636

Trial 8	Subregions	1	2	3	4	5	6	7	8	9	10	Focus	SDAT
	Runtime (sec)	3.28	3.1	3.33	3.66	3.24	2.92	2.88	3.46	3.28	2.85	3.91	210.56
	Iterations	3	3	2	3	3	3	3	3	3	2	4	3
Estimates	Xe131m	4.3	3.77	3.84	3.34	3.59	3.2	3.06	3.15	2.96	2.93	0.55	0.66
	Xe133m	26.81	27.14	26.79	26.91	27.03	26.86	27.15	26.96	26.93	26.92	28.46	28.61
	Xe133	68.88	69.08	69.37	69.75	69.38	69.94	69.78	69.89	70.1	70.15	70.99	70.73
	Xe135	0	0	0	0	0	0	0	0	0	0	0	0
	Background	0.02	0.01	0	0	0	0	0	0	0	0	0	0
True Percent	Xe131m	0	0	0	0	0	0	0	0	0	0	0	0
	Xe133m	28.57	28.57	28.57	28.57	28.57	28.57	28.57	28.57	28.57	28.57	28.57	28.57
	Xe133	71.43	71.43	71.43	71.43	71.43	71.43	71.43	71.43	71.43	71.43	71.43	71.43
	Xe135	0	0	0	0	0	0	0	0	0	0	0	0
	Background	0	0	0	0	0	0	0	0	0	0	0	0
Difference (Est-True)	Xe131m	4.3	3.77	3.84	3.34	3.59	3.2	3.06	3.15	2.96	2.93	0.55	0.66
	Xe133m	-1.76	-1.43	-1.78	-1.66	-1.54	-1.71	-1.42	-1.61	-1.64	-1.65	-0.11	0.04
	Xe133	-2.55	-2.35	-2.06	-1.68	-2.05	-1.49	-1.65	-1.54	-1.33	-1.28	-0.44	-0.7
	Xe135	0	0	0	0	0	0	0	0	0	0	0	0
	Background	0.02	0.01	0	0	0	0	0	0	0	0	0	0
ABS(diff.)	Xe131m	4.3	3.77	3.84	3.34	3.59	3.2	3.06	3.15	2.96	2.93	0.55	0.66
	Xe133m	1.76	1.43	1.78	1.66	1.54	1.71	1.42	1.61	1.64	1.65	0.11	0.04
	Xe133	2.55	2.35	2.06	1.68	2.05	1.49	1.65	1.54	1.33	1.28	0.44	0.7
	Xe135	0	0	0	0	0	0	0	0	0	0	0	0
	Background	0.02	0.01	0	0	0	0	0	0	0	0	0	0
AVG(ABS(diff.))		1.726	1.512	1.536	1.336	1.436	1.28	1.226	1.26	1.186	1.172	0.22	0.28
(diff)^2	Xe131m	18.49	14.2129	14.7456	11.1556	12.8881	10.24	9.3636	9.9225	8.7616	8.5849	0.3025	0.4356
	Xe133m	3.0976	2.0449	3.1684	2.7556	2.3716	2.9241	2.0164	2.5921	2.6896	2.7225	0.0121	0.0016
	Xe133	6.5025	5.5225	4.2436	2.8224	4.2025	2.2201	2.7225	2.3716	1.7689	1.6384	0.1936	0.49
	Xe135	0	0	0	0	0	0	0	0	0	0	0	0
	Background	0.0004	0.0001	0	0	0	0	0	0	0	0	0	0
AVG((diff.)^2)		5.6181	4.35608	4.43152	3.34672	3.89244	3.07684	2.8205	2.97724	2.64402	2.58916	0.10164	0.18544

Trial 9	Subregions	1	2	3	4	5	6	7	8	9	10	Focus	SDAT
	Runtime (sec)	2.73	3.2	2.94	3.46	3.31	3.43	3.47	3.33	3.1	3.83	3.94	320.4
	Iterations	1	1	2	1	3	3	50	3	3	3	4	5
Estimates	Xe131m	0	0	0	0	0	0	0	0	0	0	0	0.05
	Xe133m	38.57	38.46	38.31	38.51	38.64	38.1	38.04	38.3	38.37	38.51	36.72	36.25
	Xe133	61.43	61.54	61.69	61.49	61.36	61.9	60.83	61.7	61.63	61.49	62.5	63.7
	Xe135	0	0	0	0	0	0	1.13	0	0	0	0	0
	Background	0	0	0	0	0	0	0	0	0	0	0	0
True Percent	Xe131m	0	0	0	0	0	0	0	0	0	0	0	0
	Xe133m	37.5	37.5	37.5	37.5	37.5	37.5	37.5	37.5	37.5	37.5	37.5	37.5
	Xe133	62.5	62.5	62.5	62.5	62.5	62.5	62.5	62.5	62.5	62.5	62.5	62.5
	Xe135	0	0	0	0	0	0	0	0	0	0	0	0
	Background	0	0	0	0	0	0	0	0	0	0	0	0
Difference (Est-True)	Xe131m	0	0	0	0	0	0	0	0	0	0	0.78	0.05
	Xe133m	1.07	0.96	0.81	1.01	1.14	0.6	0.54	0.8	0.87	1.01	-0.78	-1.25
	Xe133	-1.07	-0.96	-0.81	-1.01	-1.14	-0.6	-1.67	-0.8	-0.87	-1.01	0	1.2
	Xe135	0	0	0	0	0	0	1.13	0	0	0	0	0
	Background	0	0	0	0	0	0	0	0	0	0	0	0
ABS(diff.)	Xe131m	0	0	0	0	0	0	0	0	0	0	0.78	0.05
	Xe133m	1.07	0.96	0.81	1.01	1.14	0.6	0.54	0.8	0.87	1.01	0.78	1.25
	Xe133	1.07	0.96	0.81	1.01	1.14	0.6	1.67	0.8	0.87	1.01	0	1.2
	Xe135	0	0	0	0	0	0	1.13	0	0	0	0	0
	Background	0	0	0	0	0	0	0	0	0	0	0	0
AVG(ABS(diff.))		0.428	0.384	0.324	0.404	0.456	0.24	0.668	0.32	0.348	0.404	0.312	0.5
(diff)^2	Xe131m	0	0	0	0	0	0	0	0	0	0	0.6084	0.0025
	Xe133m	1.1449	0.9216	0.6561	1.0201	1.2996	0.36	0.2916	0.64	0.7569	1.0201	0.6084	1.5625
	Xe133	1.1449	0.9216	0.6561	1.0201	1.2996	0.36	2.7889	0.64	0.7569	1.0201	0	1.44
	Xe135	0	0	0	0	0	0	1.2769	0	0	0	0	0
	Background	0	0	0	0	0	0	0	0	0	0	0	0
AVG((diff.)^2)		0.45796	0.36864	0.26244	0.40804	0.51984	0.144	0.87148	0.256	0.30276	0.40804	0.24336	0.601

Trial 10	Subregions	1	2	3	4	5	6	7	8	9	10	Focus	SDAT
	Runtime (sec)	3.79	3.86	3.72	3.13	3.68	3.1	3.42	3.32	3.17	2.91	3.78	203.8
	Iterations	2	2	2	2	2	2	2	2	2	2	3	3
Estimates	Xe131m	0.01	0	0	0	0	0	0	0	0	0.08	0.38	0.18
	Xe133m	16.85	16.88	16.86	16.81	16.88	16.85	16.81	16.71	16.7	16.75	16.81	16.66
	Xe133	28.73	29.09	29.09	28.97	28.94	29.11	29.05	28.75	28.88	28.81	28.89	28.21
	Xe135	0.22	0	0.11	0	0	0	0.13	0	0	0	0	0
	Background	54.19	54.03	53.94	54.22	54.18	54.04	54.01	54.54	54.42	54.36	53.92	54.94
True Percent	Xe131m	0	0	0	0	0	0	0	0	0	0	0	0
	Xe133m	16.67	16.67	16.67	16.67	16.67	16.67	16.67	16.67	16.67	16.67	16.67	16.67
	Xe133	27.78	27.78	27.78	27.78	27.78	27.78	27.78	27.78	27.78	27.78	27.78	27.78
	Xe135	0	0	0	0	0	0	0	0	0	0	0	0
	Background	55.56	55.56	55.56	55.56	55.56	55.56	55.56	55.56	55.56	55.56	55.56	55.56
Difference (Est-True)	Xe131m	0.01	0	0	0	0	0	0	0	0	0.08	0.38	0.18
	Xe133m	0.18	0.21	0.19	0.14	0.21	0.18	0.14	0.04	0.03	0.08	0.14	-0.01
	Xe133	0.95	1.31	1.31	1.19	1.16	1.33	1.27	0.97	1.1	1.03	1.11	0.43
	Xe135	0.22	0	0.11	0	0	0	0.13	0	0	0	0	0
	Background	-1.37	-1.53	-1.62	-1.34	-1.38	-1.52	-1.55	-1.02	-1.14	-1.2	-1.64	-0.62
ABS(diff.)	Xe131m	0.01	0	0	0	0	0	0	0	0	0.08	0.38	0.18
	Xe133m	0.18	0.21	0.19	0.14	0.21	0.18	0.14	0.04	0.03	0.08	0.14	0.01
	Xe133	0.95	1.31	1.31	1.19	1.16	1.33	1.27	0.97	1.1	1.03	1.11	0.43
	Xe135	0.22	0	0.11	0	0	0	0.13	0	0	0	0	0
	Background	1.37	1.53	1.62	1.34	1.38	1.52	1.55	1.02	1.14	1.2	1.64	0.62
AVG(ABS(diff.))		0.546	0.61	0.646	0.534	0.55	0.606	0.618	0.406	0.454	0.478	0.654	0.248
(diff)^2	Xe131m	0.0001	0	0	0	0	0	0	0	0	0.0064	0.1444	0.0324
	Xe133m	0.0324	0.0441	0.0361	0.0196	0.0441	0.0324	0.0196	0.0016	0.0009	0.0064	0.0196	0.0001
	Xe133	0.9025	1.7161	1.7161	1.4161	1.3456	1.7689	1.6129	0.9409	1.21	1.0609	1.2321	0.1849
	Xe135	0.0484	0	0.0121	0	0	0	0.0169	0	0	0	0	0
	Background	1.8769	2.3409	2.6244	1.7956	1.9044	2.3104	2.4025	1.0404	1.2996	1.44	2.6896	0.3844
AVG((diff.)^2)		0.57206	0.82022	0.87774	0.64626	0.65882	0.82234	0.81038	0.39658	0.5021	0.50274	0.81714	0.12036



Trial 11	Subregions	1	2	3	4	5	6	7	8	9	10	Focus	SDAT
	Runtime (sec)	3.47	3.61	3.44	2.91	2.86	2.81	2.87	2.97	2.84	3.11	3.66	152.18
	Iterations	2	3	2	3	2	3	3	3	3	3	3	2
Estimates	Xe131m	7.73	7.74	7.55	7.7	7.74	7.69	7.7	7.65	7.79	7.69	8.63	8.73
	Xe133m	8.57	8.72	8.7	8.7	8.82	8.82	8.81	8.89	8.86	8.86	8.45	8.39
	Xe133	2.67	2.47	2.75	2.74	2.3	2.42	2.23	1.92	2.12	2.01	0	0
	Xe135	0	0	0	0.05	0.16	0.12	0.29	0.22	0.2	0.31	0	0
	Background	81.02	81.07	80.99	80.81	80.98	80.94	80.96	81.32	81.03	81.13	82.92	82.88
True Percent	Xe131m	8.33	8.33	8.33	8.33	8.33	8.33	8.33	8.33	8.33	8.33	8.33	8.33
	Xe133m	8.33	8.33	8.33	8.33	8.33	8.33	8.33	8.33	8.33	8.33	8.33	8.33
	Xe133	0	0	0	0	0	0	0	0	0	0	0	0
	Xe135	0	0	0	0	0	0	0	0	0	0	0	0
	Background	83.33	83.33	83.33	83.33	83.33	83.33	83.33	83.33	83.33	83.33	83.33	83.33
Difference (Est-True)	Xe131m	-0.6	-0.59	-0.78	-0.63	-0.59	-0.64	-0.63	-0.68	-0.54	-0.64	0.3	0.4
	Xe133m	0.24	0.39	0.37	0.37	0.49	0.49	0.48	0.56	0.53	0.53	0.12	0.06
	Xe133	2.67	2.47	2.75	2.74	2.3	2.42	2.23	1.92	2.12	2.01	0	0
	Xe135	0	0	0	0.05	0.16	0.12	0.29	0.22	0.2	0.31	0	0
	Background	-2.31	-2.26	-2.34	-2.52	-2.35	-2.39	-2.37	-2.01	-2.3	-2.2	-0.41	-0.45
ABS(diff.)	Xe131m	0.6	0.59	0.78	0.63	0.59	0.64	0.63	0.68	0.54	0.64	0.3	0.4
	Xe133m	0.24	0.39	0.37	0.37	0.49	0.49	0.48	0.56	0.53	0.53	0.12	0.06
	Xe133	2.67	2.47	2.75	2.74	2.3	2.42	2.23	1.92	2.12	2.01	0	0
	Xe135	0	0	0	0.05	0.16	0.12	0.29	0.22	0.2	0.31	0	0
	Background	2.31	2.26	2.34	2.52	2.35	2.39	2.37	2.01	2.3	2.2	0.41	0.45
AVG(ABS(diff.))		1.164	1.142	1.248	1.262	1.178	1.212	1.2	1.078	1.138	1.138	0.166	0.182
(diff)^2	Xe131m	0.36	0.3481	0.6084	0.3969	0.3481	0.4096	0.3969	0.4624	0.2916	0.4096	0.09	0.16
	Xe133m	0.0576	0.1521	0.1369	0.1369	0.2401	0.2401	0.2304	0.3136	0.2809	0.2809	0.0144	0.0036
	Xe133	7.1289	6.1009	7.5625	7.5076	5.29	5.8564	4.9729	3.6864	4.4944	4.0401	0	0
	Xe135	0	0	0	0.0025	0.0256	0.0144	0.0841	0.0484	0.04	0.0961	0	0
	Background	5.3361	5.1076	5.4756	6.3504	5.5225	5.7121	5.6169	4.0401	5.29	4.84	0.1681	0.2025
AVG((diff.)^2)		2.57652	2.34174	2.75668	2.87886	2.28526	2.44652	2.26024	1.71018	2.07938	1.93334	0.0545	0.07322

Trial 12	Subregions	1	2	3	4	5	6	7	8	9	10	Focus	SDAT
	Runtime (sec)	3.44	3.7	2.87	3.39	3.28	3.42	2.9	2.97	3.17	3.15	3.99	254.6
	Iterations	2	2	2	2	3	2	3	3	2	3	4	4
Estimates	Xe131m	1.36	1.16	1.19	1.13	1.46	1.32	1.36	1.38	1.43	1.26	0.72	0.84
	Xe133m	0.07	0	0	0.04	0.04	0	0.11	0	0	0	0.23	0.07
	Xe133	0	0	0	0	0	0	0	0	0	0	0	0
	Xe135	0	0	0	0	0	0	0	0	0	0	0	0
	Background	98.57	98.84	98.81	98.83	98.5	98.68	98.53	98.62	98.57	98.74	99.05	99.09
True Percent	Xe131m	0.99	0.99	0.99	0.99	0.99	0.99	0.99	0.99	0.99	0.99	0.99	0.99
	Xe133m	0	0	0	0	0	0	0	0	0	0	0	0
	Xe133	0	0	0	0	0	0	0	0	0	0	0	0
	Xe135	0	0	0	0	0	0	0	0	0	0	0	0
	Background	99.01	99.01	99.01	99.01	99.01	99.01	99.01	99.01	99.01	99.01	99.01	99.01
Difference (Est-True)	Xe131m	0.37	0.17	0.2	0.14	0.47	0.33	0.37	0.39	0.44	0.27	-0.27	-0.15
	Xe133m	0.07	0	0	0.04	0.04	0	0.11	0	0	0	0.23	0.07
	Xe133	0	0	0	0	0	0	0	0	0	0	0	0
	Xe135	0	0	0	0	0	0	0	0	0	0	0	0
	Background	-0.44	-0.17	-0.2	-0.18	-0.51	-0.33	-0.48	-0.39	-0.44	-0.27	0.04	0.08
ABS(diff.)	Xe131m	0.37	0.17	0.2	0.14	0.47	0.33	0.37	0.39	0.44	0.27	0.27	0.15
	Xe133m	0.07	0	0	0.04	0.04	0	0.11	0	0	0	0.23	0.07
	Xe133	0	0	0	0	0	0	0	0	0	0	0	0
	Xe135	0	0	0	0	0	0	0	0	0	0	0	0
	Background	0.44	0.17	0.2	0.18	0.51	0.33	0.48	0.39	0.44	0.27	0.04	0.08
AVG(ABS(diff.))		0.176	0.068	0.08	0.072	0.204	0.132	0.192	0.156	0.176	0.108	0.108	0.06
(diff)^2	Xe131m	0.1369	0.0289	0.04	0.0196	0.2209	0.1089	0.1369	0.1521	0.1936	0.0729	0.0729	0.0225
	Xe133m	0.0049	0	0	0.0016	0.0016	0	0.0121	0	0	0	0.0529	0.0049
	Xe133	0	0	0	0	0	0	0	0	0	0	0	0
	Xe135	0	0	0	0	0	0	0	0	0	0	0	0
	Background	0.1936	0.0289	0.04	0.0324	0.2601	0.1089	0.2304	0.1521	0.1936	0.0729	0.0016	0.0064
AVG((diff.)^2)		0.06708	0.01156	0.016	0.01072	0.09652	0.04356	0.07588	0.06084	0.07744	0.02916	0.02548	0.00676

Trial 13	Subregions	1	2	3	4	5	6	7	8	9	10	Focus	SDAT
	Runtime (sec)	3.4	3.3	3.22	3.76	3.2	2.94	2.91	3.04	3.15	3.25	4.1	513.54
	Iterations	3	3	3	3	3	2	4	3	13	10	6	9
Estimates	Xe131m	0	0.01	0.06	0.04	0	0	0.06	0	0.13	0.1	0.35	0
	Xe133m	0	0	0	0	0	0	0	0	0	0	0.11	0
	Xe133	0.38	0.96	0.77	0.93	0.98	0.95	0.31	0.75	0.52	0.64	1.52	0.16
	Xe135	20.82	20.91	20.8	21.39	21.05	20.86	20.96	20.98	21.27	21.16	14.75	15.7
	Background	78.79	78.12	78.37	77.63	77.97	78.19	78.67	78.27	78.08	78.1	83.27	84.13
True Percent	Xe131m	0	0	0	0	0	0	0	0	0	0	0	0
	Xe133m	0	0	0	0	0	0	0	0	0	0	0	0
	Xe133	0	0	0	0	0	0	0	0	0	0	0	0
	Xe135	16.67	16.67	16.67	16.67	16.67	16.67	16.67	16.67	16.67	16.67	16.67	16.67
	Background	83.33	83.33	83.33	83.33	83.33	83.33	83.33	83.33	83.33	83.33	83.33	83.33
Difference (Est-True)	Xe131m	0	0.01	0.06	0.04	0	0	0.06	0	0.13	0.1	0.35	0
	Xe133m	0	0	0	0	0	0	0	0	0	0	0.11	0
	Xe133	0.38	0.96	0.77	0.93	0.98	0.95	0.31	0.75	0.52	0.64	1.52	0.16
	Xe135	4.15	4.24	4.13	4.72	4.38	4.19	4.29	4.31	4.6	4.49	-1.92	-0.97
	Background	-4.54	-5.21	-4.96	-5.7	-5.36	-5.14	-4.66	-5.06	-5.25	-5.23	-0.06	0.8
ABS(diff.)	Xe131m	0	0.01	0.06	0.04	0	0	0.06	0	0.13	0.1	0.35	0
	Xe133m	0	0	0	0	0	0	0	0	0	0	0.11	0
	Xe133	0.38	0.96	0.77	0.93	0.98	0.95	0.31	0.75	0.52	0.64	1.52	0.16
	Xe135	4.15	4.24	4.13	4.72	4.38	4.19	4.29	4.31	4.6	4.49	1.92	0.97
	Background	4.54	5.21	4.96	5.7	5.36	5.14	4.66	5.06	5.25	5.23	0.06	0.8
AVG(ABS(diff.))		1.814	2.084	1.984	2.278	2.144	2.056	1.864	2.024	2.1	2.092	0.792	0.386
(diff)^2	Xe131m	0	0.0001	0.0036	0.0016	0	0	0.0036	0	0.0169	0.01	0.1225	0
	Xe133m	0	0	0	0	0	0	0	0	0	0	0.0121	0
	Xe133	0.1444	0.9216	0.5929	0.8649	0.9604	0.9025	0.0961	0.5625	0.2704	0.4096	2.3104	0.0256
	Xe135	17.2225	17.9776	17.0569	22.2784	19.1844	17.5561	18.4041	18.5761	21.16	20.1601	3.6864	0.9409
	Background	20.6116	27.1441	24.6016	32.49	28.7296	26.4196	21.7156	25.6036	27.5625	27.3529	0.0036	0.64
AVG((diff.)^2)		7.5957	9.20868	8.451	11.12698	9.77488	8.97564	8.04388	8.94844	9.80196	9.58652	1.227	0.3213

Trial 14	Subregions	1	2	3	4	5	6	7	8	9	10	Focus	SDAT
	Runtime (sec)	3	3.17	2.99	3.04	3.18	3.2	3.17	3.43	3.36	3.28	3.53	164.68
	Iterations	2	2	2	3	2	2	2	3	2	2	2	2
Estimates	Xe131m	1.49	1.08	1.43	1.15	1.2	1.16	1.31	1.32	1.36	1.31	0	0.02
	Xe133m	0	0	0	0.03	0	0	0	0	0	0	0	0
	Xe133	15.63	15.82	15.9	15.85	16.12	16.09	15.85	16.01	15.93	16	16.73	16.83
	Xe135	0	0	0	0	0	0	0	0	0	0	0	0
	Background	82.89	83.1	82.67	82.97	82.67	82.75	82.83	82.67	82.71	82.69	83.27	83.15
True Percent	Xe131m	0	0	0	0	0	0	0	0	0	0	0	0
	Xe133m	0	0	0	0	0	0	0	0	0	0	0	0
	Xe133	16.67	16.67	16.67	16.67	16.67	16.67	16.67	16.67	16.67	16.67	16.67	16.67
	Xe135	0	0	0	0	0	0	0	0	0	0	0	0
	Background	83.33	83.33	83.33	83.33	83.33	83.33	83.33	83.33	83.33	83.33	83.33	83.33
Difference (Est-True)	Xe131m	1.49	1.08	1.43	1.15	1.2	1.16	1.31	1.32	1.36	1.31	0	0.02
	Xe133m	0	0	0	0.03	0	0	0	0	0	0	0	0
	Xe133	-1.04	-0.85	-0.77	-0.82	-0.55	-0.58	-0.82	-0.66	-0.74	-0.67	0.06	0.16
	Xe135	0	0	0	0	0	0	0	0	0	0	0	0
	Background	-0.44	-0.23	-0.66	-0.36	-0.66	-0.58	-0.5	-0.66	-0.62	-0.64	-0.06	-0.18
ABS(diff.)	Xe131m	1.49	1.08	1.43	1.15	1.2	1.16	1.31	1.32	1.36	1.31	0	0.02
	Xe133m	0	0	0	0.03	0	0	0	0	0	0	0	0
	Xe133	1.04	0.85	0.77	0.82	0.55	0.58	0.82	0.66	0.74	0.67	0.06	0.16
	Xe135	0	0	0	0	0	0	0	0	0	0	0	0
	Background	0.44	0.23	0.66	0.36	0.66	0.58	0.5	0.66	0.62	0.64	0.06	0.18
AVG(ABS(diff.))		0.594	0.432	0.572	0.472	0.482	0.464	0.526	0.528	0.544	0.524	0.024	0.072
(diff)^2	Xe131m	2.2201	1.1664	2.0449	1.3225	1.44	1.3456	1.7161	1.7424	1.8496	1.7161	0	0.0004
	Xe133m	0	0	0	0.0009	0	0	0	0	0	0	0	0
	Xe133	1.0816	0.7225	0.5929	0.6724	0.3025	0.3364	0.6724	0.4356	0.5476	0.4489	0.0036	0.0256
	Xe135	0	0	0	0	0	0	0	0	0	0	0	0
	Background	0.1936	0.0529	0.4356	0.1296	0.4356	0.3364	0.25	0.4356	0.3844	0.4096	0.0036	0.0324
AVG((diff.)^2)		0.69906	0.38836	0.61468	0.42508	0.43562	0.40368	0.5277	0.52272	0.55632	0.51492	0.00144	0.01168

Trial 15	Subregions	1	2	3	4	5	6	7	8	9	10	Focus	SDAT
	Runtime (sec)	3.59	3.41	3.15	3.29	2.89	2.86	3.12	3.26	3.36	3.17	3.71	404.67
	Iterations	4	3	2	2	2	2	2	2	2	2	3	7
Estimates	Xe131m	0	0	0	0	0	0	0	0	0	0	0.65	0.04
	Xe133m	16.42	16.34	16.37	16.34	16.37	16.28	16.39	16.39	16.44	16.37	15.64	16.7
	Xe133	0.74	0.32	0	0	0	0	0	0	0	0	0	0
	Xe135	2.11	2.48	1.56	1.31	1.23	1.53	1.43	1.5	1.43	1.74	0	0
	Background	80.73	80.87	82.07	82.35	82.4	82.19	82.18	82.12	82.13	81.89	83.71	83.26
True Percent	Xe131m	0	0	0	0	0	0	0	0	0	0	0	0
	Xe133m	16.67	16.67	16.67	16.67	16.67	16.67	16.67	16.67	16.67	16.67	16.67	16.67
	Xe133	0	0	0	0	0	0	0	0	0	0	0	0
	Xe135	0	0	0	0	0	0	0	0	0	0	0	0
	Background	83.33	83.33	83.33	83.33	83.33	83.33	83.33	83.33	83.33	83.33	83.33	83.33
Difference (Est-True)	Xe131m	0	0	0	0	0	0	0	0	0	0	0.65	0.04
	Xe133m	-0.25	-0.33	-0.3	-0.33	-0.3	-0.39	-0.28	-0.28	-0.23	-0.3	-1.03	0.03
	Xe133	0.74	0.32	0	0	0	0	0	0	0	0	0	0
	Xe135	2.11	2.48	1.56	1.31	1.23	1.53	1.43	1.5	1.43	1.74	0	0
	Background	-2.6	-2.46	-1.26	-0.98	-0.93	-1.14	-1.15	-1.21	-1.2	-1.44	0.38	-0.07
ABS(diff.)	Xe131m	0	0	0	0	0	0	0	0	0	0	0.65	0.04
	Xe133m	0.25	0.33	0.3	0.33	0.3	0.39	0.28	0.28	0.23	0.3	1.03	0.03
	Xe133	0.74	0.32	0	0	0	0	0	0	0	0	0	0
	Xe135	2.11	2.48	1.56	1.31	1.23	1.53	1.43	1.5	1.43	1.74	0	0
	Background	2.6	2.46	1.26	0.98	0.93	1.14	1.15	1.21	1.2	1.44	0.38	0.07
AVG(ABS(diff.))		1.14	1.118	0.624	0.524	0.492	0.612	0.572	0.598	0.572	0.696	0.412	0.028
(diff.)^2	Xe131m	0	0	0	0	0	0	0	0	0	0	0.4225	0.0016
	Xe133m	0.0625	0.1089	0.09	0.1089	0.09	0.1521	0.0784	0.0784	0.0529	0.09	1.0609	0.0009
	Xe133	0.5476	0.1024	0	0	0	0	0	0	0	0	0	0
	Xe135	4.4521	6.1504	2.4336	1.7161	1.5129	2.3409	2.0449	2.25	2.0449	3.0276	0	0
	Background	6.76	6.0516	1.5876	0.9604	0.8649	1.2996	1.3225	1.4641	1.44	2.0736	0.1444	0.0049
AVG((diff.)^2)		2.36444	2.48266	0.82224	0.55708	0.49356	0.75852	0.68916	0.7585	0.70756	1.03824	0.32556	0.00148

Trial 16	Subregions	1	2	3	4	5	6	7	8	9	10	Focus	SDAT
	Runtime (sec)	3.07	3.21	2.81	3.23	3.5	3.12	3.22	3.45	3.6	3.95	3.35	303.7
	Iterations	2	2	2	3	3	2	3	3	3	3	2	5
Estimates	Xe131m	15.96	16.09	16.25	16.08	15.91	16.01	16.05	16.08	15.95	16	17.03	17.04
	Xe133m	0.11	0.22	0.17	0.17	0	0	0	0	0	0	0	0
	Xe133	1.66	1.11	0.68	1.32	1.9	1.48	1.08	1.41	1.46	1.17	0	0
	Xe135	1.33	1.42	1.71	2.16	1.89	1.92	1.75	1.8	1.79	1.32	0	0
	Background	80.94	81.15	81.2	80.26	80.3	80.59	81.13	80.71	80.8	81.51	82.97	82.96
True Percent	Xe131m	16.67	16.67	16.67	16.67	16.67	16.67	16.67	16.67	16.67	16.67	16.67	16.67
	Xe133m	0	0	0	0	0	0	0	0	0	0	0	0
	Xe133	0	0	0	0	0	0	0	0	0	0	0	0
	Xe135	0	0	0	0	0	0	0	0	0	0	0	0
	Background	83.33	83.33	83.33	83.33	83.33	83.33	83.33	83.33	83.33	83.33	83.33	83.33
Difference (Est-True)	Xe131m	-0.71	-0.58	-0.42	-0.59	-0.76	-0.66	-0.62	-0.59	-0.72	-0.67	0.36	0.37
	Xe133m	0.11	0.22	0.17	0.17	0	0	0	0	0	0	0	0
	Xe133	1.66	1.11	0.68	1.32	1.9	1.48	1.08	1.41	1.46	1.17	0	0
	Xe135	1.33	1.42	1.71	2.16	1.89	1.92	1.75	1.8	1.79	1.32	0	0
	Background	-2.39	-2.18	-2.13	-3.07	-3.03	-2.74	-2.2	-2.62	-2.53	-1.82	-0.36	-0.37
ABS(diff.)	Xe131m	0.71	0.58	0.42	0.59	0.76	0.66	0.62	0.59	0.72	0.67	0.36	0.37
	Xe133m	0.11	0.22	0.17	0.17	0	0	0	0	0	0	0	0
	Xe133	1.66	1.11	0.68	1.32	1.9	1.48	1.08	1.41	1.46	1.17	0	0
	Xe135	1.33	1.42	1.71	2.16	1.89	1.92	1.75	1.8	1.79	1.32	0	0
	Background	2.39	2.18	2.13	3.07	3.03	2.74	2.2	2.62	2.53	1.82	0.36	0.37
AVG(ABS(diff.))		1.24	1.102	1.022	1.462	1.516	1.36	1.13	1.284	1.3	0.996	0.144	0.148
(diff.)^2	Xe131m	0.5041	0.3364	0.1764	0.3481	0.5776	0.4356	0.3844	0.3481	0.5184	0.4489	0.1296	0.1369
	Xe133m	0.0121	0.0484	0.0289	0.0289	0	0	0	0	0	0	0	0
	Xe133	2.7556	1.2321	0.4624	1.7424	3.61	2.1904	1.1664	1.9881	2.1316	1.3689	0	0
	Xe135	1.7689	2.0164	2.9241	4.6656	3.5721	3.6864	3.0625	3.24	3.2041	1.7424	0	0
	Background	5.7121	4.7524	4.5369	9.4249	9.1809	7.5076	4.84	6.8644	6.4009	3.3124	0.1296	0.1369
AVG((diff.)^2)		2.15056	1.67714	1.62574	3.24198	3.38812	2.764	1.89066	2.48812	2.451	1.37452	0.05184	0.05476



Trial 19	Subregions	1	2	3	4	5	6	7	8	9	10	Focus	SDAT
	Runtime (sec)	3.51	3.25	3.26	3.56	3.57	3.59	3.78	3.2	3.22	3.24	3.83	254.99
	Iterations	1	1	1	50	1	1	50	2	2	2	6	4
Estimates	Xe131m	0	0	0	0	0	0	0	0	0	0	0	0
	Xe133m	0	0	0	0	0	0	0	0	0	0	2.74	2.01
	Xe133	100	100	100	97.97	100	100	100	100	100	100	97.26	97.99
	Xe135	0	0	0	2.03	0	0	0	0	0	0	0	0
	Background	0	0	0	0	0	0	0	0	0	0	0	0
True Percent	Xe131m	0	0	0	0	0	0	0	0	0	0	0	0
	Xe133m	0	0	0	0	0	0	0	0	0	0	0	0
	Xe133	100	100	100	100	100	100	100	100	100	100	100	100
	Xe135	0	0	0	0	0	0	0	0	0	0	0	0
	Background	0	0	0	0	0	0	0	0	0	0	0	0
Difference (Est-True)	Xe131m	0	0	0	0	0	0	0	0	0	0	0	0
	Xe133m	0	0	0	0	0	0	0	0	0	0	2.74	2.01
	Xe133	0	0	0	-2.03	0	0	0	0	0	0	-2.74	-2.01
	Xe135	0	0	0	2.03	0	0	0	0	0	0	0	0
	Background	0	0	0	0	0	0	0	0	0	0	0	0
ABS(diff.)	Xe131m	0	0	0	0	0	0	0	0	0	0	0	0
	Xe133m	0	0	0	0	0	0	0	0	0	0	2.74	2.01
	Xe133	0	0	0	2.03	0	0	0	0	0	0	2.74	2.01
	Xe135	0	0	0	2.03	0	0	0	0	0	0	0	0
	Background	0	0	0	0	0	0	0	0	0	0	0	0
AVG(ABS(diff.))		0	0	0	0.812	0	0	0	0	0	0	1.096	0.804
(diff.)^2	Xe131m	0	0	0	0	0	0	0	0	0	0	0	0
	Xe133m	0	0	0	0	0	0	0	0	0	0	7.5076	4.0401
	Xe133	0	0	0	4.1209	0	0	0	0	0	0	7.5076	4.0401
	Xe135	0	0	0	4.1209	0	0	0	0	0	0	0	0
	Background	0	0	0	0	0	0	0	0	0	0	0	0
AVG((diff.)^2)		0	0	0	1.64836	0	0	0	0	0	0	3.00304	1.61604

Trial 20	Subregions	1	2	3	4	5	6	7	8	9	10	Focus	SDAT
	Runtime (sec)	3.23	3.03	2.95	2.93	2.81	2.92	2.99	3.13	3.18	3.1	3.59	152.46
	Iterations	50	3	3	6	1	4	3	3	3	3	3	2
Estimates	Xe131m	5.33	7.91	7.77	7.78	6.58	9.34	9.11	9.42	9.28	9.22	0	0
	Xe133m	89.78	92.07	92.23	92.22	93.42	90.66	90.89	90.58	90.72	90.78	100	100
	Xe133	3.54	0.02	0	0	0	0	0	0	0	0	0	0
	Xe135	1.35	0	0	0	0	0	0	0	0	0	0	0
	Background	0	0	0	0	0	0	0	0	0	0	0	0
True Percent	Xe131m	0	0	0	0	0	0	0	0	0	0	0	0
	Xe133m	100	100	100	100	100	100	100	100	100	100	100	100
	Xe133	0	0	0	0	0	0	0	0	0	0	0	0
	Xe135	0	0	0	0	0	0	0	0	0	0	0	0
	Background	0	0	0	0	0	0	0	0	0	0	0	0
Difference (Est-True)	Xe131m	5.33	7.91	7.77	7.78	6.58	9.34	9.11	9.42	9.28	9.22	0	0
	Xe133m	-10.22	-7.93	-7.77	-7.78	-6.58	-9.34	-9.11	-9.42	-9.28	-9.22	0	0
	Xe133	3.54	0.02	0	0	0	0	0	0	0	0	0	0
	Xe135	1.35	0	0	0	0	0	0	0	0	0	0	0
	Background	0	0	0	0	0	0	0	0	0	0	0	0
ABS(diff.)	Xe131m	5.33	7.91	7.77	7.78	6.58	9.34	9.11	9.42	9.28	9.22	0	0
	Xe133m	10.22	7.93	7.77	7.78	6.58	9.34	9.11	9.42	9.28	9.22	0	0
	Xe133	3.54	0.02	0	0	0	0	0	0	0	0	0	0
	Xe135	1.35	0	0	0	0	0	0	0	0	0	0	0
	Background	0	0	0	0	0	0	0	0	0	0	0	0
AVG(ABS(diff.))		4.088	3.172	3.108	3.112	2.632	3.736	3.644	3.768	3.712	3.688	0	0
(diff.)^2	Xe131m	28.4089	62.5681	60.3729	60.5284	43.2964	87.2356	82.9921	88.7364	86.1184	85.0084	0	0
	Xe133m	104.4484	62.8849	60.3729	60.5284	43.2964	87.2356	82.9921	88.7364	86.1184	85.0084	0	0
	Xe133	12.5316	0.0004	0	0	0	0	0	0	0	0	0	0
	Xe135	1.8225	0	0	0	0	0	0	0	0	0	0	0
	Background	0	0	0	0	0	0	0	0	0	0	0	0
AVG((diff.)^2)		29.44228	25.09068	24.14916	24.21136	17.31856	34.89424	33.19684	35.49456	34.44736	34.00336	0	0

Trial 21	Subregions	1	2	3	4	5	6	7	8	9	10	Focus	SDAT
	Runtime (sec)	3.06	2.77	3.16	3.08	3.13	3.08	2.86	3.14	3.53	3.4	3.79	150.62
	Iterations	3	2	2	2	2	2	2	2	2	3	2	2
Estimates	Xe131m	100	100	100	100	100	100	100	100	100	100	100	100
	Xe133m	0	0	0	0	0	0	0	0	0	0	0	0
	Xe133	0	0	0	0	0	0	0	0	0	0	0	0
	Xe135	0	0	0	0	0	0	0	0	0	0	0	0
	Background	0	0	0	0	0	0	0	0	0	0	0	0
True Percent	Xe131m	100	100	100	100	100	100	100	100	100	100	100	100
	Xe133m	0	0	0	0	0	0	0	0	0	0	0	0
	Xe133	0	0	0	0	0	0	0	0	0	0	0	0
	Xe135	0	0	0	0	0	0	0	0	0	0	0	0
	Background	0	0	0	0	0	0	0	0	0	0	0	0
Difference (Est-True)	Xe131m	0	0	0	0	0	0	0	0	0	0	0	0
	Xe133m	0	0	0	0	0	0	0	0	0	0	0	0
	Xe133	0	0	0	0	0	0	0	0	0	0	0	0
	Xe135	0	0	0	0	0	0	0	0	0	0	0	0
	Background	0	0	0	0	0	0	0	0	0	0	0	0
ABS(diff.)	Xe131m	0	0	0	0	0	0	0	0	0	0	0	0
	Xe133m	0	0	0	0	0	0	0	0	0	0	0	0
	Xe133	0	0	0	0	0	0	0	0	0	0	0	0
	Xe135	0	0	0	0	0	0	0	0	0	0	0	0
	Background	0	0	0	0	0	0	0	0	0	0	0	0
AVG(ABS(diff.))		0	0	0	0	0	0	0	0	0	0	0	0
(diff)^2	Xe131m	0	0	0	0	0	0	0	0	0	0	0	0
	Xe133m	0	0	0	0	0	0	0	0	0	0	0	0
	Xe133	0	0	0	0	0	0	0	0	0	0	0	0
	Xe135	0	0	0	0	0	0	0	0	0	0	0	0
	Background	0	0	0	0	0	0	0	0	0	0	0	0
AVG((diff.)^2)		0	0	0	0	0	0	0	0	0	0	0	0

Trial 22	Subregions	1	2	3	4	5	6	7	8	9	10	Focus	SDAT
	Runtime (sec)	2.96	2.95	3.06	3.1	3.29	2.93	2.97	2.94	3.15	3.32	3.62	202.52
	Iterations	2	3	3	3	3	3	2	3	3	3	1	3
Estimates	Xe131m	0	0	0	0	0	0	0	0	0	0	0	0
	Xe133m	0	0	0	0	0	0	0	0	0	0	0	0
	Xe133	1.12	1.44	1.6	1.64	1.9	1.8	1.53	1.03	1.17	1.39	0	0
	Xe135	0.75	1.02	0.86	1.26	1.37	1.31	1.52	1.45	1.36	1.31	0	0
	Background	98.14	97.54	97.54	97.1	96.73	96.88	96.95	97.52	97.47	97.3	100	100
True Percent	Xe131m	0	0	0	0	0	0	0	0	0	0	0	0
	Xe133m	0	0	0	0	0	0	0	0	0	0	0	0
	Xe133	0	0	0	0	0	0	0	0	0	0	0	0
	Xe135	0	0	0	0	0	0	0	0	0	0	0	0
	Background	100	100	100	100	100	100	100	100	100	100	100	100
Difference (Est-True)	Xe131m	0	0	0	0	0	0	0	0	0	0	0	0
	Xe133m	0	0	0	0	0	0	0	0	0	0	0	0
	Xe133	1.12	1.44	1.6	1.64	1.9	1.8	1.53	1.03	1.17	1.39	0	0
	Xe135	0.75	1.02	0.86	1.26	1.37	1.31	1.52	1.45	1.36	1.31	0	0
	Background	-1.86	-2.46	-2.46	-2.9	-3.27	-3.12	-3.05	-2.48	-2.53	-2.7	0	0
ABS(diff.)	Xe131m	0	0	0	0	0	0	0	0	0	0	0	0
	Xe133m	0	0	0	0	0	0	0	0	0	0	0	0
	Xe133	1.12	1.44	1.6	1.64	1.9	1.8	1.53	1.03	1.17	1.39	0	0
	Xe135	0.75	1.02	0.86	1.26	1.37	1.31	1.52	1.45	1.36	1.31	0	0
	Background	1.86	2.46	2.46	2.9	3.27	3.12	3.05	2.48	2.53	2.7	0	0
AVG(ABS(diff.))		0.746	0.984	0.984	1.16	1.308	1.246	1.22	0.992	1.012	1.08	0	0
(diff)^2	Xe131m	0	0	0	0	0	0	0	0	0	0	0	0
	Xe133m	0	0	0	0	0	0	0	0	0	0	0	0
	Xe133	1.2544	2.0736	2.56	2.6896	3.61	3.24	2.3409	1.0609	1.3689	1.9321	0	0
	Xe135	0.5625	1.0404	0.7396	1.5876	1.8769	1.7161	2.3104	2.1025	1.8496	1.7161	0	0
	Background	3.4596	6.0516	6.0516	8.41	10.6929	9.7344	9.3025	6.1504	6.4009	7.29	0	0
AVG((diff.)^2)		1.0553	1.83312	1.87024	2.53744	3.23596	2.9381	2.79076	1.86276	1.92388	2.18764	0	0

Trial 23	Subregions	1	2	3	4	5	6	7	8	9	10	Focus	SDAT
	Runtime (sec)	2.92	3	2.93	3.25	3.05	3.38	3.32	3.13	3.15	3.09	3.66	153.54
	Iterations	2	4	4	4	1	1	2	1	2	3	2	2
Estimates	Xe131m	0	0	0	0	0	0	0	0	0	0	0	0
	Xe133m	0	0	0	0	0	0	0	0	0	0	0	0
	Xe133	0	0.06	0.06	0.08	0	0.05	0.05	0	0.02	0.06	0	0
	Xe135	100	99.94	99.94	99.92	100	99.95	99.95	100	99.98	99.94	100	100
	Background	0	0	0	0	0	0	0	0	0	0	0	0
True Percent	Xe131m	0	0	0	0	0	0	0	0	0	0	0	0
	Xe133m	0	0	0	0	0	0	0	0	0	0	0	0
	Xe133	0	0	0	0	0	0	0	0	0	0	0	0
	Xe135	100	100	100	100	100	100	100	100	100	100	100	100
	Background	0	0	0	0	0	0	0	0	0	0	0	0
Difference (Est-True)	Xe131m	0	0	0	0	0	0	0	0	0	0	0	0
	Xe133m	0	0	0	0	0	0	0	0	0	0	0	0
	Xe133	0	0.06	0.06	0.08	0	0.05	0.05	0	0.02	0.06	0	0
	Xe135	0	-0.06	-0.06	-0.08	0	-0.05	-0.05	0	-0.02	-0.06	0	0
	Background	0	0	0	0	0	0	0	0	0	0	0	0
ABS(diff.)	Xe131m	0	0	0	0	0	0	0	0	0	0	0	0
	Xe133m	0	0	0	0	0	0	0	0	0	0	0	0
	Xe133	0	0.06	0.06	0.08	0	0.05	0.05	0	0.02	0.06	0	0
	Xe135	0	0.06	0.06	0.08	0	0.05	0.05	0	0.02	0.06	0	0
	Background	0	0	0	0	0	0	0	0	0	0	0	0
AVG(ABS(diff.))		0	0.024	0.024	0.032	0	0.02	0.02	0	0.008	0.024	0	0
(diff)^2	Xe131m	0	0	0	0	0	0	0	0	0	0	0	0
	Xe133m	0	0	0	0	0	0	0	0	0	0	0	0
	Xe133	0	0.0036	0.0036	0.0064	0	0.0025	0.0025	0	0.0004	0.0036	0	0
	Xe135	0	0.0036	0.0036	0.0064	0	0.0025	0.0025	0	0.0004	0.0036	0	0
	Background	0	0	0	0	0	0	0	0	0	0	0	0
AVG((diff.)^2)		0	0.00144	0.00144	0.00256	0	0.001	0.001	0	0.00016	0.00144	0	0

Trial 24	Subregions	1	2	3	4	5	6	7	8	9	10	Focus	SDAT
	Runtime (sec)	2.78	2.85	2.65	2.82	3.38	2.9	3.3	3.37	3.07	3.18	3.65	258.15
	Iterations	3	3	3	3	3	3	3	3	3	3	2	4
Estimates	Xe131m	0	0	0	0	0.51	0.53	0.45	0.72	0.54	0.44	0	0
	Xe133m	0	0	0	0	0	0	0	0	0	0	0	0
	Xe133	99.99	99.99	99.99	100	99.48	99.47	99.55	99.28	99.46	99.56	100	100
	Xe135	0	0	0	0	0	0	0	0	0	0	0	0
	Background	0.01	0.01	0.01	0	0	0	0	0	0	0	0	0
True Percent	Xe131m	0	0	0	0	0	0	0	0	0	0	0	0
	Xe133m	0	0	0	0	0	0	0	0	0	0	0	0
	Xe133	100	100	100	100	100	100	100	100	100	100	100	100
	Xe135	0	0	0	0	0	0	0	0	0	0	0	0
	Background	0	0	0	0	0	0	0	0	0	0	0	0
Difference (Est-True)	Xe131m	0	0	0	0	0.51	0.53	0.45	0.72	0.54	0.44	0	0
	Xe133m	0	0	0	0	0	0	0	0	0	0	0	0
	Xe133	-0.01	-0.01	-0.01	0	-0.52	-0.53	-0.45	-0.72	-0.54	-0.44	0	0
	Xe135	0	0	0	0	0	0	0	0	0	0	0	0
	Background	0.01	0.01	0.01	0	0	0	0	0	0	0	0	0
ABS(diff.)	Xe131m	0	0	0	0	0.51	0.53	0.45	0.72	0.54	0.44	0	0
	Xe133m	0	0	0	0	0	0	0	0	0	0	0	0
	Xe133	0.01	0.01	0.01	0	0.52	0.53	0.45	0.72	0.54	0.44	0	0
	Xe135	0	0	0	0	0	0	0	0	0	0	0	0
	Background	0.01	0.01	0.01	0	0	0	0	0	0	0	0	0
AVG(ABS(diff.))		0.004	0.004	0.004	0	0.206	0.212	0.18	0.288	0.216	0.176	0	0
(diff)^2	Xe131m	0	0	0	0	0.2601	0.2809	0.2025	0.5184	0.2916	0.1936	0	0
	Xe133m	0	0	0	0	0	0	0	0	0	0	0	0
	Xe133	0.0001	0.0001	0.0001	0	0.2704	0.2809	0.2025	0.5184	0.2916	0.1936	0	0
	Xe135	0	0	0	0	0	0	0	0	0	0	0	0
	Background	0.0001	0.0001	0.0001	0	0	0	0	0	0	0	0	0
AVG((diff.)^2)		0.00004	0.00004	0.00004	0	0.1061	0.11236	0.081	0.20736	0.11664	0.07744	0	0

Trial 25	Subregions	1	2	3	4	5	6	7	8	9	10	Focus	SDAT
	Runtime (sec)	2.79	2.88	2.89	3.32	2.95	2.9	3.08	3.36	3.09	3.04	3.38	151.57
Estimates	Iterations	1	2	3	2	2	3	2	3	3	3	1	2
	Xe131m	0.98	0.37	0.38	0.62	0.42	0.11	0.71	0.32	0.41	0.41	0	0
	Xe133m	99.02	99.63	99.62	99.38	99.58	99.89	99.29	99.68	99.59	99.59	100	100
	Xe133	0	0	0	0	0	0	0	0	0	0	0	0
	Xe135	0	0	0	0	0	0	0	0	0	0	0	0
True Percent	Background	0	0	0	0	0	0	0	0	0	0	0	0
	Xe131m	0	0	0	0	0	0	0	0	0	0	0	0
	Xe133m	100	100	100	100	100	100	100	100	100	100	100	100
	Xe133	0	0	0	0	0	0	0	0	0	0	0	0
	Xe135	0	0	0	0	0	0	0	0	0	0	0	0
Difference (Est-True)	Background	0	0	0	0	0	0	0	0	0	0	0	0
	Xe131m	0.98	0.37	0.38	0.62	0.42	0.11	0.71	0.32	0.41	0.41	0	0
	Xe133m	-0.98	-0.37	-0.38	-0.62	-0.42	-0.11	-0.71	-0.32	-0.41	-0.41	0	0
	Xe133	0	0	0	0	0	0	0	0	0	0	0	0
	Xe135	0	0	0	0	0	0	0	0	0	0	0	0
ABS(diff.)	Background	0	0	0	0	0	0	0	0	0	0	0	0
	Xe131m	0.98	0.37	0.38	0.62	0.42	0.11	0.71	0.32	0.41	0.41	0	0
	Xe133m	0.98	0.37	0.38	0.62	0.42	0.11	0.71	0.32	0.41	0.41	0	0
	Xe133	0	0	0	0	0	0	0	0	0	0	0	0
	Xe135	0	0	0	0	0	0	0	0	0	0	0	0
AVG(ABS(diff.))		0.392	0.148	0.152	0.248	0.168	0.044	0.284	0.128	0.164	0.164	0	0
(diff)^2	Xe131m	0.9604	0.1369	0.1444	0.3844	0.1764	0.0121	0.5041	0.1024	0.1681	0.1681	0	0
	Xe133m	0.9604	0.1369	0.1444	0.3844	0.1764	0.0121	0.5041	0.1024	0.1681	0.1681	0	0
	Xe133	0	0	0	0	0	0	0	0	0	0	0	0
	Xe135	0	0	0	0	0	0	0	0	0	0	0	0
	Background	0	0	0	0	0	0	0	0	0	0	0	0
AVG((diff.)^2)		0.38416	0.05476	0.05776	0.15376	0.07056	0.00484	0.20164	0.04096	0.06724	0.06724	0	0

[illegible]



Trial 27	Subregions	1	2	3	4	5	6	7	8	9	10	Focus	SDAT
	Runtime (sec)	3.09	2.93	3.06	3.11	3.3	3.06	3.33	3.27	3.33	3.22	3.79	206.1
	Iterations	1	2	1	1	2	2	2	2	2	2	4	3
Estimates	Xe131m	40.11	40.15	39.87	40.02	40.06	40.02	40.11	39.99	40.07	40.11	40.24	40.2
	Xe133m	19.75	19.77	19.84	19.84	19.8	19.89	19.79	19.84	19.85	19.83	20.13	20.17
	Xe133	20.21	20.15	20.36	20.17	20.12	20.18	20.17	20.3	20.12	20.07	19.6	19.61
	Xe135	19.93	19.93	19.93	19.97	20.02	19.91	19.93	19.88	19.96	19.99	20.03	20.03
	Background	0	0	0	0	0	0	0	0	0	0	0	0
True Percent	Xe131m	40	40	40	40	40	40	40	40	40	40	40	40
	Xe133m	20	20	20	20	20	20	20	20	20	20	20	20
	Xe133	20	20	20	20	20	20	20	20	20	20	20	20
	Xe135	20	20	20	20	20	20	20	20	20	20	20	20
	Background	0	0	0	0	0	0	0	0	0	0	0	0
Difference (Est-True)	Xe131m	0.11	0.15	-0.13	0.02	0.06	0.02	0.11	-0.01	0.07	0.11	0.24	0.2
	Xe133m	-0.25	-0.23	-0.16	-0.16	-0.2	-0.11	-0.21	-0.16	-0.15	-0.17	0.13	0.17
	Xe133	0.21	0.15	0.36	0.17	0.12	0.18	0.17	0.3	0.12	0.07	-0.4	-0.39
	Xe135	-0.07	-0.07	-0.07	-0.03	0.02	-0.09	-0.07	-0.12	-0.04	-0.01	0.03	0.03
	Background	0	0	0	0	0	0	0	0	0	0	0	0
ABS(diff.)	Xe131m	0.11	0.15	0.13	0.02	0.06	0.02	0.11	0.01	0.07	0.11	0.24	0.2
	Xe133m	0.25	0.23	0.16	0.16	0.2	0.11	0.21	0.16	0.15	0.17	0.13	0.17
	Xe133	0.21	0.15	0.36	0.17	0.12	0.18	0.17	0.3	0.12	0.07	0.4	0.39
	Xe135	0.07	0.07	0.07	0.03	0.02	0.09	0.07	0.12	0.04	0.01	0.03	0.03
	Background	0	0	0	0	0	0	0	0	0	0	0	0
AVG(ABS(diff.))		0.128	0.12	0.144	0.076	0.08	0.08	0.112	0.118	0.076	0.072	0.16	0.158
(diff)^2	Xe131m	0.0121	0.0225	0.0169	0.0004	0.0036	0.0004	0.0121	0.0001	0.0049	0.0121	0.0576	0.04
	Xe133m	0.0625	0.0529	0.0256	0.0256	0.04	0.0121	0.0441	0.0256	0.0225	0.0289	0.0169	0.0289
	Xe133	0.0441	0.0225	0.1296	0.0289	0.0144	0.0324	0.0289	0.09	0.0144	0.0049	0.16	0.1521
	Xe135	0.0049	0.0049	0.0049	0.0009	0.0004	0.0081	0.0049	0.0144	0.0016	0.0001	0.0009	0.0009
	Background	0	0	0	0	0	0	0	0	0	0	0	0
AVG((diff.)^2)		0.02472	0.02056	0.0354	0.01116	0.01168	0.0106	0.018	0.02602	0.00868	0.0092	0.04708	0.04438